The Importance of Adaptor Proteins and Cell Signalling in the Control of Peptidoglycan Synthesis

Zoe Jane Rutter

A Thesis Submitted for the Degree of Doctor of Philosophy

Newcastle University Biosciences Institute

December 2020

Abstract

Bacterial cell division is a complex process that requires tight co-ordination and regulation of chromosome replication and segregation, and the synthesis and remodelling of the bacterial cell wall. The peptidoglycan sacculus is synthesised by peptidoglycan synthases and it is a vital component of the bacterial cell structure, to withstand the turgor of the cell to prevent its lysis FtsZ is one of the first proteins to localise at midcell during cell division where it forms a ring-like structure, the Z-ring, at the inner face of the cytoplasmic membrane. After Z-ring formation, the divisome is recruited to the division site to form the septum and the elongasome is positioned at the side wall for elongation. Both the elongasome and the divisome are dynamic macromolecular complexes composed of numerous proteins at unknown stoichiometries and it is thought there are proteins in both complexes that are yet to be discovered. Understanding bacterial cell division at the molecular and cellular level is an important area of research to enable the development of novel antibiotics as well as comprehending one of biology's fundamental questions.

GpsB is a conserved Gram-positive cytosolic protein that plays an important role in the elongation-division cycle by acting as a scaffold to control the relative spatial arrangements of peptidoglycan synthases (PBPs). In this thesis the molecular interactions of GpsB with cytoplasmic mini-domains of PBPs from two human pathogens (*Listeria monocytogenes* and *Streptococcus pneumoniae*) are described using structural and biochemical techniques. The importance of the critical interacting residues for the GpsB:PBP interaction for cell wall growth and viability of *L. monocytogenes* and *S. pneumoniae* were analysed in collaboration with the Halbedel, and Massidda and Winkler groups, respectively. A novel function of PBP binding was introduced into DivIVA, a cell division regulator and GpsB homolog, by protein engineering in an attempt to understand the functional divergence between GpsB and DivIVA. Potential building blocks for the development of GpsB:PBP inhibitors were identified in the form of small fragments by an X-ray crystallography-based fragment screening experiment at Diamond Light Source.

Eukaryote-like serine/threonine protein kinases (eSTPKs) and partner phosphatases (eSTPs) are conserved in Gram-positive bacteria. They consist of an intracellular N-terminal kinase domain and an extracellular sensing region linked by a short transmembrane helix. The external regulatory region is comprised of three or four PASTA domains that bind to

peptidoglycans and compounds containing beta-lactams. eSTPKs are involved in the regulation of many cellular processes including development of regulation, control of cell growth, stress response, virulence and sporulation. The eSTPK/eSTP pair from *L. monocytogenes* are PrkA and PrpC.

This thesis concerns the importance of autophosphorylation for the function of the kinase domain of PrkA (PrkA-KD) and that phosphorylation of serine 173 is crucial for activation, agreeing with the mechanism of activation of Stk1 in *Staphylococcus aureus.* The previously uncharacterised phosphoprotein Lmo1503 (renamed ReoM) is a homologue of IreB from *Enterococcus faecalis*, a negative regulator of cephalosporin resistance. It is confirmed that ReoM is a substrate of the PrkA/PrpC pair and the crystal structure of the full length ReoM protein is presented. Isothermal titration calorimetry determined the interaction of ReoM and PrkA-KD is within the nanomolar range and there is a ten-fold reduction in affinity with a PrkA-KD^{S173A} mutation. The Halbedel group have linked ReoM phosphorylation to the activation of ClpCP-dependent degradation of the primary UDP-Glc*N*Ac 1-carboxyvinyltransferase in *L. monocytogenes*, MurA. We therefore propose that cell wall integrity sensing by PrkA is coupled to the first committed step of peptidoglycan synthesis through the intermediate proteins ReoM and ClpCP.

Acknowledgements

First and foremost, I would like to thank my supervisor Professor Richard Lewis for giving me the opportunity to undertake this PhD project. I am deeply grateful for the scientific guidance and constructive feedback that Rick provided to me throughout my studies. The completion of this work would not have been possible without his advice and support during the project and in the writing of this thesis. I would like to extend my sincere thanks to Professor Bert van den Berg and Dr David Bolam for taking over as my supervisors in the last year of my PhD and for their insightful comments and suggestions upon reading parts of my thesis. I would like to offer my special thanks to Dr Robert Cleverley for introducing me to a number of experimental methods and for his guidance in the beginning of this project. I am also grateful to Dr Arnaud Baslé for the training he provided in protein crystallography and for collecting crystallographic data. I must also thank the Halbedel, and Massidda and Winkler groups for their collaboration and contribution to this thesis. Thanks also go to Dr Claire Jennings for performing mass spectrometry experiments, Dr Owen Davies for collecting and processing SEC-MALS and SAXS data and the XChem team at Diamond Light Source especially Dr Alice Douangamath. My appreciation also goes out to my lab mates, Dr Vincent Rao, Simon Booth and Sema Ejder for their professional support and friendship. I would also like to thank Joseph McGrory, an undergraduate student who worked with me on aspects of Chapter 6. Finally, I would like to thank my friends and family for their support and encouragement and for providing emotional and practical help throughout my studies.

List of Abbreviations

Abbreviation	Definition
Å	Angstrom
α1	Helix 1
α2	Helix 2
Abs	Absorbance
AMR	Antimicrobial resistance
Amu	Atomic mass unit
APS	Ammonium persulfate
ATP	Adenosine triphosphate
Ba	*Bacillus anthracis*
BACTH	Bacterial Adenylate Cyclase-based two hybrid system
Bc	*Bacillus cereus*
Bs	*Bacillus subtilis*
BSA	Bovine serum albumin
Bt	*Bacillus thuringiensis*
CD	Circular dichroism
Cd	*Clostridioides difficile*
Cd	*Corynebacterium diphtheriae*
Co-IP	Co-immunoprecipitation
CPase	DD-carboxypeptidase
CTD	C-terminal domain
C-ter	C-terminus
Da	Daltons
DAM	Dummy atom models
DLS	Diamond Light Source
DMSO	Dimethyl sulfoxide
DNA	Deoxyribonucleic acid
dNTP	Deoxynucleotide
DP	Differential power
DTT	Dithiothreitol
E	Elution
EDTA	Ethylenediaminetetraacetic acid
Ef	*Enterococcus faecalis*
EPase	Endopeptidase
ESI	Electrospray ionisation
eSTP	Eukaryote-like serine/threonine protein phosphatase
eSTPK	Eukaryote-like serine/threonine protein kinase
FDAA	Fluorescent D-amino acid
Fnorm	Normalised fluorescence
FP	Fluorescence polarisation
FT	Flow through
GFP	Green fluorescent protein
Glc*N*Ac	*N*-acetylglucosamine
GT/GTase	Glycosyltransfer/ Glycosyltransferase
HEPES	(4-(2-hydroxyethyl)-1-piperazineethanesulfonic acid
HMM	High molecular mass
HPLC	High-performance liquid chromatography

IFM	Immunofluorescence microscopy
IM	Inner membrane
IPTG	Isopropyl β-D-1-thiogalactopyranoside
ITC	Isothermal titration calorimetry
JCSG+	Joint Center for Structural Genomics
Kb	Kilobase
Kd	Equilibrium dissociation constant
KD	Kinase domain
kDa	Kilodalton
LB	Luria Bertani broth
LBD	Lipid binding domain
LC-MS	Liquid chromatography-mass spectrometry
Lm	*Listeria monocytogenes*
LMM	Low molecular mass
Lp	*Lactobacillus plantarum*
mAU	Milli-absorbance unit
MBP	Maltose-binding protein
Meso-DAP	Meso-diaminopimelic
MOPS	3-(N-morpholino)propanesulfonic acid
mP	Milipolarisation
MS/MS	Tandem mass spectrometry
MST	MicroScale Thermophoresis
Mt	*Mycobacterium tuberculosis*
Mur*N*Ac	*N*-acetylmuramic acid
MWCO	Molecular mass cutoff
m/z	Mass-to-charge ratio
NAG	*N*-acetylglucosamine
N-*Bs*DivIVA	N-terminal *Bs*DivIVA
N-*Bs*GpsB	N-terminal *Bs*GpsB
NCBI	National Center for Biotechnology Information
Ni-NTA	Nickel nitrilotriacetic acid
nm	Nanometer
NMR	Nuclear magnetic resonance
N-*Sp*GpsB	N-terminal domain of *Sp*GpsB
NTD	N-terminal domain
N-ter	N-terminus
N-value	Number of sites
OD_{600}	Optical density at 600 nm
OM	Outer membrane
oriC	Origin of replication
PACT	pH, anion, cation
PAGE	Polyacrylamide gel electrophoresis
PANDDA	Pan-Dataset Density *Analysis*
PASTA	PBP and serine/threonine kinase associated
PB	Penicillin binding
PBP	Penicillin binding protein
PCR	Polymerase chain reaction
PDB	Protein data bank
PDB ID	Protein data bank ascension number

PEG	Polyethylene glycol
PEP	Phospho-enolpyruvate
pfu	*Pyrococcus furiosus*
PG	Peptidoglycan
pH	Potential of hydrogen
PPM	Metallo-dependent protein phosphatase
P-ReoM	Phosphorylated ReoM
PrkA-KD	Kinase domain of PrkA
Psig	Pounds per square inch gauge
P-Thr7	Phosphorylated threonine 7
Rmsd	Root mean square deviation
rpm	Revolutions per minute
Sa	*Staphylococcus aureus*
SAXS	Small-angle X-ray scattering
Sc	*Streptomyces coelicolor*
SDS	Sodium dodecyl sulphate
Se	*Staphylococcus epidermidis*
SEC-MALS	Size-exclusion chromatography coupled to multi-angle light scattering
SEDS	Shape, elongation, division and sporulation
Sm	*Streptococcus mitis*
Sp	*Streptococcus pneumoniae*
SPR	Surface plasmon resonance
Sv	*Streptomyces venezuelae*
TAE	Tris-acetate, EDTA
TAMRA	Tetramethylrhodamine-5-*maleimide*
TEV	Tobacco etch virus
TEMED	Tetramethylethylenediamine
TP/TPase	Transpeptidation/transpeptidase
Tris	Tris(hydroxymethyl)aminomethane
U	units
UDP	Uridine diphosphate
UV	Ultra-violet
V	Volts
VAN-FL	Fluorescent vancomycin
v/v	Volume per volume
Vs	Versus
WT	Wild-type
WTA	Wall teichoic acid
w/v	Weight per volume
XCE	XChem Explorer
ΔG	Gibbs free energy
ΔH	Binding enthalpy
-TΔS	Entropy factor
3D-SIM	Three-dimensional structured illumination microscopy

Table of Contents

List of Figures

List of Tables

Chapter 1: Introduction

1.1 Overview

Bacteria are a dominant life form on the planet and, while mostly beneficial, they can also cause disease. It is well known that antibiotic resistance is a significant problem in the treatment of bacterial infections (Wright, 2005). Over time bacteria have developed mechanisms to counteract antibiotic action, acquiring multi-drug resistance (Medina & Pieper, 2016). The unsuitable consumption and overuse of antibiotics has, at least in part, driven this resistance making the need for novel antibiotics paramount. Penicillin was the first antibiotic to be discovered- by Fleming and co-workers in the 1930s- which targets bacterial cell wall synthesis, a vital part of cell division (Duguid, 1946). Bacterial cell division is still a recognised target for the development of new antibiotics. Numerous breakthroughs in the field have led to the development of cell division models to create a better understanding of the underlying mechanisms of division (Schneider & Sahl, 2010). Characterising cell division will enable the design and discovery of novel and potent antibiotics.

1.2 The bacterial cell division cycle

The bacterial cell-cycle is a highly complex and robust process than enables the production of an identical daughter cell, at face value a simple process that is actually so complex that after decades of research it is still not yet completely understood. There are a number of different division mechanisms that include binary fission, hyphal growth and budding (Willis & Huang, 2017) that lead to multiple bacterial cell shapes inclusive of rods, ellipsoids, stars, spirals, rectangular boxes and also filamentous bacteria (Young, 2006) (Figure 1.1). The cell-cycle can be split into 3 periods called B, C and D. Period B is the period between division and initiation of DNA replication. The period necessary for replication is termed period C and period D is the time between the end of replication and the completion of division (Wang & Levin, 2009) (Figure 1.2).

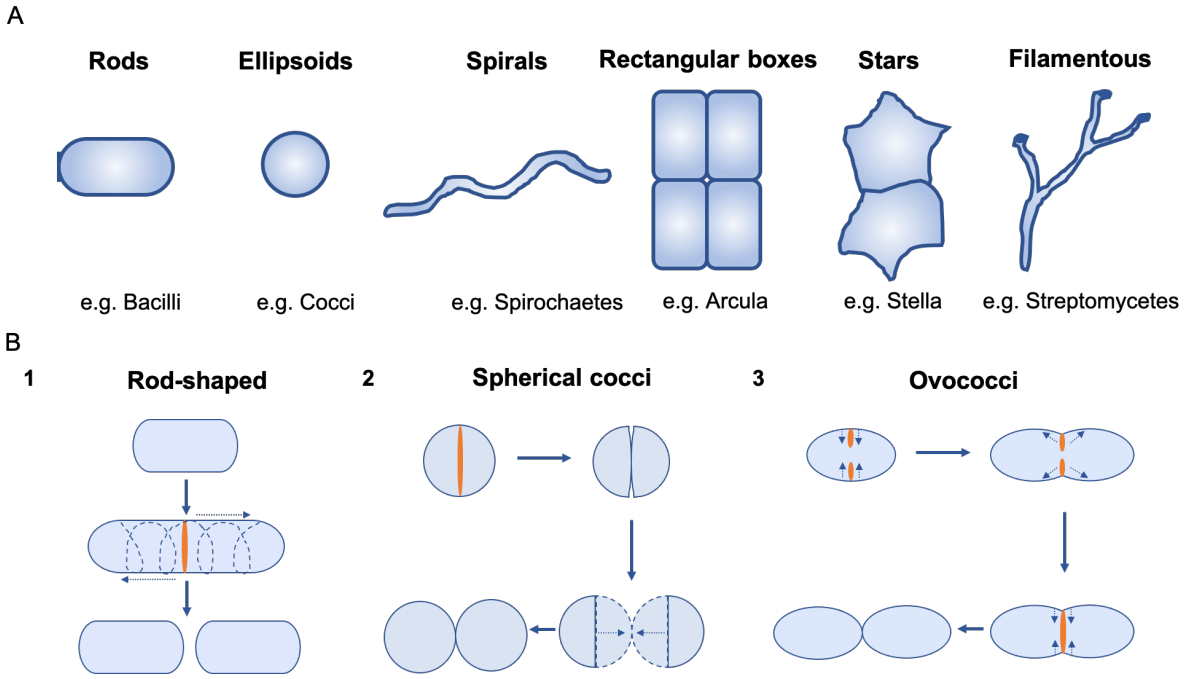

Figure 1.1: Bacterial cell shapes and division mechanisms.
Panel **A** shows a variety of cell shapes adopted by bacteria. Panel **B** shows a schematic representation of the growth and division mechanisms of rod-shaped, spherical cocci and ovococci cells. In rod-shaped cells division and elongation occur independently (1). Spherical cocci grow through division and daughter cells grow after division into spheres (2). Ovococci elongate by peripheral growth during cell division (3). The septum is indicated by an orange oval and dotted arrows show the movement of the cell wall.

Bacterial cell division requires the tight co-ordination and regulation of chromosome replication and segregation with the growth and division of the bacterial cell. DNA replication is well characterised in the model organisms for Gram-negative and Gram-positive bacteria, *Escherichia coli* and *Bacillus subtilis*, respectively. Replication is initiated by the recruitment of replisomes to the origin of replication (*oriC*) which is mediated by DnaA (Figure 1.2). This causes origin firing, which initiates the replication of a circular chromosome. Two replication forks per *oriC* are created by the spooling of DNA bidirectionally by the replisomes until the forks reach the terminus region (Wang & Levin, 2009). After the generation of two complete copies of the DNA, the chromosomes are separated so there is one copy of each chromosome per daughter cell. During this process the DNA remains in the nucleoid, a highly condensed, ribosome-depleted region (Bakshi et al., 2012). The molecular mechanism that links bacterial cell growth with DNA replication initiation is not completely understood. During the cell-cycle, cell metabolism and growth is synchronised with DNA replication initiation and the cell continues to grow throughout replication and with the assembly of the division machinery (Murray, 2016). The elongasome is required at the side wall for the elongation phase of the

bacterial cell-cycle (in rod shaped bacteria), the complex is positioned by the cytoskeletal network, critically MreB in rod shaped bacteria (Claessen et al., 2008) (Figure 1.2). Cell division is initiated towards the end of chromosome segregation. Prior to the completion of DNA replication, the duplicated *oriCs* move to be evenly spaced in the cell (Lau et al., 2003). FtsZ is one of the first proteins to localise at mid-cell during cell division where it forms a Z-ring structure at the inner face of the cytoplasmic membrane, assembled between the duplicated *oriCs*. When the formation of the Z-ring is complete, a highly dynamic macromolecular machine composed of proteins responsible for cell division, termed the divisome is recruited to the division site to form the cross wall (Söderström & Daley, 2017). The final stage of the cell-cycle involves the closure of the septum causing cells to divide producing two identical daughter cells. Multiple regulatory pathways are required for co-ordinating cell growth, DNA replication initiation and division, with DnaA, MreB and FtsZ as prime candidates (Willis & Huang, 2017).

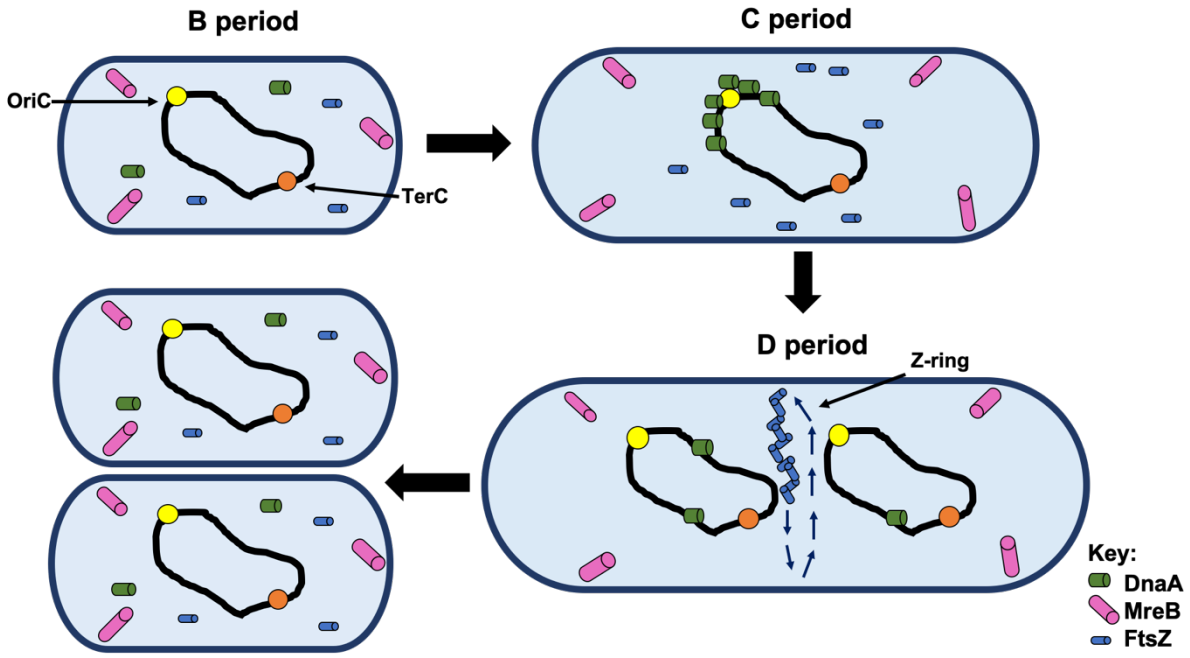

Figure 1.2: Visual representation of the three periods of rod-shaped bacterial cell-cycle. Period B is the period between division and initiation of DNA replication where DnaA is not yet associated with chromosome and FtsZ is dispersed in the cell. During period C DnaA accumulates at the origin of replication (OriC) and initiates replication. MreB is at the lateral cell wall where it serves as a platform for cell elongation. In period D FtsZ localises at the mid-cell and forms the Z-ring, the blue arrows indicate the treadmilling of the FtsZ filaments that leads to septum closure and two identical daughter cells are formed.

1.3 The bacterial cell envelope

The bacterial cell envelope is a complex structure that consists of a number of layers that serve to protect the cell cytoplasm. The composition of the cell envelope differs between Gram-negative and Gram-positive bacteria (Figure 1.3). With Gram-negatives, the complex cell envelope consists of a peptidoglycan cell wall located between a cytoplasmic inner membrane (IM) and an outer membrane (OM) (Glauert & Thornley, 1969). The exterior OM is a lipid bilayer that functions as a protective barrier to the environment and possess two main protein groups, lipoproteins and β-barrel proteins (Sankaran & Wu, 1994). Examples of β-barrel proteins include the porins OmpF and OmpC that allow small molecules to diffuse across the OM (Cowan et al., 1992). The IM consists of a phospholipid bilayer that contains proteins important for transport, lipid biosynthesis and protein secretion. Embedded between the two membranes is a single layer of peptidoglycan around 3-6 nm in thickness (Turner et al., 2014). Anchored to the stem peptides of the peptidoglycan are proteins of numerous functions (Hendrickx et al., 2011). Conversely, Gram-positive bacteria lack an OM and instead they have developed a thicker layer of peptidoglycan (10-40 nm) (Turner et al., 2014) around the IM to withstand the turgor of the cell to prevent lysis and act as a selective barrier (Claessen et al., 2008). The peptidoglycan of Gram-positives contains teichoic acids of which there are two types, wall teichoic acids (WTA) and lipoteichoic acids. WTA are covalently attached to peptidoglycan via a phosphodiester linkage to the *C*6 hydroxyl of Mur*N*Ac residues (Silhavy et al., 2010) while lipoteichoic acids are anchored to the head groups of membrane lipids (Neuhaus & Baddiley, 2003). With the absence of an OM, extracellular proteins in Gram-positives are often attached to lipid anchors, contain membrane spanning helices or are bound to peptidoglycan or teichoic acids (Silhavy et al., 2010). The branching of stem peptides in Gram-positive peptidoglycan enables the generation of attachment sites for proteins (Dramsi et al., 2008).

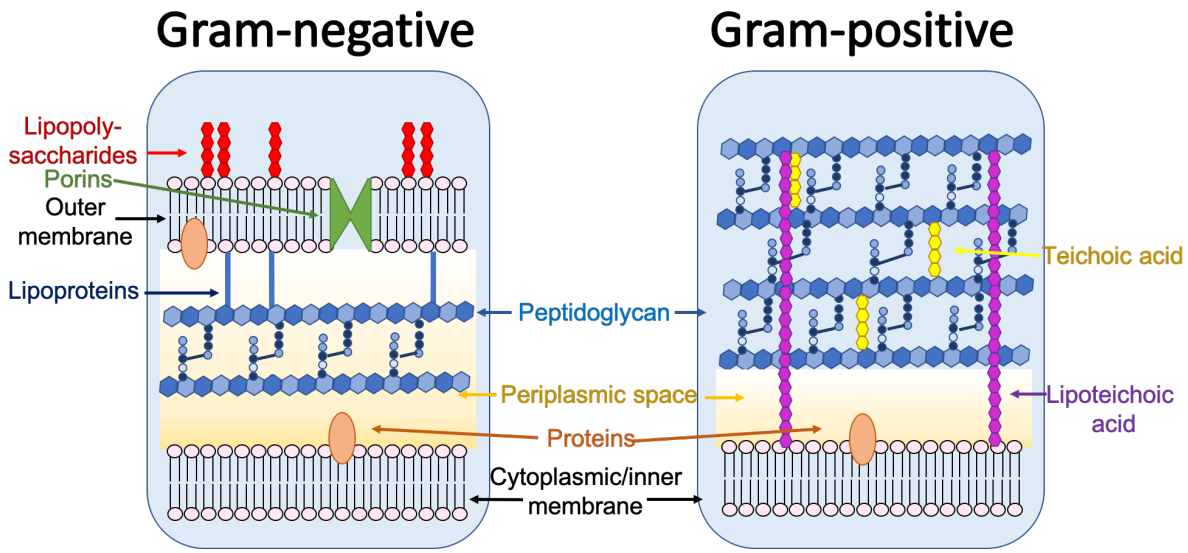

Figure 1.3: Comparison of the composition of the cell envelope of Gram-negative and Gram-positive bacteria.
Each of the cell envelope features are labelled on the diagram.

Peptidoglycan consists of polysaccharides with alternating saccharide groups of *N*-acetylglucosamine (Glc*N*Ac) and *N*-acetylmuramic acid (Mur*N*Ac) linked by β-1 → 4 bonds (Egan et al., 2017) (Figure 1.4). The glycan strands are cross-linked by short stem peptides as the D-lactoyl group of each Mur*N*Ac residue is replaced by a peptide stem. In Gram-positives the stem peptides in the final peptidoglycan structure tend to be composed of L-Ala at position 1 followed by D-Glu, L-Lys and D-Ala with a terminal D-Ala that is lost during crosslinking (Lupoli et al., 2011). Bacilli are an exception to this rule and meso-diaminopimelic acid (meso-DAP) takes the place of L-Lys at position 3 (Vollmer et al., 2008). Crosslinking tends to occur between the carboxyl group of D-Ala at position 4 with amino group of the diamino acid at position 3- called a 3-4 cross linkage (Vollmer et al., 2008). The overall structure of peptidoglycan is highly conserved, and its variations include differences in the diversity of the peptide crosslinks and glycan strand chain length (Zhao et al., 2017).

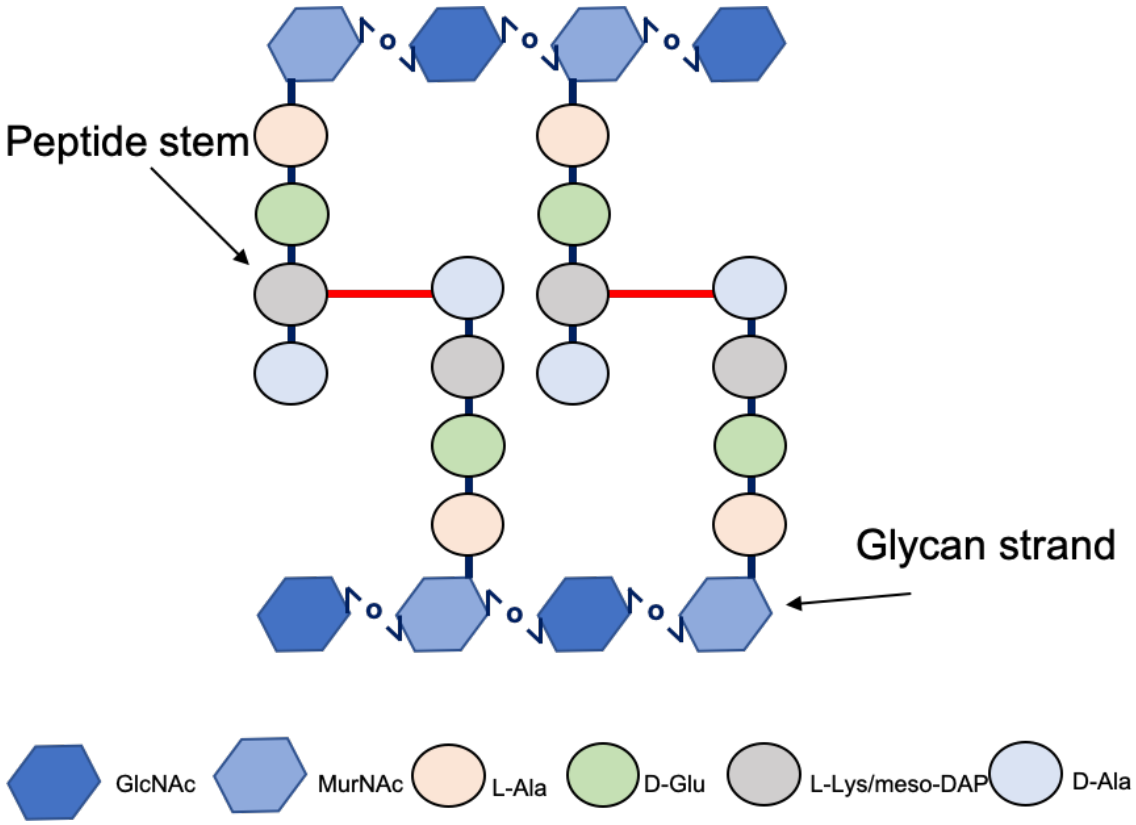

Figure 1.4: Composition of the Gram-positive bacterial cell wall.
Alternating saccharides of N-acetylglucosamine (Glc*N*Ac) and N-acetylmuramic acid (Mur*N*Ac) linked by β-1 → 4 glycosidic bonds. The most common crosslink (3-4 crosslink) is shown in red between D-Ala at position 4 with amino group of L-Lys/meso-DAP at position 3.

The synthesis of new peptidoglycan is a complex process that requires approximately 20 enzyme reactions (Figure 1.5). There are three main steps to peptidoglycan synthesis, the first occurs in the cytoplasm with the generation of the key intermediate lipid II. The generation of enolpyruvyl UDP-Glc*N*Ac is classed as the first committed step of peptidoglycan synthesis (Brown et al., 1995). This reaction is catalysed by the UDP-Glc*N*Ac 1-carboxyvinyltransferase, named MurA, that transfers an enolpyruvyl moiety from phospho-enolpyruvate (PEP) to uridine diphosphate (UDP)-*N*-acetylglucosamine (Lovering et al., 2012). The conversion of enolpyruvyl UDP-Glc*N*Ac to UDP-Mur*N*Ac is a catalysed by MurB and a set of amino acid ligases encoded by *murC-F* catalyse the progressive addition of amino acids to produce UDP-Mur*N*Ac-pentapeptide (Lovering et al., 2012). MraY ligates this precursor to an undecaprenyl (C_{55}) carrier lipid which produces the first membrane associated intermediate termed lipid I. Lipid II is then generated by the ligation of a NAG residue by the enzyme MurG and lipid II is subsequently flipped to the outer surface of the membrane by a flippase (Scheffers & Tol, 2015). The second stage of peptidoglycan synthesis is called the lipid II cycle in which lipid II provides the subunits that are polymerised into glycan strands via a transglycosylase reaction

performed by a peptidoglycan synthase enzyme (PBP) (Sauvage et al., 2008). A phosphate is then removed from the lipid carrier by a UPPase and it is then released and recycled back into the cytoplasm (Lovering et al., 2012). The final stage of peptidoglycan synthesis is the crosslinking via transpeptidase reactions and maturation of the glycan stands (Sauvage et al., 2008).

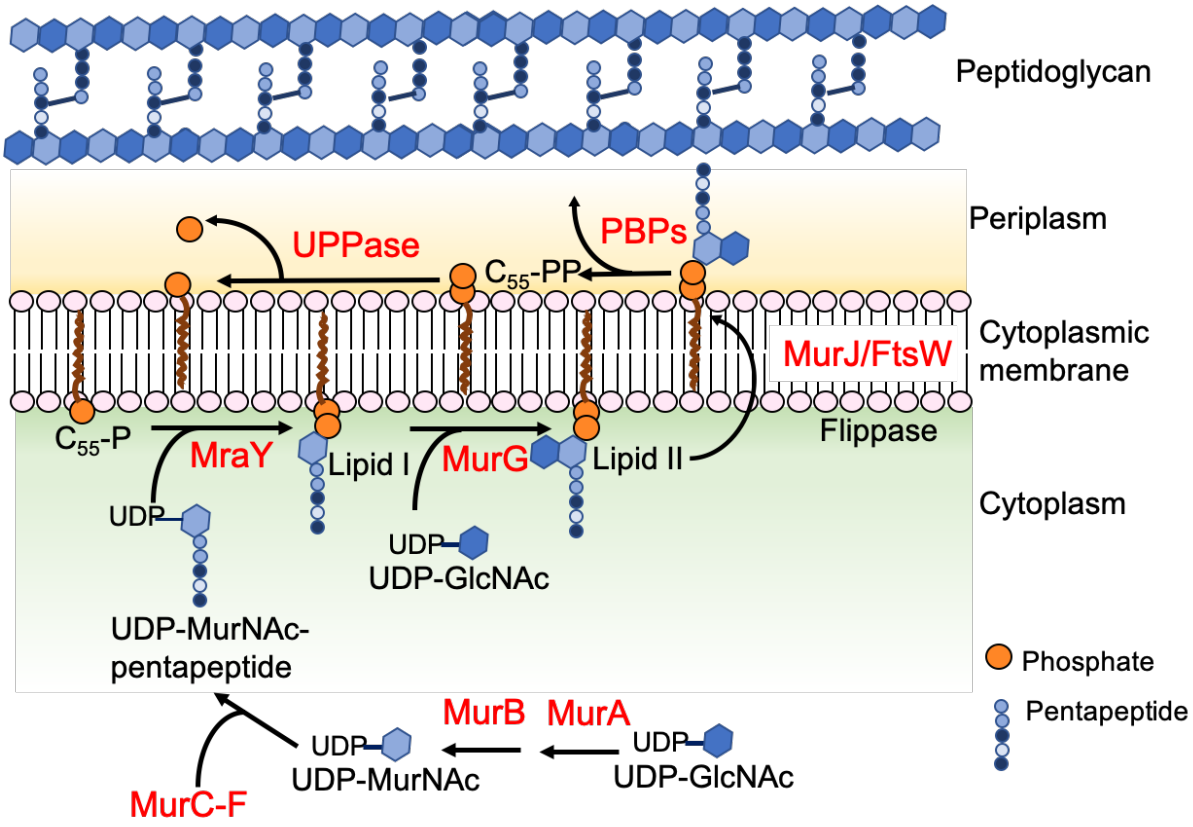

Figure 1.5: Schematic diagram displaying the main steps of peptidoglycan synthesis.
The first step involves the generation of lipid II in the cytoplasm which is subsequently flipped to the outer surface of the membrane by a flippase. Lipid II then undergoes the lipid II cycle providing the subunits that are polymerised into the glycan stand that is then crosslinked.

1.4 Penicillin-binding proteins

The study of penicillin-binding proteins (PBPs) was initiated after the discovery that cell wall synthesis was inhibited by the antibiotic penicillin (Duguid, 1946). It later transpired that PBPs were required in the final stages of peptidoglycan synthesis for the polymerisation and cross-linking of the glycan stands (Wise & Park, 1965). Treatment with penicillin inhibits the transpeptidation activity of PBPs and results in uncross-linked peptidoglycan (Wise & Park, 1965; Tipper & Strominger, 1965). The first characterisations of PBPs from *E. coli*, PBP1A and PBP1B was achieved by using mutant strains overexpressing or depleting some of the PBPs

(Nakagawà et al., 1979; Ishino et al., 1980); these studies revealed which PBPs were required for both peptidoglycan formation and cross-linking.

PBPs can be grouped into two main categories, the high molecular mass PBPs (HMM) and the low molecular mass PBPs (LMM). Polymerisation and the insertion of peptidoglycan into the pre-existing cell wall is performed by HMM PBPs which are made up of a cytoplasmic tail, transmembrane anchor and two domains that are joined by a β-rich linker (Goffin & Ghuysen, 1998). LMM PBPs are often referred to as the class C PBPs, which are peptidoglycan hydrolases with either DD-carboxypeptidase (CPase) or endopeptidase (EPase) activity (Egan et al., 2015). HMM PBPs can be split into two main classes, class A penicillin-binding proteins that have both transglycosylase (GTase) and transpeptidase (TPase) activities and class B penicillin-binding proteins that are monofunctional TPases (Typas et al., 2012). Bi-functional class A PBPs contain two active sites that belong to the two extracellular domains joined by the β-rich linker. The PB domain contains the active site for the transpeptidase reaction and the transglycosylase active site is present in the GTase domain (Sauvage et al., 2008). Class A PBPs have also been shown to exhibit CPase activity and it was observed that the TPase domain of the class A PBPs from *E. coli* PBP1A and PBP1B is similar to the CPase domain of LMM class C PBPs (Egan et al., 2015). The second extracellular domain of class B PBPs is known as the pedestal domain that has numerous functions such as positioning the TPase domain away from the cell membrane, towards the cell wall, and also interacting with a number of cell division proteins (Marrec-Fairley et al., 2000; Macheboeuf et al., 2006). The TPase domains of class A and B PBPs are similar in both sequence and structure (Goffin & Ghuysen, 1998).

Peptidoglycan GTases are part of the glycosyltransferase family 51 (GT51) (Lovering et al., 2007). The specific function of the GTase enzyme is to produce uncross-linked glycan stands from the substrate lipid II (Figure 1.6). GTases work in a progressive manner where the growing glycan strand stays at the active site of the enzyme until polymerisation is complete. The reaction is initiated by the binding of two lipid II molecules to the acceptor and donor sites of the GTase domain. After the first GTase reaction, the undecaprenol pyrophosphate is released and the resulting tetrasaccharide moves to the donor site (Sauvage et al., 2008). The next GTase reaction is then performed after the binding of another lipid II molecule to empty donor site (Fraipont et al., 2006; Perlstein et al., 2010). Different GTases can produce varying glycan stand lengths (Egan et al., 2015).

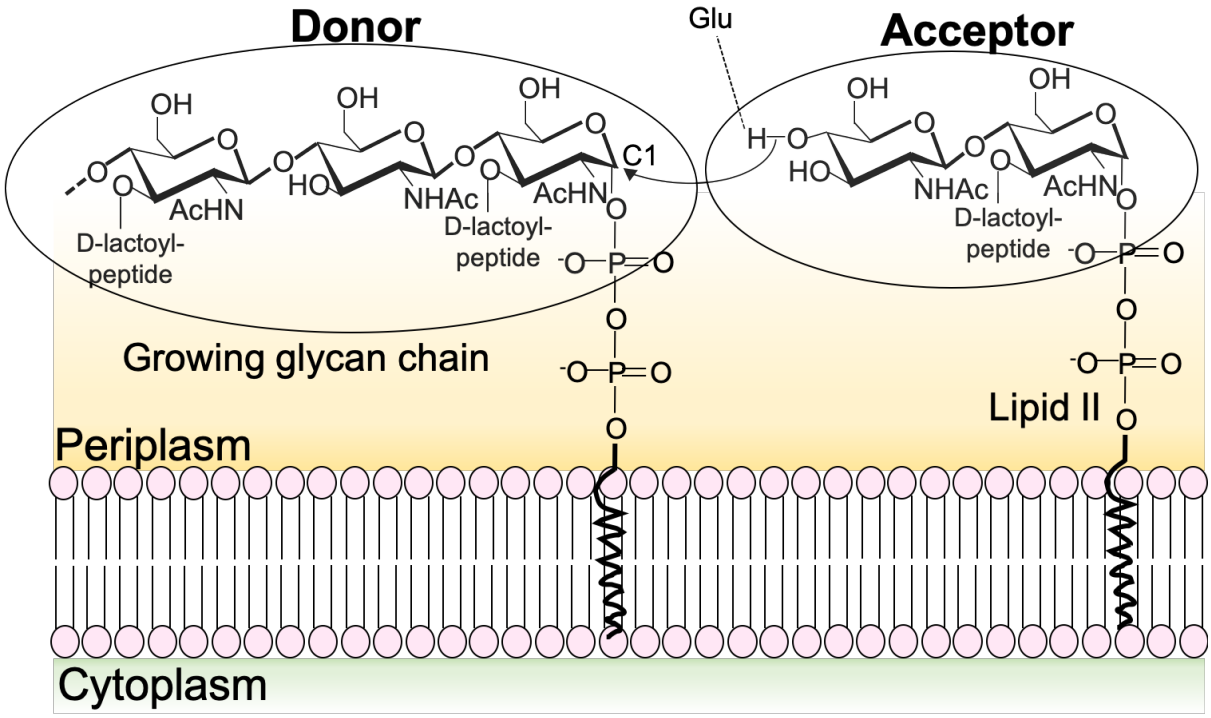

Figure 1.6: Penicillin binding protein glycosyltransferase mechanism.
The growing glycan chain is present in the donor site of the PBP and a recently flipped lipid II molecule is in the acceptor site of the enzyme. A glutamate residue (Glu) acts as a catalytic base that catalyses the deprotonation of the Glc*N*Ac 4-OH of lipid II. The nucleophile generated then attacks the C1 of Mur*N*Ac in the growing glycan chain.

Peptidoglycan TPases catalyse the reactions that lead to the formation of peptide cross-links under the release of a D-alanine residue (Figure 1.7). The reaction is initiated when a pentapeptide donor loses its terminal D-alanine residue, which results in an intermediate tetrapeptide bound to the catalytic serine residue in the TPase domain active site (Lupoli et al., 2011). This is then proceeded by a nucleophilic attack of an amino group of an acceptor peptide that resolves the intermediate and generates the peptide bond (Sauvage et al., 2008). With the same mechanism, a TPase can also accept a water molecule to produce a tetrapeptide which is why some class A PBPs can act as CPases.

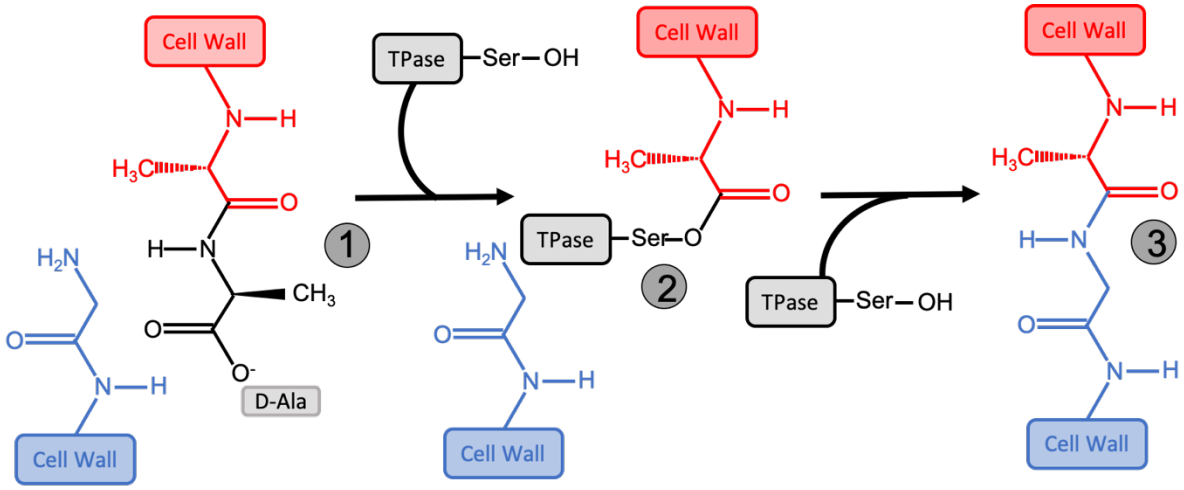

Figure 1.7: Penicillin binding protein transpeptidase mechanism.
The top strand pentapeptide loses its terminal D-alanine residue upon activation by the TPase (1) which initiates the formation of an intermediate tetrapeptide bound to the catalytic serine residue of the TPase (2). A nucleophilic attack from a bottom strand amino acid resolves the intermediate and forms a peptide bond (3).

The number of PBPs differs across bacterial species and the identification of each PBP in a number of organisms has been made possible by genome sequencing. *E. coli* contains 12 PBPs including 3 class A PBPs (PBP1A, PBP1B and PBP1C) and 2 class B PBPs (PBP2 and PBP3) (Sauvage et al., 2008). PBP1A and PBP1B are the two major bi-functional PBPs, with the deletion of both but not one being lethal (Meberg et al., 2001). PBP2 and PBP3 have been shown to have important roles in cell elongation and division, respectively (Egan et al., 2015). *B. subtilis* has 4 class A PBPs (PBP1, PBP2c, PBP4 and PBP2d) and 6 class B PBPs (PBP3, SpoVD, PBP2b, PBP2a, PbpH and PBP4b) with PBP1 and PBP2b being a major part of the cell division machinery (Sauvage et al., 2008). *Listeria monocytogenes* and *Streptococcus pneumoniae* have fewer PBPs with 7 and 6, respectively. *L. monocytogenes* has 2 class A PBPs (PBP1 and PBP4) and 3 class B PBPs (PBP2, PBP3 and lmo0441) whereas *S. pneumoniae* has 3 class A PBPs (PBP1a, PBP2a, PBP1b) and 2 class B PBPs (PBP2x and PBP2b) (Sauvage et al., 2008).

The crystal structures of a number of PBPs have been solved including the class A PBPs PBP1a and PBP1b from *S. pneumoniae* and PBP2 from *Staphylococcus aureus* (Macheboeuf et al., 2005; Contreras-Martel et al., 2006; Lovering et al., 2007) (Figure 1.8). The general fold of bi-functional PBPs includes an N-terminal GT domain coupled to a C-terminal PB domain with the interdomain linker composed of small β-sheets and one α-helix (Lovering et al., 2007). The PB domain contains two subdomains, an all helical domain and a five stranded β-sheet covered by three α-helices. The TPase active site sits between these two subdomains. The GT

domain contains a large and small lobe that is almost all α-helical, an extended cleft containing the active site separates the two lobes (Sauvage et al., 2008).

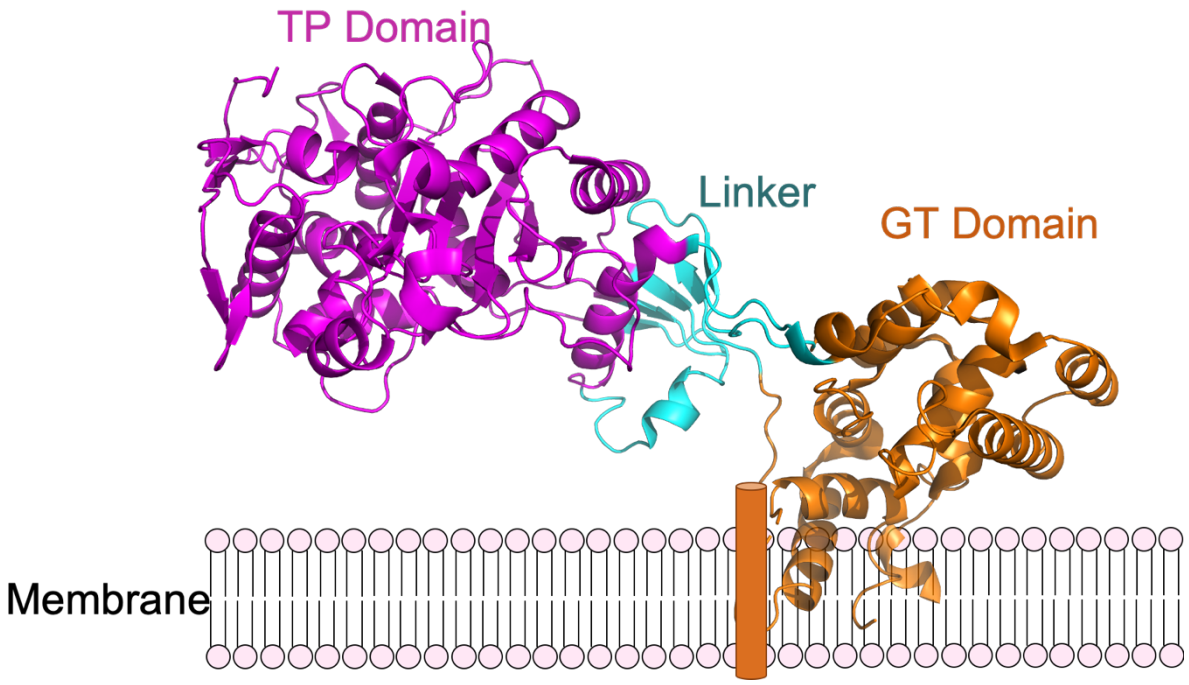

Figure 1.8: The structure of PBP2 from *S. aureus* and its position relative to the cell membrane.
Cartoon display of *Sa*PBP2 (PDB ID: 2OLU). Each domain is shown in a different colour and labelled on the figure. An orange cylinder represents where the transmembrane domain would be and the region of the GT domain close to the membrane contains the lipid II donor and acceptor sites (Lovering et al., 2007).

The cell wall must be constantly synthesised, remodelled and degraded throughout the cell-cycle which means the regulation of PBPs is essential (Claessen et al., 2008). Peptidoglycan hydrolases are a key component in bacterial growth for maintaining the thickness and the shape of the sacculus during elongation and for remodelling the peptidoglycan at cell division and separation (Typas et al., 2012). An important part of PBP regulation is through protein-protein interactions that either stimulate activity or dimerization, provide a precursor or substrate or control the subcellular localisation of PBPs. PBP3 from *E. coli* is recruited to the divisome via interactions with the FtsQLB complex and FtsW (Egan & Vollmer, 2013) whereas in *B. subtilis* two proteins called EzrA and GpsB control the localisation of PBP1 during the cell-cycle (Claessen et al., 2008). The functions of these proteins are discussed in more detail below.

1.5 The bacterial cell wall as a target for antibiotics

Antibiotics inhibit a number of different bacterial homeostasis processes including DNA replication, RNA synthesis, protein synthesis and cell wall synthesis (Wright, 2005). The peptidoglycan cell wall is a potent target for antibiotics. It provides mechanical strength for the bacteria, to withstand the turgor of the cell to prevent its lysis (Claessen et al., 2008). The cell wall is also a selective barrier to the environment that enables bacteria to up take only specific molecules (Liu & Breukink, 2016). There are two main antibiotics classes that inhibit cell wall synthesis, β-lactams and glycopeptides (Kohanski et al., 2010). These drugs cause a change in cell size and shape, induce a stress response and cause cell lysis (Tomasz, 1979). β-lactams can be used to treat infections by both Gram-positive and Gram-negative bacteria, examples include penicillins, carbapenems and cephalosporins. The β-lactam is a hydrolysable analogue of the terminal D-alanyl-D-alanine dipeptide of peptidoglycan and it binds to the transpeptidase active site of PBPs (Waxman et al., 1980). This blocks the crosslinking of peptidoglycan and ultimately leads to cell lysis (Wise & Park, 1965) (Figure 1.9).

Glycopeptides target Gram-positive bacteria due to their low permeability, examples include vancomycin and teicoplanin. The mode of action of glycopeptides is to bind directly to the terminal D-alanyl-D-alanine dipeptide and block the transpeptidase and transglycosylase activities of PBPs (Kahne et al., 2005)(Figure 1.10). Other examples of antibiotics that interfere with cell wall synthesis include fosfomycin that inhibits the synthesis of peptidoglycan subunits, bacitracin that inhibits the transport of peptidoglycan subunits and lipopeptides such as daptomycin, which affects the structural integrity of the cell by inserting into and depolarising the membrane (Kohanski et al., 2010).

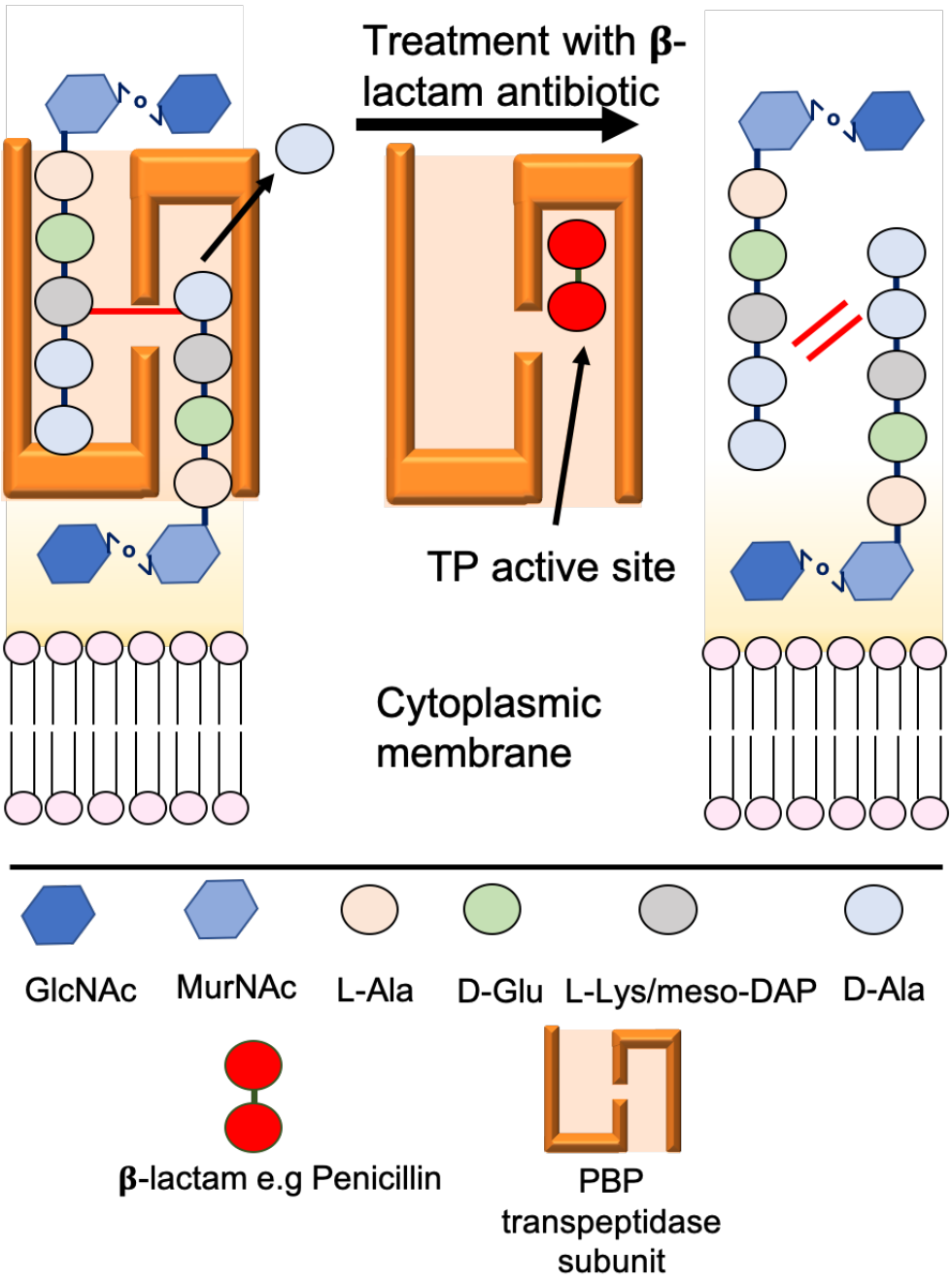

Figure 1.9: A schematic diagram showing the action of β-lactams on Gram-positive bacteria. The left panel shows where the PBP TPase subunit would normally bind to peptidoglycan to catalyse the transpeptidation reaction forming a 3-4 crosslink (red) and the release of the terminal D-Ala. β-lactams such as penicillin binds to the active site of the TPase which prevents the crosslinking of glycan stands demonstrated by the two red lines on the right panel.

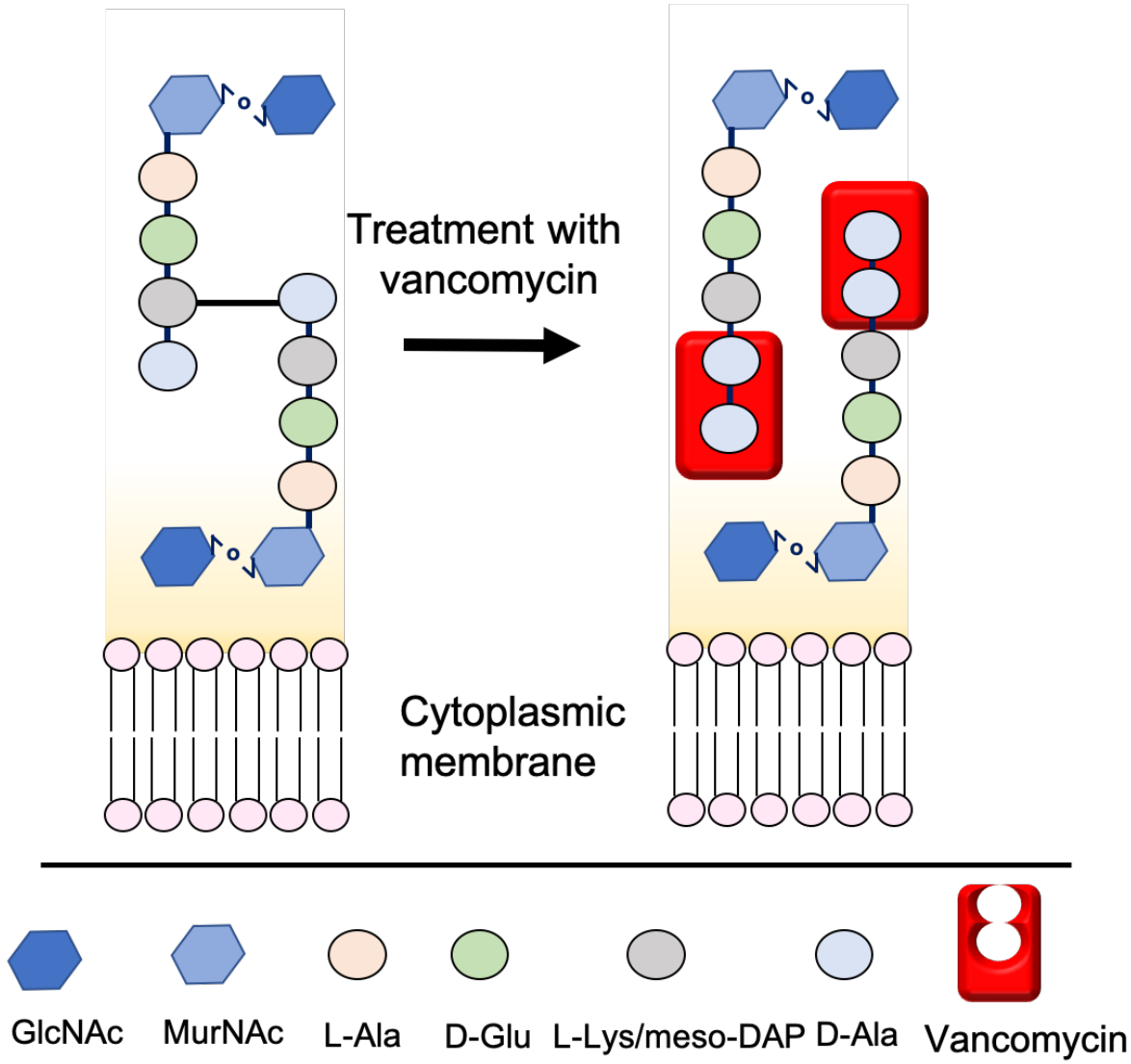

Figure 1.10: Schematic diagram showing the action of vancomycin on Gram-positive bacteria.
The left panel shows untreated peptidoglycan compared to the right panel treated with vancomycin. Vancomycin binds directly to the terminal D-alanyl-D-alanine dipeptides and blocks PBP activity.

1.6 Building the divisome

The divisome has been most extensively studied in rod-shaped bacteria, specifically *E. coli* and *B. subtilis* (Figure 1.11 A). Approximately 20-30 divisome proteins have been discovered so far and it is likely there are yet more to be found. Cytokinesis is initiated by the early division proteins starting with the recruitment of FtsZ to the mid-cell where it polymerises in a GTP-dependent fashion (Lutkenhaus & Addinall, 1997). Although there are differences in the composition of the divisome across bacteria, the accumulation of FtsZ is conserved and it is central to the divisome (Lutkenhaus & Addinall, 1997). FtsA, another highly conserved early division protein, acts as the connector between FtsZ and the cytoplasmic membrane (Loose &

Mitchison, 2014) and this tethering is further aided by ZipA in Gram-negative bacteria (Pazos et al., 2018) and potentially SepF in Gram-positives (Hamoen et al., 2006). The FtsZA filaments treadmill around the division septum and act as a scaffold for other divisome proteins (Bisson-Filho et al., 2017).

EzrA, negative regulator of Z-ring formation, also belongs to the group of early division proteins in Gram-positive bacteria and it is one of the first proteins to be recruited by FtsZ (Gamba et al., 2009). EzrA was initially discovered in *B. subtilis* and its deletion affected the localisation of FtsZ and caused the formation multiple Z-rings at the cell poles as well as mid-cell (Levin et al., 1999; Claessen et al., 2008). EzrA directly interacts with FtsZ impeding the formation of FtsZ filaments (Land et al., 2014) and the crystal structure of ErzA revealed how this might be possible. EzrA has an N-terminal transmembrane helix and a 60 kDa cytoplasmic domain that forms a curved rod, resembling a semicircle (Cleverley et al., 2014). The area inside of the EzrA crescent is large enough to fit an FtsZ protofilament to physically prevent the bundling of polymerised FtsZ (Cleverley & Lewis, 2015). EzrA has also been shown to play a role in septum-specific peptidoglycan synthesis: in *B. subtilis* EzrA recruits PBP1 to the septum (Claessen et al., 2008) and is required for peptidoglycan synthesis in *S. aureus* (Steele et al., 2011). The prevention of abnormal Z-ring formation, and the binding of peptidoglycan synthases, has highlighted EzrA as a major Gram-positive divisome component.

The progression of the Z-ring to the mature divisome is achieved by the recruitment of the late division proteins that are important for the remodelling of the cell wall. There are variations in this group of proteins across bacterial species, essentiality is not maintained and the exact function of certain proteins have been difficult to interpret. Five proteins that are widely-conserved in Gram-negatives and Gram-positives are FtsW, FtsI, FtsQ, FtsB and FtsL (*E. coli* names) (den Blaauwen et al., 2017). FtsW is an essential integral membrane protein that has reported lipid II flippase and transglycosylase activity and FtsI (PBP3) is a class B peptidoglycan synthase (Mohammadi et al., 2011; den Blaauwen et al., 2017). FtsW has been extensively examined, along with two other essential integral membrane proteins MurJ and RodA, as the prime lipid II flippase (Ruiz, 2008; Sieger et al., 2013; Sham et al., 2014). The discovery of FtsW and RodA as peptidoglycan polymerases (Emami et al., 2017; Taguchi et al., 2019) and recent structures and modelling of MurJ strengthens the assignment of MurJ as the flippase (Kuk et al., 2017; Zheng et al., 2018a; Kuk et al., 2019).

FtsQ, FtsB and FtsL (DivIB, DivIC and FtsL in Gram-positives, respectively) are transmembrane proteins each consisting of a small N-terminal cytoplasmic domain, a single transmembrane helix and a large C-terminal extracellular domain (Gonzalez et al., 2010). The extracellular region of FtsQ/DivIB contains a PASTA domain to interact with peptidoglycan (Bottomley et al., 2014). The assembly of these proteins into an independent trimeric complex has been demonstrated in both *E. coli* and *B. subtilis* (Buddelmeijer & Beckwith, 2004; Robson & King, 2006). For a while, it was believed that the FtsQBL (DivIB/C/FtsL) complex acted as a divisome scaffold, and interactions with multiple division proteins were identified including FtsW, FtsI (Goehring et al., 2006) and PBPs such as *Bs*PBP2b (Angeles et al., 2019). However, a recent study in *E. coli* has shown that the complex regulates the activities of peptidoglycan synthases in coordination with FtsN and FtsA, thus providing a link between early division and cell wall remodelling (Boes et al., 2019). The FtsQBL complex inhibits the transglycosylase activity of PBP1b mainly though FtsB and FtsL, whereas FtsQ inhibits FtsI activity (Boes et al., 2019). GpsB and DivIVA are two highly-related and conserved Gram-positive divisome proteins that will be discussed in more depth below.

1.7 The elongasome

During the cell-cycle, rod-shaped bacteria elongate before dividing, which requires the growth and remodelling of the cell side-wall by a macromolecular complex known as the elongasome (or the Rod system) (Figure 1.11 B). The elongasome is composed of MreB, MreC, MreD, RodA, PBP2 and RodZ and both class A and B PBPs synthesise the peptidoglycan used for elongation (Dion et al., 2019). The *mreBCD* operon is conserved in rod-shaped bacteria and this operon encodes the three important elongation proteins, MreB MreC and MreD, and mutation in any of these genes causes rods to become spherical (Jones et al., 2001; Lee & Stewart, 2003; Leaver & Errington, 2005). Spherical bacteria do not elongate and thus the Rod system is absent in most cocci.

MreB is a homologue of actin and polymerises to form cytoskeletal filaments in a helical structure that is found under the membrane at the cylindrical part of the cell (Jones et al., 2001; Leaver & Errington, 2005). Fluorescent vancomycin staining (VAN-FL) showed spots of peptidoglycan synthesis in a similar cylindrical pattern (Leaver & Errington, 2005). It was later shown that filaments of MreB move around the width of rod-shaped bacteria circumferentially positioning the Rod complex that moves in unison (Dominguez-Escobar et

al., 2011; Garner et al., 2011). This motion is disturbed when either MreC, MreD, RodA or PBP2 are lost (Dominguez-Escobar et al., 2011; Garner et al., 2011). MreB filaments were shown to preferentially orientate along the direction of the greatest principle membrane curvature, which in rod-shaped bacteria is the rod circumference (Hussain et al., 2018). The spatial activity of PBPs are constrained by this orientation of the MreB filaments causing the insertion of peptidoglycan in a circumferential direction maintaining the rod shape (Hussain et al., 2018). MreB filaments do not define cell width, *B. subtilis* cells were only slightly wider when the *mreBCD* operon was replaced by the operon from *Bacillus megaterium* which is 1.7-fold wider than *B. subtilis* (Dion et al., 2019). However, it was shown in the same study that the circumferentially moving Rod system reduces the cell diameter and the non-circumferentially moving class A PBP (PBP1) has a widening effect on *B. subtilis* cells. It was further shown that when the activity of RodA and PBP2 is no longer orientated by MreB and when the two proteins are in excess they can widen cells outside of the Rod system (Dion et al., 2019).

The proposed role of MreC in the Rod system is to act as a scaffold for other elongasome components. MreC has been shown to interact with MreD and MreB by BACTH (Kruse et al., 2005) as well as multiple high molecular weight peptidoglycan synthases (Divakaruni et al., 2005; Van Den Ent et al., 2006) and PBP2 of *Caulobacter crescentus* exhibits a similar helical localisation pattern (Figge et al., 2004). BACTH studies (Van Den Ent et al., 2006) and analysis of the structures of MreC (Van Den Ent et al., 2006; Lovering & Strynadka, 2007) have demonstrated that it has a tendency to self-associate, leading to oligomers, strengthening the assignment of MreC as a scaffold protein. The complex structure of rod-shape determining proteins, PBP2:MreC solved from *Helicobacter pylori* showed two distinct interaction surfaces of MreC. One surface bound to the N-terminal domain of PBP2 and the other was identified as a self-association surface for binding to a partner MreC molecule (Contreras-Martel et al., 2017).

RodA, a member of the SEDS family (for shape, elongation, division and sporulation) is also tightly associated with elongation (Meeske et al., 2016). RodA is essential for the cylindrical growth of both Gram-negative and Gram-positive rods and was originally suggested as the lipid II flippase during elongation (Begg & Donachie, 1998; Henriques et al., 1998). More recently, RodA has been shown to have glycosyltransferase activity and act with class B PBPs, polymerising the glycan strand during elongation that is then crosslinked by the PBP partner (Meeske et al., 2016; Cho et al., 2016). In *B. subtilis* the class B PBP that pairs with RodA is

PBP2a and/or PbpH (Jones et al., 2001). A recent study demonstrated that PBP2, along with MreC, stimulated the polymerisation of peptidoglycan by RodA and induced the polymerisation of MreB filaments (Rohs et al., 2018). The proposed activation pathway starts with MreC associating with PBP2 inducing a conformational change that activates RodA. This complex is proposed to have a higher affinity for MreB, leading to MreB polymerisation which orientates the synthesised peptidoglycan produced by RodA/PBP2.

MreB, MreD and RodA have been shown by BACTH to form multiple interactions with each other and with the Mur/Mra enzymes important for the synthesis of peptidoglycan precursors (White et al., 2010). This discovery links early lipid II synthesis to the cell wall synthesis machinery through RodA, MreD and MreC.

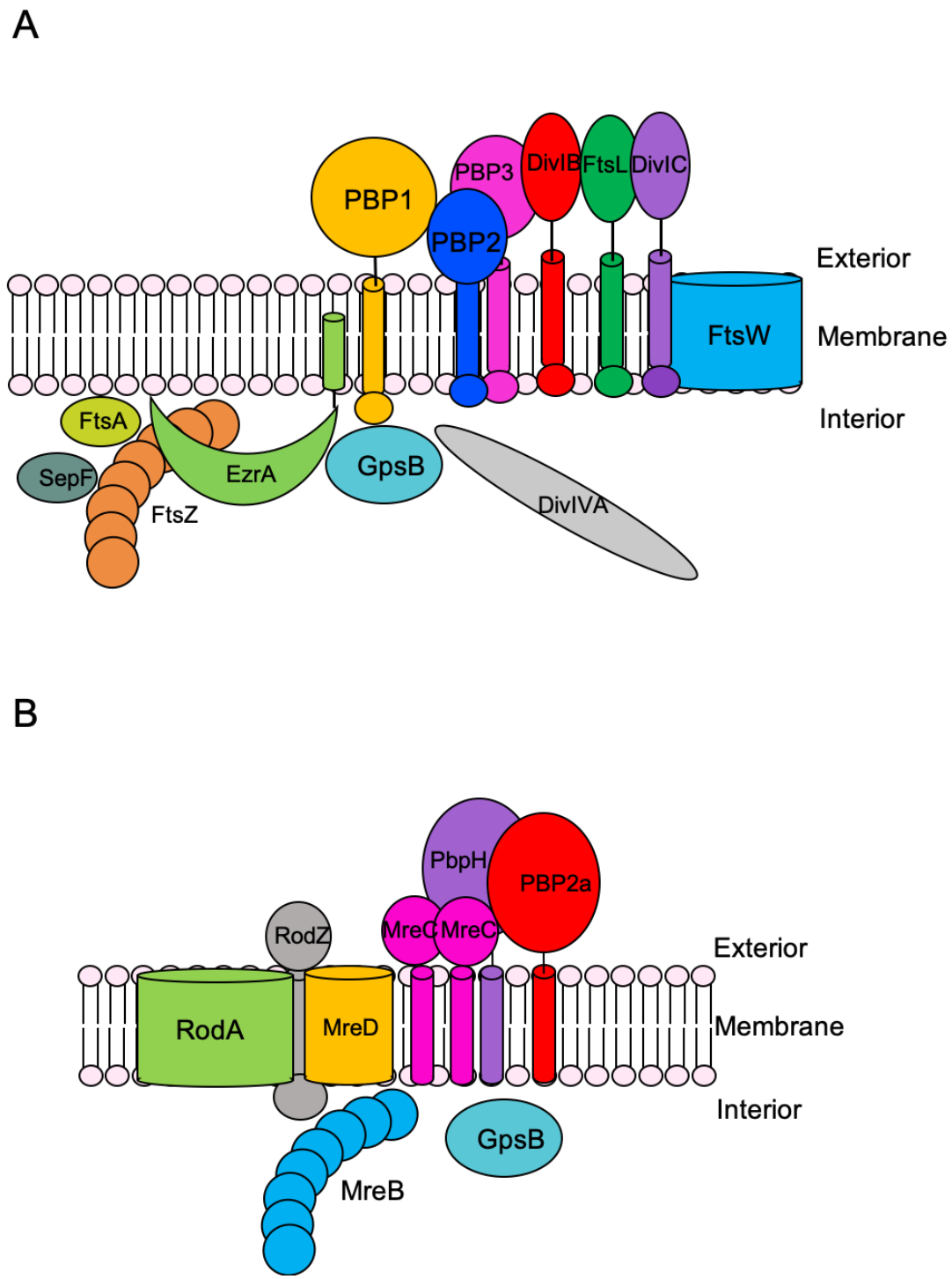

Figure 1.11: Schematic diagram representing the *Bacillus subtilis* divisome (A) and elongasome (B).

Each complex is composed of a cytoskeletal network formed by the polymerisation of FtsZ/MreB filaments that acts as a scaffold for the recruitment and assembly of the respective macromolecular complex. Both the divisome and elongasome contain peptidoglycan synthases for cell wall synthesis at the septum and side-wall, respectively.

1.8 GpsB and its function in the cell-cycle

1.8.1 Discovery of GpsB

GpsB (previously YpsB) was first identified as a potential division protein by sequence comparisons that showed the downstream chromosomal region of *ftsZ* in *S. pneumoniae* encoded an open reading frame with sequence similarity to *B. subtilis* DivIVA, which in turn had sequence similarity to GpsB of 64% over 57 amino acids (Massidda et al., 1998). Ten years later, the role of GpsB in growth and division was described in *B. subtilis*, a model for cell division in Gram-positive bacteria (Claessen et al., 2008; Tavares et al., 2008). Phylogenetic analysis and sequence comparisons of GpsB and DivIVA demonstrated that the proteins are paralogues (Tavares et al., 2008). At the time, DivIVA was known to be involved in cell division and this led to the hypothesis that GpsB may have a division function (Edwards & Errington, 1997).The *gpsB* gene encodes a protein 98 amino acids in length and it is in a conserved region of the chromosome that also contains the gene (*ponA*) for PBP1 in *B. subtilis* (Tavares et al., 2008) and an interaction between PBP1 and GpsB was confirmed by Claessen *et al.* In a synthetic lethal genetic screen in the absence of the cell division protein EzrA, it was found that cells lacking *gpsB* were synthetically sick (Claessen et al., 2008). In the same study, sequences of homologues of GpsB were observed in a number of Gram-positive bacteria such as *L. monocytogenes* and *S. pneumoniae* highlighting a potentially important role for GpsB in division (Claessen et al., 2008), which has been confirmed in the subsequent decade's worth of research.

1.8.2 Δ*gpsB* and its effect on the cell

The impact of *gpsB* deletions and depletions on cell viability, growth and morphology has been widely studied to gain an understanding of the function of GpsB in different species of bacteria (Figure 1.12). *B. subtilis* strains lacking *gpsB* had no apparent division phenotype, and the cells were viable and grew the same as wild-type cells under normal growth conditions (Claessen et al., 2008; Tavares et al., 2008). However, in high salt (0.6 M NaCl) growth media, the *B. subtilis gpsB* null mutant was prone to lysis, and the cell was notably longer compared to the wild-type; the mutant also formed polar bulges (when viewed by phase contrast microscopy), suggesting a role for GpsB under salt stress (Claessen et al., 2008). GpsB appeared neither essential for sporulation nor for vegetative growth (Tavares et al., 2008). A strain in which both *ezrA* and *gpsB* were deleted not only showed a cell division phenotype but the strain was

also thinner than the wild type, an indication of defective elongation (Claessen et al., 2008). By contrast, Tavares *et al.* reported that there was no synthetic phenotype in *ezrA gpsB* double mutants, but there was with *ftsA gpsB* double mutants (Tavares et al., 2008). The absence of *gpsB* was studied in *L. monocytogenes* in which a temperature sensitive phenotype was observed (Rismondo et al., 2016), indicating a function for GpsB at high temperatures. The *gpsB* null strain (LMJR19) grew normally at 30°C, showed a reduced growth rate at 37°C and there was no growth at 42°C (Rismondo et al., 2016). As in *B. subtilis, gpsB* deletion in *L. monocytogenes* produced elongated cells and increased lysis was observed (Rismondo et al., 2016). In addition, although there was no change to the thickness of the cell wall, the Δ*gpsB* cells had an increased penicillin sensitivity (Rismondo et al., 2016). GpsB is essential in the encapsulated S. *pneumoniae* strain D39 (Land et al., 2013; Fleurie et al., 2014a; Rued et al., 2017) and its depletion causes larger elongated cells with bulges, as seen in other Gram-positive bacteria (Land et al., 2013). By comparison, the unencapsulated *S. pneumoniae* lab strains R6, R800 and Rx1 can survive *gpsB* deletions (Fleurie et al., 2014a; Rued et al., 2017) but in all cases cell are elongated, R800 cells have an irregular width (Fleurie et al., 2014a), R6 cells are larger and Rx1 cells grow poorly (Rued et al., 2017). These results clearly indicate a role for GpsB in cell division, and also in some cases elongation, and that GpsB could also function in cell stress.

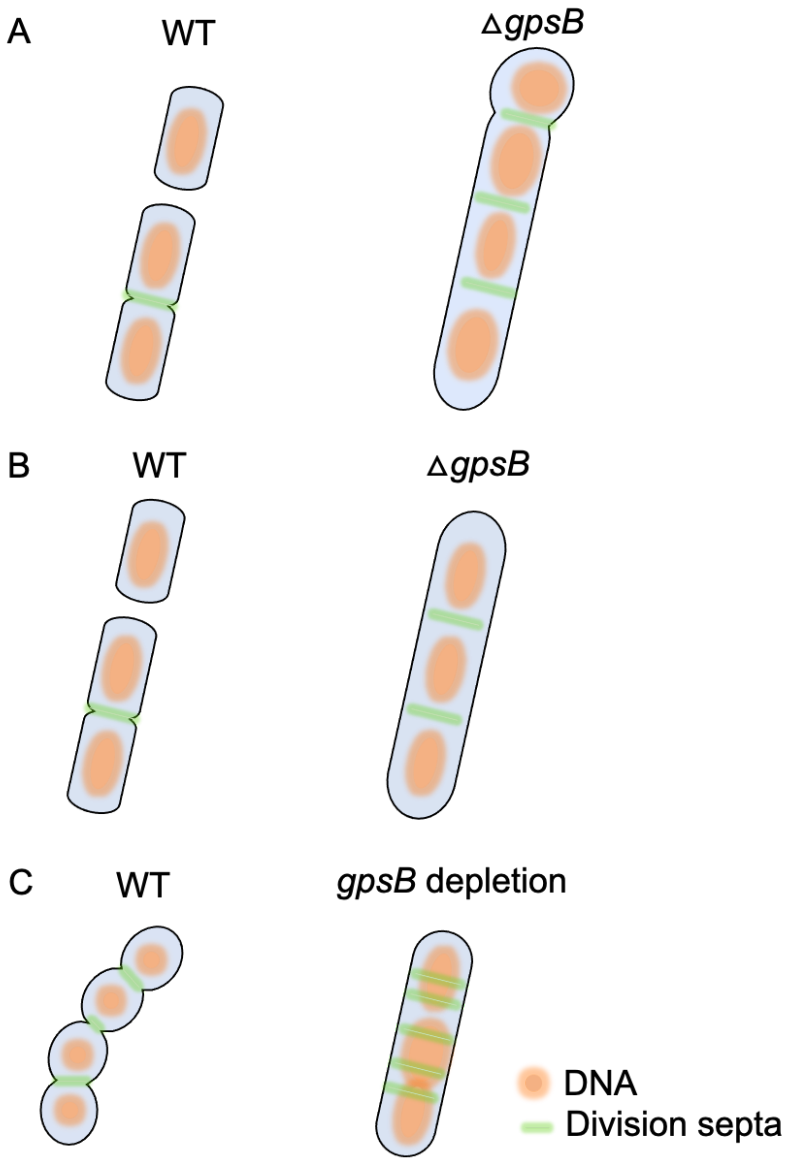

Figure 1.12: Representations of cell morphologies due to *gpsB* deletions and depletions in Gram-positive bacteria.
Panel **A** shows the effect of a *gpsB* deletion (Δ*gpsB*) in *B. subtilis* cells (right) compared to wild-type (WT) (left) in high salt growth media (Claessen et al., 2008). Δ*gpsB* cells are elongated and form polar bulges. Panel **B** shows the effect of a *gpsB* deletion in *L. monocytogenes* (right) compared to WT (left) at 37 °C. Δ*gpsB* cells showed a reduced growth rate and were elongated (Rismondo et al., 2016). Panel **C** shows the depletion of *gpsB* in *S. pneumoniae* cells (right) compared to WT (left). Cells have an irregular width, are elongated and form multiple division septa (Land et al., 2013; Fleurie et al., 2014a; Rued et al., 2017).

1.8.3 Localisation of GpsB

The cellular localisation of GpsB has also been explored in order to gain an understanding of its role in the elongation-division cycle. Fluorescence microscopy studies of GFP-tagged *B. subtilis* GpsB (both N- and C-terminal tags) have shown that it is located at both peripheral membranes and at mid-cell at different stages of the cell-cycle (Claessen et al., 2008; Tavares

et al., 2008). Claessen *et al.* proposed a localisation pattern for GpsB based on time-lapse microscopy that showed shuttling of GpsB to the septum during the cell division stage and to the lateral cell wall during the elongation stage (Figure 1.13). GpsB is thus involved in both elongation and division. The same localisation pattern has also been observed in *L. monocytogenes* in which GpsB-GFP cells were seen with either peripheral fluorescence or a weaker peripheral fluorescence and strong septal fluorescence (Rismondo et al., 2016). The shuttling model was strengthened by the similar localisation pattern of pneumococcal GpsB (Rued et al., 2017). GpsB fluorescence was diffuse in early cell division and localised around the cell equators after division, but is located at mid-cell of dividing cells and persists at division septa (Rued et al., 2017). *B. subtilis* GpsB was present in both membrane and soluble fractions (Tavares et al., 2008) and Western blotting showed GpsB to be enriched at the *L. monocytogenes* membrane (Rismondo et al., 2016). Consistent with the localisation data these observations support the idea that GpsB is a dynamic membrane associated protein.

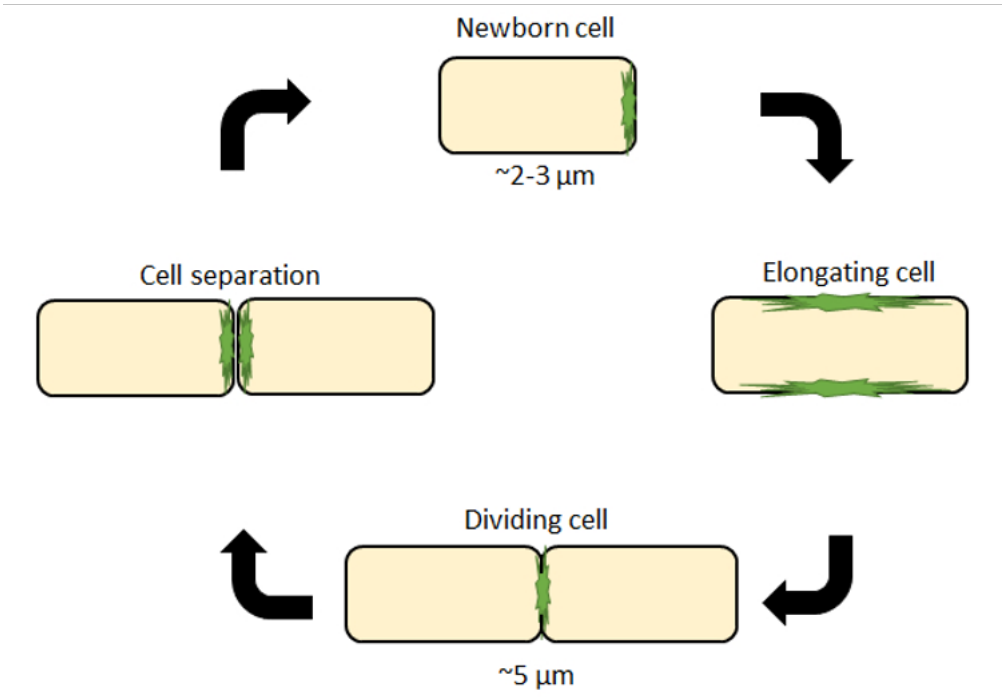

Figure 1.13: GpsB localisation pattern in *B. subtilis*.
Schematic diagram representing the localisation pattern of GpsB during the cell-cycle of *B. subtilis*. Areas highlighted in green show GpsB-GFP fluorescence observed by time-lapse microscopy (Claessen et al., 2008).

The subcellular localisation experiments not only yielded insights into the position of GpsB at different stages of the cell-cycle but also suggested potential interacting partners and their co-localisation relationships. The cell-cycle localisation of *B. subtilis* PBP1 is severely perturbed

when GpsB is depleted at the same time as EzrA (Claessen et al., 2008). EzrA and GpsB, which both interact with PBP1 (Claessen et al., 2008), therefore appear to have partially overlapping functions in the control of wall synthesis in *B. subtilis* with EzrA shuttling PBP1 and GpsB to the septum for division and GpsB shuttling PBP1 to the side wall for elongation (Claessen et al., 2008). By contrast, *L. monocytogenes* GpsB did not affect PBPA1 (an orthologue of PBP1) localisation (Rismondo et al., 2016). The relative localisation patterns of GpsB and FtsZ have been determined in *B. subtilis* and *S. pneumoniae* (Tavares et al., 2008; Land et al., 2013). In both cases GpsB and FtsZ have different localisation patterns, however, at distinct times in the cell-cycle the proteins co-localise indicating an overlapping disposition. GpsB and FtsZ co-localise at midcell in pre-divisional cells and during mid-division FtsZ is present at the constricting septa whereas GpsB extends from the septa and along the inner hemispheres (Land et al., 2013). The major difference in localisation of FtsZ and GpsB is in the late stage of cell division where FtsZ relocates to the equators of daughter cells but GpsB remains at septal regions (Tavares et al., 2008; Land et al., 2013). In longer *B. subtilis* cells about to divide, and in smaller cells at the start of the cell-cycle, GpsB was located at the old division site at the same time that new Z-rings were forming (Tavares et al., 2008). A similar co-localisation pattern was seen using standard-resolution dual-protein IFM (immunofluorescence microscopy) (Land et al., 2013), and high-resolution 3D-SIM (three-dimensional structured illumination microscopy) (Land et al., 2013) IFM was used to show an overlapping localisation pattern of FtsZ with GpsB in *S. pneumoniae* (Land et al., 2013).

The importance of specific domains and residues of GpsB to its localisation has also been explored by fusing truncations of GpsB to GFP, and visualising cellular localisation by fluorescence (Tavares et al., 2008). The coiled-coil domain, the C-terminal domain and the N-terminal domain of GpsB were important for GpsB localisation in the wild-type strain and in a strain lacking endogenous GpsB, respectively (Tavares et al., 2008). The N-terminal domain was also shown to be crucial for membrane association in *L. monocytogenes* GpsB by Western blotting of cellular and membrane fractions (Rismondo et al., 2016).

1.8.4 Interacting partners of GpsB

A number of different *in vivo* and *in vitro* techniques have been used to study the interactions between cell division and elongation proteins such as GpsB (Figure 1.14). Highlighting and understanding these interactions will help build a picture of the components of the cell-cycle

and their potential roles in space and time. Since EzrA and GpsB have important roles in coordinating the localisation of PBP1 within the cell-cycle, the potential for the two proteins to interact has been investigated. Bacterial two-hybrid (BACTH) screens have consistently shown an interaction between GpsB and EzrA both in *B. subtilis* and in *S. pneumoniae* (Claessen et al., 2008; Pompeo et al., 2015; Fleurie et al., 2014a; Rued et al., 2017). This interaction has also been extended to *S. aureus*, also identified by BACTH (Steele et al., 2011). A Kd of ~ 0.8 µM for the interaction of EzrA with GpsB in *S. pneumoniae* has been determined by SPR (Fleurie et al., 2014a). An interaction between EzrA and FtsZ has also been observed in both BACTH and by SPR (Claessen et al., 2008; Fleurie et al., 2014a; Cleverley et al., 2014), whereas there has been no detected interaction of GpsB with FtsZ by BACTH in *S. pneumoniae* (Fleurie et al., 2014a). The localisation and interaction relationships of ErzA, GpsB and FtsZ suggests EzrA acts as a connector between the Z-ring and GpsB. A recent study in *S. aureus* has indicated that GpsB interacts directly with FtsZ, increasing its GTPase activity and promoting the formation of FtsZ bundles (Eswara et al., 2018). At present, this function of GpsB is restricted to *S. aureus* and confirmation of the effect of GpsB on FtsZ function in another Gram-positive organism is currently lacking.

Furthermore, a series of interaction studies in a range of Gram-positive bacteria has indicated a role for GpsB in the regulation of wall synthesis through its binding to PBPs. GpsB and the major bi-functional PBPs in *B. subtilis* and *L. monocytogenes,* PBP1 and PBPA1, respectively, have been shown to interact by BACTH (Claessen et al., 2008; Rismondo et al., 2016). GpsB still bound strongly to PBP1 when the just the latter's cytoplasmic tail and transmembrane region were present; the C-terminal domain of *L. monocytogenes* GpsB is completely dispensable for the interaction with PBPA1 (Claessen et al., 2008; Rismondo et al., 2016). *Bs*GpsB and *Bs*PBP1 interact with an SPR-measured Kd of ~0.7 µM; binding is still seen with just the N-terminal domain of GpsB, and the first 16 amino acids of PBP1 are crucial for this interaction (Rismondo et al., 2016; Cleverley et al., 2019). Fluorescence polarisation studies of the N-terminal domain of *B. subtilis* and fluorescein-labelled $PBP1_{1\text{-}32}$ supported the previous observations that the N-terminal domain of GpsB interacts with the N-terminal cytoplasmic domain of PBP1 (Cleverley et al., 2019). An *in vitro* HPLC-based fluorescent PG synthesis assay indicated that *Bs*GpsB does not affect the TPase or GTase activity of PBP1, which has led to the idea that GpsB influences wall synthesis by acting as a scaffold to coordinate the activities of PBPs rather than modulating the specific enzyme activities *per se* (Cleverley et al., 2016).

Co-IP experiments have also illustrated that S. *pneumoniae* GpsB interacts with bPBP2b and aPBP2a and not with bPBP2x or aPBP1a (Rued et al., 2017)(b= class B PBP, a= class A PBP). Rued *et al.* also suggested that GpsB was required for aPBP2a activity and that GpsB was needed for the migration of bPBP2x to the middle of the division septa. The absence of an interaction of GpsB with bPBP2x by co-IP is therefore surprising, however, this could be explained if their interaction was weak or transient.

The N-terminal domain of *L. monocytogenes* GpsB has been reported by BACTH to interact with the FtsZ membrane tethering protein, SepF (Cleverley et al., 2019). This imposes a new function for GpsB - to connect the early stages of cytokinesis with peptidoglycan remodelling. In the same study, *Lm*GpsB was shown to interact with the late divisome proteins DivIB and DivIC by BACTH. GpsB interacted with MreC in 3 different organisms, *B. subtilis*, *L. monocytogenes* and S*. pneumoniae*, which supports the observation from localisation studies that GpsB plays a role in the elongation of rod-shaped bacteria and the peripheral cell wall remodelling of spherical bacteria (Claessen et al., 2008; Rued et al., 2017; Cleverley et al., 2019). Other interacting partners of GpsB that have been identified include PrkC (StkP in S. *pneumoniae*) and DivIVA, interactions that will be discussed in more detail below (Claessen et al., 2008; Fleurie et al., 2014a; Pompeo et al., 2015; Rued et al., 2017).

GpsB has recently been shown to play a role in the sporulation of *B. subtilis* (Muchová et al., 2020), although its presence is not essential for sporulation to occur (Tavares et al., 2008). An initial BACTH screen and further pull-down assays revealed that GpsB interacted with the cytosolic region of the essential sporulation protein SpoIIE (Muchová et al., 2020). SpoIIE is a large membrane protein that is needed for asymmetric septum formation between the mother cell and the forespore during sporulation (Feucht et al., 1996). Fluorescence microscopy showed that GpsB and SpoIIE co-localised close to one of the cell poles in the early stages of sporulation (Muchová et al., 2020). As sporulation progressed, GpsB accumulated at the foci and either end of the septum where it could coordinate peptidoglycan synthesis. Conversely, SpoIIE is recaptured on the forespore face of the asymmetric septum by SpoIIQ in the later stages of sporulation (Muchová et al., 2020). In vegetative and polar septum formation the same set of division proteins are required, but the polar septum is thinner, probably because of the unique presence of SpoIIE (Barák & Youngman, 1996; Barák & Muchová, 2018; Muchová et al., 2020). The recent work by Muchovà *et al.* has demonstrated that GpsB could be the link between peptidoglycan synthesis and asymmetric division, and the

role of GpsB as a cell-cycle adapter protein is maintained during the formation of a vegetative septum and the polar septum formed during sporulation.

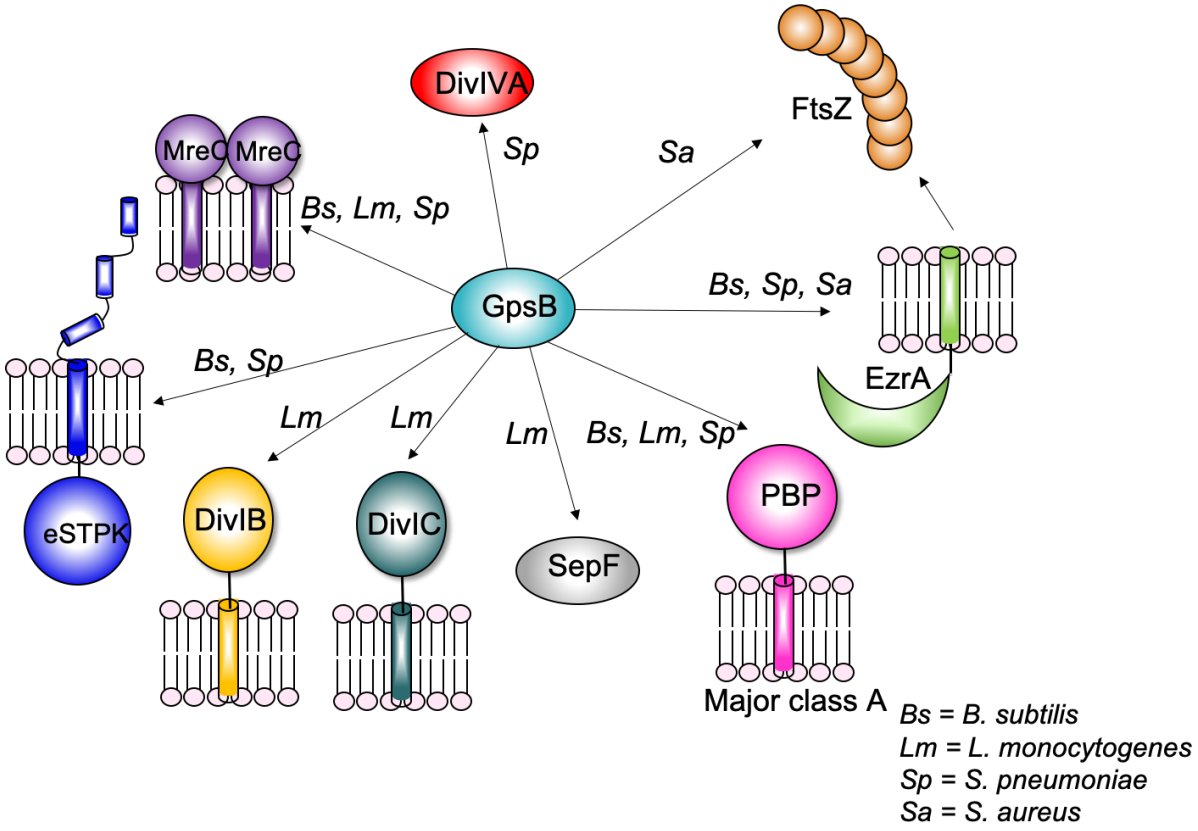

Figure 1.14: Diagram indicating identified interacting partners of GpsB.
GpsB has been shown to interact with EzrA (Claessen et al., 2008; Steele et al., 2011; Fleurie et al., 2014a; Pompeo et al., 2015; Rued et al., 2017), PBPs (Claessen et al., 2008; Rismondo et al., 2016; Cleverley et al., 2016; Rued et al., 2017; Cleverley et al., 2019), MreC (Claessen et al., 2008; Rued et al., 2017; Cleverley et al., 2019), eSTPks (Pompeo et al., 2015; Fleurie et al., 2014a; Rued et al., 2017), DivIVA (Fleurie et al., 2014a), SepF (Cleverley et al., 2019), FtsZ (Eswara et al., 2018) and DivIB and DivIC (Cleverley et al., 2019). Labels at each arrow indicate which Gram-positive organism the interaction has been identified in.

1.8.5 Structures of GpsB

To gain an understanding of GpsB at the molecular level, and how it interacts with PBPs, various crystal structures were solved (Figure 1.15) immediately before the commencement of my PhD studies. Obtaining good quality diffracting crystals for full length GpsB has not proved possible thus far, however, crystal structures of the N- and C-terminal domains have been determined (Rismondo et al., 2016), and how these subunits are arranged into a hexamer in the full-length protein has been determined by small-angle X-ray scattering (SAXS) (Cleverley et al., 2016). These published structures have been complemented with more recent

structures of the N-terminal domain of GpsB bound to a PBP-derived peptides from *B. subtilis, L. monocytogenes and S. pneumoniae* (Cleverley et al., 2019).

Structures of the N-terminal domain of GpsB from both *B. subtilis* (*Bs*GpsB$_{1-68}$) and *L. monocytogenes* (*Lm*GpsB$_{1-73}$) were first solved by X-ray crystallography in the absence of bound peptides (Rismondo et al., 2016). The structures are essentially identical; both are parallel coiled-coil dimers of identical monomers. The main difference between the two structures is restricted to a flexible region at the very N-terminal region of the protein. A key feature of both structures is a negatively charged surface cavity of conserved amino acids that appears to be the binding site for the positively charged cytoplasmic domains of PBPs. BACTH and complementation assay studies confirmed an important role for Val32 and Leu36 for self-interaction in *L. monocytogenes* GpsB, as implied from the crystal structure. A number of experiments showed that two aspartates (Asp33 and Asp37 in *L. monocytogenes,* and their equivalents in *B. subtilis*, Asp31 and Asp35) in the negatively-charged surface cavity of GpsB were crucial for binding to PBPA1/PBP1 - a complete lack of binding was observed when these residues were mutated to alanine (Rismondo et al., 2016).

The co-crystallisation of *Bs*GpsB$_{5-64}$ with a PBP1 peptide containing residues 1-17 supported the role of the highly conserved Asp31 and Asp35 in PBP1 binding. A groove between two α-helices was observed to be the binding site for PBP1$_{1-17}$ in which the side chain and peptide backbone amide of Arg8 interacted with Asp31 and Asp35, respectively. Arg11 of PBP1$_{1-17}$ was also involved in contacts with Leu14 and Glu17 of *Bs*GpsB$_{5-64}$. A significant reduction in binding affinity was established by fluorescence polarisation when either Arg8 or Arg11 were mutated to alanine, or when a residue such as proline was introduced to disturb the helix, as the structure of the complex revealed that PBP1$_{1-17}$ is predominantly α-helical (Cleverley et al., 2019).

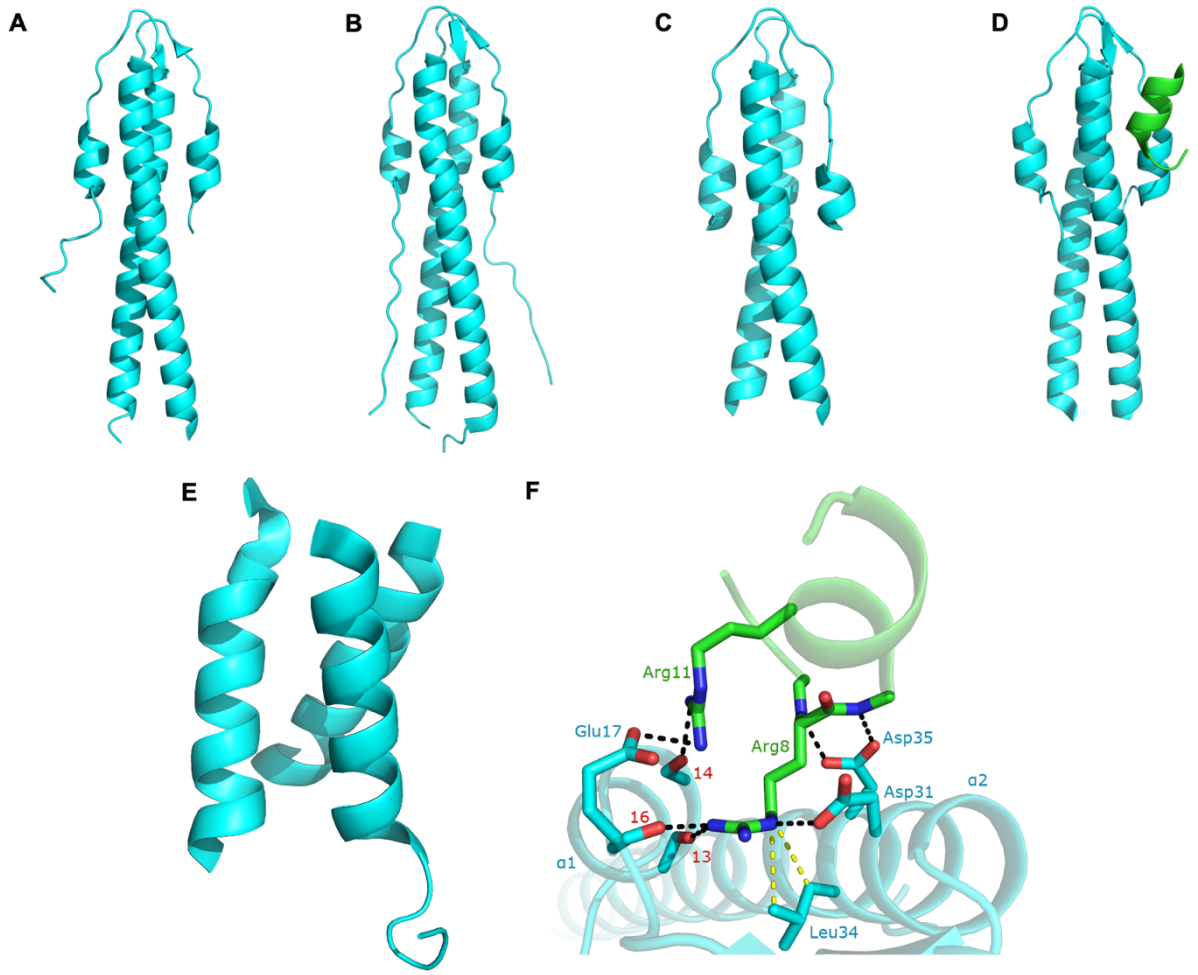

Figure 1.15: Crystal structures of GpsB and DivIVA.
(**A**) GpsB N-terminal domain from *B. subtilis* (*Bs*GpsB$_{1-68}$) (PBD ID: 4UG3) (Rismondo et al., 2016). (**B**) The GpsB N-terminal domain from *L. monocytogenes* (*Lm*GpsB$_{1-73}$) (PDB ID: 4UGI) (Rismondo et al., 2016). (**C**) The DivIVA N-terminal domain from *B. subtilis* (*Bs*DivIVA$_{1-57}$) (PDB ID: 2WUJ) (Oliva et al., 2010). (**D**) The structure of N-terminal *Bs*GpsB bound to *Bs*PBP1 cytoplasmic domain peptide (Cleverley et al., 2019). *Bs*GpsB$_{5-64}$ in cyan, *Bs*PBP1$_{1-17}$ in green. (**E**) A representative trimer of the GpsB C-terminal domain from *B. subtilis* (PDB Id: 5AN5) (Rismondo et al., 2016). (**F**) Zoomed-in view of the *Bs*PBP1$_{1-17}$:*Bs*GpsB$_{5-64}$ binding site. Key residues for binding are shown in stick form, hydrogen bonds are represented by black dashed lines and van der Waals' interactions by yellow dashed lines.

The crystal structure of the C-terminal domain of *B. subtilis* GpsB (*Bs*GpsB$_{76-98}$) is a trimer of a parallel triple-helical coiled-coil. Arg83 and Glu88 (Arg96 and Glu101 in *L. monocytogenes*) stabilise the trimer by forming a network of salt bridges that is a characteristic feature of the conserved RhxxhE motif of this domain. Complementation assay analysis in *L. monocytogenes* showed Arg96 and Glu101 were essential for the function of GpsB, which could mean they are crucial for hexamer formation. The conserved hydrophobic residues Phe78, Leu81 and Phe92 in *B. subtilis* GpsB also contribute to hexamer formation as they are buried in the crystal lattice but in isolated trimers they are solvent exposed (Rismondo et al., 2016).

The low-resolution quaternary structure of *L. monocytogenes* GpsB was deduced by SAXS (Cleverley et al., 2016). The arrangement of subunits in hexameric GpsB was concluded to be a 'tripod like' arrangement consisting of three N-terminal dimers (legs) and two C-terminal trimers (base). The roles of Phe91 and Phe105 (equivalent of Phe78 and Phe92 *B. subtilis* GpsB as discussed above) in hexamer formation was investigated and it was found that *L. monocytogenes* cannot grow with the GpsB^{Phe105Ala} allele (Cleverley et al., 2016). The discovery of a GpsB hexamer suggests that GpsB can interact and coordinate simultaneously the activities of multiple PBP1 molecules and/or multiple different proteins by acting as a scaffold (Cleverley et al., 2016) (Figure 1.16).

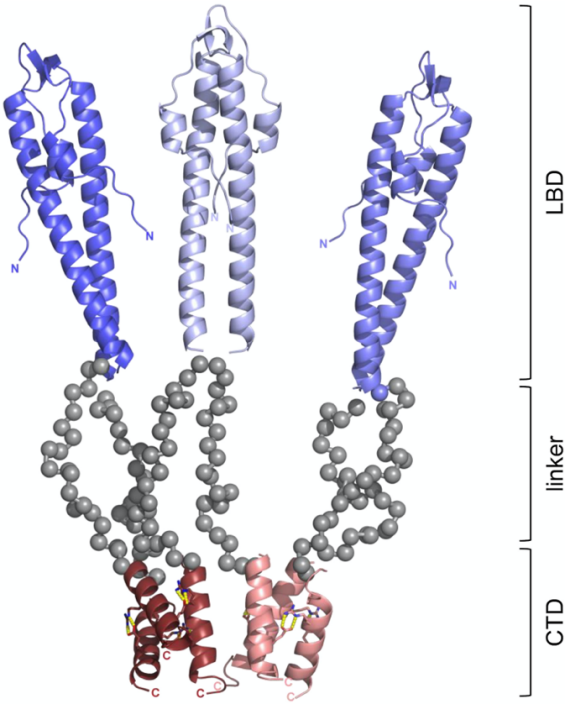

Figure 1.16: The quaternary structure of *B. subtilis* GpsB.
Arrangement of domains in the GpsB hexamer as determined by SAXS analysis of the full-length *B. subtilis* GpsB protein (Cleverley et al., 2016). Figure taken from Halbedel and Lewis, 2019. The structure of 3 N-terminal domain dimers of *Bs*GpsB (also known as LBD: lipid binding domain) are shown in shades of blue. The 2 C-terminal domain (CTD) trimers of *Bs*GpsB are shown in shades of red with domain stabilising salt bridges residues as sticks and hydrogen bonds as yellow dashed lines. The unstructured linker is represented as grey spheres.

1.8.6 GpsB and DivIVA

As mentioned previously, DivIVA was involved in the discovery and initial identification of GpsB. The proteins have been studied extensively since then to determine if there is a relationship or shared overlapping function in cell division. Both proteins are highly conserved in Gram-positive bacteria. Deletion of *divIVA* causes filamentous growth in *B. subtilis* (Edwards

& Errington, 1997) and chaining is observed in *S. pneumoniae* (Fleurie et al., 2014a; Straume et al., 2017), suggesting that DivIVA is important in cell division and could potentially interact with a number of other division proteins.

Localisation studies have revealed differences and similarities between GpsB and DivIVA. DivIVA localised to the poles and septal regions in S. *pneumoniae* (Fadda et al., 2007), and was targeted to negatively curved membranes in *B. subtilis*, where it accumulated (Lenarcic et al., 2009). Unlike DivIVA, GpsB shuttled between the lateral cell wall and the division septum during the cell-cycle and did not accumulate at negatively curved membranes (Claessen et al., 2008). GpsB and DivIVA have been shown to localise independently of each other in *B. subtilis,* and they associate simultaneously with the divisome during the later stages of the division cycle (Tavares et al., 2008; Gamba et al., 2009).

The genetic relationship between GpsB and DivIVA in *S. pneumoniae* was explored to determine whether the two proteins have an epistatic relationship (Rued et al., 2017). As mentioned previously, a deletion of *gpsB* in the R6 strain caused the growth of elongated and larger cells. The deletion of *divIVA* in the same strain caused a different phenotype as the cells appeared shorter and rounder and chaining was observed. Fluorescent D-amino acid (FDAA) labelling was used in each deletion strain. The label acts as a substitute for FtsZ localisation as FDAA indicates TPase activity and septal and peripheral peptidoglycan synthesis are linked with Z-ring formation in *S. pneumoniae* (Kuru et al., 2012; Boersma et al., 2015). Δ*gpsB* cells had multiple FDAA rings whereas each individual bud in the Δ*divIVA* chaining-phenotype strain contained a single FDAA ring. A double *gpsB divIVA* deletion produced cells that grew significantly slower than the single deletions and the cells contained thick FDAA rings. As with Δ*gpsB*, the double mutant cells were elongated and large, but they were also misshapen. The increased severity of the double mutant indicated that Δ*divIVA* is not epistatic to Δ*gpsB*, at least in *S. pneumoniae* R6.

DivIVA and GpsB are both comprised of two main domains (Figure 1.17). Their N-terminal domains are highly homologous in structure, sharing the same coiled-coil dimer arrangement of alpha helices (Oliva et al., 2010; Rismondo et al., 2016). The DivIVA N-terminal domain functions as the lipid binding domain that is required to bind to negatively curved membranes (Lenarcic et al., 2009), and which is mediated by hydrophobic amino acids in the loop region (Oliva et al., 2010). These amino acids are not maintained in GpsB orthologues but the N-

terminal domain has been shown to be required for the recruitment to membrane fractions in *L. monocyogenes* (Rismondo et al., 2016).

The C-terminal domains (CTD) of GpsB and DivIVA differ markedly; while the GpsB C-terminal domain is a parallel trimer of short helices, the equivalent domain in *B. subtilis* DivIVA is an extended coiled-coil tetramer (Oliva et al., 2010). However, the CTD of DivIVA is not well conserved, and pneumococcal proteins have an additional C-terminal region compared to *B. subtilis* DivIVA, which is essential for native localisation in *S. pneumoniae* (Straume et al., 2017). The CTD of both GpsB and DivIVA play important roles in oligomerisation (Muchová et al., 2002; Rismondo et al., 2016). The DivIVA CTD interacts with various soluble cell-cycle proteins whereas the CTD of GpsB seemingly acts only as a multimerisation motif (Halbedel & Lewis, 2019).

The precise role of DivIVA in cell division in different Gram-positive bacteria is not clear. It has been reported that DivIVA associates with the divisome and acts as a scaffold to localise division proteins (Fadda et al., 2007; Oliva et al., 2010). *B. subtilis* DivIVA seems to function in the recruitment of MinCD, an inhibitor of FtsZ assembly (Edwards & Errington, 1997; Marston et al., 1998). However, Gram-positive cocci, even the ovococcoid *S. pneumoniae,* do not encode a MinCD system, and DivIVA must play an important other role. In the absence of DivIVA, elongation of *S. pneumoniae* is hindered (Fleurie et al., 2014a), perhaps because DivIVA is part of the elongasome complex in wild type cells (Straume et al., 2017). Therefore, like GpsB, DivIVA appears to have important roles in elongation as well as division. In the genuine coccus *S. aureus* that lacks the *min* genes, DivIVA is not required for division as its absence caused no observable change in cell morphology (Pinho & Errington, 2004). *Sa*DivIVA does however, localise at division sites (Pinho & Errington, 2004; Bottomley et al., 2017), and various interactions between divisome proteins and DivIVA have been determined by BACTH (Bottomley et al., 2017). A role for *Sa*DivIVA in chromosome segregation has been proposed by Bottomley *et al.* who demonstrated interactions with the chromosome partitioning protein SMC and DnaK. DnaK is a heat stress molecular chaperone (Bukau & Horwich, 1998) and Bottomley *et al.* showed there was a higher frequency of non-viable anucleate cells with a Δ*divIVA dnaK::kan* double mutant. The specific roles played by DivIVA and GpsB are distinct, and DiviVA has, seemingly, different functions in various Gram-positive species, perhaps as a function of cell shape.

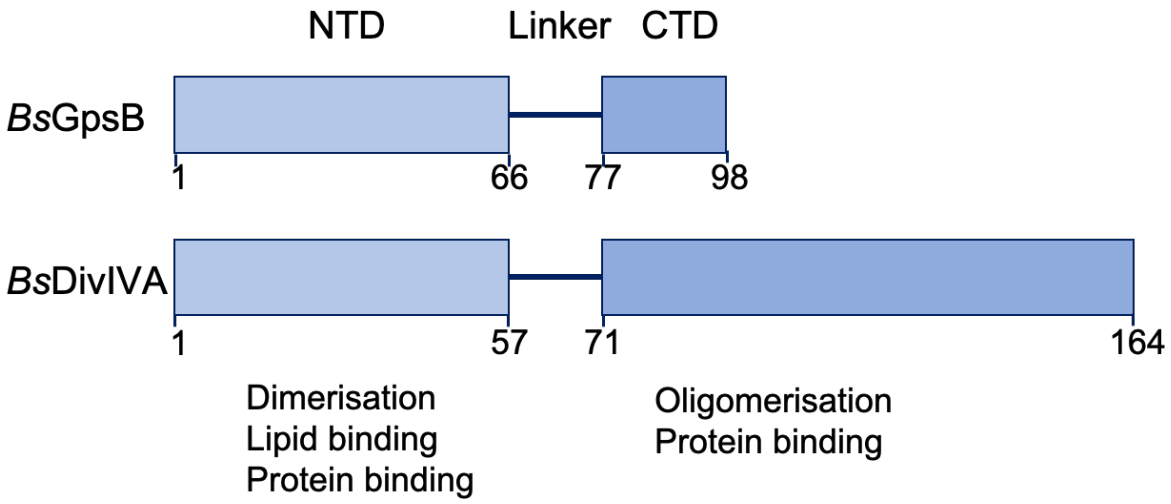

Figure 1.17: Domains of GpsB and DivIVA from *B. subtilis.*
GpsB and DivIVA are both split into two domains with a linker between the two. The boundaries of each domain are labelled on the figure. The suggested roles of the NTD (N-terminal domain) and CTD (C-terminal domain) of DivIVA and GpsB are listed underneath.

1.8.7 Conclusion

Taking into account all of the data discussed above, it appears that GpsB plays an important role in the elongation-division cycle by acting as a scaffolding protein that controls the relative spatial arrangement of PBPs and potentially other proteins during both vegetative and asymmetric division (during sporulation). Structural studies were vital to confirming predictions from localisation, deletion and interaction experiments. There are similarities and differences in GpsB function in a number of different Gram-positive bacteria, and hence the function of GpsB in cell division might differ slightly from species to species. The importance of GpsB in high growth temperatures in *L. monocytogenes* and its essentiality in *S. pneumoniae*, along with the absence of a GpsB homologue in humans, could also point to GpsB as a novel target for antibiotic development.

1.9 The importance of protein kinases and cell signalling in cell division

1.9.1 Bacterial serine/threonine protein kinase family

Around 2% of eukaryotic genes encode protein kinase domains, highlighting the importance of phosphorylation in living organisms, and since the 1950's studies have shown protein phosphorylation to be a major regulatory mechanism (Rubin et al., 2000). Phosphorylation of proteins on serine, threonine and tyrosine residues was once restricted to eukaryotes but it is now clear that protein phosphorylation is widespread among bacteria (Gruszczyński et al.,

2010). In prokaryotes protein phosphorylation also occurs on histidine, cysteine, aspartate and arginine residues. Gram-positive bacteria possess a conserved family of serine/threonine protein kinases (eSTPKs) that have various roles in the cell-cycle such as the development of regulation, control of cell growth, stress response, virulence and sporulation (Madec et al., 2002).

1.9.2 Structure of eSTPKs

The overall structure of eSTPKs consists of an intracellular N-terminal kinase domain and an extracellular sensing region linked by a short transmembrane helix (Pompeo et al., 2018). The kinase domain is composed of two lobes, the N-lobe which is predominantly made up of β-sheets and one α-helix (αC) and the C-lobe which is α-helical (Huse & Kuriyan, 2002) (Figure 1.18). ATP binds at the deep cleft between the two lobes. The N-lobe has a number of important functional features, the first of which is the P-loop, which is a glycine rich loop with the consensus sequence GXGXYGXXXV. The presence of many glycine residues makes the P-loop flexible which acts as a clamp to cover the bound ATP molecule and stabilise it in the ATP binding cleft (Manuse et al., 2015). An invariant lysine residue (Lys40 of *Mycobacterium tuberculosis* PknB, *Mt*PknB) in the N-lobe interacts with the α and β phosphates of the ATP molecule which helps anchor and orientate the molecule and a glutamate residue (Glu59 of *Mt*PknB) stabilises the lysine by forming a hydrogen bond with it (Cox et al., 1994). The C-lobe of the N-terminal domain contains both the catalytic and activation loops. The catalytic domain contains crucial asparagine and aspartate residues (Asn143 and Asp138 of *Mt*PknB) for phosphorylation. Asn143 positions Asp138 in the correct position to act as a catalytic base to attack the hydroxyl group of the phosphorylation substrate (Manuse et al., 2015). The activation loop contains a number of conserved threonine and serine residues that are phosphorylated for the activation of the kinase. A P+1 loop is formed by the last 4 amino acids of the activation loop and this is what determines the specificity of the kinase for threonine and serine residues (Taylor et al., 1995). Next to the kinase domain is a highly flexible uncharacterised juxtamembrane domain that is phosphorylated and is thought to contribute to activation of the kinases and help with the docking of target proteins (Durán et al., 2005).

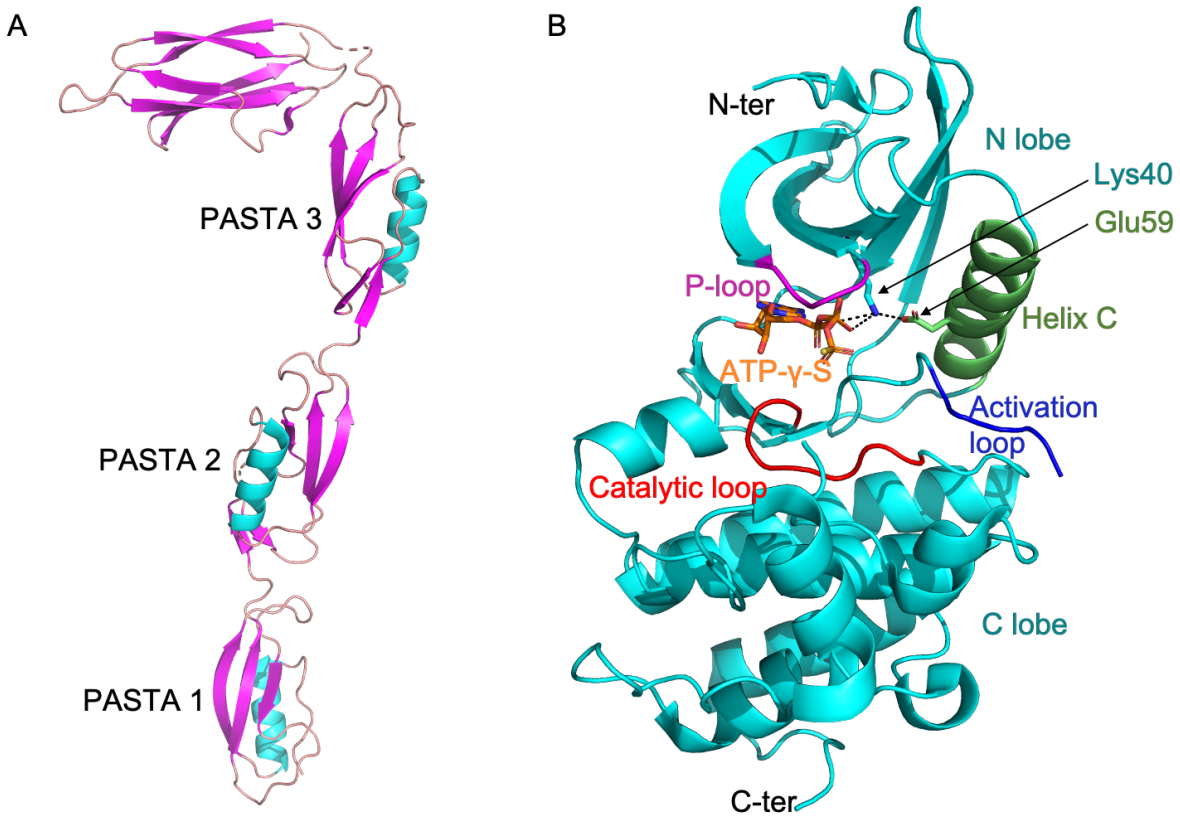

Figure 1.18: Structures of eSTPK domains.
Panel **A** shows the structure of extracellular domain of Stk1 from *S. aureus* (PDB ID:3PY9) in cartoon form. The structure is coloured by secondary structure with β-sheets coloured in magenta, α-helices coloured cyan and loops in peach. Each PASTA domain is labelled. Panel **B** shows the intracellular kinase domain of PknB from *M. tuberculosis* bound to ATP- γ -S (PDB ID: 1MRU). Specific structural and functional features are coloured and labelled on the figure. Dotted black lines indicate salt bridges.

The extracellular domain of eSTPKs contain a number of PASTA (PBP and serine/threonine kinase associated) domains with the number differing among bacterial species (Figure 1.18). *M. tuberculosis* PknB contains 4 PASTA domains whereas PrkC (*B. subtilis*) and Stk1 (*S. aureus*) contain 3 (Manuse et al., 2015). The first structure of a PASTA domain was from a class B PBP from *S. pneumoniae* PBP2x and this structure revealed that the domain is a globular fold formed by three β-strands and one α-helix (Gordon et al., 2000). PrkC and Stk1 contain an additional C-terminal extension of ~80 amino acids that form two β-sheets. This extension has potential adhesive properties and could be involved, for instance, in cell to cell interactions (Ruggiero et al., 2011; Squeglia et al., 2011).

1.9.3 Localisation and essentiality of eSTPKs

The importance of eSTPKs in a variety of Gram-positive species and their localisation during the cell-cycle has been studied by a number of groups. The intracellular kinase domain and the extracellular PASTA domains of StkP are essential for normal division in *S. pneumoniae*: phase-contrast microscopy revealed that Δ*stkP* cells were more spherical compared to the usual ovoid shape and the cells grew as chains (Fleurie et al., 2012). Conversely, the inactivation of *B. subtilis* PrkC did not affect cell growth, division or shape (Madec et al., 2002) and in *L. monocytogenes* PrkA is essential (Wamp et al., 2020). In dividing cells, *Bs*PrkC and *Sp*StkP and *Mt*PknB are located at the septum (Mir et al., 2011; Fleurie et al., 2012; Pompeo et al., 2015) highlighting an important role for eSTPKs during division. The mid-cell localisation of *Sp*StkP and *Mt*PknB requires the extracellular PASTA domains of the respective kinase (Mir et al., 2011; Fleurie et al., 2012) but *Bs*PrkC appears to exert this same localisation pattern without its PASTA domains (Pompeo et al., 2018). Furthermore, *Bs*PrkC is dispersed all over the cell wall during the stationary phase of non-diving cells, suggesting a different role in non-diving cells (Pompeo et al., 2018). The cell division regulator GpsB is required for the localisation of *Sp*Stk1 (Fleurie et al., 2014a) but the localisation of PrkC is not dependent on GpsB in *B. subtilis* (Pompeo et al., 2015).

1.9.4 Activity of eSTPKs

Various reports have linked the activity of eSTPKs during the cell-cycle with its localisation pattern, binding muropeptides to the extracellular PASTA domains and activation of the kinase domain by GpsB. A number of studies have demonstrated that PASTA domains in *Mt*PknB, *Bs*PrkC, *Sa*Stk1 and *Sp*StkP are able to bind to peptidoglycan fragments and β-lactams (Paracuellos et al., 2010; Maestro et al., 2011; Mir et al., 2011; Squeglia et al., 2011). An early model based on *Mt*PknB that was proposed by Mir *et al.*, states that the extracellular domains of eSTPKs contribute to their cellular localisation, which during cell division is at the septum. The increase in kinase concentration promotes homodimerisation and activation. The interaction of PASTA domains with cell division proteins and peptidoglycan signal information from the cell wall to endogenous phosphorylation targets. Since then, the hypothesis that the binding of muropeptides directly causes the dimerisation and activation of the extracellular domains of eSTPKs has been studied in a number of species. The isolated extracellular domain of *Sa*Stk1 was shown to be monomeric and dimerisation was not induced by muropeptides

(Ruggiero et al., 2011). Dynamic light scattering revealed an increased hydrodynamic diameter of *Bs*PrkC with the addition of peptidoglycan fragments suggesting induced oligomerisation (Pompeo et al., 2018). In *S. pneumoniae*, muropeptides are not required for kinase activation but activation is dependent on its PASTA domains (Zucchini et al., 2018), whereas in *B. subtilis* the isolated catalytic domain of PrkC is active *in vitro* (Absalon et al., 2009). Further analysis of the activation of *Bs*PrkC showed that deletion of the PASTA domains had no effect on the ability of the kinase to autophosphorylate *in vivo* during the exponential phase of growth but the PASTA domains were required for kinase autophosphorylation during stationary phase (Pompeo et al., 2018).

In 2015 Pompeo *et al*. proposed a role for GpsB in the activation of PrkC in *B. subtilis* (Pompeo et al., 2015). An interaction between the catalytic domain of PrkC and GpsB was discovered by BACTH and no autophosphorylation of PrkC was detected in Δ*gpsB* cells compared to wild-type. Substitution of the identified phosphorylation site in GpsB, Thr75, for a phospho-mimetic glutamic/aspartic acid caused a weak signal for PrkC autophosphorylation compared to wild-type GpsB and a phosphoablative GpsB mutant (Thr75Ala). The activation of PrkC by GpsB to phosphorylate two substrates, CpgA and YvcK *in vitro* was also shown (Pompeo et al., 2015). Together these data indicated that unphosphorylated GpsB activates PrkC and phosphorylated GpsB had lost this activating capability. In agreement with this conclusion, GpsB is required for StkP autophosphorylation in *S. pneumoniae* in multiple strains (Rued et al., 2017). It has not yet been shown if GpsB interacts with and is phosphorylated by PrkA in *L. monocytogenes*.

Putting this information together it is clear that the activation mechanism of eSTPKs varies among Gram-positive species. A model for PrkC activation has been proposed by Pompeo *et al.* that states during the stationary phase when cells are not dividing PrkC is dispersed in the cell and is activated though the binding of peptidoglycan fragments in response to external stimuli (Pompeo et al., 2018). The model also predicts that in the exponential phase of growth, PrkC will be located at mid-cell during division and is activated by GpsB but not peptidoglycan fragments.

1.9.5 Activation mechanism of the kinase domain

The catalytic and activation mechanism of the kinase domain of eSTPKs has been extensively studied in *M. tuberculosis* and *S. aureus*. The positions of the N- and C-lobes with respect to

each other form the inactive or active conformations and the phosphorylation of multiple activation loop residues dictates the catalytic state of the kinase (Cox et al., 1994). The activation loop is disordered in the inactive conformation and blocks the substrate binding site (Manuse et al., 2015). Dimerisation of the N-lobes induces allosteric activation, which results in kinase *cis*-autophosphorylation on an activating Thr/Ser residue (Thr172 in *S. aureus*) (Zheng et al., 2018b). Molecular modelling of Stk1 suggests that the autophosphorylation moves the activation loop from a closed conformation to an active one, revealing the substrate binding site and enabling ATP access to allow *trans*-phosphorylation of a second kinase (Zheng et al., 2018b) (Figure 1.19). In this conformation the conserved N-lobe Lys and Glu residues then form the hydrogen bond interaction that is required for phosphoyltransfer to take place (Manuse et al., 2015). The active kinase is then able to phosphorylate cellular targets until dephosphorylation inactivates the system. Complete autophosphorylation of the activation loop involves the phosphorylation of a number of Thr/Ser residues. It has been reported that there are 4 activation loop residues that are phosphorylated on PrkC in *B. subtilis*, Thr162, Thr163, Thr156 and Thr167 (Madec et al., 2003). In *M. tuberculosis*, PknB phosphorylation of Thr171 and Thr173 (equivalent to PrkC Thr156 and Thr167) is essential for kinase activity (Durán et al., 2005). In *S. aureus* Stk1 a total of 6 residues are phosphorylated in the activation loop Thr161, Ser162, Thr164, Th166 and Thr172 and when Thr172 is mutated to an alanine the kinase is rendered inactive and no activation loop residues are phosphorylated (Zheng et al., 2018b), indicating that Thr172 is a critical residue for Stk1 function.

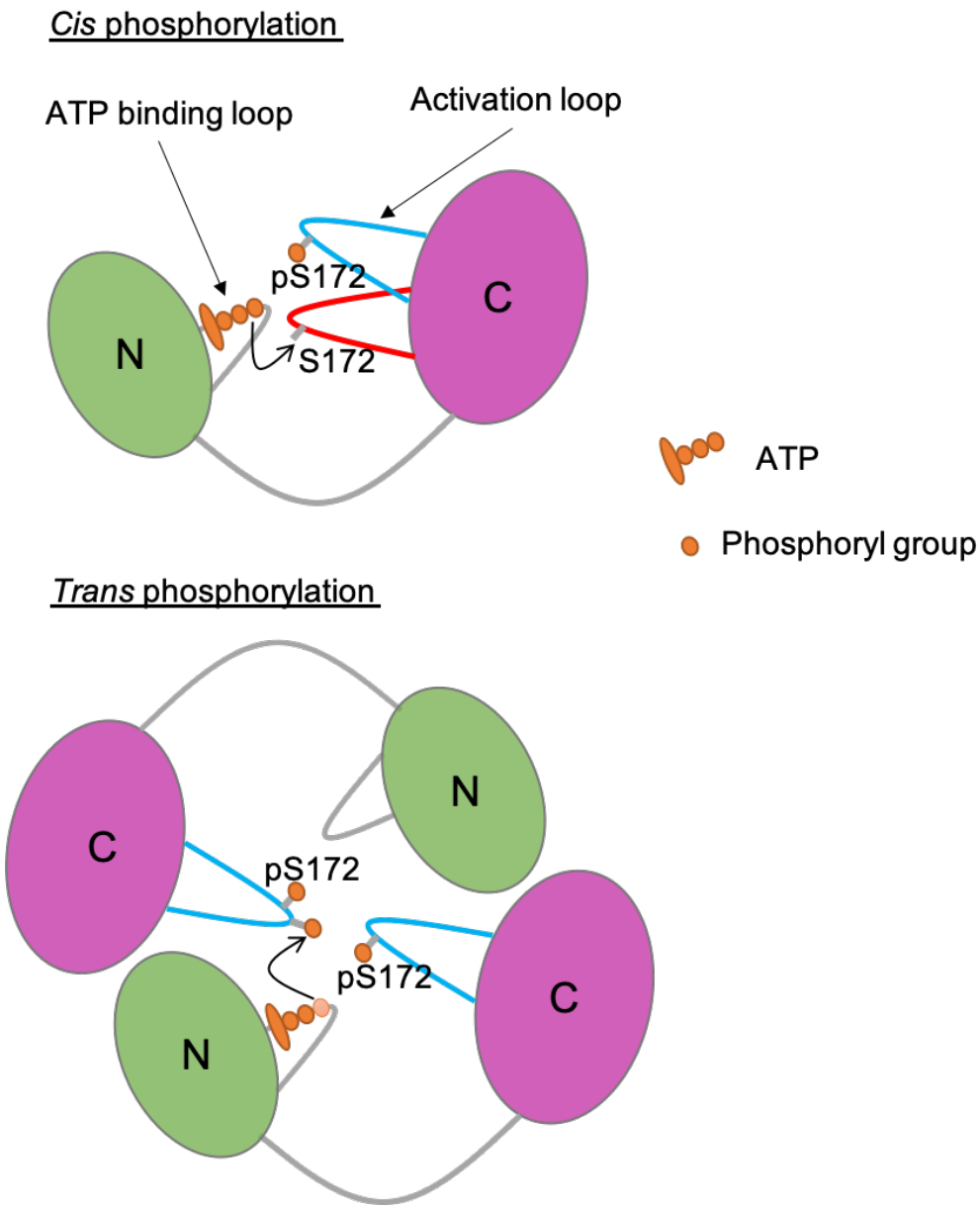

Figure 1.19: Proposed activation mechanism of Stk1.
A schematic diagram showing the activation mechanism of Stk1 (Zheng et al., 2018b). The binding of an ATP molecule in the ATP binding loop of the N-lobe enables the *Cis* phosphorylation of serine 172. This induces a conformational change causing the activation loop to move from a closed (red) to an open (cyan) conformation. This activated kinase can then activate other kinase molecules by *Trans* phosphorylation. The N-lobe of the kinase domain is coloured green and the C-lobe is coloured magenta.

1.9.6 Cellular roles of eSTPKs

The cellular roles of eSTPKs have been studied in a number of Gram-positive species. DivIVA, suggested to participate in the control of cell shape and localisation of PBP sites, is phosphorylated specifically by StkP in *S. pneumoniae in vivo* (Nováková et al., 2010). Phosphorylation occurs on Thr201 and mutation of this threonine residue to alanine causes

the cells to elongate and polar bulges are observed (Fleurie et al., 2012). GpsB is required for the StkP-dependent phosphorylation of DivIVA (Fleurie et al., 2014a). In *M. tuberculosis* Wag31, an orthologue of DivIVA, is phosphorylated by PknB to regulate cell shape (Kang et al., 2005). Conversely, DivIVA is not phosphorylated by PrkC in *B. subtilis* (Madec et al., 2002). StkP has also been shown to phosphorylate MapZ and FtsZ: MapZ positions FtsZ at mid-cell and its phosphorylation on Thr67 and Thr78 regulates the closure of the Z-ring (Fleurie et al., 2014b).

The eSTPK in *B. subtilis*, PrkC, is not essential for cell division but nonetheless is an important regulator of sporulation and biofilm formation (Shah et al., 2008; Madec et al., 2002). Cells that are deficient in PrkC are unable to germinate and consequently muropeptides appear to act as a spore germinant (Shah et al., 2008). Several proteins have been discovered as PrkC targets, including CpgA, YvcK and GpsB. CpgA is a GTPase associated with the small subunit of the ribosome, which is essential in *B. subtilis*, as cell morphology defects are observed with its depletion (Cladière et al., 2006). CpgA is phosphorylated on Thr166, which regulates the GTPase activity and the ability of CpgA to bind to the 30S ribosome (Pompeo et al., 2012). This discovery links CpgA to peptidoglycan synthesis and cell growth through the regulation of protein synthesis. YvcK is a protein essential for cell growth and maintenance on gluconeogenic sources (Görke et al., 2005). It is phosphorylated on Thr304, and it has been suggested that it could have a valuable role in glucogenesis for the synthesis of cell wall precursors (Foulquier et al., 2014).

In vitro phosphorylation assays and mass spectrometry revealed Thr75 to be the single phosphorylation site in *B. subtilis* GpsB by PrkC (Pompeo et al., 2015). As discussed above, Pompeo *et al.* demonstrated that for the autophosphorylation of PrkC, GpsB is required and this autophosphorylation is inhibited by phosphorylated GpsB, implying a negative feedback relationship. Phosphorylation of GpsB by PrkA in *L. monocytogenes* has yet to be shown, although the equivalent residue to *Bs*GpsB^{Thr75} is Thr88 and the phosphomimetic mutant Thr88Asp was inactive in *L. monocytogenes* even though the hexameric structure of this GpsB variant was maintained *in vitro* (Cleverley et al., 2016). GpsB is important for division site localisation and activation of StkP in *S. pneumoniae*, though without a requirement to be phosphorylated (Fleurie et al., 2014a). Therefore, the role of phosphorylation with regards to GpsB still needs clarification.

1.10 Aims of this study

This thesis details the functions of two important cell division proteins found in Gram-positive bacteria, GpsB and ReoM. GpsB has been previously shown to interact with a number of cell division proteins and its main role is to co-ordinate the activities of PBPs via a direct interaction with the PBP cytoplasmic mini-domain (Cleverley et al., 2016). The critical structural features of the GpsB interaction with the major class A PBP (PBP1) in *B. subtilis* have been determined (Cleverley et al., 2019). These features will be examined in two pathogenic organisms, *L. monocytogenes* and *S. pneumoniae*, to gain a wider understanding of the interaction across Gram-positive bacteria (Chapter 3). The N-terminal domain of *Bs*GpsB is highly homologous in structure to the N-terminal domain of *Bs*DivIVA and when the crystal structures are overlaid they show only slight differences. *Bs*DivIVA, however, does not bind to PBP1, therefore, mutants of *Bs*DivIVA will be made by comparison to *Bs*GpsB in an attempt to engineer PBP1 binding to DivIVA and, combined with mutagenesis that abrogates binding of GpsB to PBP, will yield an understanding of what is crucial for the binding of PBPs to this critical cell division regulator (Chapter 4). A fragment-based X-ray screening experiment was performed on GpsB to try and identify a lead fragment for the development of a potential drug to block the crucial GpsB:PBP binding in *S. pneumoniae* (Chapter 5). In *L. monocytogenes*, a *gpsB* suppressor mutation was mapped to the *lmo1503* gene encoding a protein of unknown function (Wamp et al., 2020). The protein encoded by *lmo1503* is a homologue of *Enterococcus faecalis* IreB, which has been implicated as a negative regulator of cephalosporin resistance (Hall et al., 2013). The structure and function of this previously uncharacterised protein Lmo1503 (herein named ReoM) in cell division was explored and its relationship with a major protein kinase PrkA was determined (Chapter 6).

Chapter 2: Methods

2.1 Molecular biology

2.1.1 Chemical suppliers

Unless otherwise stated, all chemicals were purchased from Fisher Scientific, Formedium or Sigma Aldrich. Molecular biology reagents and kits were purchased from Thermo Scientific.

2.1.2 General buffers and solutions

Tris and HEPES buffers were made by dissolving Tris/HEPES base powder in MilliQ water and were adjusted to the desired pH using hydrochloric acid.

Below is a list of general buffers and solutions:

- 1x TAE: 0.4 M Tris-acetate pH 8.0, 0.1 M EDTA.
- 5x DNA loading dye: 40 mM Tris.HCl pH 6.8, 10 % (w/v) glycerol, 0.1 % bromophenol blue, 3 % SDS.
- 1x SDS running buffer: 25 mM Tris.HCl pH 8.5, 250 mM glycine, 0.1 % (w/v) SDS.
- 6x SDS loading dye: 50 mM Tris.HCl pH 6.8, 10 % (w/v) SDS, 0.1 % (w/v) bromophenol blue, 10 % (w/v) glycerol, 1 mM DTT.
- 1x native-PAGE running buffer: 0.192 M glycine, 250 mM Tris.HCl.
- 6x native load dye: 50 mM Tris.HCl pH 8.5, 0.1 % (w/v) bromophenol blue, 10 % (w/v) glycerol.
- 10x Tris-tricine anode buffer: 1 M Tris.HCl pH 8.9.
- 10x Tris-tricine cathode buffer: 1 M Tris, 1 M tricine, 1 % SDS.
- Coomassie blue stain: 40 % ethanol, 10 % acetic acid, 0.25 % Coomassie blue R-250.
- Destain: 20 % ethanol, 10 % acetic acid.

2.1.3 Growth medium

20 g/L of LB-Broth Lennox from Formedium was used as growth medium and 1.5 % (w/v) agar (Formedium) was added to LB prior to autoclaving for LB agar plates.

2.1.4 Plasmids

The plasmids used in this study are listed in Table 2.1. Kanamycin at 50 μg/mL or ampicillin at 100 μg/mL were added to the growth medium for the selection of transformed bacteria.

Plasmid	Antibiotic resistance	Description
pETM11	Kanamycin	Plasmid with a T7 promoter. Contains a multiple cloning site which allows the fusion of a His_6-tag to the N-terminus of the expressed protein that is cleavable with TEV protease.
pMAT11	Ampicillin	Plasmid with a high copy number and a T7 promoter. Thrombin and TEV cleavable N-terminal His_6-tag-MBP fusions. No *Nco*I site within the MBP coding region.
pET28a	Kanamycin	Plasmid with a T7 promoter. Contains a multiple cloning site with His_6-tag incorporation at either the N- or C-terminus. N-terminal His_6-tag is cleavable with thrombin protease.

Table 2.1: A list of the plasmids used in this study

2.1.5 Bacterial strains

The bacterial strains used in this study are summarised in Table 2.2.

E. coli strain	Genotype	Description
BL21 (DE3)	F^- *ompT hsd*S_B (r_B^-, m_B^-) *gal dcm* (DE3)	Expression strain with high efficiency. The most widely used host for protein expression using *E. coli* and T7 expression system
XL1-blue	*recA1 endA1 gyrA96 thi-1 hsdR17 supE44 relA1 lac [F´ proAB lacIq ZΔM15 Tn10 (Tetr)].*	Strain allows blue-white colour screening for recombinant plasmids and host strain for routine cloning applications.
T7 Express	*fhuA2 lacZ::T7 gene1 [lon] ompT gal sulA11 R(mcr-73::miniTn10--TetS)2 [dcm] R(zgb-210::Tn10--TetS) endA1 Δ(mcrC-mrr)114::IS10*	High-efficiency chemically competent cells suitable for T7 protein expression.

Table 2.2: A list of bacterial strains used in this study

2.1.6 Preparation of competent cells

10 mL of LB medium was inoculated with a single colony from an LB agar plate and the culture was incubated at 37 °C for 15-18 hours. 5 mL of the saturated starter culture was used to

inoculate a 100 mL culture that was grown at 37 °C to an absorbance at 600 nm of 0.5. The culture was cooled on ice for 15 minutes before being split into two 50 mL falcon tubes and centrifuged at 4500 rpm for 10 minutes. The supernatant was discarded and the pellets were resuspended in 6 mL total of TfbI (see below) and cooled on ice for 15 minutes. A second centrifugation step at 4000 rpm was followed by resuspension of the pellet in 1.2 mL TfbII (See below). The cells were then aliquoted in 50 µL volumes, flash frozen in liquid nitrogen and stored at -80 °C.

- TfbI: 100 mM rubidium chloride, 50 mM manganese chloride, 30 mM potassium acetate pH 5.8 (with acetic acid), 10 mM calcium chloride, 15 % (v/v) glycerol.
- TfbII: 10 mM MOPS pH 6.8 (with NaOH), 10 mM rubidium chloride, 75 mM calcium chloride, 15 % (v/v) glycerol.

2.1.7 Transformation of competent cells

A 50 µL aliquot was defrosted on ice and ~100 ng of plasmid or 4 µL of mutagenesis reaction was added. The cells were incubated on ice for 30 minutes and then heat shocked at 42 °C for 45 seconds. The cells were cooled for 2 minutes on ice and 1 mL of LB medium was added before a one hour recovery at 37 °C. Transformed cells were plated onto LB agar with the appropriate antibiotic and incubated at 37 °C overnight or 20 °C for 48 hours.

2.1.8 Quikchange mutagenesis

The list of primers used for Quikchange mutagenesis can be found in Table Apx B.1. All primers were manufactured by Eurofins Genomics.

In the 50 µL reaction 50 ng of plasmid template was used with 100 ng of both the forward and reverse primers. dNTPs were added to a final concentration of 0.25 mM along with 1 x *Pfu* reaction buffer and 2.5 U of *Pfu* polymerase. The cycling parameters can be found in Table 2.3 below. All reactions were carried out in a T100™ Thermal Cycler (Bio-Rad).

Segment	Cycles	Temperature	Time
1	1	95 °C	1 minute
2	15	95 °C	30 seconds
		55 °C	1 minute
		68 °C	8.5 minutes

Table 2.3: Cycling parameter for Quikchange mutagenesis

In the event of unsuccessful mutagenesis using the above method, a second longer Quikchange method was used were a single-primer extension reaction was carried out before the standard Quikchange reaction. (Wang & Malcolm, 1999). For this experiment there were two reaction mixes with the same reagents used in the first method, however each reaction contained one primer. Both reactions underwent the cycling parameters in Table 2.4 before 25 µL of each reaction with a single primer were added together along with 2.5 U of *Pfu* polymerase and undergoing the cycling parameters in Table 2.5.

Parental DNA was digested with 16 U of *Dpn*I and the reaction was incubated for 2 hours at 37 °C.

Segment	Cycles	Temperature	Time
1	1	95 °C	1 minute
2	9	95 °C	30 seconds
		55 °C	1 minute
		68 °C	8 minutes
3	1	68 °C	10 minutes

Table 2.4: Cycling parameters for step one of longer Quikchange method

Segment	Cycles	Temperature	Time
1	1	95 °C	1 minute
2	15	95 °C	30 seconds
		55 °C	1 minute
		68 °C	8 minutes
3	1	68 °C	10 minutes

Table 2.5: Cycling parameters for step two of longer Quikchange method

2.1.9 PCR amplification of target genes from genomic DNA

The primers used in PCR amplification can be found in Table Apx B.2.

Genomic DNA from *Listeria monocytogenes* EGD-e was supplied by Dr. S. Halbedel (Division of Enteropathogenic bacteria and *Legionella*, Robert Koch Institute, Germany). *Streptococcus pneumoniae* R6 genomic DNA was supplied by Prof. W. Vollmer (Newcastle University). PCR reaction mixes consisted of 50 ng of template, 50 pmol of forward and reverse primer, 0.2 mM dNTPs, 1x Phusion buffer and 1 U of Phusion polymerase. The cycling parameters for the reaction can be found in Table 2.6. All reactions were carried out in a T100™ Thermal Cycler (Bio-Rad).

Segment	Cycles	Temperature	Time
1	1	98 °C	30 seconds
2	34	98 °C	10 seconds
		55 °C	20 seconds
		72 °C	40 seconds
3	1	72 °C	5 minutes

Table 2.6: Cycling parameters for amplification of target genes

2.1.10 Agarose gel electrophoresis, visualisation of PCR products and purification of DNA

Mutagenesis products were analysed on 1 % (w/v) agarose gels and PCR amplification products were analysed on 2 % (w/v) agarose gels, and both were stained with 0.5 µg/mL of GelRed (Sigma-Aldrich). 6 x loading dye was added to the samples and 0.5 ng of 1 kb or 1 kb Plus DNA ladder was used as a marker (Thermo Fisher). Gels were run at 100 V for 45 minutes and were imaged using a Gel Doc XR+ (Bio-Rad) (Figure 2.1). PCR amplification gels were visualised using a UV transilluminator and PCR products of the appropriate sizes were excised and purified using a GeneJET PCR purification kit (Fisher).

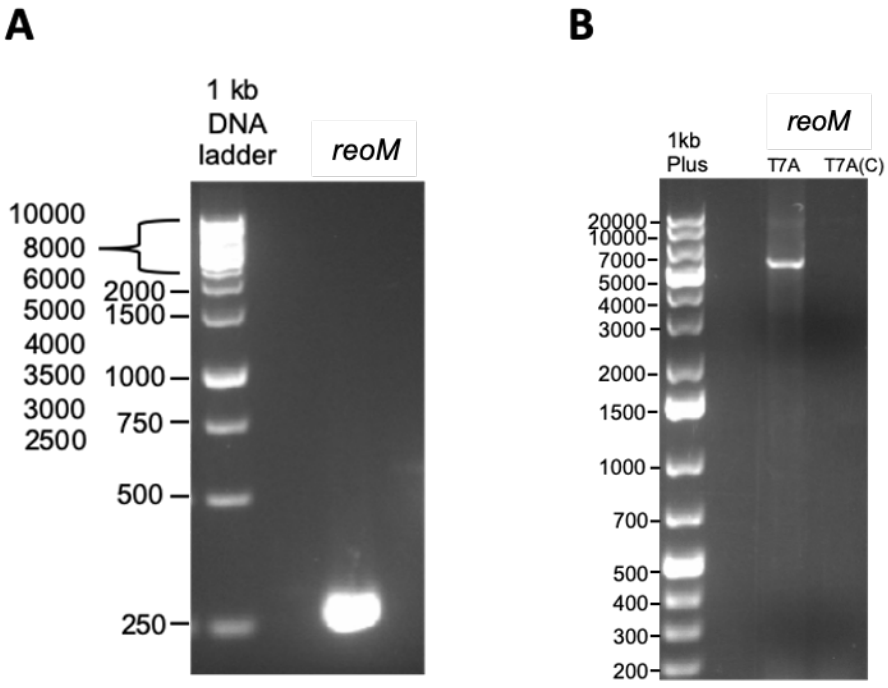

Figure 2.1: Representative agarose gels.
A representative PCR amplification gel is shown in panel **A** and a representative mutagenesis gel in panel **B**.

2.1.11 Restriction digests of DNA and plasmids

The purified PCR fragment was digested with 30 units of each restriction enzyme (*Nco*I and *Xho*I) (Thermo Fisher Scientific) in 1 x Tango buffer with a total reaction volume of 200 µL for 2 hours at 37 °C. 3-4 µg of plasmid was digested in the same way. Both the plasmid and the DNA insert were purified using the GeneJET PCR purification kit (Fisher).

2.1.12 Ligation of DNA into plasmids

10 µL ligation reactions were carried out at 16 °C for 2 hours. Reactions contained 1 x T4 ligase buffer, 37.5 ng of vector, DNA insert at 1:5 molar ratio (vector to insert) and 1 U of T4 ligase (NEB). A control reaction without the DNA insert was used.

2.1.13 Small-scale cultures and isolation of plasmids

Successful Quikchange and ligation reactions (determined by the presence of a band of the correct length on an agarose gel) were transformed into XL1-blue cells, which were then plated onto LB agar plates. 10 mL LB cultures with the appropriate antibiotic were inoculated with a single colony from an LB agar plate and grown overnight at 37 °C. The cells were pelleted by centrifugation at 4000 xg for 10 minutes and the supernatant was discarded. The plasmid was extracted and purified from the cells using a GeneJET plasmid miniprep kit (Fisher) per the manufacturer's instructions.

2.1.14 DNA sequencing

All DNA sequencing was carried out by Eurofins Genomics (formerly GATC biotech) using universal T7 primers (T7 and pET-RP).

2.1.15 Analysis of proteins by SDS-PAGE and Native-PAGE electrophoresis

All gels were constructed using a Mini-PROTEAN® tetra handcast system (Bio-Rad). 12 % Tris-glycine gels and 17 % Tris-tricine gels were used. The components of each gel are listed in Table 2.7. 1- 10 µL of sample was mixed with 6x SDS loading dye and heated at 100 °C for 1 minute before being loaded on the gel. 3 µL of prestained protein ladder (Geneflow Ltd) was also loaded. Tris-glycine gels were run at 200 V for 45 minutes and Tris-tricine gels were run at 150 V for 1 hour and 15 minutes. 20 % native gels (see below) were used; 10 µL of sample with 6x native load dye were loaded and the gels were run at 200 V on ice for 1-2 hours. Gels

were stained using for 20 minutes and de-stained for 10 minutes before being transferred to water and heated for 1 minute in a microwave set to 'high'. A representative SDS-PAGE gel is shown in Figure 2.2.

Gel	Number of gels	Stacking gel	Resolving gel
12 % Tris-glycine	4	dH_2O- 5.84 mL Acrylamide (40 %)- 1 mL 1 M Tris pH 6.8- 3.3 mL 10 % SDS- 80 µL 10 % APS- 80 µL TEMED- 8 µL	dH_2O- 8.6 mL Acrylamide (40 %)- 6 mL 1.5 M Tris pH 8.8- 5 mL 10 % SDS- 200 µL APS- 200 µL TEMED- 10 µL
17 % Tris-tricine	2	dH_2O- 5.34 mL Acrylamide (40 %)- 1.25 mL 3 M Tris, 0.3 % SDS pH 8.5- 3.3 mL 10 % APS- 100 µL TEMED- 8 µL	Glycerol- 1 g dH_2O- 2.25 mL Acrylamide (40 %)- 4.25 mL 3 M Tris, 0.3 % SDS pH 8.5- 3.3 mL 10 % APS- 200 µL TEMED- 16 µL
20 % Native	2	N/A	dH_2O- 3.59 mL Acrylamide (40 %)- 7.5 mL 1.5M Tris pH 8.8- 3.75 mL 10 % APS- 150 µL TEMED- 10 µL

Table 2.7: PAGE gel components

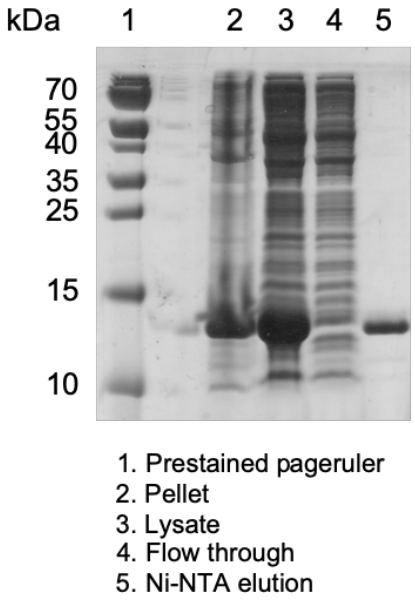

Figure 2.2: Representative SDS-PAGE gel.
A 17 % Tris-tricine gel of the Ni-NTA purification of His_6-tagged ReoM.

2.2 Recombinant protein overexpression and purification

2.2.1 Large-scale cultures for the overexpression of target proteins

N-terminally His_6-tagged GpsB proteins, N-terminally tagged DivIVA, ReoM, PrkA and PrpC were expressed in *E. coli* BL21 (DE3) cells. Cell cultures were grown in LB liquid medium at 37 °C with 50 µg/mL kanamycin to an OD_{600} 0.6-0.8. Expression of the target protein was induced with 0.4 mM IPTG and the cultures were incubated at 20 °C for 18 hours. The cells from 2 L of cell culture were harvested by centrifugation (3500 x g) for 30 minutes.

MBP-PBP peptide fusion proteins were expressed in *E. coli* BL21 (DE3) and *E. coli* T7 Express cells. *E. coli* cells were grown in 1 L cultures in LB liquid medium containing 100 µg/mL ampicillin at 37 °C until they reached an OD_{600} of 0.6-0.8 (BL21) or 0.3-0.5 (T7 express). MBP-PBP expression was induced with 0.2 mM IPTG and overnight incubation at 20 °C before the cells were harvested by centrifugation (3500 x g).

2.2.2 Purification of target proteins by metal affinity chromatography (Ni-NTA)

Cell pellets from 2 L of cultures were resuspended in 70 mL of buffer (50 mM Tris.HCl, pH 8, 300 mM NaCl, 10 mM imidazole) with 500 Kunitz units of DNase I and 1 mL Roche complete protease inhibitor cocktail at 25x working concentration. MBP-PBP peptide fusion lysis buffer also contained 1 mM DTT. The 70 mL of resuspended cells were lysed for 5 minutes on ice by sonication (Sonopuls HD2070- Bandelin) at 100 % power, 50 % cycle and clarified at 19000 x g for 20 minutes. The supernatant was filtered using a 0.45 µm filter and the cell lysate was loaded onto a 5 mL Ni-NTA column (Qiagen) at 1.5 mL/min that had been equilibrated in 50 mM Tris.HCl, pH 8, 300 mM NaCl, 10 mM imidazole. The column was subsequently washed at 5 mL/min with 80 mL of the same buffer and proteins were eluted with 50 mM Tris.HCl, pH 8, 300 mM NaCl, 250 mM imidazole. MBP-peptide fusions were eluted in 50 mM Tris.HCl, pH 7, 300 mM NaCl, 250 mM imidazole. Peptide fusions were labelled straight after elution and a drop to pH 7 increased the efficiency of labelling of the cysteine residue in the peptide with either fluorescein-maleimide (Vector laboratories) or TAMRA-maleimide (Santa Cruz Biotechnology). A representative Ni-NTA chromatogram is shown in Figure 2.3.

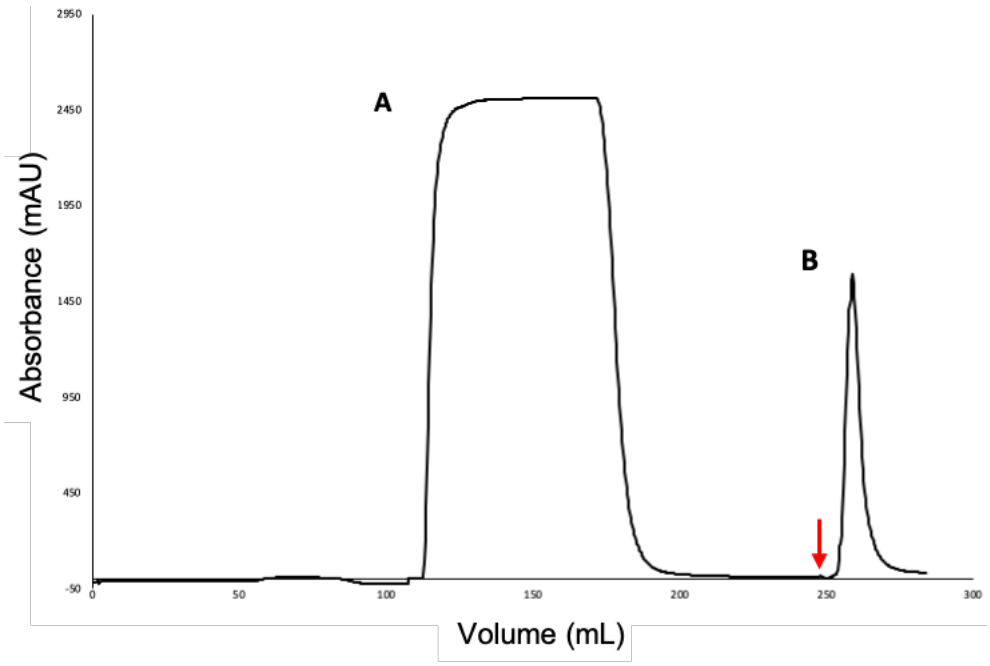

Figure 2.3: Representative chromatogram of His_6-ReoM purification from cell lysate using a Ni-NTA column.
Peak A is the flow-through of the cell lysate and peak B is the elution of His_6-ReoM with an increase on imidazole concentration to 250 mM at 250 mL indicated by the red arrow.

2.2.3 Removal of His_6-tag/His6-tagged MBP by TEV/ thrombin cleavage

The N-terminal His_6 tag was cleaved with thrombin (1 unit for 0.25 mg of protein) or TEV protease (1mg TEV for 20 mg of protein). TEV cleavage was carried out during dialysis against 1 L of 50 mM Tris.HCl pH 8, 300 mM NaCl and 1 mM DTT at 4 °C (ReoM at 20 °C). The His_6-tag was not cleaved from PrpC to allow separation after incubation with PrkA (section 2.5.3). MBP-peptide fusions were cleaved after labelling with fluorescein or TAMRA maleimide and is described in 2.2.6.

2.2.4 Separation of His_6-tag, uncleaved protein and histidine rich proteins from cleaved target by metal affinity chromatography (Ni-NTA)

Proteins cleaved by TEV protease were passed over a 5 mL Ni-NTA column (Qiagen) for a second time to remove the His_6-tagged TEV protease, histidine-rich contaminants and any uncleaved protein. Imidazole was added to the cleaved protein mix to 10 mM to prevent non-specific binding to the column before filtering with a 0.45 µm filter. The column was equilibrated with 50 mM Tris.HCl, pH 8, 300 mM NaCl and 10 mM imidazole and the protein was passed over the column at 5 mL/min and the flow though containing cleaved protein was collected. Contaminants and remaining His-tagged proteins were then eluted from the column

with 50 mM Tris.HCl, pH 8, 300 mM NaCl, 250 mM imidazole. A representative chromatogram is shown in Figure 2.4.

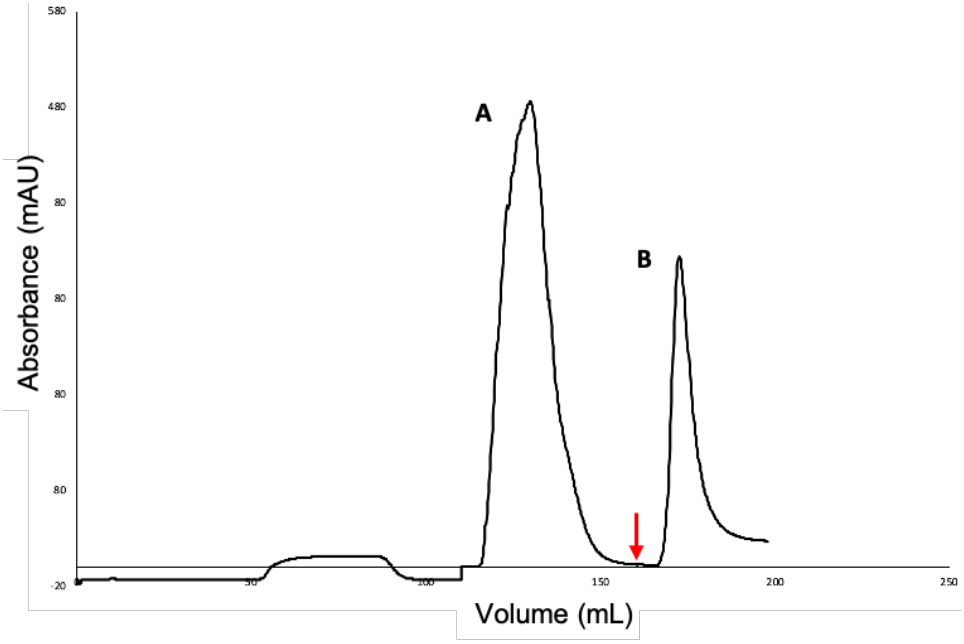

Figure 2.4: Representative chromatogram of TEV cleaved His_6-ReoM using a Ni-NTA column. Peak A is the flow-through of the TEV cleavage reaction which contains ReoM without a His_6 tag. Peak B is the elution of the TEV cleavage reaction with an increase on imidazole concentration to 250 mM at 155 mL (red arrow) which contains TEV protease, uncleaved His_6-ReoM and histidine rich contaminants.

2.2.5 Fluorescent labelling of PBP peptides

MBP-peptide fusions purified by metal affinity chromatography at 5 mg/mL were labelled with either TAMRA-maleimide (Santa Cruz Biotechnology) or fluorescein maleimide (Vector laboratories), by conjugation of the labelling agent to the cysteine residue introduced at the C-terminus of the peptide. The final concentration of the labelling agent was 625 µM and 1 mM, respectively and stocks were made by dissolving the power in 100% DMSO to a final concentration of 20 mM and 40 mM, respectively. Labelling was carried out at 4 °C overnight and the following day a PD 10 desalting column was used to remove excess labelling agent and to buffer exchange the MBP-peptide into 10 mM Tris.HCl pH8 and 250 mM NaCl. Complete buffer exchange was achieved by dialysis in 1 L of the same buffer at 4 °C for 4 hours.

2.2.6 Separation of MBP from PBP peptides

1 mg of TEV protease for 50 mg of protein was used to cleave the His_6-MBP protein from the PBP peptide at 4 °C overnight. The TEV protease, uncleaved MBP-peptide and His_6-MBP were separated from the peptide by concentrating through a 30 kDa molecular mass cutoff (MWCO) centrifugal ultrafiltration device, allowing only the peptide to pass through. Peptides were further concentrated in a 3 kDa (MWCO) centrifugal ultrafiltration device to 30-100 µM and stored at -20 °C.

2.2.7 Purification of proteins by size-exclusion chromatography (Superdex 75 and 200)

The proteins were concentrated in a 3-30 kDa (MWCO) concentrator depending on MW to 5 mL and loaded onto either a Superdex 75 XK16/60 or Superdex 200 XK16/60 column (GE Healthcare) equilibrated with 10 mM Tris.HCL, pH 8, 250 mM NaCl for proteins to be used in FP experiments, or 10 mM HEPES.HCl pH 8 and 100 mM NaCl for proteins used in ITC and crystallisation, with a flow rate of 1 mL/min. A representative chromatogram is shown in Figure 2.5. The fractions from gel filtration were analysed on SDS-PAGE, concentrated to 20-40 mg/mL and aliquots were snap frozen in liquid nitrogen and stored at -80 °C.

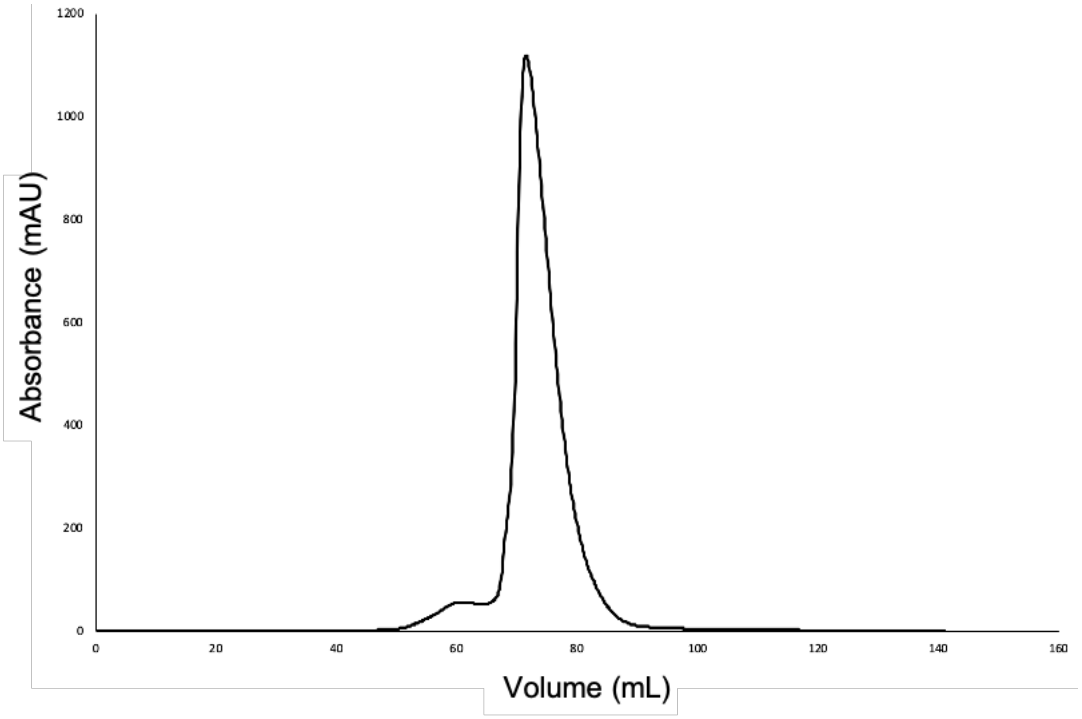

Figure 2.5: Representative chromatogram.
ReoM elution from a Superdex S75 HiLoad 16/60 size exclusion column.

2.2.8 Analytical size-exclusion chromatography

1 mM of ReoM and 250 µM of PrkA-KD diluted in 10 mM HEPES.HCl pH 8.0 and 100 mM NaCl to a total volume of 100 µL was initially incubated at 37 °C for 20 minutes (same conditions as phosphorylation reactions, section 2.5.1). The protein complex was then loaded into a Superdex 200 Increase 10/300 GL column at 0.75 mL/min equilibrated in 10 mM HEPES.HCl pH 8.0 and 100 mM NaCl. The individual proteins at the same concentrations were run in the same way as controls as well as ReoM and P-ReoM at 1 mM.

2.3 Biophysical and biochemical characterisation of proteins

2.3.1 Determination of protein/peptide concentration

Protein concentration was routinely determined using a NanoDrop lite spectrophotometer (Thermo Fisher) that measured the absorbance at 280 nm. The concentration in mg/mL and M was calculated from the absorbance value using the extinction coefficient and absorbance 0.1 % (=1 g/l) of the protein calculated from the protein sequence by ProtParam.

Fluorescent peptide concentrations were determined using a NanoDrop 1000 (Labtech) measuring at 555 nm for TAMRA and 495 nm for fluorescein and using the extinction coefficient (TAMRA maleimide = 65,000 $cm^{-1}M^{-1}$, fluorescein maleimide = 75,000 $cm^{-1}M^{-1}$) of the respective labelling agent to determine the molar concentration.

2.3.2 Circular Dichroism

CD was performed to monitor the secondary structure content of all purified proteins. CD scans were performed at a wavelength range of 190 nm - 260 nm at 20 °C, using a Jasco J-180 spectropolarimeter equipped with a Jasco 4235 Peltier cooler. The band width was 2 nm with a four second response time and 10 nm/min scan speed. CD measurements were performed with samples of proteins at 2.5-10 µM diluted in dH_2O using a 0.1cm path length quartz cuvette. Scans were repeated nine times. All CD data were buffer subtracted using buffer runs done prior to each protein run. The data from these runs were analysed using beStSel (Micsonai et al., 2018). CD thermal melt scans were also performed in a temperature range of 20 °C to 90 °C, at a fixed wavelength of 222 nm, 2 nm bandwidth, eight second response time with no time delay.

For CD spectra of peptides, full wavelength scans were done with a scan speed of 10 nm/min and a response time of 4 seconds was used. The final spectra were the average of at least four measurements. CD spectra were recorded at 40 µM in 20mM sodium phosphate buffer, pH 7.8.

2.3.3 Detection of protein:protein interactions and phosphorylation by native-PAGE electrophoresis

The effect of phosphorylation and dephosphorylation on ReoM and PrkA-KD proteins was analysed by 20% non-denaturing PAGE. Phosphorylation reactions consisted of 18.5 µM ReoM, 3.7 µM PrkA-KD, 5 mM ATP and 5 mM $MgCl_2$, diluted in 10 mM HEPES.HCl pH 8.0 and 100 mM NaCl. Dephosphorylation reactions consisted of 37 µM P-ReoM, 3.7 µM PrkA-KD, 18.5 µM PrpC and 1 mM $MnCl_2$, diluted in 10 mM HEPES.HCl pH 8.0 and 100 mM NaCl. In each case individual proteins were loaded at the same concentrations. The reactions were incubated at 37 °C for 20 minutes prior to electrophoresis at 200 V for 2.5 hours on ice.

2.3.4 Isothermal titration calorimetry

ITC was used to determine the thermodynamic parameters of the ReoM:PrkA interaction. These measurements were made using a Malvern MicroCal PeaQ-ITC microcalorimeter. All proteins were diluted to the desired concentrations with 10 mM HEPES.HCl pH 8.0 and 100 mM NaCl. Twenty 0.5 µL injections, all with a four second duration and a jacket temperature of 20 °C, were made in each ITC titration. The reference power was 6 µcal/s and the spin speed was 750 rpm. Control buffer runs were performed to determine any thermodynamic effect of diluting each protein. Data were analysed using the MicroCal PEAQ-ITC analysis software with the single set of identical sites model.

2.3.5 Fluorescence polarisation (FP) assays

FP experiments were done in a buffer of 10mM Tris.HCl pH 8.0, 250mM NaCl, 0.1% reduced Triton X-100. A PHERAstar FS (BMG Labtech) microplate reader was used to record fluorescence polarisation with 384-well plates. The excitation wavelength for fluorescein was 485 nm and for TAMRA 540 nm, with the fluorescence emission recorded above 520 nm for fluorescein and above 590 nm for TAMRA. The N-terminal domains of GpsB proteins were used in all experiments in preference to the full-length GpsB proteins due to the high solubility of the former, which facilitated achieving the high protein concentrations necessary to

saturate peptide binding. A target polarisation of 35 mP in wells with free labelled peptide was used to adjust the focus and gain. A 20 µL sample of GpsB (0-4 mM) with 40 nM labelled peptide corresponds to each data set. Kd values ± the standard error, generated after simultaneously fitting all the binding data to a 1:1 interaction model, were reported and there were three separate measurements at each data point in a titration.

2.3.6 MicroScale Thermophoresis

MicroScale Thermophoresis (MST) experiments were carried out using a Monolith NT.115 (NanoTemper). A medium MST-power of 40 % and an excitation power of 20 % were used with the excitation type as blue. MST experiments were done in a buffer of 10mM Tris.HCl pH 8.0, 250mM NaCl, 0.1% reduced Triton X-100. Each capillary contained 40 nM of fluorescein labelled *Lm*PBPA1$_{1\text{-}20}$ and were titrated in 12 steps against a 2-fold decrease of *Bs*GpsB$_{1\text{-}68}^{Lys32Glu}$ from 1500 µM to 0.366 µM. Three measurements were taken for each data point and the data were analysed using the MO.Affinity Analysis v2.2.4 software.

2.3.7 Size exclusion chromatography with multi-angle light scattering

Experiments were performed and processed by Dr Owen Davies at Newcastle University Biosciences Institute. Protein samples at 10 mg/mL were loaded onto a Superdex 200 increase 10/300 GL size exclusion chromatography column (GE Healthcare) in 20 mM Tris pH 8.0, 250 mM KCl, 2 mM DTT, at 0.5 mL/min. The column outlet was fed into a DAWN HELEOS II MALS detector (Wyatt Technology), followed by an Optilab T-rEX differential refractometer (Wyatt Technology). Light scattering and differential refractive index data were collected and analysed using ASTRA 6 software (Wyatt Technology). Molecular weights and estimated errors were calculated across eluted peaks by extrapolation from Zimm plots using a dn/dc value of 0.1850 mL/g.

2.3.8 Small-angle X-ray scattering

Data were collected and processed by Dr Owen Davies.

2.3.9 Mass spectrometry

Mass spectrometry experiments were carried out by Dr Claire Jennings. All liquid chromatography-mass spectrometry (LC-MS) analyses were performed using an Agilent 6530 Q-TOF instrument with electrospray ionisation (ESI) in positive ion mode, coupled to an

Agilent 1260 Infinity II LC system, utilising a mobile phase of 0.1% (v/v) formic acid in LC-MS grade water (A) and acetonitrile (B). Prior to peptide mapping, 10 µL of purified proteins (~1 mg/mL) were digested using Smart Digest Soluble Trypsin Kit (Thermo Fisher Scientific) according to the manufacturer's guidelines. Tryptic peptides and intact protein samples were extracted using HyperSep Spin Tip SPE C18 and C8 tips, respectively (ThermoFisher Scientific) before analysis. For phosphor-site analysis, 10 µL of digest was injected onto an Acclaim RSLC 120 C18 column (Thermo Fisher Scientific, 2.1 x 100mm, 2.2 µm, 120 Å) for reverse phase separation at 60 °C and 0.4 mL/min, over a linear gradient of 5-40% B over 25 min, 40-90% B over 8 min followed by equilibration at 5% B for 7 min. ESI source conditions were nebuliser pressure of 35 psig, drying gas flow of 13 L/min and gas temperature of 290 °C. Sheath gas temperature of 275 °C and gas flow of 12 L/min, capillary voltage of 4000V and nozzle voltage of 300V were also applied. Mass spectra were acquired using MassHunter Acquisition software (version B.08.00) over the 100-3000 m/z range, at a rate of 5 spectra/s and 200 ms/spectrum, using standard mass range mode (3200 m/z) with extended dynamic range (2 GHz) and collection of both centroid and profile data. MS/MS fragmentation spectra were acquired over the 100-3000 m/z range, at a rate of 3 spectra/s and 333.3 ms/spectrum. For intact protein analysis,10 µL of desalted protein (~1 mg/mL) was injected onto a Zorbax 300Å Stable Bond C8 column (Agilent Technologies, 4.6 x 50 mm, 3.5 µM) for reversed phase separation at 60 °C and 0.4 mL/min, over a linear gradient of 15-75% B over 14 min, 75-100% B over 11 min followed by post-run equilibration at 15% B for 10 min. ESI source conditions were nebuliser pressure of 45 psig, drying gas flow of 5 L/min and source gas temperature of 325 °C were applied. Sheath gas temperature of 400 °C and gas flow of 11 L/min, capillary voltage of 3500V and nozzle voltage of 2000V were also used. Mass spectra were acquired using MassHunter Acquisition software (version B.08.00) over a mass range of 100-3000 m/z, at a rate of 1 spectra/s and 1000 ms/spectrum in extended mass range (20000 m/z) at 1 GHz. Acquired MS and MS/MS spectra were analysed using Agilent MassHunter BioConfirm software (version B.10.00) for identification of phosphorylated residues and subsequent intact mass determination with processing of raw data using maximum entropy deconvolution.

2.4 X-ray crystallography and structure determination

2.4.1 Crystallisation trials

20 mg/mL of *Sp*GpsB$_{4-63}$ and 23 mg/mL of ReoM in 10 mM Na-HEPES pH 8, 100 mM NaCl were subjected to crystallisation by sparse matrix screening using commercial screens PACT, JCSG+, Morpheus, Index and Structure (Molecular Dimensions). For co-crystallisation of *Bs*GpsB$_{5-64}^{Lys32Glu}$:*Lm*PBPA1$_{1-15}$, *Sp*GpsB$_{4-63}$:*Sp*PBP2a$_{27-40}$ and *Sp*GpsB$_{4-63}$:*Sp*PBP2x$_{13-28}$ 20 mg/mL of the N-terminal domain of GpsB was mixed with PBP peptide at 25 mg/mL, corresponding to a 1:5 molar ratio of protein:peptide, in 10 mM Na-HEPES pH 8, 100 mM NaCl and crystallised in sparse matrix screens. 100 nL drops of apo GpsB or GpsB:PBP complex and 200 nL of screen solution were dispensed into 96 well MRC 2-well crystallisation plates (Molecular Dimensions) by a Mosquito (TTP Labtech) liquid handling robot and left to incubate for 1-2 weeks at 20 °C.

2.4.2 Screening of crystals for diffraction

Crystals of *Sp*GpsB$_{4-63}$ were transferred to a cryoprotectant consisting of the well solution supplemented with 20% v/v PEG 400. After 5 seconds the crystals were mounted onto rayon loops and cyro-cooled by plunging in liquid nitrogen. Crystals of *Sp*GpsB$_{4-63}$:*Sp*PBP2a$_{27-40}$ and *Sp*GpsB$_{4-63}$:*Sp*PBP2x$_{13-28}$ were transferred to a drop of the well solution containing 2.5 mg/mL of the respective peptide and after 30 seconds the crystals were mounted in rayon loops and frozen in liquid nitrogen. Crystals of *Bs*GpsB$_{5-64}^{Lys32Glu}$:*Lm*PBPA1$_{1-15}$ were transferred to a cryoprotectant comprising the well solution supplemented with 20% v/v PEG 300 and 2.5 mg/mL of the *Lm*PBPA1$_{1-15}$ peptide; after 30 seconds the crystals were mounted in rayon loops and frozen in liquid nitrogen. ReoM crystals were mounted onto rayon loops (Hampton Research) directly from the crystallization drops and cryo-cooled by plunging in liquid nitrogen.

Crystals were mounted onto an in-house Bruker gallium Metaljet and two images per crystal were collected at relative phi angles of 0° and 90°. Crystals were then ranked on diffraction pattern and resolution and full data sets were either collected in house or at the Diamond Light Source (Didcot, UK).

2.4.3 Data collection

*Sp*GpsB$_{4-63}$ crystals from JCSG + condition D6 (0.2 M magnesium chloride, 0.1 M Tris pH 8.5 and 20 % w/v PEG 8000) gave the best dataset. Diffraction data were collected in house using a Bruker gallium Metaljet, (wavelength 1.35 Å). The best diffracting crystals of *Bs*GpsB$_{5-64}^{Lys32Glu}$:*Lm*PBPA1$_{1-15}$ were obtained from JCSG+ condition E6 (0.2 M zinc acetate, 0.1 M imidazole pH 8, 20% PEG3K) (Page et al., 2003). Diffraction data were collected at the Diamond light source (DLS) synchrotron at the I04 beamline. Crystals of *Sp*GpsB$_{4-63}$:*Sp*PBP2a$_{27-40}$ from JCSG+ condition D7 (0.2 M lithium sulphate, 0.1 M Tris pH 8.5, 40 % w/v PEG 400) were obtained. Diffraction data were collected at the DLS synchrotron at the I03 beamline. Crystals of *Sp*GpsB$_{4-63}$:*Sp*PBP2x$_{13-28}$ were obtained from JCSG+ D7 and data were collected at I24 at the DLS. The ReoM crystals that were subsequently used for diffraction experiments were obtained in 0.1 M phosphate/citrate pH 4.2, 0.2 M lithium sulfate, 20 % w/v PEG 1000 from the JCSG+ screen. Diffraction data were collected on beamline I03 at the Diamond Light Source (DLS) synchrotron.

2.4.4 Data processing, model building and refinement

For *Sp*GpsB$_{4-63}$ diffraction images were indexed, integrated, scaled and merged with PROTEUM3 (Bruker). PHASER (McCoy et al., 2007) was used to generate the initial model using chain A of PDB entry 4UG1 to solve the structure by molecular replacement. BUCCANEER (Cowtan, 2012) was used to build the *Sp*GpsB sequence into the model which was built in COOT (Emsley et al., 2010) and refined in REFMAC (Murshudov et al., 1997) and PHENIX.REFINE (Afonine et al., 2010).

Diffraction images of *Bs*GpsB$_{5-64}^{Lys32Glu}$:*Lm*PBPA1$_{1-15}$ crystals were integrated in XDS (Kabsch, 2010) and scaled and merged with AIMLESS (Evans & Murshudov, 2013). The initial model was generated by molecular replacement in PHASER (McCoy et al., 2007) using residues 5-64 of *Bs*GpsB from the *Bs*PBP1$_{1-17}$:*Bs*GpsB$_{5-64}$ structure as the search model. The model was built in COOT (Emsley et al., 2010) and refined with PHENIX.REFINE (Afonine et al., 2010).

For *Sp*GpsB$_{4-63}$:*Sp*PBP2a$_{27-40}$ images were indexed and integrated with XDS, scaled in XSCALE (Diederichs et al., 2003) and merged with AIMLESS (Evans & Murshudov, 2013). The initial model was produced in PHASER (McCoy et al., 2007) by molecular replacement using the apo

*Sp*GpsB$_{4-63}$ structure as a model. The final model was built in COOT (Emsley et al., 2010) and refined with REFMAC (Murshudov et al., 1997) and PHENIX.REFINE (Afonine et al., 2010).

With *Sp*GpsB$_{4-63}$:*Sp*PBP2x$_{13-28}$, diffraction images were indexed and integrated in MOSFLM (Battye et al., 2011) and scaled and merged in AIMLESS (Evans & Murshudov, 2013). PHASER was used to solve the phases by molecular replacement with the apo *Sp*GpsB$_{4-63}$ structure. The final model was built in COOT (Emsley et al., 2010) and refined with REFMAC (Murshudov et al., 1997).

Images of ReoM were integrated in MOSFLM (Battye et al., 2011) and scaled and merged with AIMLESS (Evans & Murshudov, 2013). The initial model was generated by molecular replacement in PHASER (McCoy et al., 2007) using the dimeric, 20-conformer ensemble model (PDB ID 5US5) of IreB solved by nuclear magnetic resonance (Hall et al., 2017) as a search model. The final model was produced by iterative cycles of model building COOT (Emsley et al., 2010) with refinement in REFMAC (Murshudov et al., 1997) until convergence.

2.4.5 Model validation

MolProbity (Chen et al., 2010) was used to validate all the structures. The statistics for data collection and refinement are listed in Table 3.1, Table 3.2 , Table 5.1, Table 5.2 and Table 6.1.

2.5 Protein phosphorylation and dephosphorylation

2.5.1 Phosphorylation assays

Upscaled phosphorylation reactions consisted of 37 µM ReoM, 3.7 µM PrkA-KD, 5 mM ATP and 5 mM $MgCl_2$, diluted in 10 mM HEPES.HCl pH 8.0 and 100 mM NaCl, to a total volume of 5 mL. Reactions were carried out at 37 °C for 20 minutes.

2.5.2 Isolation of phosphorylated ReoM

The protein mix was loaded onto a PD-10 desalting column to remove excess ATP and protein fractions were loaded onto a MonoQ 5/50 GL anion exchange column (GE Healthcare). Buffer A consisted of 10 mM HEPES.HCl pH 8.0 and 100 mM NaCl and buffer B was 10 mM HEPES.HCl pH 8.0 and 1M NaCl. Bound proteins were eluted over 25 mL with a 15-35% gradient of buffer B.

2.5.3 Isolation of dephosphorylated PrkA

Upscaled dephosphorylation reaction consisted of 12 µM PrkA, 60 µM PrpC and 2 mM $MnCl_2$ in 10 mM HEPES.HCl pH 8 and 100 nM NaCl. The reaction was incubated at 37 °C for 1 hour and the solution was passed over a 5 mL Ni-NTA column equilibrated with 50 mM HEPES.HCl pH8, 300 mM NaCl and 10 mM imidazole. Dephosphorylated PrkA was collected in the flow through and column-bound His_6-tagged PrpC was eluted with 50 mM HEPES.HCl pH8, 300 mM NaCl and 250 mM imidazole. The proteins were dialysed back into 10 mM HEPES.HCl pH 8 and 100 nM NaCl.

2.6 Fragment Screening-XChem

2.6.1 Production of reproducible crystals

Crystallisation conditions for N-*Sp*GpsB had already been established prior to the allocation of XChem beamline as stated in 2.4. To ensure a ready supply of crystals, a microseed stock was prepared by crushing ~20 crystals, each no bigger than 200 µm, in 50 µL of 0.1 M Tris.HCl pH 8.5, 0.2 M $MgCl_2$, 24 % PEG 8000. 600 nL sitting drop crystallisation experiments of N-*Sp*GpsB were set up in SwissCi 3-drop plates (Molecular Dimensions), using a Mosquito (TTP Lab Tec) pipetting workstation, by mixing 300 nL of N-*Sp*GpsB at 20 mg/mL (in a buffer of 10 mM HEPES.HCl pH 8 and 100 mM NaCl), with 100 nL seed stock and 200 nL of reservoir solution, (0.1 M Tris.HCl pH 8.5, 0.2 M $MgCl_2$, 16 % PEG 8000).

2.6.2 Experimental procedure

Images of the crystal drops were recorded and TeXRank (Tsing Ng et al., 2014) was used to select the drops containing crystals to be soaked. 40 of these crystals were used for DMSO- and cryo-testing. DMSO was tested from 0 to 30 % and soaking was done for 1-3 hours with and without a cryoprotectant of 20 % PEG 200 added before harvesting. It was determined from the diffraction patterns that the N-*Sp*GpsB crystals could withstand 20 % DMSO for 3 hours and that no cryoprotectant was required. Subsequently, 547 crystals were soaked with fragments from the DSi-Poised Library (Enamine) using the XChem ECHO acoustic liquid handler (Labcyte). A crystallisation plate containing 100-150 chosen drops was soaked for an hour and then the crystals were harvested manually with the aid of a Shifter, a microscope x-y stage that also handles unsealing and resealing as well as automatically tracking samples

(Oxford Lab Technologies). It took approximately 1-1.5 hours to harvest the crystals from a single tray. The same process was repeated 4 times to harvest all of the chosen crystals.

2.6.3 Data collection

Diffraction data were collected on i04-1 (DLS) in an automated, unattended mode using loop centring as the crystals were larger than the loops (> 200 µm). All crystals diffracted to between 1.2 and 1.8 Å.

2.6.4 Data processing and structure solution

From the 547 crystals that were soaked, a total of 536 useful diffraction datasets were collected and used for subsequent structural analysis. For the remaining 11 samples, data collection failed due to empty or broken loops. Data were processed using the auto-processing pipeline (https://www.diamond.ac.uk/industry/Industry-News/Latest-News/Synchrotron-Industry-News---MXnews4/Auto-processing-Pipeline.html) at the Diamond Lightsource Synchrotron. Each data set was solved using Dimple (http://ccp4.github.io/dimple/) with the structure of N-*Sp*GpsB as a molecular replacement model.

2.6.5 Model building

PANDDA.analyse (Pearce et al., 2017a) was used to find residual difference density and PANDDA.inspect (Pearce et al., 2017b) was used to view these sites and model the ligands. REFMAC (Murshudov et al., 1997) was used to refine the final structures.

2.6.6 Competition assay (FP)

The compounds of 12 individual 'hits' were synthesised by Enamine and the ability of the ligands to bind to N-*Sp*GpsB was tested using ITC. The same equipment and experimental parameters were used as explained in 2.3.5 but with 30 µM of N-*Sp*GpsB in the cell and a syringe with 20 mM of each compound.

The ability of the compounds to compete with the binding of *Sp*PBP2a was tested using FP. The same equipment was used as explained in 2.3.6. In each well there was 40 nM of TAMRA-conjugated *Sp*PBP2a$_{23\text{-}45}$ and 100 µM of N-*Sp*GpsB with increasing concentrations of the individual compound from 15-2000 µM with triplicates of each data point being recorded. A target polarisation of 35 mP in wells with free labelled peptide was used to adjust the focus

and gain and the polarisation of each well was recorded. The FP was plotted against compound concentration. The ability of unlabelled *Sp*PBP2a$_{27-40}$ to complete with the bound labelled peptide was also tested with the same parameters.

Chapter 3: The Cell-Cycle Regulator GpsB Functions as a Cytosolic Adaptor for Multiple Cell Wall Enzymes

3.1 Introduction

It has become evident that GpsB is a major regulator of peptidoglycan synthesis, ensuring the correct subcellular localisation of penicillin binding proteins (PBPs) by binding to their cytoplasmic mini-domains (Cleverley et al., 2016). GpsB and the major bi-functional PBPs in *B. subtilis* and *L. monocytogenes,* PBP1 and PBPA1, respectively, have been shown to interact by bacterial two-hybrid screens (Claessen et al., 2008). More specifically, SPR and fluorescence polarisation have demonstrated that the N-terminal domain of *B. subtilis* GpsB interacts with the N-terminal cytoplasmic mini-domain of PBP1 (Cleverley et al., 2016, 2019). Co-IP experiments have illustrated that *S. pneumoniae* GpsB interacts with bPBP2b and aPBP2a and not with bPBP2x or aPBP1a (Rued et al., 2017) (b= class B PBP, a= class A PBP).

Crystal structures of the N- and C-terminal domains of GpsB have been determined to gain an understanding of how GpsB interacts with PBPs at the molecular level (Rismondo et al., 2016). How these subunits are arranged into a hexamer has been shown by the use of small-angle X-ray scattering (SAXS) (Cleverley et al., 2016). The structure of *Bs*GpsB$_{5-64}$ bound to *Bs*PBP1$_{1-17}$ confirmed the role of a negatively charged groove between helix 1 and 2 for binding, specifically the highly conserved aspartate pair Asp31 and Asp35 (Cleverley et al., 2019). The structure also revealed that *Bs*PBP1 binding was centred on two of its arginine residues, Arg8 and Arg11, which are part of a conserved SRxxR(R/K) motif across *Bacilaceae* PBP1 (Cleverley et al., 2019).

This chapter will focus on determining the molecular interactions of GpsB with PBPs from two human pathogens, *L. monocytogenes* and *S. pneumoniae.* Since GpsB is important for virulence in *L. monocytogenes* (Rismondo et al., 2016) and essential in *S. pneumoniae* (Land et al., 2013), determining how GpsB interacts with PBPs is important as GpsB could be a potential target for new antibiotics in the treatment of disease.

3.2 Binding of the *L. monocytogenes* PBPA1 cytoplasmic domain to the N-terminal domain of *Lm*GpsB

3.2.1 Generation of a cytoplasmic domain peptide of *Lm*PBPA1

In order to establish whether GpsB from *L. monocytogenes* interacts with the class A PG synthase PBPA1, like its homologue in *B. subtilis*, a cytoplasmic domain peptide of PBPA1 was generated. The first 29 amino acids of PBPA1 form the cytoplasmic mini-domain, and in this

region, there are numerous positively-charged residues. The first 20 residues were chosen in the creation of the peptide as this encompassed the conserved sequence TRxxYR that is the closest equivalent to the SRxxR(R/K) motif of *Bacillaceae* PBP1 (Figure 3.1). A sequence alignment of the first 17 residues of *Lm*PBPA1 and *Bs*PBP1 is shown in Figure 3.2.

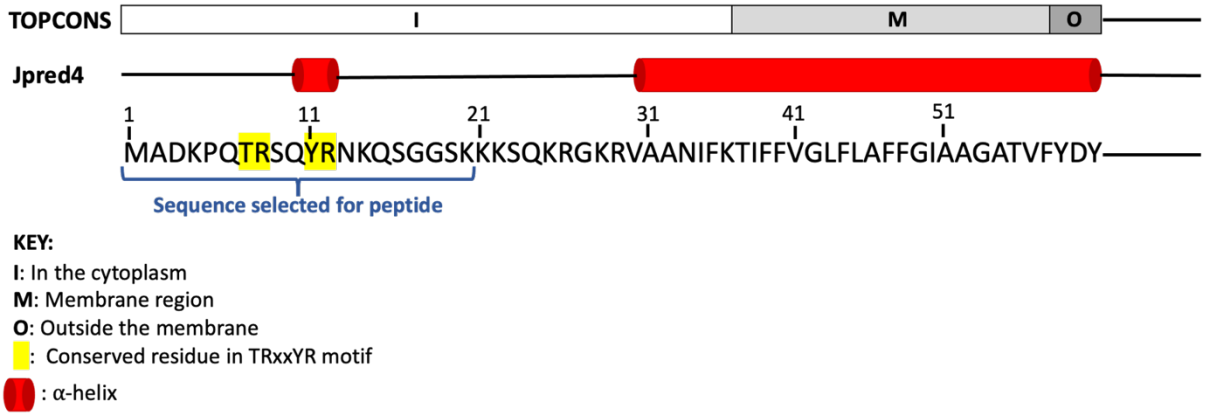

Figure 3.1: Analysis of the N-terminal domain of *L. monocytogenes* PBPA1.
Protein topology prediction (TOPCONS) (Tsirigos et al., 2015) and secondary structure prediction (Jpred4) (Drozdetskiy et al., 2015) analysis of the first 60 residues of *Lm*PBPA1. The key explains the figure's main features. The sequence of the cytoplasmic mini-domain selected for peptide generation is shown by the blue brace.

```
LmPBPA1     MADKPQTRSQYRNKQSG   17
BsPBP1      MSDQFNSREARRKANSK   17
            *:*: ::*.  *: :*
```

Figure 3.2: A sequence alignment of the first 17 residues of *Lm*PBPA1 and *Bs*PBP1.
Fully conserved residues are indicated by an asterisk, sites with strong similarity are indicated by a colon and sites with weak similarity are indicated by a period.

The sequence encoding these first 20 residues was cloned into a pMAT11 vector for TEV-cleavable conjugation to MBP to enhance the expression of the peptide in *E. coli*. To create a fluorescent peptide, serine 19 was mutated to a cysteine to enable labelling with fluorescein maleimide and lysine 21 was mutated to a stop codon (Figure 3.3).

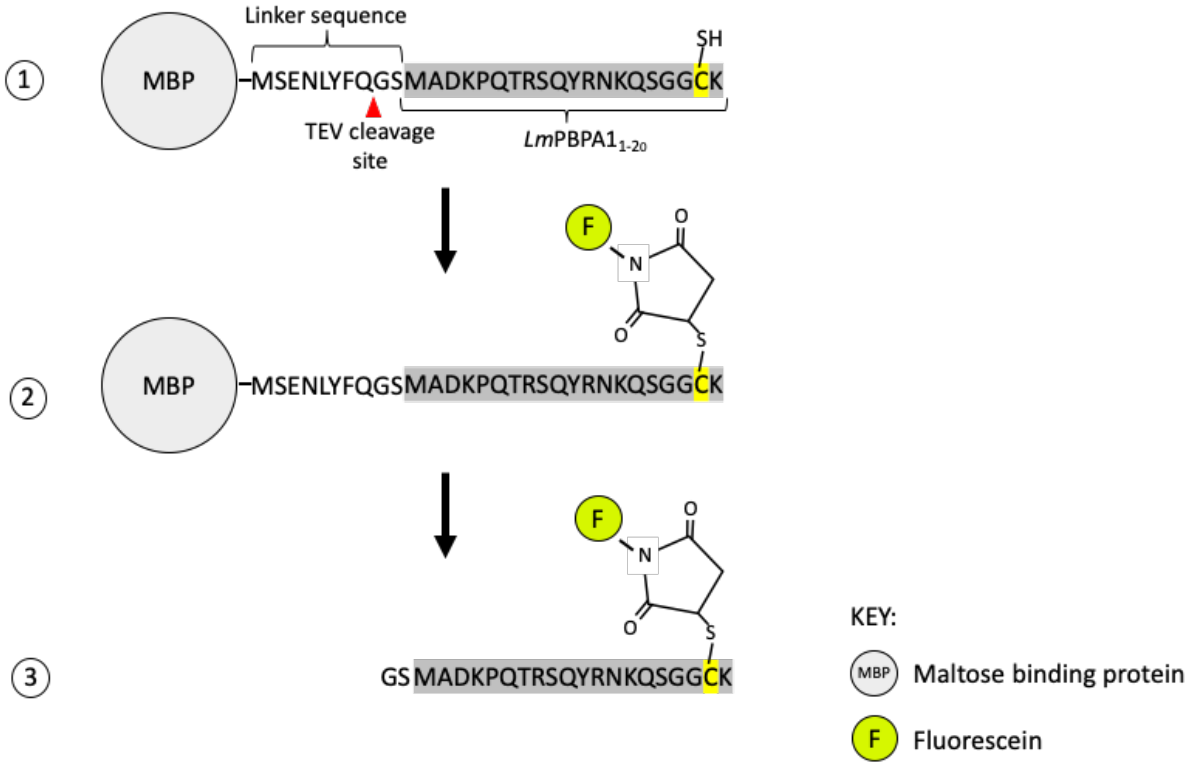

Figure 3.3: Generation of a fluorescently-labelled cytoplasmic domain peptide of *Lm*PBPA1. Steps taken in the generation of a fluorescein maleimide-conjugated *Lm*PBPA1$_{1-20}$ peptide. Step 1 shows the purified expression product from the pMAT11 vector. The first 20 residues of *Lm*PBPA1, highlighted in grey, are linked to maltose binding protein (MBP) by a linker sequence containing a TEV cleavage site. The mutated serine 19 to cysteine residue in *Lm*PBPA1 is highlighted in yellow with the thiol group annotated. Step 2 is the result of the incubation of the expression product with fluorescein maleimide which is linked to the protein by a reaction with the thiol group of the cysteine residue. Step 3 is TEV cleavage, in which the result is a fluorescently-labelled *Lm*PBPA1 cytoplasmic domain peptide. The two residues not highlighted in grey are two remaining residues from the linker sequence after TEV cleavage.

3.2.2 Quantifying the interaction by fluorescence polarisation

A Kd of 200 ± 20 µM was determined for the affinity of *Lm*GpsB$_{1-73}$ for *Lm*PBPA1$_{1-20}$ by fluorescence polarisation (FP) (Figure 3.4). This binding affinity is comparable to that previously observed for the binding of *Bs*PBP1$_{1-32}$ to *Bs*GpsB$_{1-68}$, measure by FP (Cleverley et al., 2019).

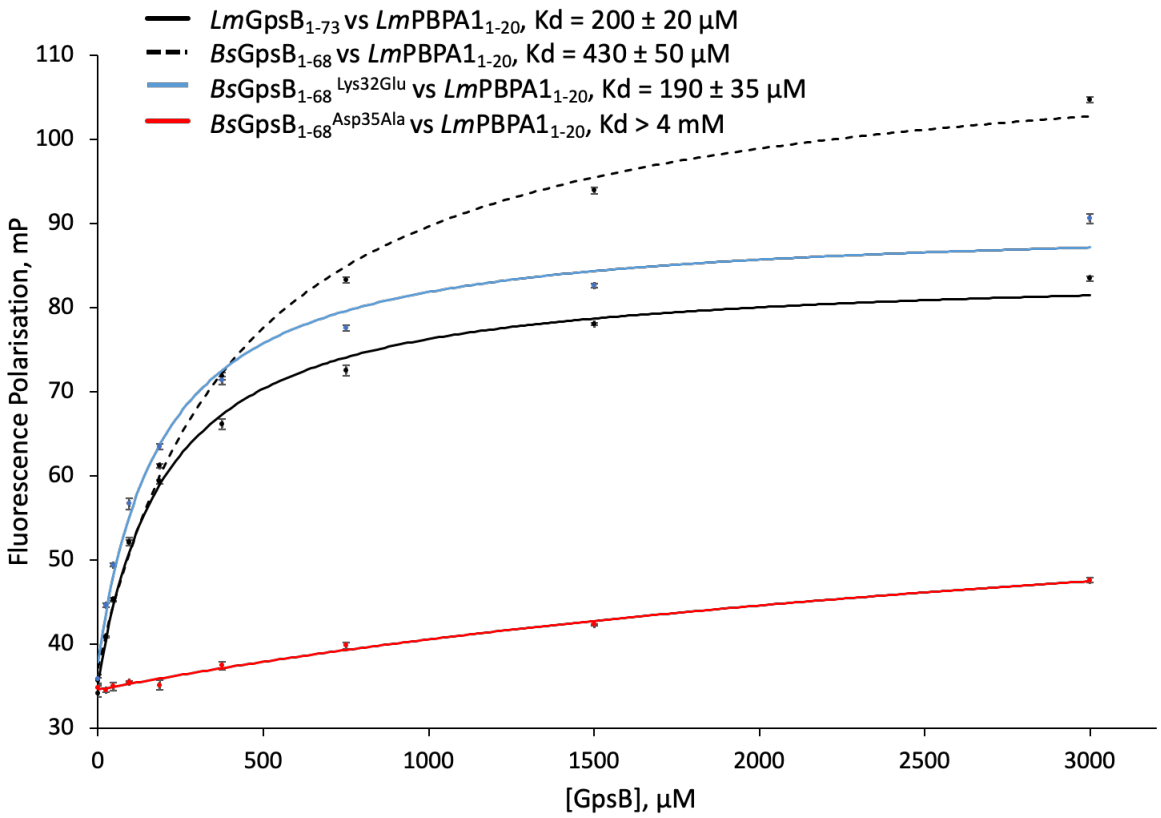

Figure 3.4: Interaction of the cytoplasmic domain peptide of *Lm*PBPA1 with the N-terminal domain of GpsB.
Interaction of fluorescein-labelled *Lm*PBPA1$_{1\text{-}20}$ peptides with wild-type N-terminal domains of GpsB from *L. monocytogenes* (*Lm*GpsB$_{1\text{-}73}$), *B. subtilis* (*Bs*GpsB$_{1\text{-}68}$), a variant of *B. subtilis* GpsB mutated to mimic *L. monocytogenes* GpsB (*Bs*GpsB$_{1\text{-}68}^{Lys32Glu}$) and *Bs*GpsB$_{1\text{-}68}^{Asp35Ala}$, as monitored by fluorescence polarisation. Binding data and the fit of the data to a 1:1 binding model in Sigma plot for each of the data sets are plotted in the graph. The average of three measurements and the standard error for each data point is shown. The key shows which data set is represented by colouring and the respective Kd that was determined in Sigma plot.

Co-crystallisation attempts of *Lm*GpsB constructs in complex with *Lm*PBPA1$_{1\text{-}15}$ failed; there was very little precipitation observed in a number of crystal screens and no crystals were obtained. The N-terminal domain of *B. subtilis* GpsB appeared to be more 'crystallisable' than *Lm*GpsB. In the structure of *Bs*GpsB$_{5\text{-}64}$ bound to *Bs*PBP1$_{1\text{-}17}$, the only residue that differs between *Lm*GpsB and *Bs*GpsB within 8 Å of the binding interface is *Bs*GpsB Lys32, which is a glutamate in *Lm*GpsB; otherwise all of the residues that contact the peptide are conserved, as well as residues that indirectly help shape the binding site. Fluorescence polarisation data showed that *Lm*PBPA1$_{1\text{-}20}$ bound to *Bs*GpsB$_{1\text{-}68}^{Lys32Glu}$ with a Kd of 190 ± 35 µM and to *Bs*GpsB$_{1\text{-}68}$ with a K_d of 430 ± 50 µM (Figure 3.4). This demonstrates that *Lm*PBPA1$_{1\text{-}20}$ binding is 2-fold stronger when the binding site of *Bs*GpsB is '*Lm*GpsB like'. In a control experiment carried out to test the binding of *Lm*PBPA1$_{1\text{-}20}$ to *Bs*GpsB$_{1\text{-}68}^{Asp35Ala}$, the Kd was shown to be greater than

4 mM. Asp35 is an important residue for *Bs*GpsB to bind to *Bs*PBP1 and mutating it to alanine abolished binding (Rismondo et al., 2016; Cleverley et al., 2019). Therefore *Lm*PBPA1$_{1-20}$ binds to *Bs*GpsB$_{1-68}^{Lys32Glu}$ as though the proteins are derived from the same biological source, and that binding is strong enough to attempt co-crystallisation.

3.3 Co-crystallisation of the N-terminal domain of *Bs*GpsB with *Lm*PBPA1 cytoplasmic peptide

3.3.1 Crystallisation trials of *Bs*GpsB^{Lys32Glu}:*Lm*PBPA1$_{1-15}$

Crystals of *Bs*GpsB$_{5-64}^{Lys32Glu}$:*Lm*PBPA1$_{1-15}$ grew in two conditions from the JCSG+ sparse matrix screen, E6 (0.2 M Zinc acetate dihydrate, 0.1 M imidazole pH 8, and 20 % w/v PEG 3000) and C7 (0.2 M Zinc acetate dihydrate, 0.1 M sodium acetate pH 4.5 and 10 % w/v PEG 3000) (Figure 3.5). The crystals were rod shaped and often grew in clusters with just the odd single crystal. Crystals from each condition were harvested in rayon loops and transferred to a drop of well solution supplemented with 20 % v/v PEG 400 as a cryoprotectant. The crystals were then transferred back into the rayon loops and cryo-cooled in liquid nitrogen. Diffraction data were collected at Diamond Light Source on beamline I04.

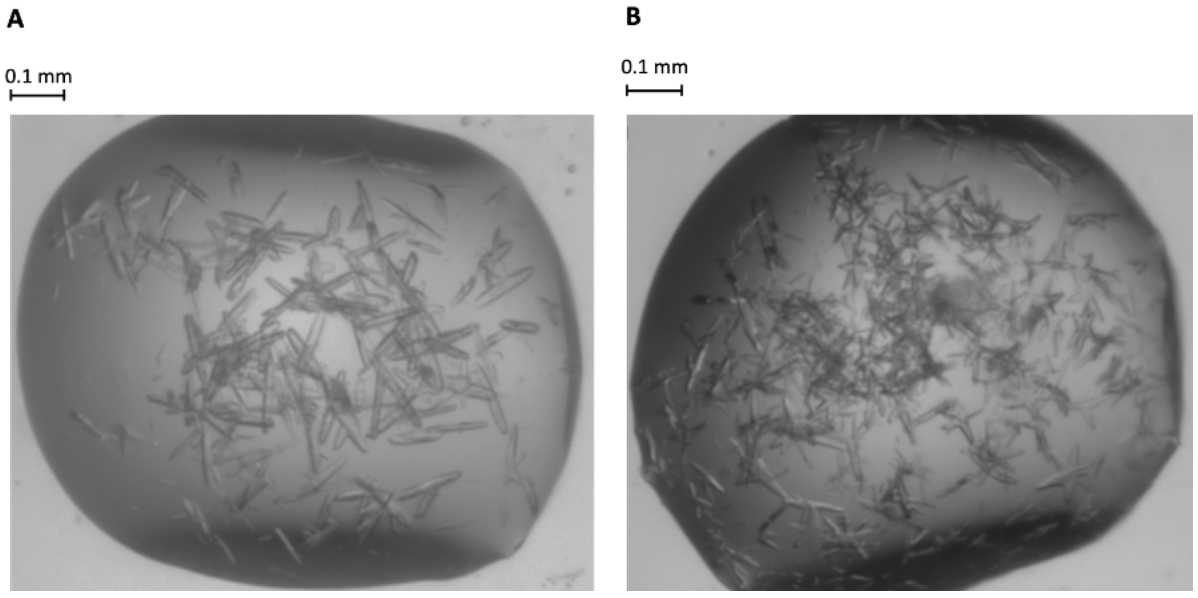

Figure 3.5: Crystals of *Bs*GpsB$_{5-64}^{Lys32Glu}$:*Lm*PBPA1$_{1-15}$.
Panel **A** is a drop from JCSG+ E6 and panel **B** is a drop from JCSG+ C7. The scale bars above each image provide a visual indication of the size of each crystal.

3.3.2 Data processing, molecular replacement and model building

Diffraction data collected from crystals obtained from JCSG+ E6 were processed as described in 2.4.4. The structure of *Bs*GpsB$_{5\text{-}64}^{Lys32Glu}$:*Lm*PBPA1$_{1\text{-}15}$ was solved using data to 1.6 Å by molecular replacement (PHASER) (McCoy et al., 2007) with GpsB residues 5-64 of the *Bs*GpsB$_{5\text{-}64}$:*Bs*PBP1$_{1\text{-}17}$ structure as the search model. The final atomic model was built in COOT (Emsley et al., 2010) and refined in REFMAC (Murshudov et al., 1997). The full list of data collection and refinement statistics can be found in Table 3.1.

3.3.3 Analysis of the *Bs*GpsB^{Lys32Glu}:*Lm*PBPA1$_{1\text{-}15}$ structure

The crystal structure showed that the N-terminal domain of *Bs*GpsB was almost identical to previously-determined structures; the main difference is restricted to the presence of glutamate at position 32 instead of lysine (Figure 3.6 A). Only one of the monomers in the dimer is bound to peptide, as observed in the structure of *Bs*GpsB$_{5\text{-}64}$:*Bs*PBP1$_{1\text{-}17}$, because the second peptide binding site is blocked by residues from a neighbouring GpsB molecule in the crystal lattice. *Lm*PBPA1$_{1\text{-}15}$ appeared to bind in the same binding site as *Bs*PBP1$_{1\text{-}17}$. However, most of the *Lm*PBPA1$_{1\text{-}15}$ peptide is disordered: arginine 8 is the only residue of the peptide that is sufficiently ordered to be built and refined satisfactorily in the electron density (Figure 3.6 B and C). Consequently, most of the specific contacts of the peptide to GpsB could not be determined, and the only interactions that could be described were from Arg8. The side chain of Arg8 penetrates into the groove of *Bs*GpsB as has been seen by Cleverley *et al*. with the corresponding Arg8 in *Bs*PBP1$_{1\text{-}17}$ forming the same set of interactions (Cleverley et al., 2019) (Figure 3.6 D). Since Arg8 is the only visible residue in the complex, the secondary structure of the peptide cannot be built either, but it is notable that the backbone torsion angles of Arg8 are consistent with a residue in an alpha-helix.

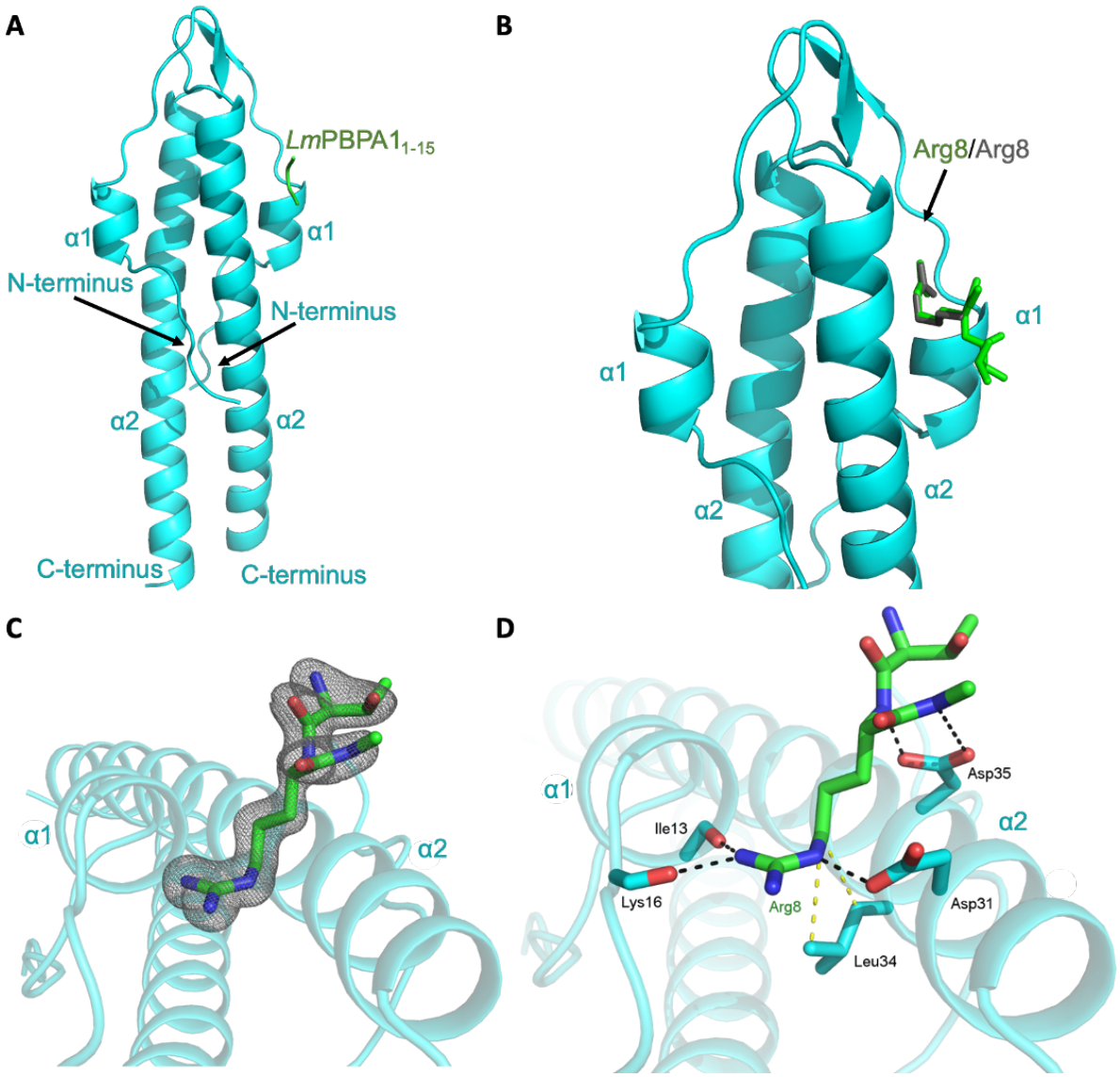

Figure 3.6: Structure of the N-terminal domain of *Bs*GpsB^{Lys32Glu} bound to *Lm*PBPA1$_{1-15}$.
The two subunits of the GpsB N-terminal dimer are coloured cyan in cartoon form and the peptide is coloured green. Arg8 is completely visible and Thr7 and Ser9 are only partially visible in the structure of the peptide which is bound in a groove between helix 1 (α1) and helix 2 (α2) of one subunit (chain B). (**A**) The structure in cartoon form highlighting the N and C-terminus and α1 and α2 of each subunit of the GpsB dimer. (**B**) Zoomed-in view of the binding site with the peptide in stick form. The side chain of Arg8 penetrates into the groove between the two helices. The position of Arg8 of *Bs*PBP1 from the superimposition of *Bs*GpsB$^{Lys32Glu}{}_{5-64}$:*Lm*PBPA1$_{1-15}$ with *Bs*GpsB$_{5-64}$:*Bs*PBP1$_{1-17}$ is shown in grey sticks. (**C**) Zoomed-in view of the binding site looking down at helix 1 and 2 from chain B. *Lm*PBPA1 shown in stick form and the electron density map is represented by a grey mesh. The map shown is the final Refmac-weighted 2mF$_{obs}$-DF$_{calc}$ map contoured at 0.14 electrons per Å^3 with a PyMol "carve" value of 1.6. (**D**) Residues important in binding are shown in stick form coloured by atom. Salt bridges and hydrogen bonds are represented by dashed black lines and van der Waals' contacts by dashed yellow lines.

3.4 Important features of *Lm*PBPA1 cytoplasmic domain peptide for *Bs*GpsB N-terminal binding

The small part of the *Lm*PBPA1$_{1\text{-}15}$ peptide that was visible in the crystal structure meant that essential residues, contacts from these residues and the importance of secondary structure for binding to GpsB could not be determined. To gain an understanding of the features of the *Lm*PBPA1 cytoplasmic peptide that are vital for binding, a number of mutants of *Lm*PBPA1$_{1\text{-}20}$ were produced and the binding to *Bs*GpsB$_{1\text{-}68}^{Lys32Glu}$ was analysed by fluorescence polarisation (Figure 3.7).

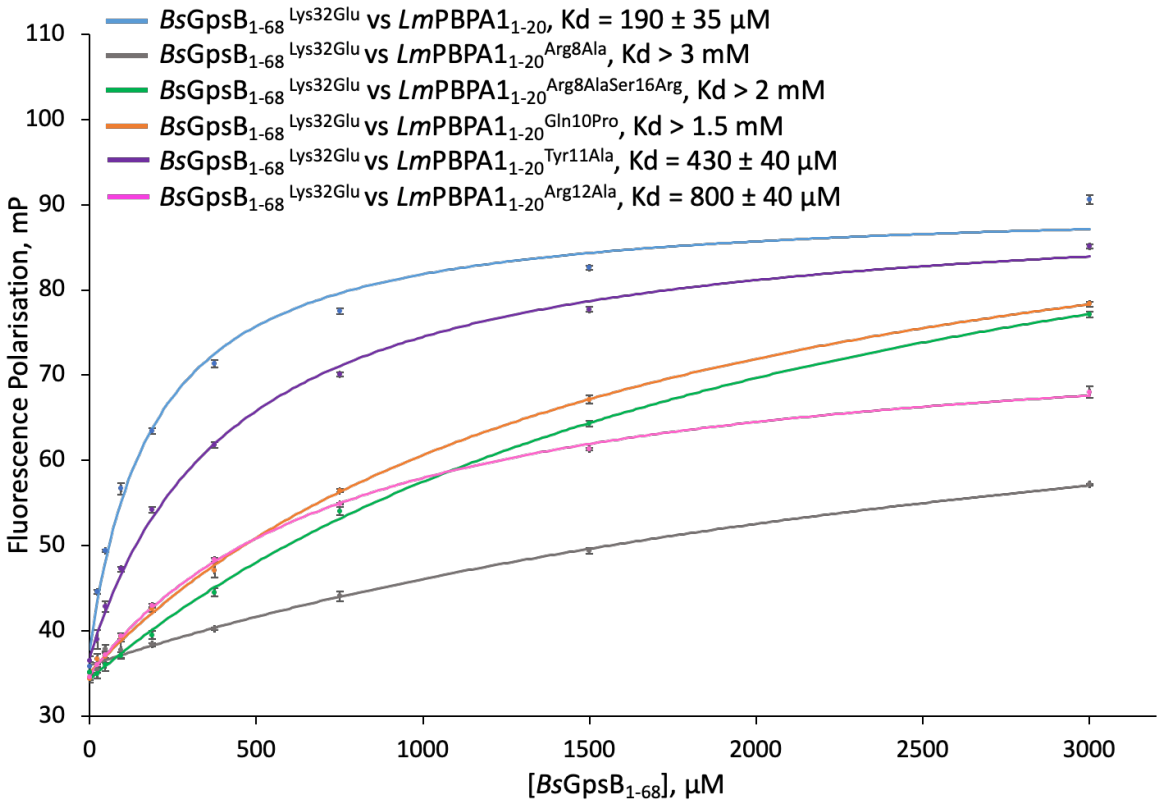

Figure 3.7: Interaction of *Lm*PBPA1$_{1\text{-}20}$ mutants with *Bs*GpsB^{Lys32Glu}.
The binding of wild type *Lm*PBPA1$_{1\text{-}20}$ and mutant peptides to *Bs*GpsB$_{1\text{-}68}^{Lys32Glu}$, as monitored by fluorescence polarisation. Raw data and the fit of the data to a 1:1 binding model in Sigma plot for each of the data sets are plotted. The average of three measurements and the standard error bars for each data point is shown. The key shows which data set is represented by colouring and the respective Kd that was determined in Sigma plot.

First, a mutant was produced in which Arg8 was mutated to alanine to verify the importance of this arginine for binding (*Lm*PBPA1$_{1\text{-}20}^{Arg8Ala}$). At 3 mM, the Kd was 15-fold higher than that of the wild-type (WT), with a Kd of 190 ± 35 µM, therefore Arg8 was crucial for binding. To check that this was a specific interaction and that *Bs*GpsB does not simply have a tendency to

bind to arginine *per se*, another arginine residue was introduced into the *Lm*PBPA1$_{1\text{-}20}^{Arg8Ala}$ peptide at position 16 (Ser16Arg). This position is outside the proposed binding motif and is in a region of lower alpha helix-forming propensity, as determined by secondary structure predictions (Figure 3.1). The binding of *Lm*PBPA1$_{1\text{-}20}^{Arg8AlaSer16Arg}$ to *Bs*GpsB was determined to have a Kd of 2 mM, which indicates that the interaction between Arg8 of *Lm*PBPA1 with *Bs*GpsB was indeed specific, and that the critical arginine of PBPA1 needs to be in an alpha helical conformation to interact with GpsB. A third mutant was made that had a proline residue introduced to the alpha helical region of the binding motif (*Lm*PBPA1$_{1\text{-}20}^{Gln10Pro}$). Proline has the lowest alpha helical propensity of all amino acids and it is the least likely amino acid to be present in an alpha helix (Pace & Scholtz, 1998). *Lm*PBPA1$_{1\text{-}20}^{Gln10Pro}$ had a Kd of 1.5 mM, which compared to WT peptide is a 10-fold weaker binding. This result suggested that the introduction of proline disrupted the formation of the alpha helix and although Arg8 was present in the peptide, there was a significant reduction in affinity for *Bs*GpsB as it was not in the correct alpha helical form.

The structure of the *Bs*GpsB$_{5\text{-}64}$:*Bs*PBP1$_{1\text{-}17}$ complex showed that two arginine residues in the PBP (Arg8 and Arg11) were involved in key salt bridges and hydrogen bonds to GpsB (Figure 1.15 F). In *Lm*PBPA1 the equivalent residue at position 11 is a tyrosine with an arginine at position 12. Tyr11Ala and Arg12Ala mutants (*Lm*PBPA1$_{1\text{-}20}^{Tyr11Ala}$ and *Lm*PBPA1$_{1\text{-}20}^{Arg12Ala}$) reduced the binding affinity by 2- and 4-fold, respectively, indicating that Arg12 contributed to the binding capability of *Lm*PBPA1 but the interaction is highly dependent on Arg8 (Figure 3.7).

A second technique, microscale thermophoresis (MST) was used to confirm the interaction between *Bs*GpsB$_{1\text{-}68}^{Lys32Glu}$ and *Lm*PBPA1$_{1\text{-}20}$ and to compare the binding affinities of two techniques. A Kd of 70 ± 2.5 µM was determined by MST, which is in the same range as the affinity determined by FP (200 ± 20 µM). The experiment was repeated with the *Lm*PBPA1$_{1\text{-}20}^{Arg8Ala}$ mutant, with which no observable Kd was detected (Figure 3.8). However, it was concluded that MST was not the best method for determining the µM interaction between GpsB and PBP peptides as the high concentration of protein required to saturate the interaction caused the solution in the capillary to become viscous hampering free diffusion of the protein, which underpins the MST method.

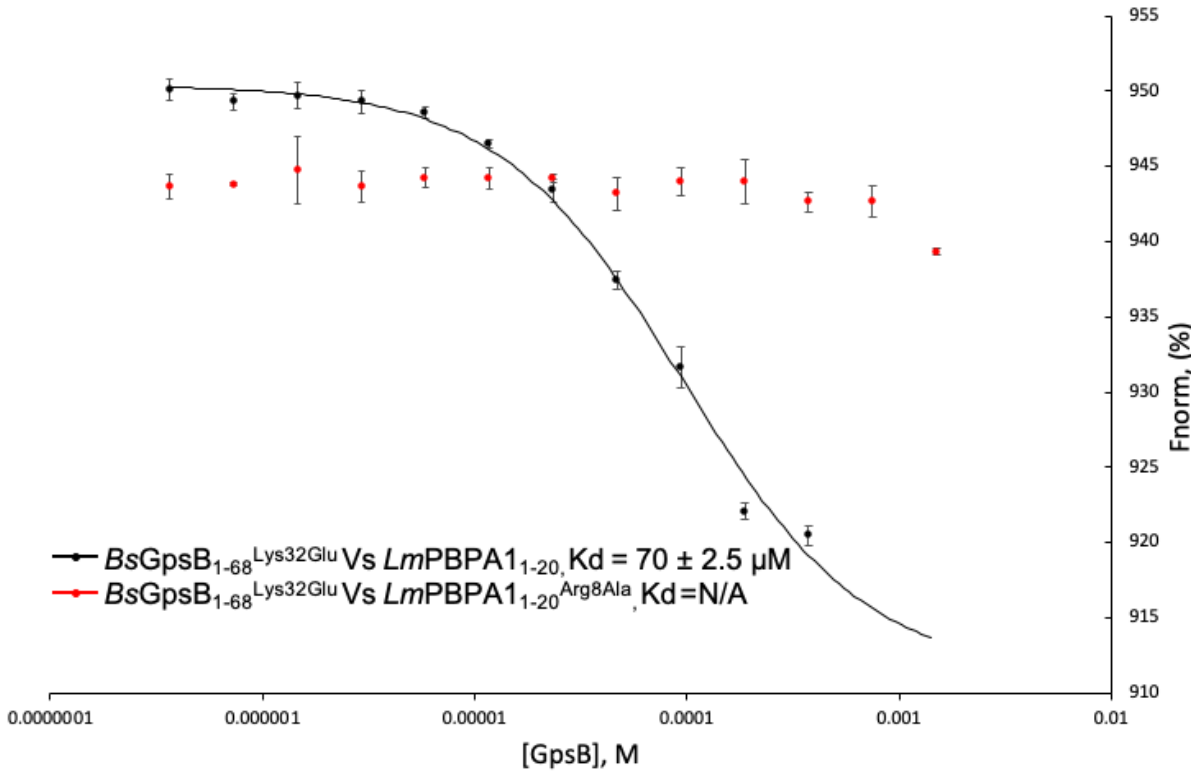

Figure 3.8: Confirmation of the affinity of *Lm*PBPA1 for *Bs*GpsB^{Lys32Glu}.
The affinity of *Lm*PBPA1$_{1-20}$ for *Bs*GpsB$_{1-68}^{Lys32Glu}$ compared to the non-binding mutant *Lm*PBPA1$_{1-20}^{Arg8Ala}$, as monitored by MST. The average of three measurements and the standard error bars for each data point is shown. The key shows which data set is represented by colouring and the respective Kd that was determined by the MO.Affinity Analysis v2.2.4 software.

Bacterial-two-hybrid experiments carried out by the Halbedel lab supported the assignment of the crucial GpsB binding residues in PBPA1 (Cleverley et al., 2019). *Lm*PBPA1$_{1-20}^{Arg8Ala}$ and *Lm*PBPA1$_{1-20}^{Arg12Ala}$ mutants had a significant negative impact on the *Lm*GpsB:*Lm*PBPA1 interaction. The mutation of Tyr11 to alanine had a milder impact on the binding capacity consistent with FP data. As expected, alanine substitutions of positively charged residues downstream of residue 14 had no impact on binding.

The effects of these identified GpsB binding residues (Section 3.4) in PBPA1 were tested in *Listeria* using fosfomycin as a reporter, because Δ*gpsB* mutants are more susceptible to this antibiotic at 37 °C (Rismondo et al., 2017). Mutants carrying the *pbpA1*^{Arg8AlaArg12Ala} and *pbpA1*^{Gln10Pro} alleles had an increased sensitivity to fosfomycin but only when the paralogue of *Lm*PBPA1, *Lm*PBPA2 was also absent (Halbedel lab, personal communication). This highlights the importance of these residues for the function of PBPA1 *in vivo* but these residues are not essential for the bacteria as *Lm*PBPA2 can carry out the same role when *Lm*PBPA1 is mutated.

3.5 Crystallisation of the N-terminal domain of GpsB from *S. pneumoniae*

3.5.1 Crystallisation trials of *Sp*GpsB

The recombinantly-expressed and purified N-terminal domain of GpsB from *S. pneumoniae* *Sp*GpsB$_{1-63}$ at 20 mg/mL was subjected to crystallisation in a number of sparse matrix crystallisation screens. The low frequency of high-quality crystals prompted the design of a new construct, *Sp*GpsB$_{4-63}$, in which the flexible N-terminal residues were deleted in order to produce a more crystallisable protein. Crystals of *Sp*GpsB$_{4-63}$ grew in 5 different conditions from 3 different crystallisation screens (Figure 3.9). Crystals from JCSG+ D6 (0.2 M magnesium chloride hexahydrate, 0.1 M Tris pH 8.5 and 20 % w/v PEG 8000) were parallelepipedal in shape in comparison to crystals from C11 (0.1 M sodium acetate pH 4.6 and 2 M ammonium sulphate) that grew as plates. Two conditions E7 (0.12 M ethylene glycols, 0.1 M buffer system 2 pH 7.5 and 30 %GOL_P4K) and F9 (0.12 M monosaccharides, 0.1 M buffer system 3 pH 8.5 and 30% P550MME_P20K) from the Morpheus screen yielded crystals. Crystals from E7 where long needles and crystals in F9 grew as thin plates. A single large crystal 200 µM x 100 µM x 100 µM in size formed in the PACT screen condition D11 (0.2 M calcium chloride, 0.1 M Tris pH 8 and 20 % w/v PEG 6000).

3.5.2 Data processing, molecular replacement and model building

For the crystal harvested from JCSG+ D6, diffraction data were collected and processed in house as described in 2.4.4. The diffraction data for the other 4 conditions were collected at Diamond Light Source on beamline I24. Images were indexed and integrated in DIALS (Beilsten-Edmands et al., 2020) and scaled and merged with AIMLESS (Evans & Murshudov, 2013). In each case the initial model was produced in PHASER (McCoy et al., 2007) by molecular replacement using chain A of the N-terminal domain of *Lm*GpsB (PDB ID:4UG1) as a model. BUCCANEER (Cowtan, 2012) was used to build the *Sp*GpsB sequence into each model that was rebuilt in COOT (Emsley et al., 2010) and refined in REFMAC (Murshudov et al., 1997). The models from crystals grown in JCSG+ C11, Morpheus E7 and F9 and PACT D11 underwent a few refinement cycles and were analysed as potential candidates for peptide soaking. The model from JCSG+ D6 was fully refined for deposition. The data collection and refinement statistics of each model can be found in Table 3.2.

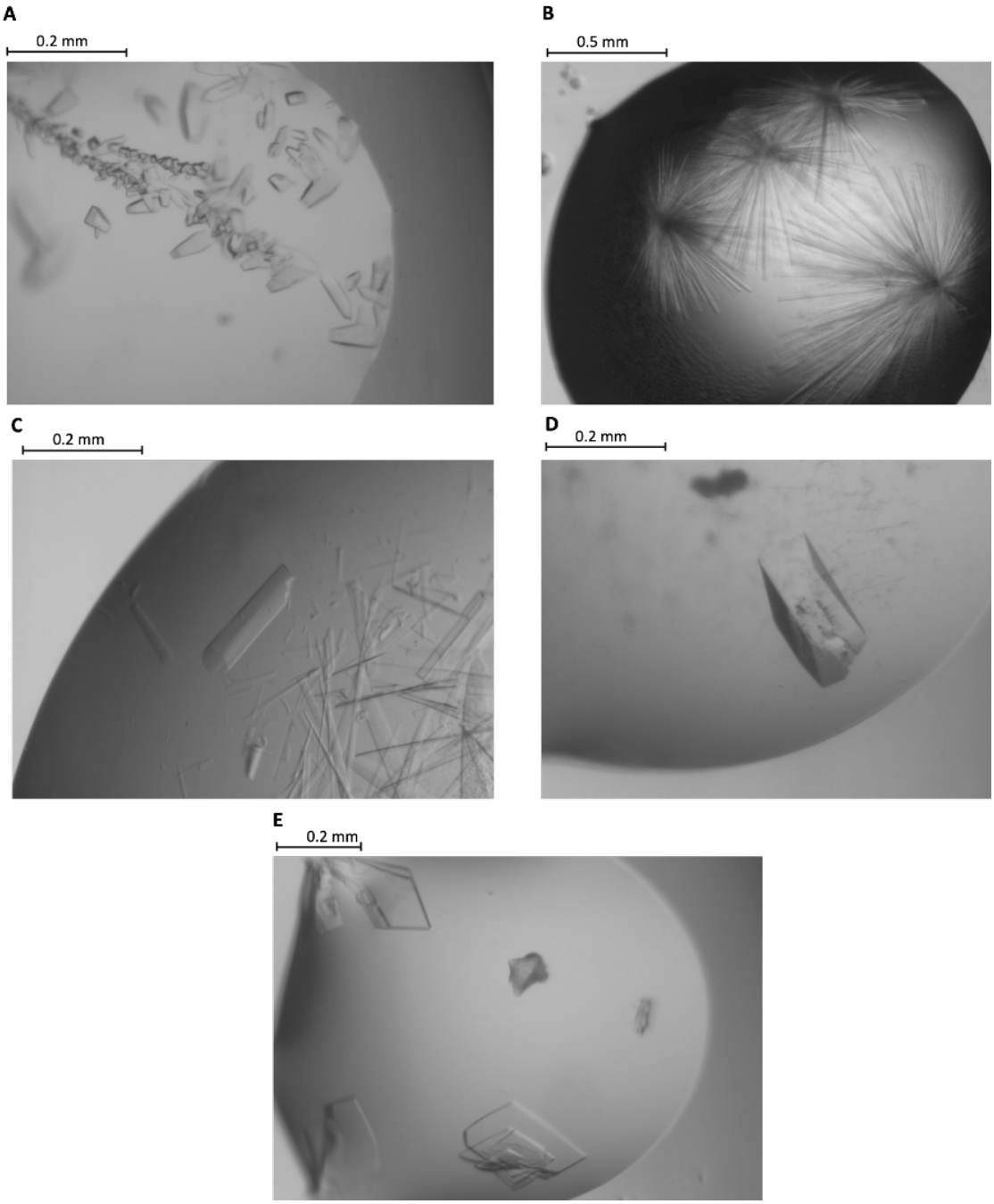

Figure 3.9: Crystals of *Sp*GpsB$_{4-63}$.
Panel **A** is a drop from JCSG+ D6, panel **B** is a drop from Morpheus E7, panel **C** is a drop from Morpheus F9, panel **D** is a drop from PACT D11 and panel **E** is a drop from JCSG+ C11 in which crystals of *Sp*GpsB$_{4-63}$ grew. The scale bar above each image provides an indication of the size of each crystal.

3.5.3 Analysis of the *Sp*GpsB structure

The structure of *Sp*GpsB$_{4-63}$ was solved to 1.9 Å and is formed of two identical subunits forming a dimer with each monomer composed of 2 alpha-helices as seen for the structures of *Lm*GpsB$_{1-73}$ and *Bs*GpsB$_{1-68}$ (Figure 3.10 A) (Rismondo et al., 2016). In the structure there are 4 molecules in the crystallographic asymmetric unit with monomer:monomer rmsds of 0.51 ±

0.07 Å which is comparable with the monomer:monomer rmsds of *Bs*GpsB$_{1-68}$ (Rismondo et al., 2016). The structure of *Sp*GpsB$_{4-63}$ was solved a total of 5 times to try and obtain a candidate for PBP peptide soaking. In all cases the binding site was involved in crystal lattice contacts to neighbouring GpsB molecules so that the solvent channels were not large enough to allow for soaking with a ~20 residue peptide (Figure 3.10 B and C). It was therefore concluded that co-crystallisation would be the most realistic route to obtain *Sp*GpsB:*Sp*PBP complexes, described in sections 3.7.1 and 3.10.1.

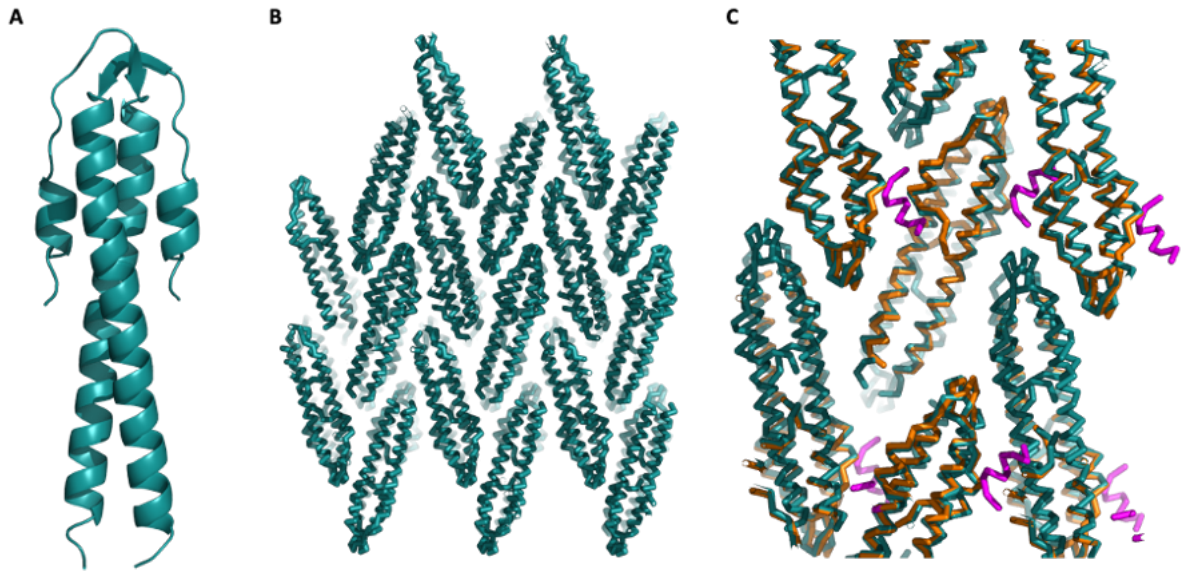

Figure 3.10: Analysis of the *Sp*GpsB$_{4-63}$ structure.
The analysis of the structure of *Sp*GpsB$_{4-63}$ solved from a crystal grown in JCSG+ D6. Panel **A** shows the *Sp*GpsB$_{4-63}$ dimer in cartoon form. Panel **B** shows the arrangement of the *Sp*GpsB$_{4-63}$ dimer in the crystal lattice, highlighting small solvent channels between each molecule. Panel **C** is a zoomed-in view of panel **B** in which the structure of *Bs*GpsB$_{5-64}$:*Bs*PBP1$_{1-17}$ has been superimposed onto *Sp*GpsB$_{4-63}$. *Bs*GpsB$_{5-63}$ is coloured orange and *Bs*PBP1$_{1-17}$ is coloured magenta. Residues from *Bs*PBP1$_{1-17}$ clash with *Sp*GpsB$_{4-63}$ which indicated that this crystal form was probably not suitable for peptide soaking.

3.6 Interaction of *Sp*PBP2a with the *Sp*GpsB N-terminal domain

3.6.1 Generation of a cytoplasmic domain peptide of *Sp*PBP2a

The essentiality of GpsB in *S. pneumoniae* presumably reflects its importance as a protein interaction scaffold, especially for PBPs (Land et al., 2013). It had been suggested that GpsB is required for PBP2a activity in *S. pneumoniae* and shown that PBP2a and GpsB were pulled-down by co-IP (Rued et al., 2017). Synthetic lethality studies with Δ*gpsB* suppressor mutants revealed that *pbp1a* became essential in the absence of *gpsB*, which indicated that *Sp*PBP2a

is the class A PBP regulated by *Sp*GpsB (Rued et al., 2017). The cytoplasmic domain of *Sp*PBP2a contains an RRSRSDR (residues 30-36) sequence that contributes to an (S/R)RS(R/G)(K/S)xR conserved motif across *Streptococcaceae* PBP2a proteins (Figure 3.11) (Cleverley et al., 2019), and SRSDRK (residues 32-37) is a perfect match to the consensus SRxxR(R/K) motif of *Bacillaceae* PBP1. To probe the interaction of *Sp*PBP2a with *Sp*GpsB, a cytoplasmic domain peptide was produced as for *Lm*PBPA1$_{1\text{-}20}$, encompassing residues 23-45 (*Sp*PBP2a$_{23\text{-}45}$) in which glycine 43 was mutated to a cysteine for TAMRA maleimide labelling (Figure 3.12).

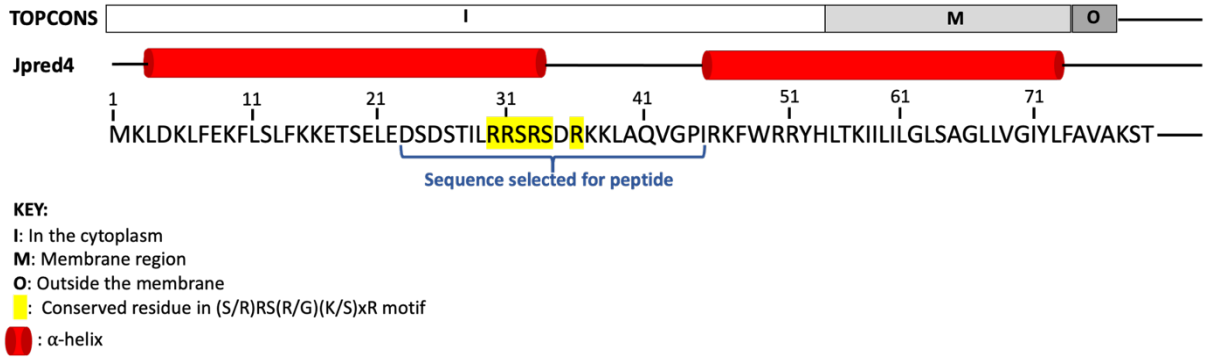

Figure 3.11: Analysis of the N-terminal domain of *S. pneumoniae* PBP2a.
Protein topology prediction (TOPCONS) (Tsirigos et al., 2015) and secondary structure prediction (Jpred4) (Drozdetskiy et al., 2015) analysis of the first 80 residues of *Sp*PBP2a. The key explains the figure's main features. The sequence of the cytoplasmic mini-domain selected for peptide generation is shown by the blue brace.

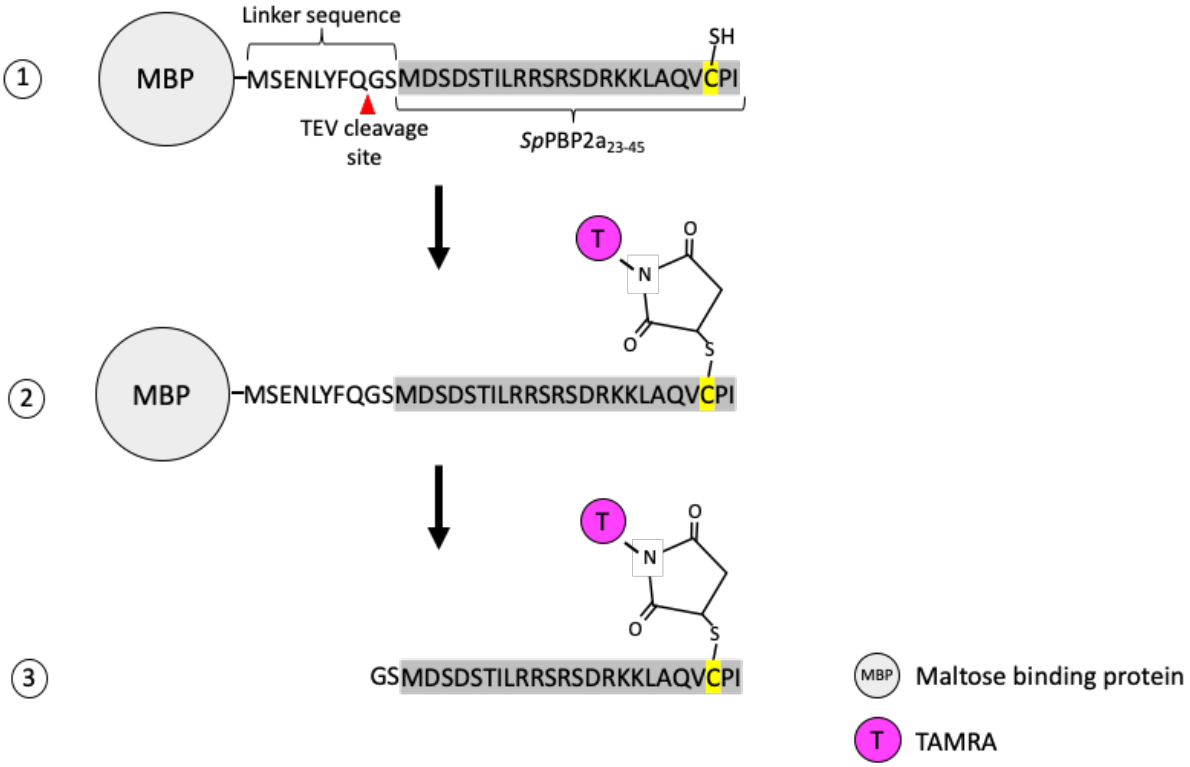

Figure 3.12: Generation of a fluorescently-labelled cytoplasmic domain peptide of *Sp*PBP2a. The steps taken in the generation of a TAMRA maleimide-conjugated *Sp*PBP2a$_{23-45}$ peptide. Step 1 shows the purified expression product from the pMAT11 vector. Residues 23-45 of *Sp*PBP2a, highlighted in grey, are linked to maltose binding protein (MBP) by a linker sequence containing a TEV cleavage site. The mutated glycine 43 to cysteine residue in *Sp*PBP2a is highlighted in yellow with the thiol group annotated. Step 2 is the result of the incubation of the expression product with TAMRA maleimide which is linked to the protein by a reaction with the thiol group of the cysteine residue. Step 3 is TEV cleavage, from which the result is a fluorescently-labelled *Sp*PBP2a cytoplasmic domain peptide. The two residues not highlighted in grey are two residual residues from the linker sequence after TEV cleavage.

3.6.2 Analysis by fluorescence polarisation

*Sp*PBP2a$_{23-45}$ bound to *Sp*GpsB$_{1-63}$ with a Kd of 74 ± 14 µM, similar to the affinity of *Bs*GpsB and *Lm*GpsB for their respective PBP1 and PBPA1 peptide binding partners. As a control, a mutant of *Sp*GpsB$_{1-63}^{Asp33Ala}$ was produced, which is the equivalent of *Bs*GpsB$_{1-68}^{Asp35Ala}$ that does not bind to *Bs*PBP1. A Kd of > 3mM was recorded for this interaction, which highlights the importance of this conserved aspartate residue for binding of partner proteins to GpsB, irrespective of their genetic source (Figure 3.13).

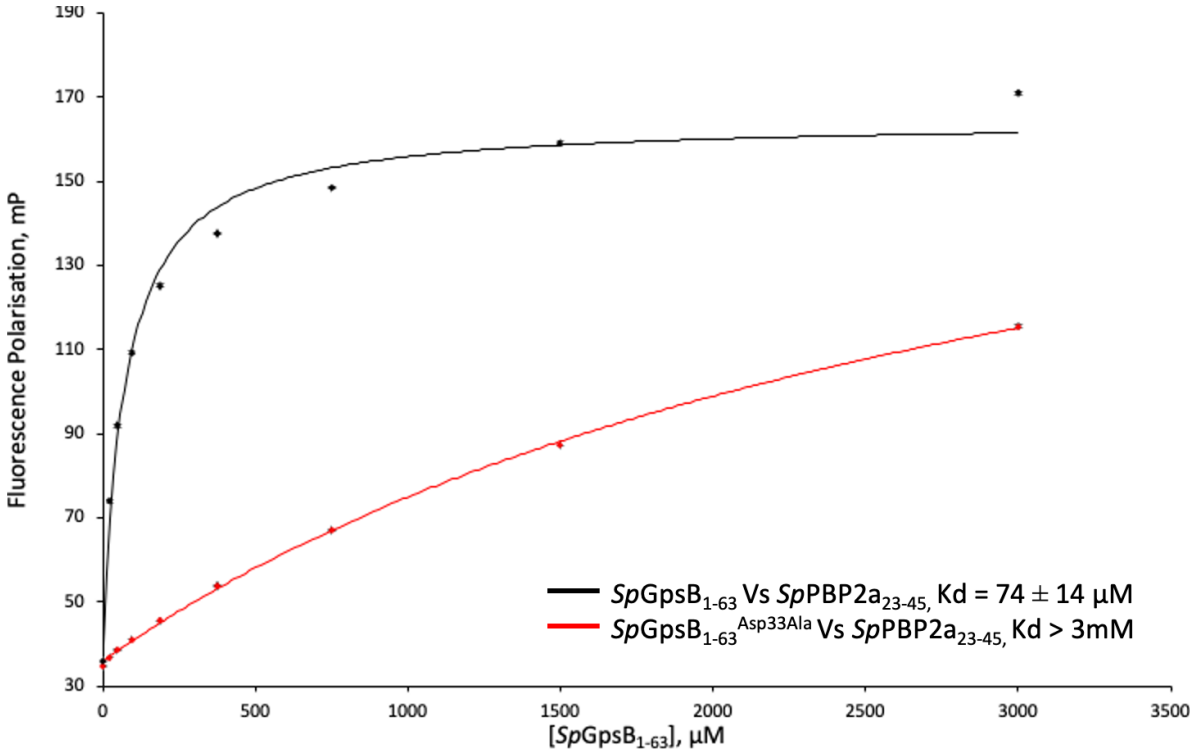

Figure 3.13: Interaction of the cytoplasmic domain peptide of *Sp*PBP2a with the N-terminal domain of GpsB.
The interaction of TAMRA-labelled *Sp*PBP2a$_{23-45}$ peptides with the wild-type N-terminal domain of GpsB from *S. pneumoniae* (*Sp*GpsB$_{1-63}$) and the mutant *Sp*GpsB$_{1-63}^{Asp35Ala}$, as monitored by fluorescence polarisation. Binding data and the fit of the data to a 1:1 binding model in Sigma plot for each of the data sets are plotted. The average of three measurements and the standard error bars for each data point is shown. The key shows which data set is represented by colouring and the respective Kd that was determined in Sigma plot.

3.6.3 Determining the thermodynamic parameters of the interaction using isothermal titration calorimetry

The interaction of *Sp*GpsB$_{1-63}$ with unlabelled *Sp*PBP2a$_{27-40}$ was analysed by ITC, revealing a Kd of 7.33 ± 0.52 µM (Figure 3.14). The 10-fold increase in affinity measured by ITC could be explained by the bulky fluorophore, which could inhibit the binding of the PBP peptide to GpsB. FP was favoured to ITC for GpsB:PBP interactions studies because the technique requires considerably less protein and experiments take seconds to run as opposed to an hour for an individual ITC run. The binding enthalpy (ΔH) of the interaction was -2.81 kcal/mol, which indicates a favourable interaction that is comprised of hydrogen bonding and salt bridges. The entropy factor (-TΔS) was also favourable at -4.09 kcal/mol, which highlights that no conformational changes were required for binding. This is consistent with the absence of conformational changes in structures of GpsB N-terminal domains, from all species, in the presence/absence of bound peptide. The expected stoichiometry of the interaction was 1 as

there are two peptide binding sites for every GpsB dimer. However, the N-value determined for the interaction was 1.6. The N-value only equals the stoichiometry if the concentrations used for fitting are 100 % correct and active, suggesting that one or both of the protein/peptide concentrations are not accurate.

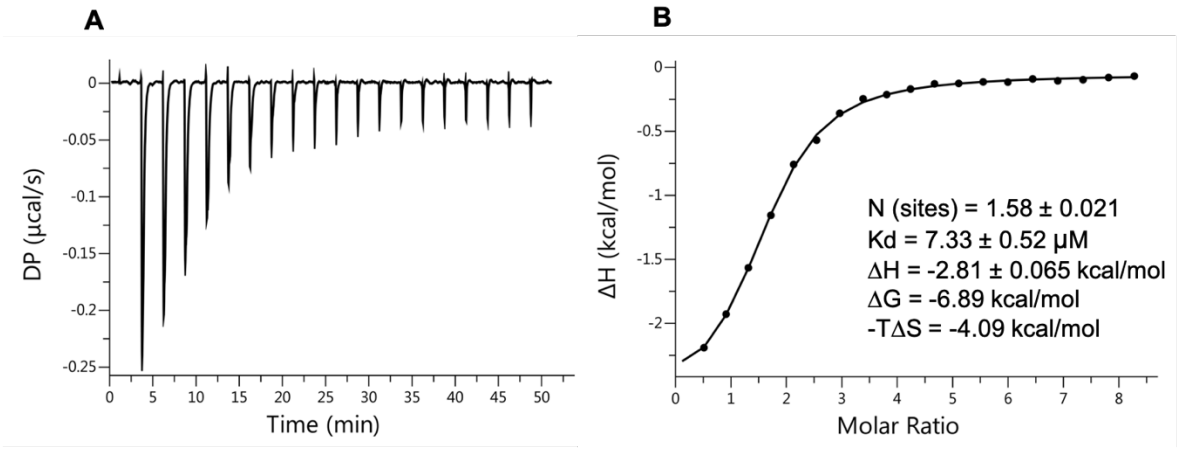

Figure 3.14: Determining the thermodynamic parameters of the *Sp*GpsB$_{1-63}$:*Sp*PBP2a$_{27-40}$ interaction.
Panel **A** shows the ITC raw heat plot of 25 µM *Sp*GpsB$_{1-63}$ in the cell with 20 syringe injections of *Sp*PBP2a$_{27-40}$ at 1 mM. Panel **B** shows the corresponding binding isotherm, also known as a Wiseman plot, from which a number of thermodynamic parameters (N, Kd, ΔH, ΔG and -TΔS) can be determined.

3.7 Co-crystallisation of the *Sp*GpsB N-terminal domain in complex with S*p*PBP2a cytoplasmic domain peptide

3.7.1 Crystallisation trials of *Sp*GpsB$_{4-63}$:*Sp*PBP2a$_{27-40}$

Co-crystallisation attempts of the N-terminal domain of *Sp*GpsB with a *Sp*PBP2a peptide was carried out by combining *Sp*GpsB$_{4-63}$ (at a final concentration of 20 mg/mL) with *Sp*PBP2a$_{27-40}$ (25 mg/mL final; 1:5 molar ratio of protein:peptide) and subjecting the mix to sparse matrix crystallisation screening. Crystals grew in two conditions, JCSG+ D7 (0.2 M lithium sulphate, 0.1 M Tris pH 8.5 and 40 % v/v PEG 400) and PACT D12 (0.002 M zinc chloride, 0.1 M tris pH 8, 20 % w/v PEG 6000). Crystals from JCSG+ D6 were cuboidal and those from PACT D12 were needle-like (Figure 3.15). Crystals were transferred to a drop of the well solution containing 2.5 mg/mL of *Sp*PBP2a$_{27-40}$ peptide, supplemented with 20 % PEG 400 for PACT D12. After 30 seconds the crystals were mounted in rayon loops and cryo-cooled in liquid nitrogen.

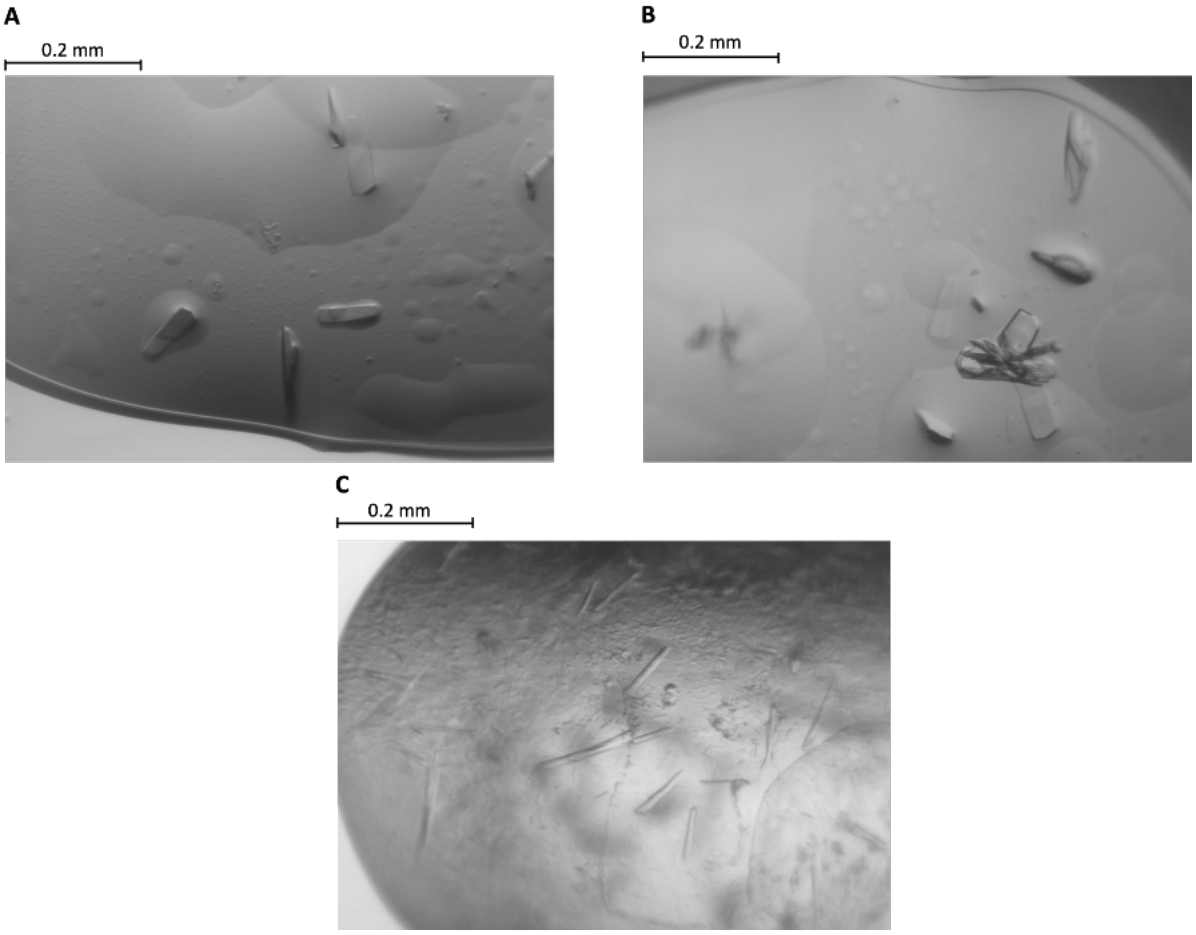

Figure 3.15: Crystals of *Sp*GpsB$_{4-63}$:*Sp*PBP2a$_{27-40}$.
Panel **A** and **B** are drops from JCSG+ D7 and panel **C** is a drop from PACT D12 in which crystals grew from *Sp*GpsB$_{4-63}$:*Sp*PBP2a$_{27-40}$. The scale bar above each image provides a visual indication of the size of each crystal.

3.7.2 Data processing, molecular replacement and model building

Data were collected a Diamond light source I03; crystals from JCSG+ D7 diffracted to 1.8 Å whereas crystals from PACT D12 did not diffract. Diffraction data were processed and the structure of *Sp*GpsB$_{4-63}$:*Sp*PBP2a$_{27-40}$ was solved by molecular replacement following the same procedures as described in 2.4.4. Each PBP2a molecule was manually built into the electron density using COOT (Emsley et al., 2010) and refined until convergence.

3.7.3 Analysis of the *Sp*GpsB$_{4-63}$:*Sp*PBP2a$_{27-40}$ structure

There were two molecules of *Sp*GpsB$_{4-63}$:*Sp*PBP2a$_{27-40}$ in the asymmetric unit, which comprised a single *Sp*GpsB dimer and peptide was present in the binding site of each *Sp*GpsB monomer (Figure 3.16 A). The whole peptide was built into both binding sites with the exception of threonine 27 in binding site 1 as there was insufficient electron density to

confidently build this residue; the majority of each peptide was in an extended conformation (Figure 3.17 A and C). The binding of S*p*PBP2a in both sites was heavily centred on two arginine residues as seen in *Bs*PBP1, but the peptide is bound in different conformations in each binding site. In binding site 1, Arg33 and Arg36 penetrate into the space between helix 1 and 2 of the *Sp*GpsB monomer with the residues being positioned at the start and end of a single turn alpha helix. Conversely, arginine residues Arg31 and Arg36 occupy the same sites in the second site and they are in a type I beta turn. Arg31/33 bind in the same position as Arg8 in *Bs*GpsB$_{5-64}$:*Bs*PBP1$_{1-17}$ and Arg36 in both sites is the same as Arg11 (Figure 3.16 B).

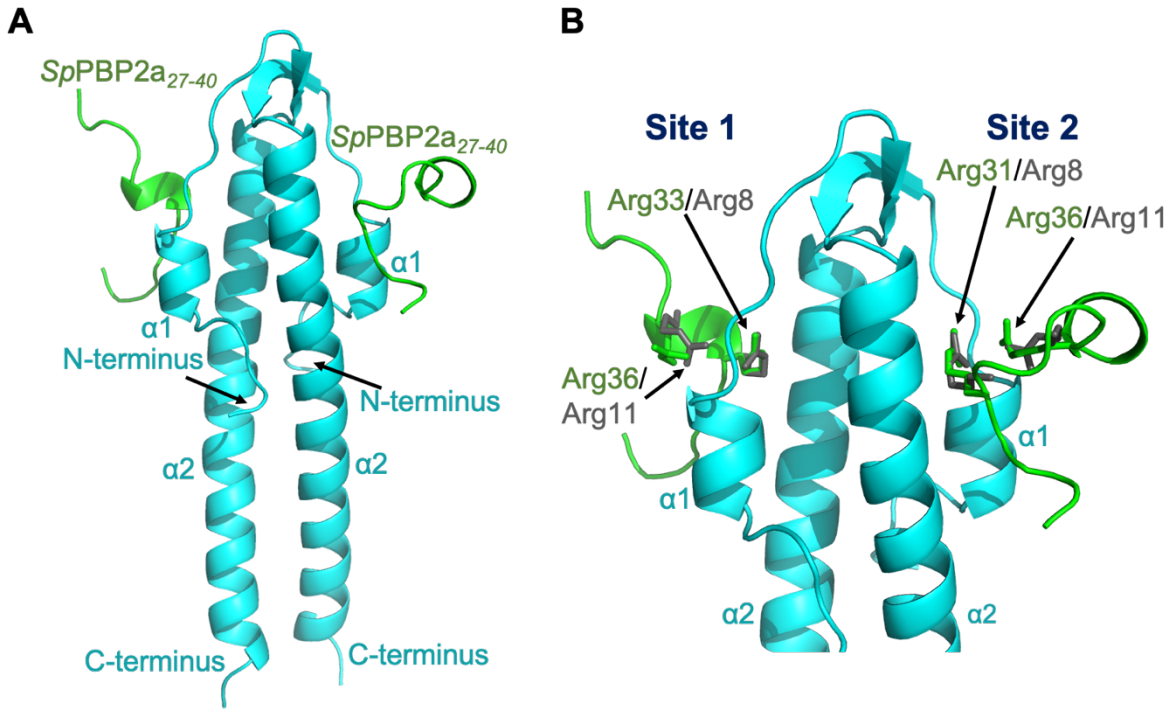

Figure 3.16: Structure of the N-terminal domain of *Sp*GpsB bound to residues 27-40 of *Sp*PBP2a.
The two subunits of the GpsB N-terminal dimer are coloured cyan and are shown as cartoons, and the peptide is coloured in green. (**A**) highlight of each of the *Sp*PBP2a peptides and α1 and α2 of each subunit of the *Sp*GpsB dimer. (**B**) Zoomed-in view of the binding site. The side chains of Arg33 and Arg36 in binding site 1 and Arg31 and Arg36 in binding site 2 penetrate into the groove between the two helices and are shown in sticks. The positions of Arg8 and Arg11 of *Bs*PBP1 from the superimposition of *Sp*GpsB$_{4-63}$:*Sp*PBP2a$_{27-40}$ with *Bs*GpsB$_{5-64}$:*Bs*PBP1$_{1-17}$ are shown as sticks and coloured grey.

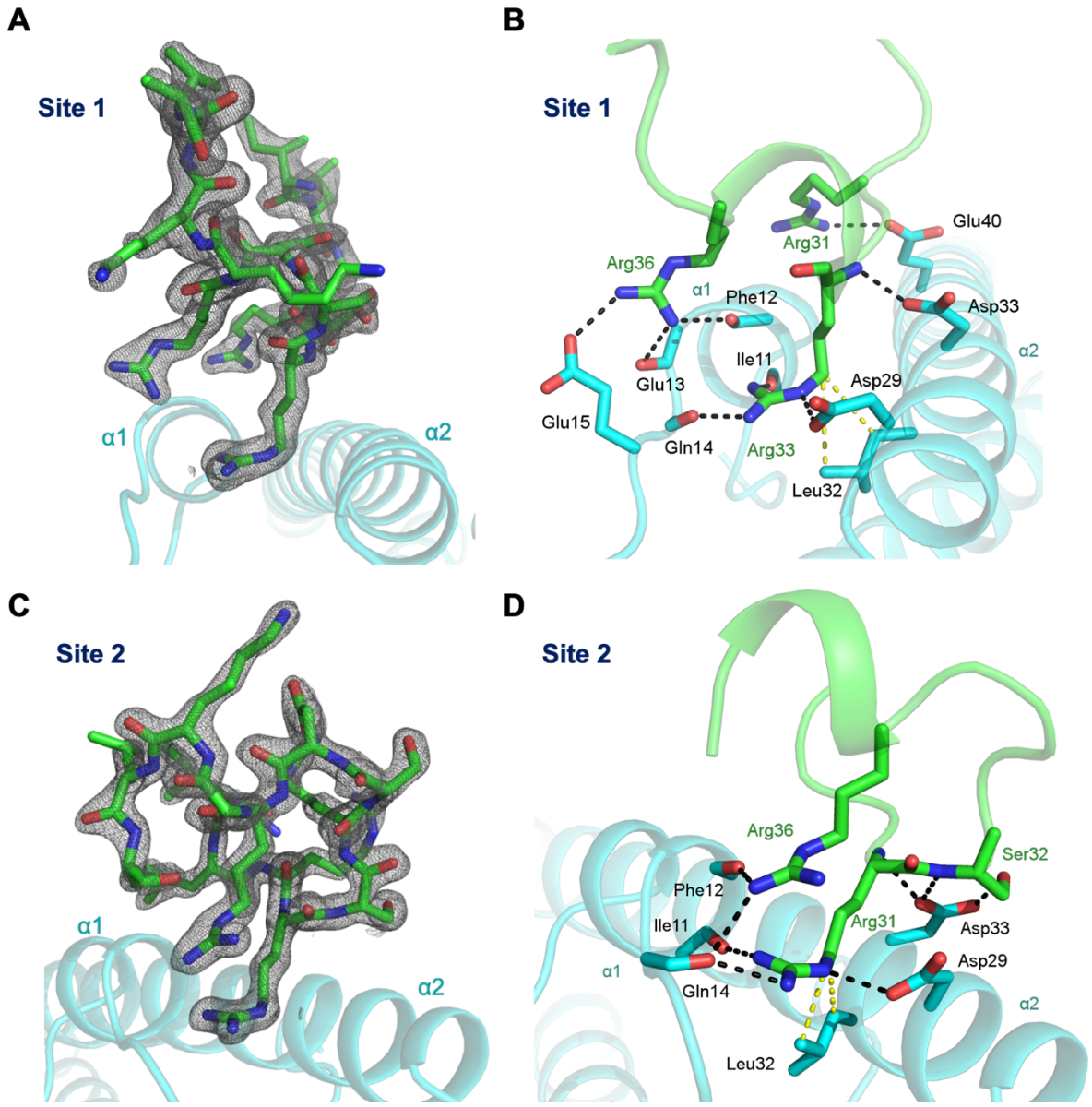

Figure 3.17: Structure of the N-terminal domain of *Sp*GpsB bound to residues 27-40 of *Sp*PBP2a.
Zoomed-in view of binding site 1 (**A**) and binding site 2 (**C**) looking down at helix 1 and 2. *Sp*PBP2a peptides shown as sticks and the electron density map is represented by a grey mesh. The map shown is the final Refmac-weighted $2mF_{obs}$-DF_{calc} map contoured at 0.5 electrons per $Å^3$ with a PyMol 'carve' value of 1.6. (**B** and **D)** Residues important in binding are shown as sticks and coloured by atom, binding site 1 (**B**) and binding site 2 (**D**). Salt bridges and hydrogen bonds are represented by dashed black lines and van der Waals' interactions by dashed yellow lines.

The arginine pairs form a similar set of interactions with *Sp*GpsB as seen in the *Bs*GpsB$_{5-64}$:*Bs*PBP1$_{1-17}$ structure. In binding site 1 there are hydrogen bonds between the *Sp*GpsB carbonyl oxygens of Phe12 and Glu13 with *Sp*PBP2a Arg36 and the carbonyl oxygens of Ile11 and Gln14 with *Sp*PBP2a Arg33. *Sp*PBP2a Arg31, 33 and 36 form salt bridges with the carboxylic acids of *Sp*GpsB Glu40, Asp29 and Glu15, respectively. There are also van der Waals'

interactions between *Sp*GpsB Leu32 and *Sp*PBP2a Arg33 and the peptide backbone amide of Arg33 interacts with *Sp*GpsB Asp33 (Figure 3.17 B).

In binding site 2, there are hydrogen bonds between *Sp*GpsB carbonyl oxygens of Phe12 and Gln14 with *Sp*PBP2a Arg36 and carbonyl oxygens of Ile11 and Gln14 with Arg31. Asp29 from *Sp*GpsB in this site forms a salt bridge with Arg31 and Leu32 forms van der Waals' contacts with the same residue. The peptide backbone amides of *Sp*PBP2a Arg31 and Ser32 and the backbone carbonyl of Ser32 interact with *Sp*GpsB Asp33 (Figure 3.17 D).

3.8 Important features of *Sp*PBP2a cytoplasmic domain peptide for *Sp*GpsB N-terminal domain binding.

The crystal structure of *Sp*GpsB:*Sp*PBP2a demonstrates that binding is centred on 3 arginine residues compared to 2 arginines with *Bs*PBP1 and *Lm*PBPA1, and the binding capacity was highly reliant on a single arginine residue at the start of a binding motif. To confirm the importance of Arg31, Arg33 and Arg36, each residue was mutated separately to an alanine to establish if any of these mutants compared to the reduction in binding seen by the Arg8Ala mutant of both *Bs*PBP1 and *Lm*PBPA1 (Figure 3.18). *Sp*PBP2a$_{23\text{-}45}^{Arg31Ala}$, *Sp*PBP2a$_{23\text{-}45}^{Arg33Ala}$ and *Sp*PBP2a$_{23\text{-}45}^{Arg36Ala}$ had a reduced affinity for *Sp*GpsB$_{1\text{-}63}$ by 3-, 7- and 3.5-fold, respectively, which suggested that *Sp*PBP2a was not dependent on a single arginine residue for *Sp*GpsB binding, as seen previously with the 15-fold reduction in affinity of Arg8Ala mutations of *Bs*PBP1 and *Lm*PBPA1.

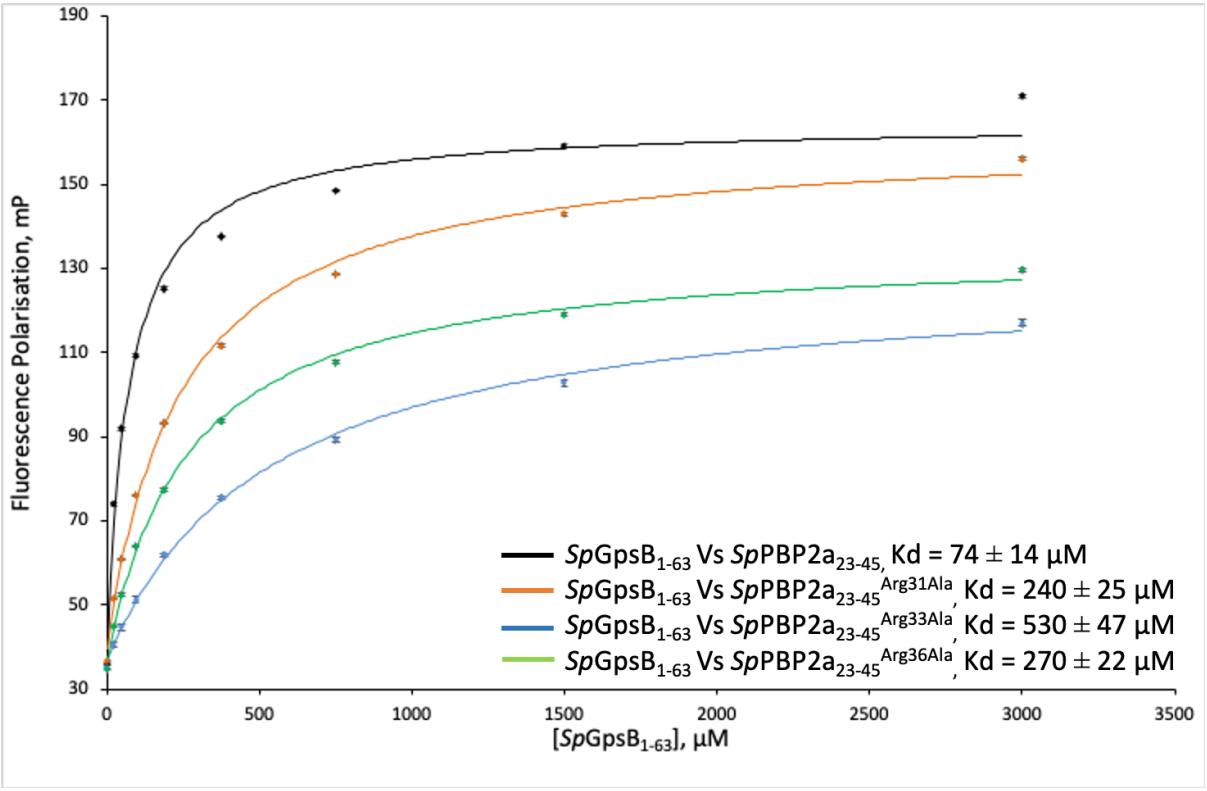

Figure 3.18: Interaction of *Sp*PBP2a$_{23-45}$ mutants with *Sp*GpsB$_{1-63}$.
The binding of wild-type *Sp*PBP2a$_{23-45}$ and Arg to Ala mutant peptides with *Sp*GpsB$_{1-63}$, as monitored by fluorescence polarisation. Data and the fit of the data to a 1:1 binding model in Sigma plot for each of the data sets are shown. The average of three measurements and the standard error bars for each data point are shown. The key shows which data set is represented by colouring and states the respective Kd that was determined in Sigma plot.

The structure indicated that an alpha helical conformation was not essential for the binding of *Sp*PBP2a to *Sp*GpsB, as was seen with *Bs*PBP1 and implicit in the complex with *Lm*PBPA1. To confirm this by FP, two potential alpha helix-disrupting mutant were made that were chosen according to the disruption of model helical proteins (Doig & Baldwin, 1995; Iqbalsyah, 2004). *Sp*PBP2a$_{23-45}^{Ser32Ala}$ reduced the binding affinity by 3.5-fold and *Sp*PBP2a$_{23-45}^{Asp35Pro}$ by only 2-fold. The equivalent proline introduction in *Bs*PBP1 and *Lm*PBPA1 affected binding capacity by ~10-fold, which showed *Sp*PBP2a does not have the same secondary structure requirements for binding to GpsB (Figure 3.19). Another explanation for the reduction in binding with the introduction of a proline residue is the loss of hydrogen bonding as proline does not contain a hydrogen on its backbone amide. Leu29 of *Sp*PBP2a is a conserved hydrophobic residue across Streptococci PBP2a proteins and along with Ile28, contacts to a hydrophobic pocket in *Sp*GpsB could contribute to binding. In binding site 2 of the *Sp*GpsB$_{4-63}$:*Sp*PBP2a$_{27-40}$ structure, *Sp*PBP2a^{Leu29} makes van der Waals' contacts with *Sp*GpsB^{Ile36}.

However, there was less than a 2-fold reduction in affinity with a *Sp*PBP2a^{Ile28AlaLeu29Ala} mutant, suggesting these residues were not crucial for binding (Figure 3.19).

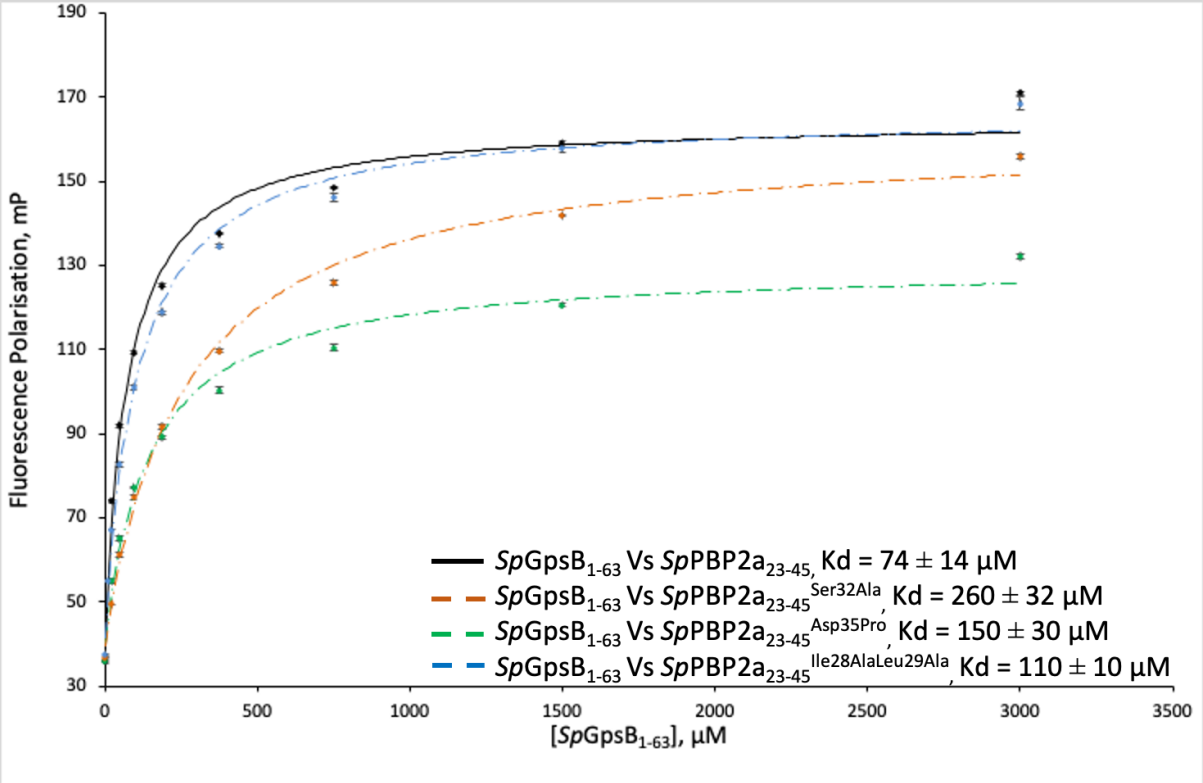

Figure 3.19: Interaction of *Sp*PBP2a$_{23-45}$ mutants with *Sp*GpsB$_{1-63}$.
The binding of wild-type *Sp*PBP2a$_{23-45}$ and mutants with *Sp*GpsB$_{1-63}$, monitored by fluorescence polarisation. Data and the fit of the data to a 1:1 binding model in Sigma plot for each of the data sets are shown. The average of three measurements and the standard error bars for each data point are shown. The key shows which data set is represented by colouring and states the respective Kd that was determined in Sigma plot.

Arginine to lysine mutations were made to evaluate the impact of reducing the hydrogen bonding capacity without changing the overall charge of the peptide (Figure 3.20). The affinities of *Sp*PBP2a$_{23-45}^{Arg31Lys}$ and *Sp*PBP2a$_{23-45}^{Arg36Lys}$ were comparable to the equivalent alanine substitutions while *Sp*PBP2a$_{23-45}^{Arg33Lys}$ reduced the affinity by 5-fold. The crystal structure showed that Arg31 and Arg33 of *Sp*PBP2a can occupy the same position as the crucial binding residue, Arg8, in *Bs*PBP1 and *Lm*PBPA1. A double mutant in which both Arg31 and 33 were mutated to lysine (*Sp*PBP2a$_{23-45}^{Arg31LysArg33Lys}$) reduced the binding affinity to GpsB by 27-fold. *Sp*PBP2a can thus bind to *Sp*GpsB in two different conformations and when one of these is prevented, either by crystal contacts or by mutation, the peptide can compensate by binding in the other.

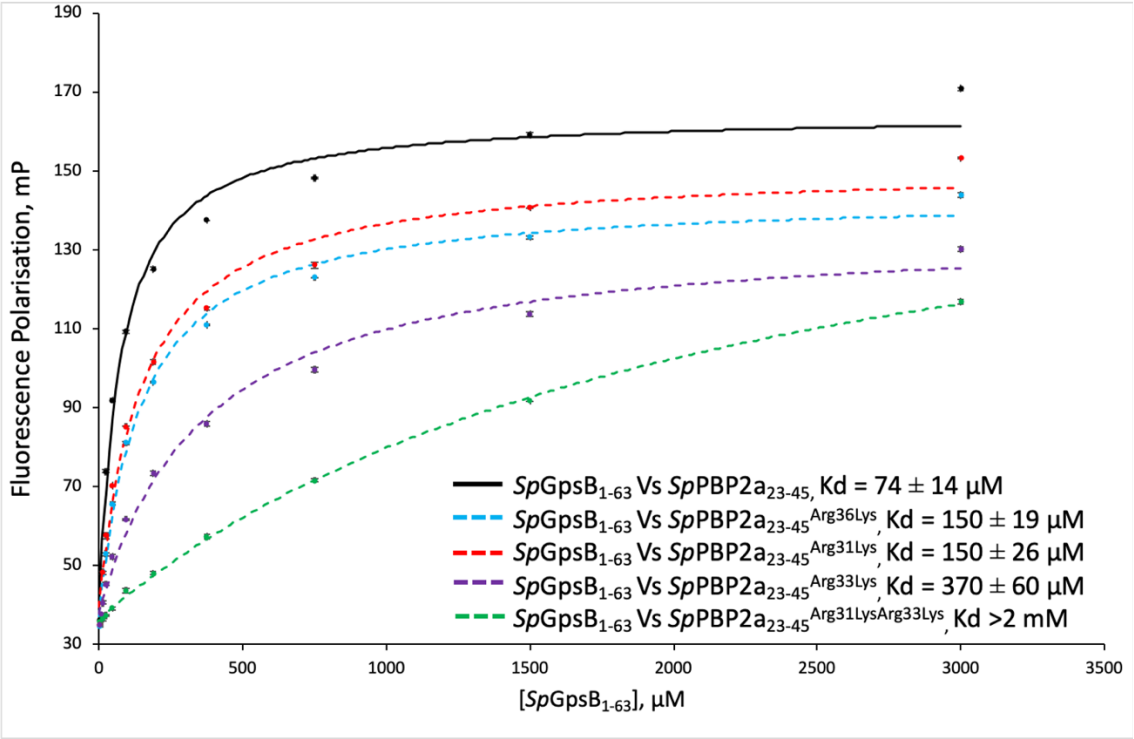

Figure 3.20: Interaction of *Sp*PBP2a$_{23\text{-}45}$ mutants with *Sp*GpsB$_{1\text{-}63}$.
The binding of wild-type *Sp*PBP2a$_{23\text{-}45}$ and Arg to Lys mutants with *Sp*GpsB$_{1\text{-}63}$, monitored by fluorescence polarisation. Data and the fit of the data to a 1:1 binding model in Sigma plot for each of the data sets are shown. The average of three measurements and the standard error bars for each data point are shown. The key shows which data set is represented by colouring and states the respective Kd that was determined in Sigma plot.

The binding of *Sp*PBP2a to *Sp*GpsB was confirmed by BACTH by the Massidda group and important residues for the interaction were confirmed (Cleverley et al., 2019). The binding was lost completely with *Sp*GpsB^{Tyr23Ala}, *Sp*GpsB^{Val28Ala}, *Sp*GpsB^{Asp29Ala}, *Sp*GpsB^{Leu32Ala} and *Sp*GpsB^{Asp33Ala} variants, and with *Sp*GpsB^{Ile36Ala} the interaction was reduced, though it was not possible to quantify the reduction in interaction using this method. The Winkler group also showed there were severe growth and morphological defects of *S. pneumoniae* strains harbouring the 5 different alleles that caused complete loss of binding in BACTH (Cleverley et al., 2019). The same growth defects were not observed with *S. pneumoniae Δpbp1a* strains carrying *Sp*PBP2a^{Arg31Ala}, *Sp*PBP2a^{Arg33Ala} or *Sp*PBP2a^{Arg31AlaSer32Ala} alleles. *Sp*PBP2a mutants with longer stretches of amino acids deleted such as residues 32-37 or 27-38 or 26-45 in a *Δpbp1a* strain showed progressively reduced growth rates. In each case *pbp1a* was deleted to separate the mutational effects of *Sp*PBP2a from *Sp*PBP1a activity. This data suggests that *Sp*PBP2a binding is just one function of *Sp*GpsB as a more severe phenotype is observed when the interacting residues of *Sp*GpsB are mutated compared to *Sp*PBP2a.

3.9 Interaction of *Sp*PBP2x with the *Sp*GpsB N-terminal domain

3.9.1 Generation of a cytoplasmic domain peptide of *Sp*PBP2x

S. pneumoniae PBP2x contains a conserved NR pair (residues 21 and 22) in its cytoplasmic domain that is essential for its function (Berg et al., 2014). The rest of the cytoplasmic domain of *Sp*PBP2x has an abundance of arginine residues and the NR pair is part of a consensus NRx(R)VG motif. The NR pair could be the functional equivalent of the SR (residues 7 and 8) at the start of the SRxxR(R/K) motif in *Bacillaceae* PBP1 that is essential for binding to *Bs*GpsB (Figure 3.21). However, co-IP experiments have not supported the idea that *Sp*PBP2x and SpGpsB interact through this motif (Rued et al., 2017).

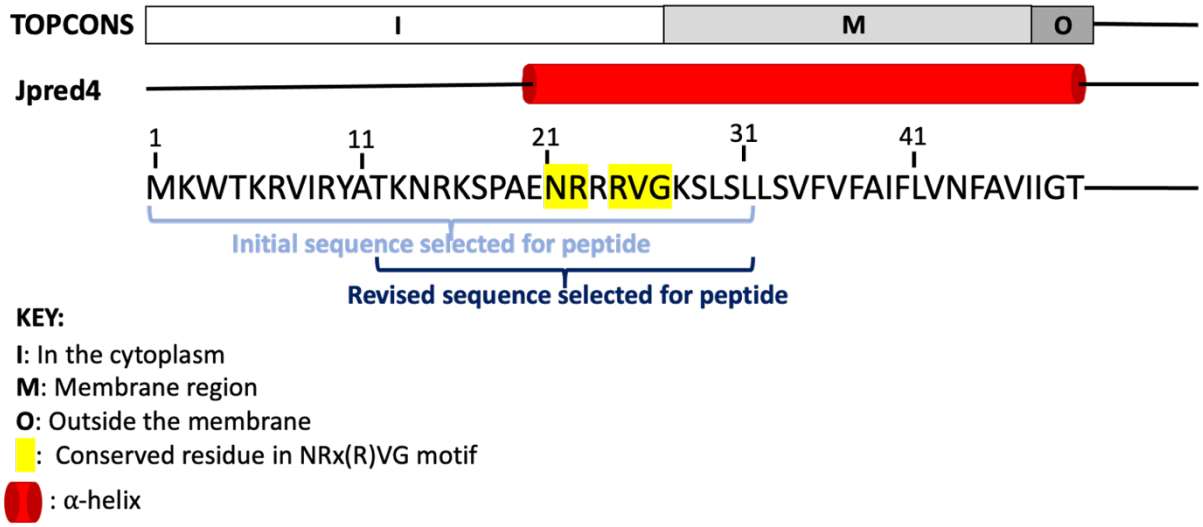

Figure 3.21: Analysis of the N-terminal domain of *S. pneumoniae* PBP2x.
Protein topology prediction (TOPCONS) (Tsirigos et al., 2015) and secondary structure prediction (Jpred4) (Drozdetskiy et al., 2015) analysis of the first 50 residues of *Sp*PBP2x. The key explains the figure's main features. The sequences of the cytoplasmic mini-domain selected for the generation of the peptides are shown by a light blue and dark blue brace.

In order to test the binding of the cytoplasmic domain of *Sp*PBP2x to the N-terminal domain of *Sp*GpsB by fluorescence polarisation, two peptides were created that contained residues 1-31 and 12-31 (*Sp*PBP2x$_{1\text{-}31}$ and *Sp*PBP2x$_{12\text{-}31}$) (Figure 3.22). *Sp*PBP2x$_{12\text{-}31}$ was created as initial attempts to purify the full cytoplasmic domain were challenging, possibly because of an amphipathic helix between residues 5-11 interacting non-specifically with the MBP fusion partner used to generate the peptide (Figure 3.23). Fluorescently labelled PBP peptides were separated from the MBP fusion protein by concentrating through a 30 kDa molecular mass cutoff (MWCO) centrifugal ultrafiltration device, allowing only the peptide to pass through.

With *Sp*PBP2x$_{1-31}$, the peptide remained in the concentrator with the cleaved MBP fusion partner, whereas *Sp*PBP2x$_{12-31}$ passed through.

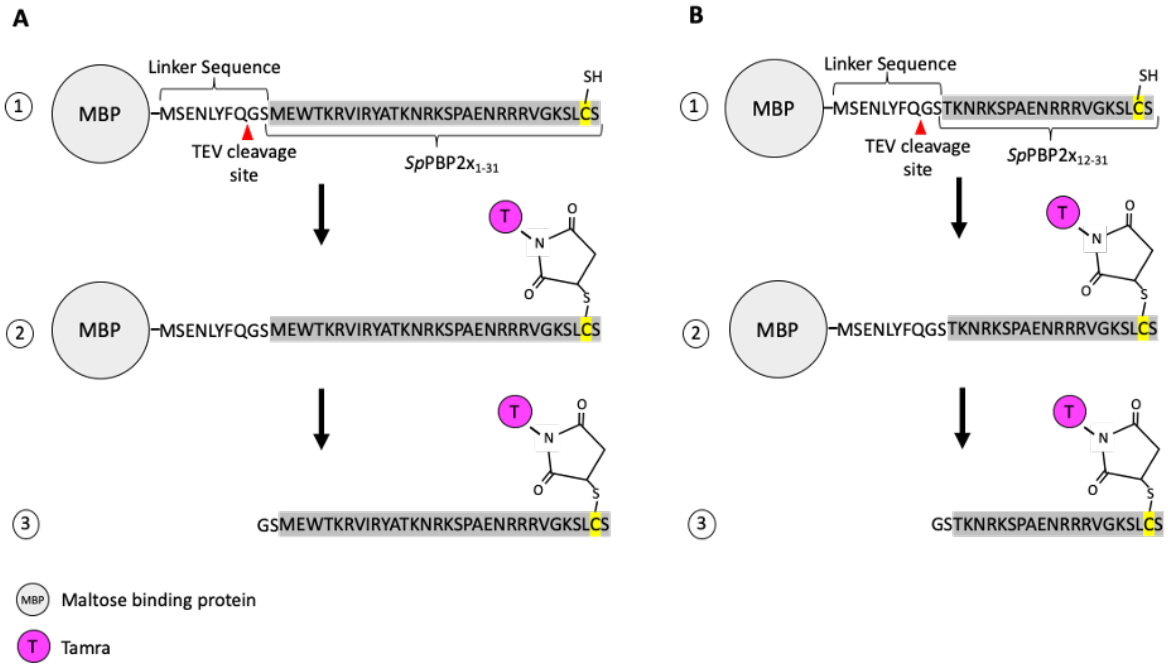

Figure 3.22: Generation of a fluorescently-labelled cytoplasmic domain peptide of *Sp*PBP2x. Panel **A** shows the steps taken in the generation of a TAMRA maleimide conjugated *Sp*PBP2x$_{1-31}$ peptide and panel **B** shows the same process but with residues 12-31 of *Sp*PBP2x. Step 1 shows the purified expression product from the pMAT11 vector. Residues 1-31/12-31 of *Sp*PBP2x, highlighted in grey, are linked to maltose binding protein (MBP) by a linker sequence containing a TEV cleavage site. The mutated serine 30 to cysteine residue in *Sp*PBP2x is highlighted in yellow with the thiol group highlighted. Leucine 31 was mutated to a serine to keep the peptide hydrophobicity down and to have a less bulky residue near the cysteine to facilitate labelling. Step 2 is the result of the incubation of the expression product with TAMRA maleimide which is linked to the protein by a reaction with the thiol group of the cysteine residue. Step 3 is TEV cleavage, in which the result is a fluorescently-labelled *Sp*PBP2x cytoplasmic domain peptide. The two residues not highlighted in grey are residual residues from the linker sequence after TEV cleavage.

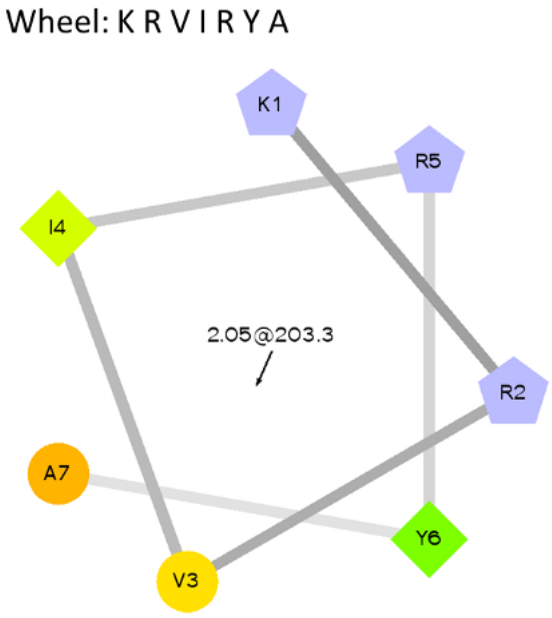

Figure 3.23: *Sp*PBP2x cytoplasmic domain peptide amphipathic helix.
A helical wheel projection of the secondary structure predicted alpha-helix KRVIRYA (residues 5-11) of *Sp*PBP2x$_{1-31}$. Hydrophilic residues are circles, hydrophobic residues are diamonds and positively charged residues are pentagons. The most hydrophobic residue is green, and the amount of green is decreases proportionally to the hydrophobicity, with zero hydrophobicity coded as yellow. Hydrophilic residues are coded red, and the amount of red decreases proportionally to the hydrophilicity. Positively charged residues are coloured blue.

3.9.2 Analysis by fluorescence polarisation

*Sp*GpsB$_{1-63}$ bound to *Sp*PBPx$_{1-31}$ and *Sp*PBP2x$_{12-31}$ with modest affinities, Kd of 370 ± 60 µM and 620 ± 80 µM, respectively. *Sp*PBP2x$_{12-31}$ appeared to bind to the same site on GpsB as *Bs*PBP1, *Lm*PBPA1 and *Sp*PBP2a as there was a 5-fold decrease in affinity of *Sp*PBP2x$_{12-31}$ for *Sp*GpsB$_{1-63}^{Asp33Ala}$ (Figure 3.24). It was unwise to conclude that these affinities were accurate as there was no evidence of saturation and the data resembled more of a straight line than a hyperbolic curve.

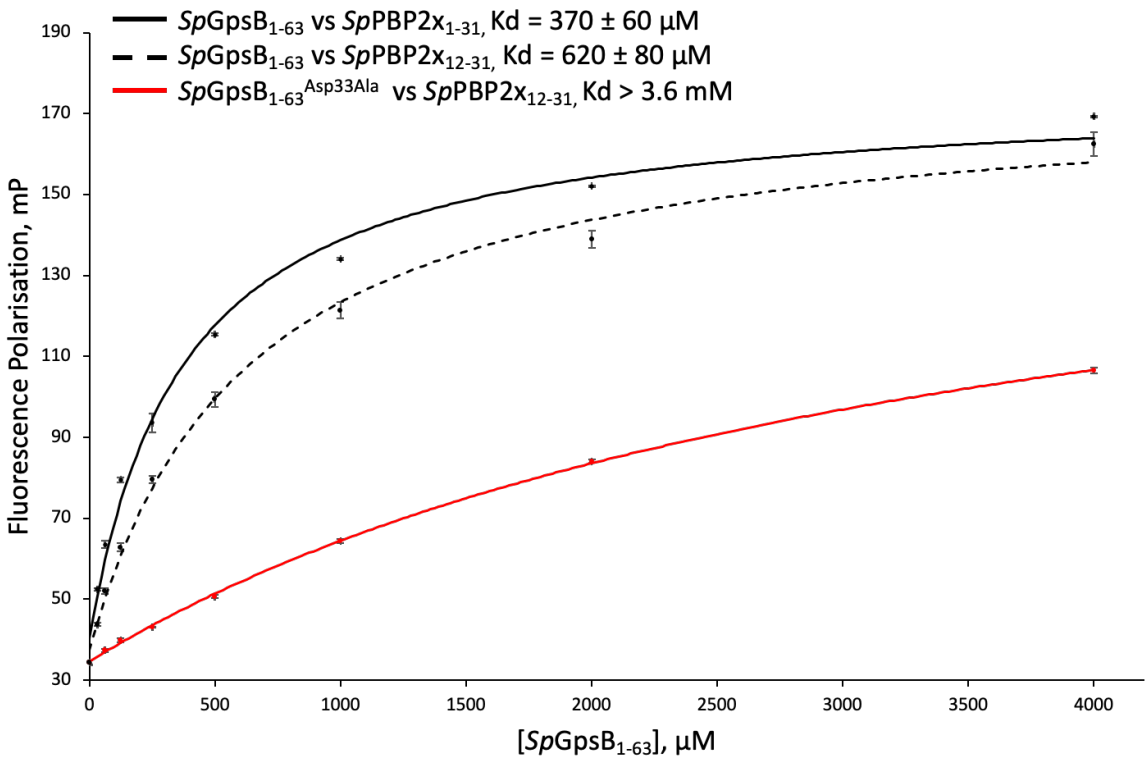

Figure 3.24: Interaction of the cytoplasmic domain peptide of *Sp*PBP2x with the N-terminal domain of GpsB.
The interaction of TAMRA-labelled *Sp*PBP2x$_{1-31}$ and *Sp*PBP2x$_{12-31}$ peptides with wild-type N-terminal domain of GpsB from *S. pneumoniae* (*Sp*GpsB$_{1-63}$) and the mutant *Sp*GpsB$_{1-63}^{Asp33Ala}$, monitored by fluorescence polarisation. Data and the fit of the data to a 1:1 binding model in Sigma plot for each of the data sets are shown. The average of three measurements and the standard error bars for each data point are shown. The key shows which data set is represented by colouring and states the respective Kd that was determined in Sigma plot.

3.10 Co-crystallisation of the *Sp*GpsB N-terminal domain with a *Sp*PBP2x cytoplasmic domain peptide

3.10.1 Crystallisation trials of *Sp*GpsB$_{4-63}$:*Sp*PBP2x$_{13-28}$

Co-crystallisation attempts of *Sp*GpsB with *Sp*PBP2x were carried out by combining *Sp*GpsB$_{4-63}$ (at a final concentration of 20 mg/mL) with *Sp*PBP2x$_{13-28}$ (25 mg/mL final; 1:5 molar ratio of protein:peptide) and subjecting the mix to sparse matrix crystallisation screening. Crystals grew in two conditions, JCSG+ D7 (0.2 M lithium sulphate, 0.1 M Tris pH 8.5 and 40 % v/v PEG 400) and JCSG+ C11 (0.1 M sodium acetate pH 4.6 and 2 M ammonium sulphate). Crystals from JCSG+ D7 were parallelepipedal and crystals from C11 grew as plates (Figure 3.25). Crystals were transferred to a drop of the well solution containing 2.5 mg/mL of *Sp*PBP2x$_{13-28}$

peptide and 20 % PEG 400 for JCSG+ C11. After 30 seconds the crystals were mounted in rayon loops and cryo-cooled in liquid nitrogen.

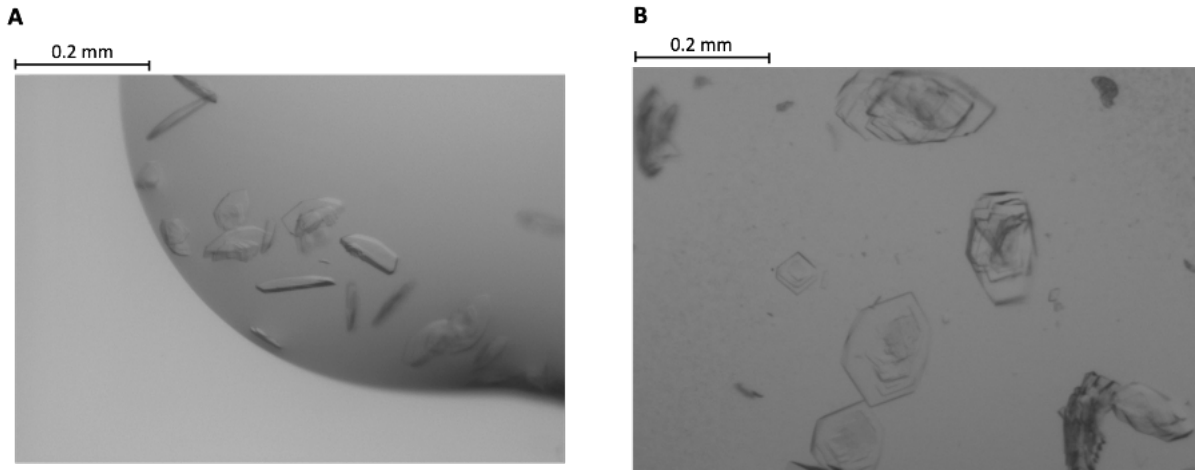

Figure 3.25: Crystals of *Sp*GpsB$_{4-63}$:*Sp*PBP2x$_{13-28}$.
Panel **A** is a drop from JCSG+ D7 and panel **B** is a drop from JCSG+ C11 in which crystals grew from *Sp*GpsB$_{4-63}$:*Sp*PBP2x$_{13-28}$. The scale bar above each image provide a visual indication of the size of each crystal.

3.10.2 Data processing, molecular replacement and model building

Data were collected at Diamond Light Source I24. Crystals from JCSG+ D7 diffracted to 1.8 Å and crystals from JCSG+ C11 diffracted to 4 Å. Diffraction data were processed, and the structure of *Sp*GpsB$_{4-63}$:*Sp*PBP2x$_{13-28}$ was solved by molecular replacement, as described in Chapter 2, using the dataset collected from the crystal grown in JCSG+ D7 and the co-ordinates of *Sp*GpsB$_{4-63}$ as the search model. Each *Sp*PBP2x molecule was manually built into the electron density using COOT (Emsley et al., 2010), and the structure was refined until convergence.

3.10.3 Analysis of the *Sp*GpsB$_{4-63}$:*Sp*PBP2x$_{13-28}$ structure

The *Sp*GpsB$_{4-63}$:*Sp*PBP2x$_{13-28}$ structure contained two molecules in the asymmetric unit and there was visible electron density in both of the *Sp*PBP2x binding sites in *Sp*GpsB (Figure 3.26 A). This electron density was sufficient to build an 8-residue peptide (spanning residues 20-27) into binding site 1 (Figure 3.27 A) and a dipeptide into binding site 2 (Figure 3.27 C).

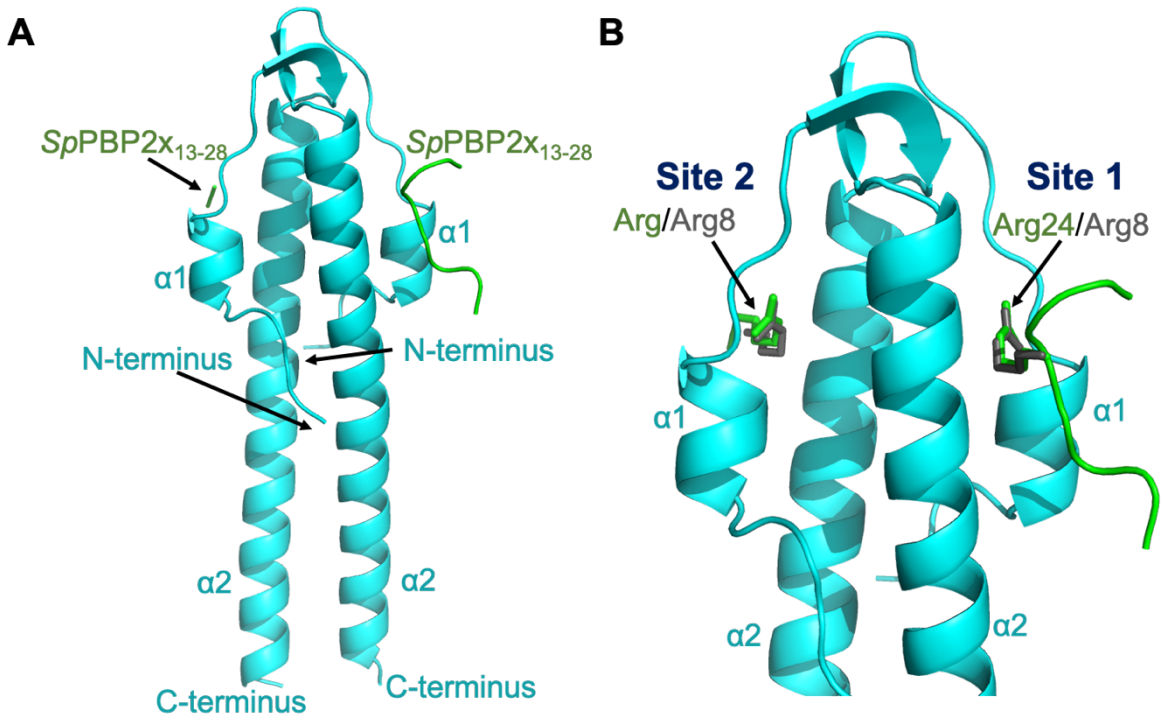

Figure 3.26: Structure of the N-terminal domain of *Sp*GpsB bound to residues 13-28 of *Sp*PBP2x.
(**A** and **C**) Zoomed-in view of binding site 1 (**A**) and binding site 2 (**C**) looking down at helix 1 and 2. *Sp*PBP2x peptides are shown as sticks and the electron density map is represented by a grey mesh. The map shown is the final Refmac-weighted $2mF_{obs}$-DF_{calc} map contoured at 0.22 electrons per $Å^3$ with a PyMol 'carve' of 1.6. (**B** and **D)** Residues important in binding are shown as sticks coloured by atom, for binding site 1 (**B**) and binding site 2 (**D**). Salt bridges and hydrogen bonds are represented by dashed black lines, van der Waals' interactions by dashed yellow lines and intra-molecular interactions by a dashed red line.

Residues 24-27 of *Sp*PBP2x in binding site 1 form a type II beta turn stabilised by an interaction between the carbonyl oxygen of Arg24 and the backbone amide of Lys27 (Figure 3.27 B). In binding site 1, Arg24 of *Sp*PBP2x was bound in the same site as Arg8 in *Bs*GpsB$_{5-64}$:*Bs*PBP1$_{1-17}$ and *Bs*GpsB$_{5-64}^{Lys32Glu}$:*Lm*PBPA1$_{1-15}$ and Arg31/33 in *Sp*GpsB$_{4-63}$:*Sp*PBP2a$_{27-40}$ (Figure 3.26 B), forming a similar set of interactions with GpsB (Figure 3.27 B). The identity of the coordinated arginine residue in binding site 2 could not be determined due to the lack of peptide that could be confidently built into the electron density. This arginine is bound in the same site as the central arginine residues in the other GpsB:PBP structures (Figure 3.26 B), coordinated in a similar fashion by GpsB (Figure 3.27 D). In binding site 1 with an 8 residue peptide built, there was not a second arginine residue binding near the carbonyl oxygens of *Sp*GpsB residues 11-14 like seen with *Bs*GpsB$_{5-64}$:*Bs*PBP1$_{1-17}$ (Figure 1.15 F) and *Sp*GpsB$_{4-63}$:*Sp*PBP2a$_{27-40}$ (Figure 3.17). *Sp*PBP2x has a lower hydrogen binding capacity at this site and this supported the observation from FP that *Sp*PBP2x had a weaker affinity for GpsB than the other PBP peptides

studied. A second arginine residue of *Sp*PBP2x, Arg22, forms a salt bridge with *Sp*GpsB Glu40 (Figure 3.27 B) which is comparable to the interaction seen between *Sp*GpsB Glu40 and *Sp*PBP2a Arg31 in binding site 1 of *Sp*GpsB$_{4\text{-}63}$:*Sp*PBP2a$_{27\text{-}40}$ (Figure 3.17 B). *Sp*PBP2x^{Asn21} is pointed away from the binding interface and does not make any direct contacts with *Sp*GpsB (Figure 3.27 B).

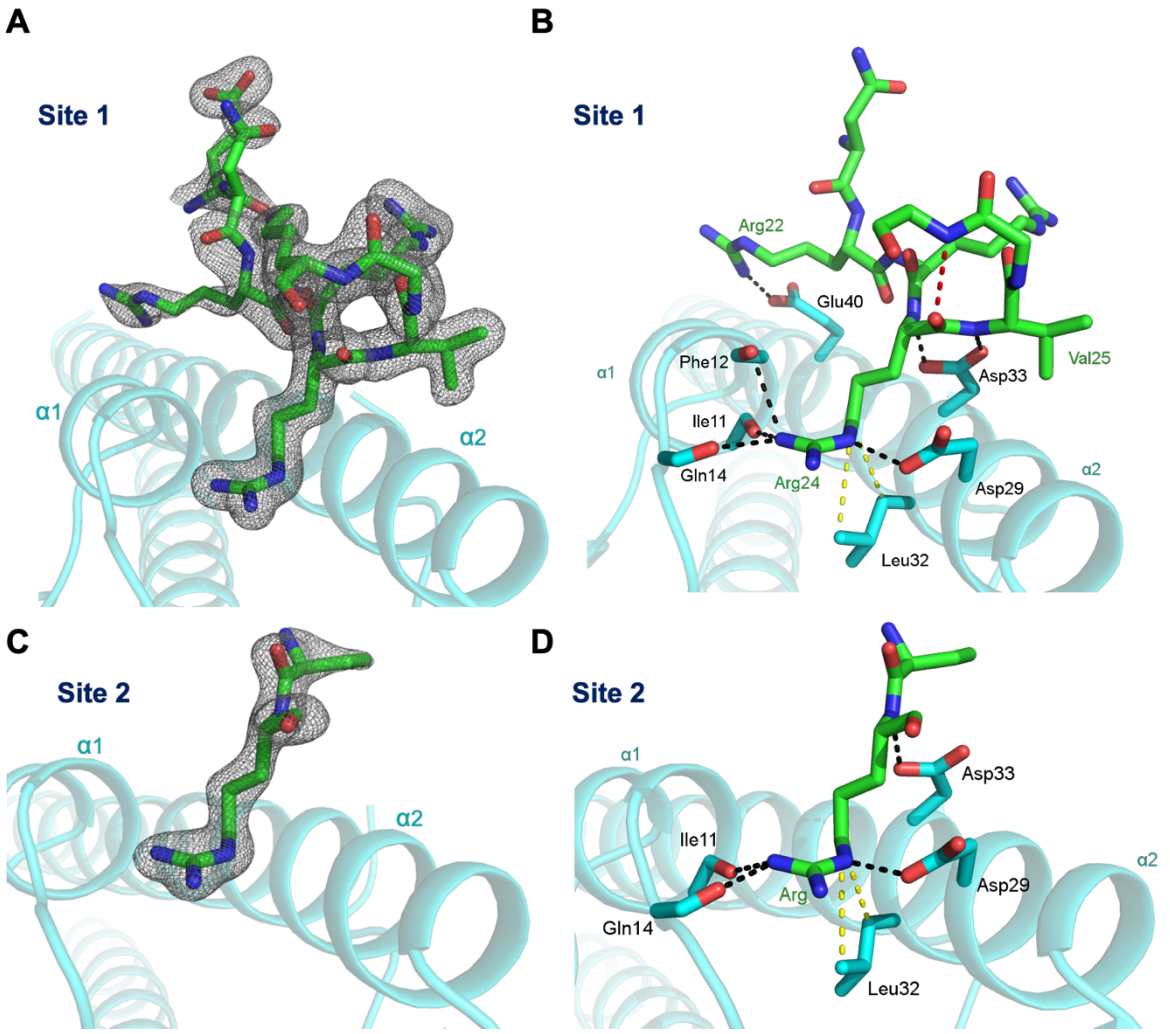

Figure 3.27: Structure of the N-terminal domain of *Sp*GpsB bound to residues 13-28 of *Sp*PBP2x.
(**A** and **C**) Zoomed-in view of binding site 1 (**A**) and binding site 2 (**C**) looking down at helix 1 and 2. *Sp*PBP2x peptides are shown as sticks and the electron density map is represented by a grey mesh. The map shown is the final Refmac-weighted 2mF_{obs}-DF_{calc} map contoured at 0.22 electrons per Å^3 with a PyMol 'carve' of 1.6. (**B** and **D)** Residues important in binding are shown as sticks coloured by atom, for binding site 1 (**B**) and binding site 2 (**D**). Salt bridges and hydrogen bonds are represented by dashed black lines, van der Waals' interactions by dashed yellow lines and intra-molecular interactions by a dashed red line.

3.11 Important features of the *Sp*PBP2x cytoplasmic domain peptide for binding the *Sp*GpsB N-terminal domain

The effect of arginine to lysine mutations, alongside an Asn21Ala mutation of *Sp*PBP2x, in binding to *Sp*GpsB was probed using fluorescence polarisation, since it had been reported previously that Asn21 and Arg22 are required for function (Berg et al., 2014) (Figure 3.28). *Sp*PBP2x$_{12\text{-}31}^{Asn21Ala}$ and *Sp*PBP2x$_{12\text{-}31}^{Asn21AlaArg22Lys}$ decreased the affinity for *Sp*GpsB$_{1\text{-}63}$ less than 2-fold compared to the WT peptide, whereas *Sp*PBP2x$_{12\text{-}31}^{Asn21AlaArg24Lys}$ and *Sp*PBP2x$_{12\text{-}31}^{Asn21AlaArg22LysArg23LysArg24Lys}$ each had more than 4-fold decreases in affinity. This supported the interaction observed by crystallography that Arg24 is the central arginine residue in the binding of *Sp*PBP2x to *Sp*GpsB. However, whilst Asn21 might be important in the function of *Sp*PBP2x *in vivo* it is not essential for the binding of *Sp*PBP2x$_{12\text{-}31}$ to *Sp*GpsB$_{4\text{-}63}$ *in vitro*.

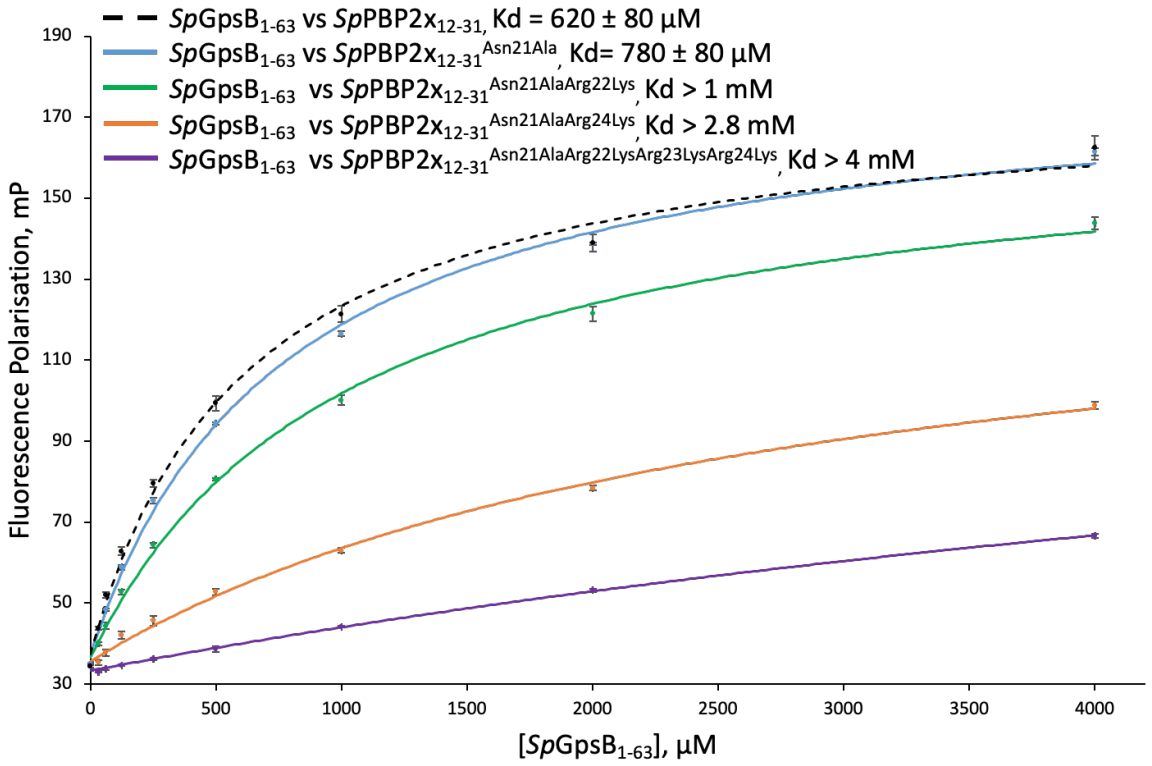

Figure 3.28: Interaction of *Sp*PBP2x$_{12\text{-}31}$ mutants with *Sp*GpsB$_{1\text{-}63}$.
The binding of wild-type *Sp*PBP2x$_{12\text{-}31}$ and binding mutants with *Sp*GpsB$_{1\text{-}63}$, monitored by fluorescence polarisation. Data and the fit of the data to a 1:1 binding model in Sigma plot for each of the data sets are shown. The average of three measurements and the standard error bars for each data point are shown. The key shows which data set is represented by colouring and states the respective Kd that was determined in Sigma plot.

3.12 Secondary structure analysis of cytoplasmic domain peptides by circular dichroism

The secondary structures of *Lm*PBPA1$_{1\text{-}15}$, *Sp*PBP2a$_{27\text{-}40}$ and *Sp*PBP2x$_{13\text{-}28}$ were determined using CD (Figure 3.29 A). Each of the cytoplasmic mini-domains contained secondary structure as the traces did not resemble disordered peptides. The predicted secondary structure composition of each of the peptides was determined using beStsel (Micsonai et al., 2018) (Figure 3.29 B). For each peptide around 50 % of the peptide fell under the category 'Others' which is composed of: 3,10-helix, π-helix, β-bridge, bend, loop and invisible regions in the three-dimensional structure. The second highest structural element for each peptide was antiparallel which ranged from 32-38 %. Putting together this data with the structural and functional data it is apparent that secondary structural elements are important in PBPs for binding to GpsB. The backbone torsion angles of *Lm*PBPA1^{Arg8} in the *Bs*GpsB$_{5\text{-}64}{}^{lys32Glu}$:*Lm*PBPA1$_{1\text{-}15}$ structure were consistent with a residue in an alpha-helix and disruption of this helix negatively impacted the binding. An alpha-helical conformational was not required for *Sp*PBP2a and *Sp*PBP2x to bind to *Sp*GpsB, but the key arginine residues formed either a single turn alpha-helix (*Sp*PBP2a), a type I beta turn (*Sp*PBP2a) or a type II beta turn (*Sp*PBP2x). These secondary structural elements are key to positioning the binding PBP residues in the GpsB binding site.

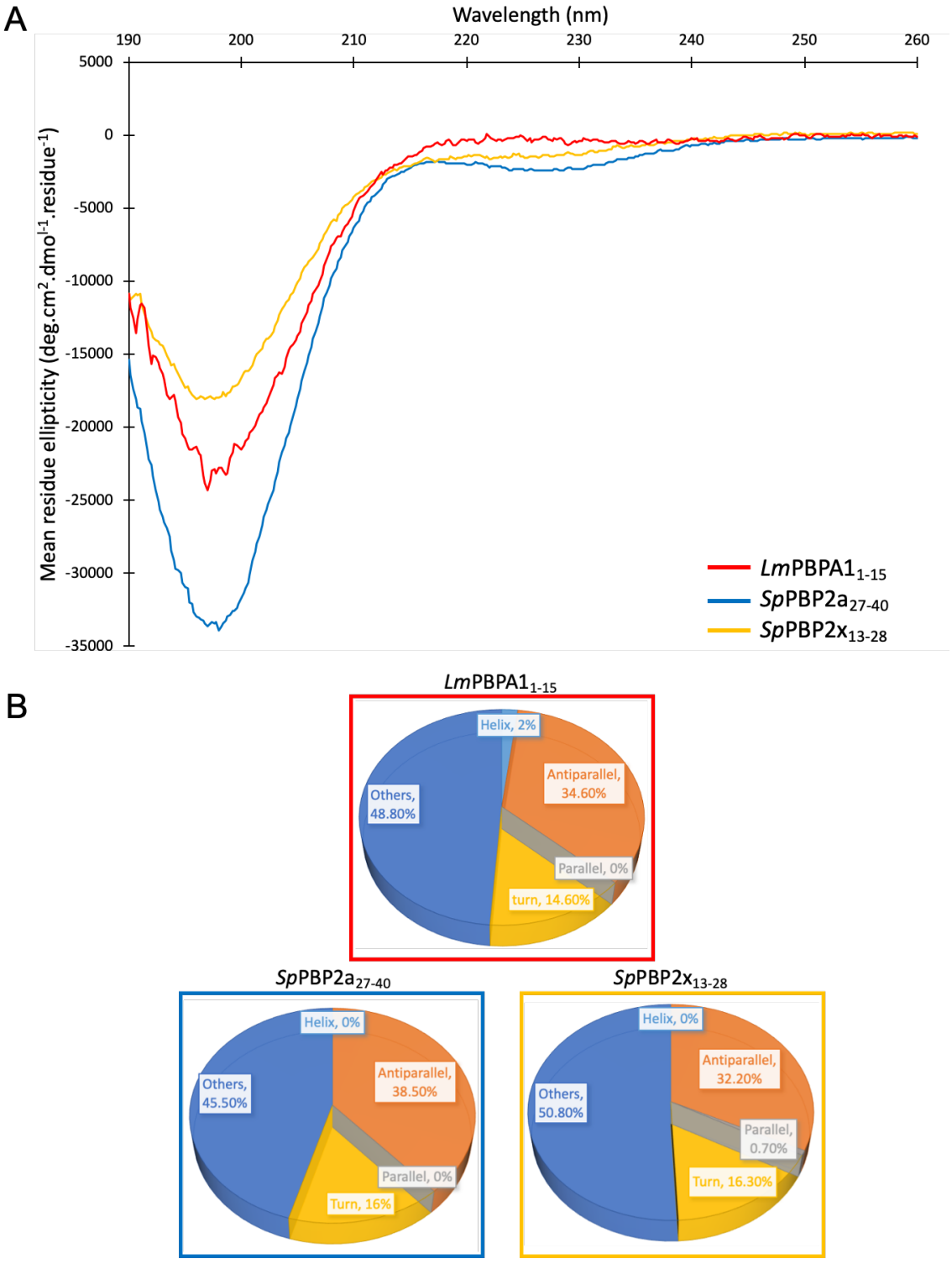

Figure 3.29: Secondary structure determination of cytoplasmic domain PBP peptides.
A. Circular dichroism spectra of the cytoplasmic domain peptides of *Lm*PBPA1, *Sp*PBP2a and *Sp*PBP2x. These data were analysed using BeStsel (Micsonai et al., 2018) and CD spectra were converted from millidegrees to mean residue ellipticity. Shown here are the experimental data and the key indicates which data set is represented on the graph. **B.** Secondary structure prediction of each of the peptides determined by BeStsel (Micsonai et al., 2018) from the CD spectra. The percentage of each element is displayed in a pie chart.

3.13 Summary

Recent work on *B. subtilis* GpsB and its interaction with the class A PBP1, including the structure of *Bs*GpsB$_{5-64}$:*Bs*PBP1$_{1-17}$, has supported the hypothesis that GpsB regulates cell division though interactions with the positively charged cytoplasmic domain motifs in PBPs (Cleverley et al., 2019). In this study, the crystal structures of GpsB in complex with PBPs were solved from 2 pathogenic organisms, *L. monocytogenes* in which GpsB is important during stress (Rismondo et al., 2016), and *S. pneumoniae* where GpsB is essential (Land et al., 2013).

In each case, as with *Bs*GpsB$_{5-64}$:*Bs*PBP1$_{1-17}$, no more than 3 residues from the PBP are required for binding to GpsB. Of these residues, a single positively charged arginine residue pokes into a negatively charged groove between the two alpha-helices of a GpsB monomer. In each structure this arginine residue is fixed in the same orientation and forms a similar set of interactions with GpsB (Figure 3.6, Figure 3.17 and Figure 3.27). It was observed by fluorescence polarisation that mutating this arginine residue in *Lm*PBPA1 (*Lm*PBPA1^{Arg8Ala}) significantly reduced the affinity of the peptide for *Lm*GpsB (Figure 3.7). Two binding modes of *Sp*PBP2a were observed in which either Arg31 or Arg33 can act as the central arginine residue. The double mutation of both of these arginine residues, *Sp*PBP2a^{Arg31LysArg33Lys}, gave a comparable reduction in affinity to GpsB as *Lm*PBPA1^{Arg8Ala} (Figure 3.20). The multiple binding modes of *Sp*PBP2a may suggest why it has a stronger affinity for GpsB than the other 3 peptides.

GpsB binding to PBP peptides is favoured by secondary structural environments that simultaneously stabilise the torsion angles at an arginine residue and yet ensure nearby main chain amide protons are accessible for forming intermolecular hydrogen bonds with GpsB. In *Bs*PBP1, *Lm*PBPA1 and in one binding mode of *Sp*PBP2a, the arginine residue is required to be in an alpha-helical conformation. In the second binding mode of *Sp*PBP2a and in *Sp*PBP2x the arginine residue is in a beta turn. The binding of *Bs*PBP1 and *Sp*PBP2a involves a second arginine residue making key contacts in the binding groove, *Bs*PBP1^{Arg11} and *Sp*PBP2a$^{Arg33/Arg36}$ (Figure 1.15 F and Figure 3.17). The reduction in affinity seen with *Lm*PBPA1$_{1-20}{}^{Arg12Ala}$ (Figure 3.7) could suggest that this is the second arginine residue to bind alongside Arg8, however, this could not be confirmed due to the lack of ordered peptide in the crystal structure.

This work represents the first demonstration of a specific interaction between the cytoplasmic domain of *S. pneumoniae* PBP2x and GpsB (Figure 3.24). Although further work will be

required to clarify how prominent this is *in vivo,* even a transient interaction between these two proteins could explain the previous observation that depletion of GpsB impacts the localisation of PBP2x during cell division (Rued et al., 2017).

There are a conserved set of GpsB residues required for PBP binding: Tyr25, Asp31 and Asp35 in *B. subtilis* (Tyr27/Asp33/Asp37 in *L. monocytogenes* and Tyr23/Asp29/Asp33 in *S. pneumoniae*) (Figure 1.15 F and Figure 3.17) (Cleverley et al., 2019). *L. monocytogenes* cells with mutations in these residues show growth defects and in *S. pneumoniae* these mutations are lethal (Cleverley et al., 2019). So far *Lm*GpsB^{Asp37} and *Sp*GpsB^{Asp33} have been shown to be important, specifically in the binding of PBPs were they form interactions with the mainchain amide of the central arginine residue and its downstream residue. *Lm*GpsB^{Asp33} and *Sp*GpsB^{Asp29} are important for both PBP binding and also other proteins, such as MreC. BACTH screens showed reduced binding of *Lm*GpsB^{Asp33} and *Sp*GpsB^{Asp29} mutants with MreC, however *Lm*GpsB^{Asp37} and *Sp*GpsB^{Asp33} mutants bound to MreC like WT (Cleverley et al., 2019). This data suggests that different surfaces are used by GpsB to bind to PBPs and MreC.

L. monocytogenes has increased sensitivity to fosfomycin *in vivo* with *Lm*PBPA1^{Arg8AlaArg12Ala} and *Lm*PBPA1^{Glu10Pro} mutants when *Lm*PBP2A is also absent (Cleverley et al., 2019). In *S. pneumoniae* there was no observed defect when arginine residues alone were mutated even though there was a large reduction in affinity to GpsB *in vitro*. Reduced growth rates were, however, seen in *Δpbp1a* strains with *Sp*PBP2a lacking residues 32-37, 27-38 or 26-45 (Cleverley et al., 2019). An explanation for this could be that without the critical arginine residues there are other, less-well conserved positively-charged residues around the binding core, including the PBP juxtamembrane region. These residues could contribute to affinity, meaning that larger stretches of amino acids need to be deleted to inhibit the interaction with GpsB. The mutation of the cytoplasmic domain of PBP2a does not resemble the phenotype of a GpsB depletion in *S. pneumoniae*, however, and nor does a *pbpA1* deletion phenocopy a *gpsB* deletion in *L. monocytogenes* (Cleverley et al., 2019). This indicates that there must be another GpsB-dependent interaction occurring that leads to the more severe phenotype with a GpsB deletion/depletion compared to that associated with PBP disruption.

	***Bs*GpsB$_{5-64}^{Lys32Glu}$:*Lm*PBPA1$_{1-15}$**	**Unbound *Sp*GpsB$_{4-63}$**	***Sp*GpsB$_{4-63}$:*Sp*PBP2a$_{27-40}$**	***Sp*GpsB$_{4-63}$:*Sp*PBP2x$_{13-28}$**
Data Statistics*				
Beamline	Diamond I04	Gallium METALJET™	Diamond I03	Diamond I24
Date	20/01/17	31/08/17	15/10/17	09/12/17
Wavelength (Å)	0.9795	1.35	0.9762	0.9787
Resolution (Å)	31.42-1.6 (1.63-1.6)	27.22-1.9 (1.94-1.9)	39.85-1.8 (1.84-1.8)	66.5-1.8 (1.84-1.8)
Rpim	0.044 (0.386)	0.041 (0.311)	0.051 (0.269)	0.051 (0.230)
Space group	*P* 1 2_1 1	*P* 1 2_1 1	*C* 1 2 1	*P* 2_1 2_1 2_1
Unit-cell parameters				
a (Å)	26.6	39.1	83.1	32.2
b (Å)	31.4	54.5	26.4	33.2
c (Å)	81.0	61.6	65.9	133.0
α - β - γ (°)	90-92.4-90	90-106.1-90	90-106.4-90	90-90-90
Solvent content (%)	41.6	42.8	49.0	50.0
No. of measured reflections	63406 (3019)	497944 (28050)	46904 (2454)	83894 (5059)
No. of independent reflections	17944 (902)	19776 (1353)	13052 (763)	13950 (798)
Completeness (%)	99.8 (99.9)	100 (100)	99.8 (99.9)	100 (100)
Redundancy	3.5 (3.3)	25.2 (20.7)	3.6 (3.2)	6.2 (6.0)
CC1/2 (%)	99.7 (74.3)	99.8 (78)	97.6 (88.3)	99.5 (80.6)
<I>/<σ(I)>	8.4 (1.8)	13.9 (4.0)	9 (2.2)	9 (3.2)
Refinement Statistics*				
R_{work}	0.173	0.188	0.178	0.193
R_{free}	0.204	0.249	0.225	0.225
No. of non-H atoms:				
Protein	986	1919	999	981
Peptide	20	-	220	87
Ligand/ion	5/8	-	30/1	5
Water	106	260	87	131
R.m.s. deviation from ideal values				
Bond angle (°)	1.372	1.399	1.393	1.435
Bond length (Å)	0.016	0.0170	0.015	0.007
Average B factor (Å²)				
Protein	25.2	24.8	18.7	20.8
Peptide	36.0	-	32.5	34.1
Ligand/ion	30.9/36.5	-	57.9/12.1	27.3
Water	35.6	30.6	28.1	31.9

**Values in parenthesis are for the highest resolution shell*

Table 3.1: Data statistics and refinement details

	JCSG+ D6	Morpheus E7	JCSG+ C11	Morpheus F9	PACT D11
Data Statistics					
Beamline	Gallium METALJET™	I24	I24	I24	I24
Date	31/08/17				
Wavelength (Å)	1.35	0.97958	0.97888	0.97889	0.97888
Resolution (Å)	27.22-1.9 (1.94-1.9)	54.28 -2.3 (2.38-2.3)	42.98-2.8 (2.95-2.8)	67.43-2.9 (3.08-2.9)	56.53-3.1 (3.31-3.1)
Rpim	0.041 (0.311)	0.0064 (0.084)	0.245 (2.136)	0.156 (0.588)	0.129 (0.414)
Space group	$P\ 1\ 2_1\ 1$	$I\ 1\ 2\ 1$	$C\ 2\ 2\ 2_1$	$P\ 2_1\ 2_1\ 2_1$	$P\ 1\ 2_1\ 1$
Unit-cell parameters					
a (Å)	39.1	57.9	33.4	44.6	37.3
b (Å)	54.5	33.3	171.9	90.3	56.5
c (Å)	61.6	91.1	46.8	101.5	111.9
α - β - γ (°)	90-106.1-90	90-106.2-90	90-90-90	90-90-90	90-90-90
Solvent content (%)	42.8	58.0	47.4	47.7	39.6
No. of measured reflections	497944 (28050)	26684 (2798)	23752 (3389)	66344 (10337)	31128 (5631)
No. of independent reflections	19776 (1353)	7589 (754)	3593 (492)	9537 (1496)	8612 (1541)
Completeness (%)	100 (100)	99.7 (99.5)	100 (100)	99.6 (99.0)	99.9 (99.9)
Redundancy	25.2 (20.7)	3.5 (3.7)	6.6 (6.9)	7 (6.9)	3.6 (3.7)
CC1/2 (%)	99.8 (78)	98.4 (95.5)	96.4 (17.1)	97.7 (65.4)	98.8 (61.4)
<I>/<σ(I)>	13.9 (4.0)	9.1 (6.9)	3 (1.6)	3.3 (1.4)	3.8 (1.4)
Refinement Statistics					
R_{work}	0.19	0.26	0.38	0.27	0.31
R_{free}	0.25	0.34	0.41	0.33	0.39
No. of non-H atoms					
Protein	1919	985	1014	3013	7772
Water	260				
R.m.s. deviation from ideal values					
Bond angle (°)	1.399	1.525	1.412	1.527	1.422
Bond length (Å)	0.0170	0.0145	0.0113	0.0122	0.0050
Average B factor (Å²)					
Protein	24.8	20.14	62.70	57.7	74.94
Water	30.6				

**Values in parenthesis are for the highest resolution shell*

Table 3.2: Data statistics and refinement details for *Sp*GpsB$_{4-63}$

Chapter 4: Functional Divergence Between DivIVA and GpsB

4.1 Introduction

DivIVA and GpsB are both important cytosolic proteins involved in regulating the cell division of Gram-positive bacteria. It was initially demonstrated that GpsB is required for the cellular localisation of PBP1 in *B. subtilis*, coordinating the activity of this PG synthase (Claessen et al., 2008). DivIVA is thought to play a similar role as GpsB in division, associating with the divisome to act as a scaffold for the localisation of division proteins (Fadda et al., 2007; Oliva et al., 2010). Both proteins have been linked to the elongation stage of the cell-cycle; GpsB has been shown to interact with the elongation factor MreC in a range of Gram-positives by BACTH and co-immunoprecipitation (Claessen et al., 2008; Rued et al., 2017; Cleverley et al., 2019) and elongation is hindered in *S. pneumoniae* lacking DivIVA (Fleurie et al., 2014a). GpsB was discovered by sequence comparisons and phylogenetic analysis with DivIVA (Tavares et al., 2008). Since then, the two proteins have been studied extensively to determine if there is a relationship or overlapping function in cell division (Halbedel & Lewis, 2019; Hammond et al., 2019). Both proteins are highly conserved in Gram-positive bacteria and localisation studies have revealed some similarities and differences between GpsB and DivIVA: the latter localised to the poles and septal regions in *S. pneumoniae* (Fadda et al., 2007), and was shown to be targeted to negatively curved membranes in *B. subtilis*, where it accumulated (Lenarcic et al., 2009). Unlike DivIVA, GpsB shuttled between the lateral cell wall and the division septum during the cell-cycle and did not accumulate at negatively curved membranes (Claessen et al., 2008). GpsB and DivIVA have been shown to localise independently of each other in *B. subtilis*, and they associate simultaneously with the divisome at the later stages of the division cycle (Tavares et al., 2008; Gamba et al., 2009).

Both DivIVA and GpsB are composed of two main domains with varying levels of sequence conservation (Figure 4.1). Their N-terminal domains are highly homologous in structure, sharing the same coiled-coil dimer arrangement of alpha helices (Oliva et al., 2010; Rismondo et al., 2016). The DivIVA N-terminal domain functions as the lipid binding domain to bind to negatively curved membranes (Lenarcic et al., 2009), which is mediated by hydrophobic amino acids in the loop region (Oliva et al., 2010). The N-terminal domain of GpsB is important for membrane association and binding to the cytoplasmic mini-domains of peptidoglycan synthases (Rismondo et al., 2016; Cleverley et al., 2019). A number of residues are conserved

in the N-terminal domains of GpsB and DivIVA proteins (Figure 4.1 A). They both possess a conserved hydrophobic-arginine pair in their N-terminal domains required for membrane association as well as numerous conserved amino acids in the hydrophobic face of the coiled-coil dimer (Oliva et al., 2010; Rismondo et al., 2016; Halbedel & Lewis, 2019). Val25, Phe28 and Leu36 of *Bs*DivIVA are the most well conserved hydrophobic residues in the core of the helical bundle across GpsB and DivIVA proteins. The essential PBP binding residues of *Bs*GpsB Try25, Asp31, Asp35 and Ile38 are highly conserved across GpsB proteins compared to DivIVA in the *Firmicute* phylum. The C-terminal domains of GpsB and DivIVA differ markedly; while the GpsB C-terminal domain is a parallel trimer of short helices (Rismondo et al., 2016), the equivalent domain in *B. subtilis* DivIVA is an extended coiled-coil tetramer (Oliva et al., 2010). However, the C-terminal domain of DivIVA is not well conserved, and pneumococcal proteins have an additional C-terminal region compared to *B. subtilis* DivIVA, which is essential for native localisation in *S. pneumoniae* (Straume et al., 2017). Figure 4.1 B shows very little sequence conservation between GpsB and DivIVA C-terminal domains. The conserved salt bridge residues required for the formation of a GpsB C-terminal domain trimer (Rismondo et al., 2016) are not conserved in DivIVA.

GpsB and DivIVA appear to have important roles in overlapping areas of the Gram-positive cell-cycle, however, their specific roles are distinct and DivIVA has, seemingly, different functions in various Gram-positive species. This chapter explores the structure/function relationship of *B. subtilis* GpsB and DivIVA, specifically seeking greater understanding at the molecular level why the N-terminal domain of *Bs*GpsB can bind to *Bs*PBP1 but *Bs*DivIVA cannot. Pioneering work was performed by engineering a novel PBP binding function into *Bs*DivIVA, by targeted mutagenesis, to confirm the structural requirements of the *Bs*GpsB:*Bs*PBP1 interaction.

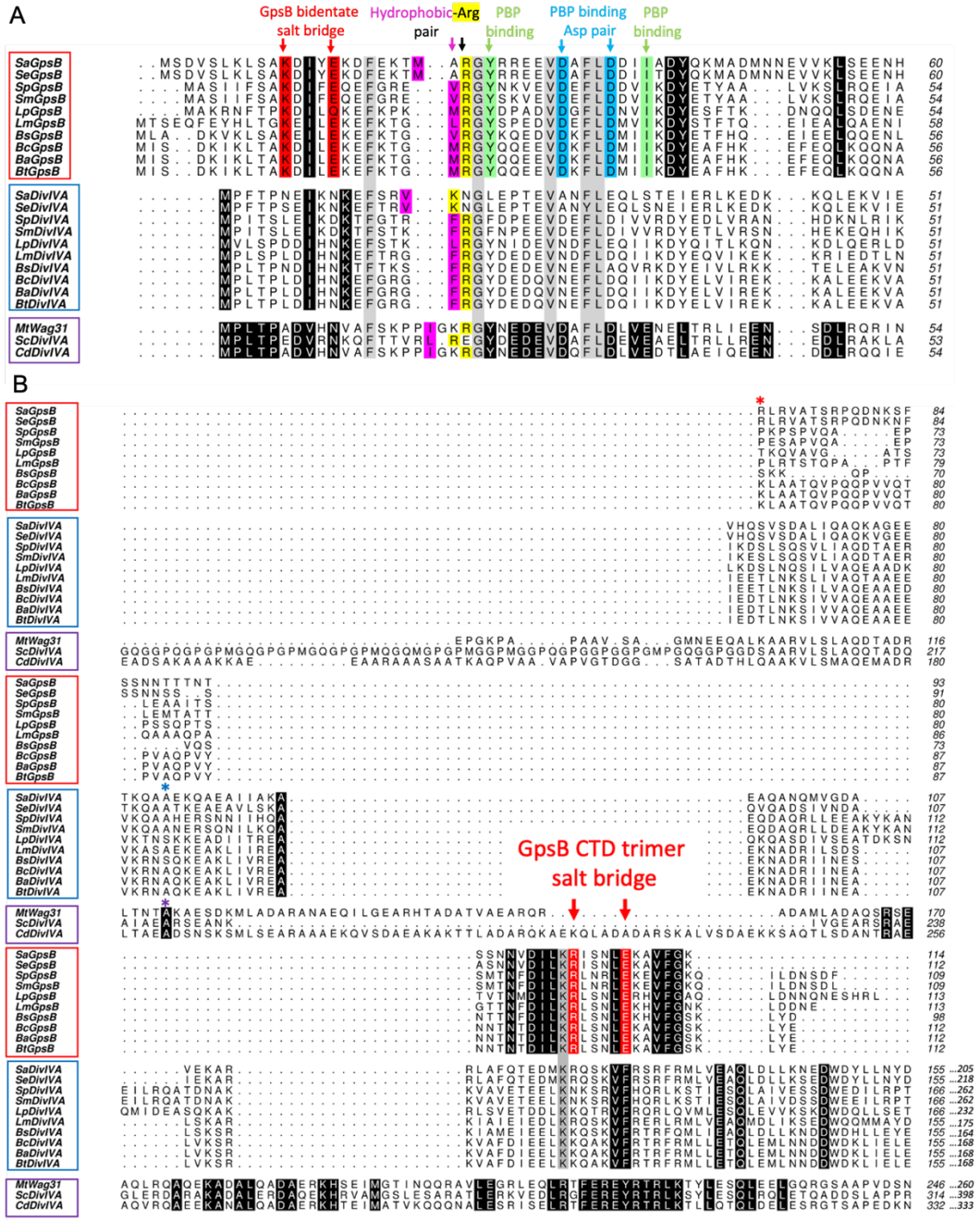

Figure 4.1: A multiple sequence alignment of GpsB and DivIVA proteins.
Panel **A** shows the sequence alignment of the N-terminal domains and panel **B** is the alignment of the overlapping C-terminal domain regions of GpsB proteins from *Firmicutes* (indicated by a red box) and DivIVA proteins from *Firmicutes* (blue box) and *Actinobacteria* (purple box). Important conserved residues are coloured and labelled. Amino acids that are conserved within a subgroup are shaded black and amino acids that are conserved across subgroups are shaded grey. In panel **B**, an asterisk indicates the start of the C-terminal domain (CTD) of each sub group. Abbreviations: *Sa, Staphylococcus aureus; Se, Staphylococcus epidermidis; Sp, Streptococcus pneumoniae; Sm, Streptococcus mitis; Lp, Lactobacillus plantarum; Lm, Listeria monocytogenes; Bs, Bacillus subtilis; Bc, Bacillus cereus; Ba, Bacillus anthracis; Bt, Bacillus thuringiensis; Mt, Mycobacterium tuberculosis; Sc, Streptomyces coelicolor; Cd, Corynebacterium diphtheriae.*

4.2 Comparison of the N-terminal domains of GpsB and DivIVA from *B. subtilis*

One of the major differences between the cell division proteins *Bs*DivIVA and *Bs*GpsB in terms of function is that *Bs*GpsB can bind to PBPs and *Bs*DivIVA cannot, even though their N-terminal domains are structural homologues that are almost indistinguishable (r.m.s.d of 0.69 Å). This near indistinguishable structural homology raises the question of how does *Bs*PBP1 thus discriminate between *Bs*GpsB and *B*sDivIVA? Fluorescence polarisation assays were used to investigate the binding of *Bs*DivIVA and *Bs*GpsB to *Bs*PBP1. These data revealed that the N-terminal domain of GpsB (*Bs*GpsB$_{1-68}$) interacted with the cytoplasmic domain of PBP1 (*Bs*PBP1$_{1-32}$) with a Kd of 150 ± 20 µM. However, the same PBP peptide did not interact with the N-terminal domain of DivIVA (*Bs*DivIVA$_{1-62}$) at all, with no evidence of saturation of binding and a ~linear increase of polarisation with protein concentration resulting in a fitted Kd > 4 mM, suggesting only non-specific binding occurred between the *Bs*PBP1 peptide and *Bs*DivIVA$_{1-62}$ (Figure 4.2).

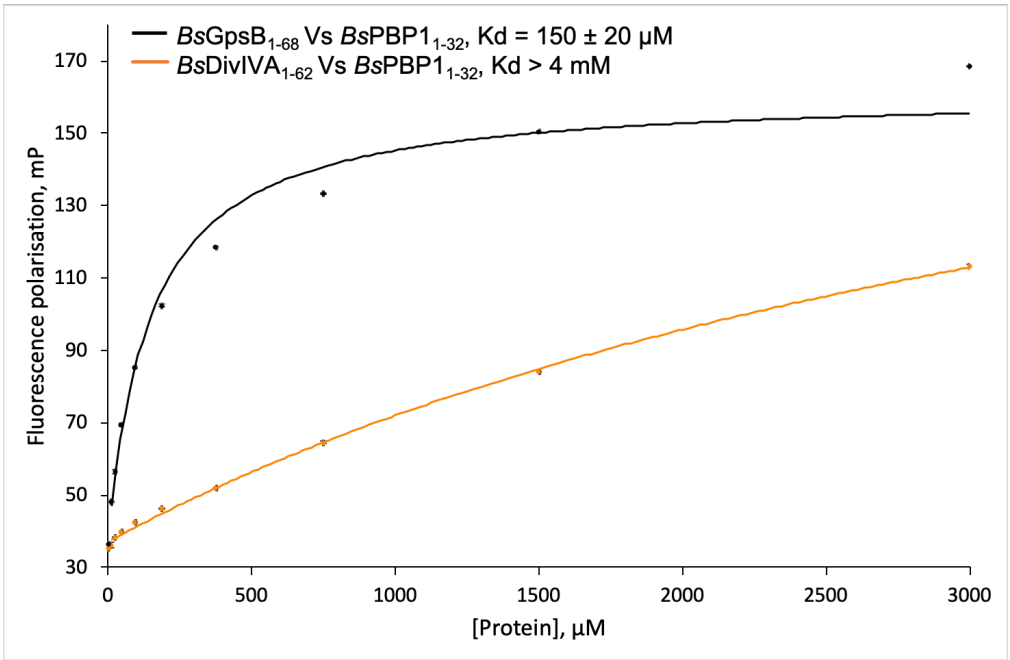

Figure 4.2: Interaction of a cytoplasmic domain peptide of *Bs*PBP1 with the N-terminal domains of *Bs*GpsB and *Bs*DivIVA.
The interaction of fluorescein-labelled *Bs*PBP1$_{1-32}$ with wild-type *Bs*GpsB$_{1-68}$ and *Bs*DivIVA$_{1-62}$, as monitored by fluorescence polarisation. Binding data and the fit of the data to a 1:1 binding model in Sigma plot for each of the data sets are plotted on the graph. The average of three technical replicates and the standard error for each data point is shown. The key shows which data set is represented by colouring and the respective Kd estimate that was determined in Sigma plot.

The N-terminal domains of *Bs*GpsB and *Bs*DivIVA share a sequence similarity of 32.1 %. GpsB proteins have a conserved pair of aspartate residues that are essential for binding to PBPs (Figure 4.1 A) (Cleverley et al., 2019); in *B. subtilis*, these residues are Asp31 and Asp35. The crystal structure of *Bs*GpsB$_{5\text{-}64}$:*Bs*PBP1$_{1\text{-}17}$ showed Asp35 formed an interaction with the backbone amides of Arg8 and Glu9 of PBP1 and Arg8 also formed a salt bridge with Asp31 (Cleverley et al., 2019) (Figure 4.3).

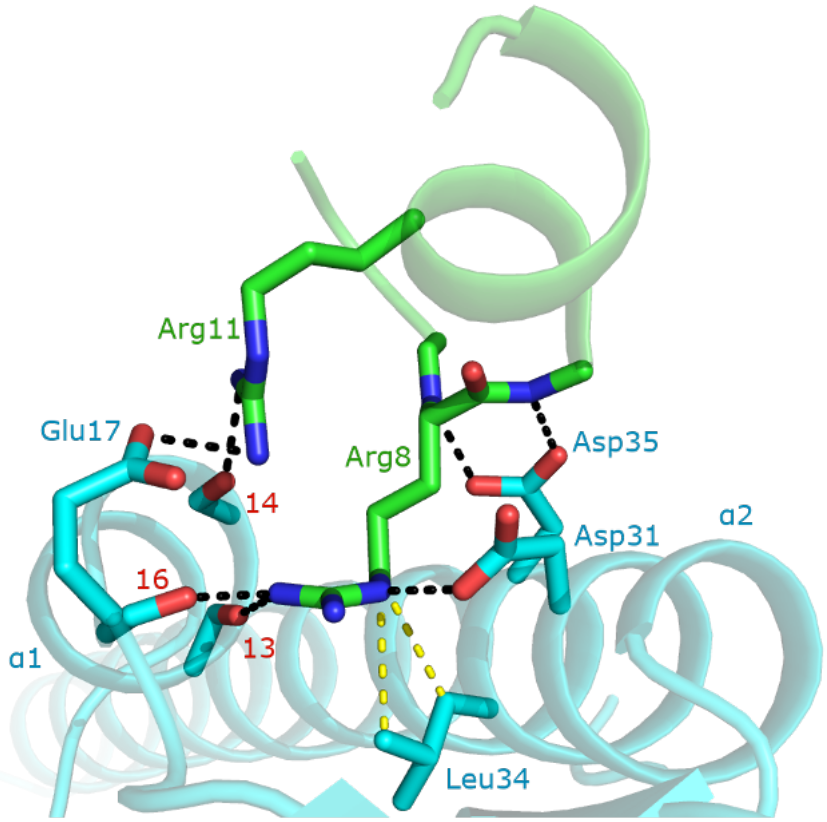

Figure 4.3: The *Bs*GpsB:*Bs*PBP1 interaction requires conserved arginines in the cytoplasmic mini-domain of *Bs*PBP1.
The formation of the *Bs*GpsB$_{5\text{-}64}$:*Bs*PBP1$_{1\text{-}17}$ complex (PDB ID: 6GP7) is dependent upon a conserved SRxxR(R/K) motif in *Bs*PBP1 (Cleverley et al., 2019). Key interfacial residues in the complex are shown in sticks and coloured and are labelled. *Bs*GpsB$_{5\text{-}64}$ is coloured in cyan and *Bs*PBP1$_{1\text{-}17}$ is coloured in green. The carbonyl oxygens of *Bs*GpsB$_{5\text{-}64}^{Ile13}$, *Bs*GpsB$_{5\text{-}64}^{Leu14}$ and *Bs*GpsB$_{5\text{-}64}^{Lys16}$ are labelled with their respective red numerals. Hydrogen bonds are shown as black dashed lines and van der Waals' interactions are shown as yellow dashed lines.

These conserved aspartate residues in GpsB are not maintained in DivIVA proteins (Figure 4.1 A) and the equivalent residues in *Bs*DivIVA are Asn26 and Ala30 (highlighted by red arrows in Figure 4.4). The first step in an attempt to introduce *Bs*PBP1 binding-function in *Bs*DivIVA was to introduce these key *Bs*GpsB aspartate residues at the equivalent positions in *Bs*DivIVA. Therefore, Asn26 and Ala30 of *Bs*DivIVA were both mutated to aspartic acid and the ability of

this double mutant to bind to *Bs*PBP1$_{1-32}$ was assessed by fluorescence polarisation. However, the *Bs*DivIVA$_{1-62}^{Asn26AspAla30Asp}$ change had no effect on the affinity measured to *Bs*PBP1$_{1-32}$ (Kd > 5mM; Figure 4.6), suggesting that the lack of binding of *Bs*DivIVA to *Bs*PBP1 was not solely due to the absence of the twin aspartates.

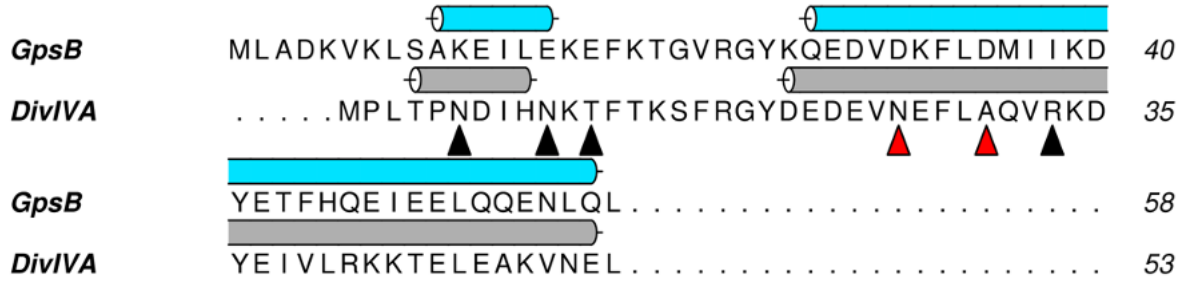

Figure 4.4: Comparison of *Bs*GpsB and *Bs*DivIVA sequences for construction of DivIVA binding mutants.
A sequence alignment of the N-terminal domains of GpsB and DivIVA from *B. subtilis.* The triangles indicate the residues in *Bs*DivIVA that were mutated to the equivalent *Bs*GpsB residue in an attempt to confer binding to *Bs*PBP1. The red triangles highlight the conserved aspartate residues in *Bs*GpsB, Asp31 and Asp35 that are essential for the binding of *Bs*PBP1. The equivalent residues in *Bs*DivIVA are Asn26 and Ala30. The N-terminal domains of *Bs*GpsB and *Bs*DivIVA contain two α-helices, the positions of these helices are shown above each sequence by a cartoon helix.

4.3 Structural differences in the N-terminal domains of GpsB and DivIVA from *B. subtilis*

Close inspection of the superimposition of the crystal structures of N-*Bs*GpsB and N-*Bs*DivIVA provides a potential explanation as to why *Bs*DivIVA cannot bind to *Bs*PBP1 (Figure 4.5). In *Bs*DivIVA the C-terminal end of helix 1 stops two amino acids before the equivalent helix in *Bs*GpsB and a loop between helix 1 and 2 protrudes somewhat into the binding site of *Bs*PBP1, where the side chain of *Bs*PBP1 Arg8 would penetrate into the groove between the two helices (Figure 4.5). There is no such blockage in *Bs*GpsB, the molecular basis of which could be explained by the conserved salt bridge between Lys11 and Glu15 that stabilises helix 1 (Figure 4.1 A). This Lys/Glu salt bridge is not conserved in DivIVA proteins; the equivalent residues in *Bs*DivIVA are Asn6 and Asn10. Another trait of *Bs*GpsB that could contribute to the binding site is the presence of the bulky amino acid Ile38 in helix 2 that packs against helix 1, constraining its position and steering the path of the main chain downstream of the helix away from the PBP binding site. In *Bs*DivIVA, the corresponding residue is Arg33, which does not have the ability to constrain helix 1. A conserved glutamate at position 17 in *Bs*GpsB is also required to form a salt bridge with Arg11 of *Bs*PBP1 as shown in the structure of the GpsB/PBP

complex (Figure 4.3). Again, this residue is not conserved in DivIVA sequences and in *Bs*DivIVA it is a threonine.

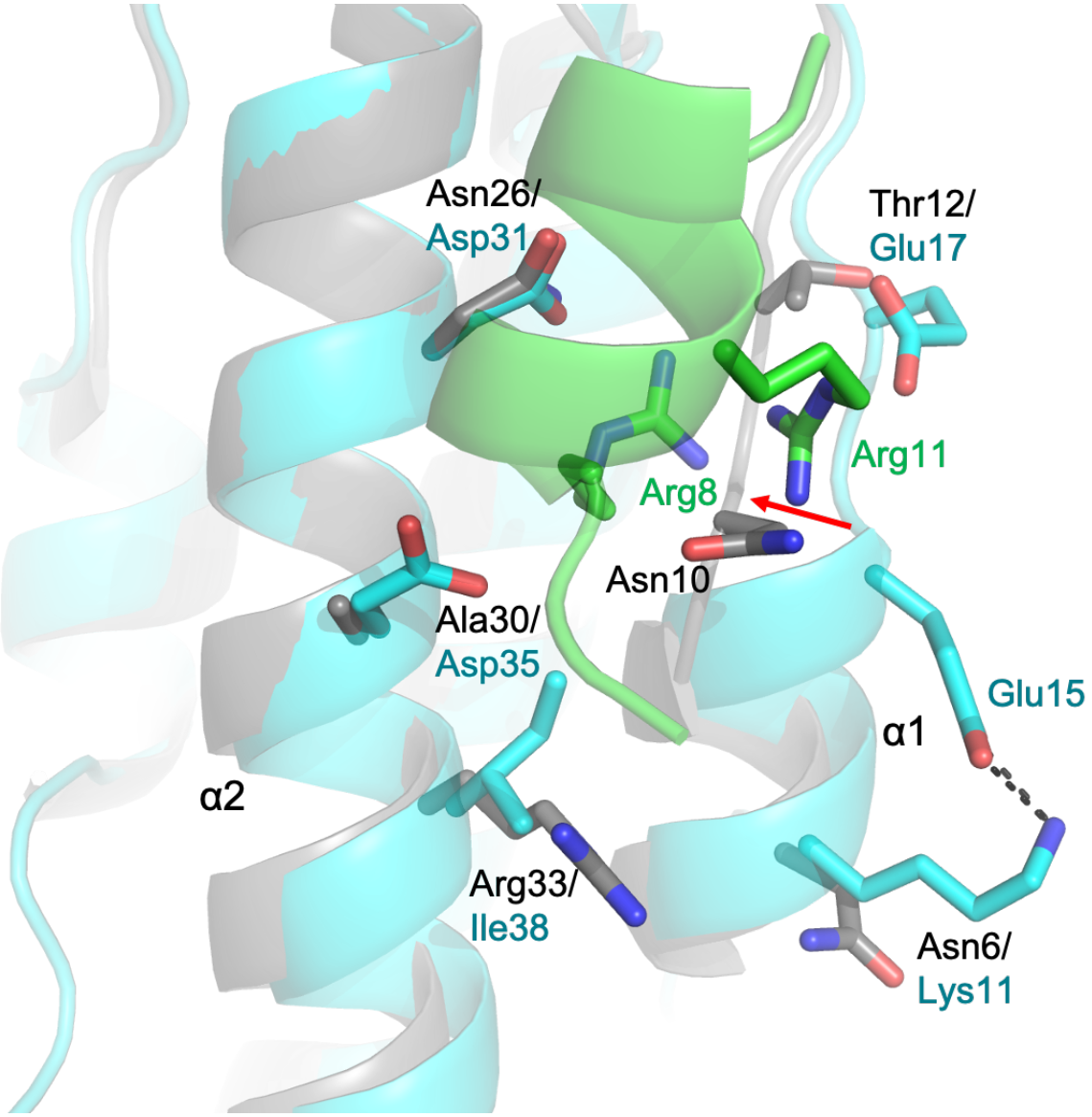

Figure 4.5: Structural differences between *Bs*GpsB and *Bs*DivIVA.
The structure of *Bs*GpsB$_{5-64}$:*Bs*PBP1$_{1-17}$ (PDB ID: 6GP7) superimposed onto *Bs*DivIVA$_{1-57}$ (PDB ID: 2WUJ). GpsB is coloured cyan, the bound *Bs*PBP1 peptide is coloured green and *Bs*DivIVA is in grey. The six *Bs*DivIVA residues and equivalent *Bs*GpsB residues to which their sequences were mutated are labelled and shown in stick form. The colouring of the labels corresponds to the structure. Arg8 and Arg11 of *Bs*PBP1 are shown in stick form to demonstrate how the loop between α1 and α2 (indicated by the red arrow) blocks the peptide binding site in *Bs*DivIVA but not in *Bs*GpsB. The black dotted lines represent the salt bridge between Lys11 and Glu15 of *Bs*GpsB.

4.4 Binding of *Bs*DivIVA mutants to *Bs*PBP1

Further mutations were made to the *Bs*DivIVA$_{1-62}^{Asn26AspAla30Asp}$ variant based on the structural analysis described in Section 3.3 in an attempt to 'open up' the engineered PBP binding site

between helix 1 and 2 of *Bs*DivIVA to enable the necessary contacts between the key aspartate residues and *Bs*PBP1. The ability of these mutants to bind to *Bs*PBP1 were also tested by fluorescence polarisation (Figure 4.6). The selected mutation sites, based on structural analysis, are highlighted in Figure 4.4 with black triangles indicating the introduced substitutions. Introducing the potential salt bridge residues, Lys and Glu to replace Asn6 and Asn10, respectively, to the *Bs*DivIVA$_{1\text{-}62}^{\text{Asn26AspAla30Asp}}$ mutant did not contribute substantially to the binding affinity of *Bs*DivIVA for *Bs*PBP1. The new quadruple mutant, *Bs*DivIVA$_{1\text{-}62}^{\text{Asn6LysAsn10Glu26AspAla30Asp}}$, had a Kd of >2 mM for *Bs*PBP1$_{1\text{-}32}$. By contrast, mutating Arg33 to Ile, to produce the triple mutant *Bs*DivIVA$_{1\text{-}62}^{\text{Asn26AspAla30AspArg33Ile}}$, had a bigger impact on the affinity for *Bs*PBP1$_{1\text{-}32}$, a Kd of 980 ± 20 µM was measured and the binding curve began to adopt a hyperbolic, saturable curve, consistent with a specific binding event. Incorporating both of these features enhanced the binding of the *Bs*DivIVA penta-mutant (*Bs*DivIVA$_{1\text{-}62}^{\text{Asn6LysAsn10GluAsn26AspAla30AspArg33Ile}}$) to *Bs*PBP1$_{1\text{-}32}$ leading to a measured Kd of 670 ± 20 µM. This interaction was considerably stronger than for the WT *Bs*DivIVA (Kd > 4mM) but was still 4-fold weaker than the binding of the *Bs*PBP1 peptide to WT *Bs*GpsB. Finally, a 6-residue mutant was constructed that introduced a glutamate at position 12 (*Bs*DivIVA$_{1\text{-}62}^{\text{Asn6LysAsn10GluThr12GluAsn26AspAla30AspArg33Ile}}$), in an attempt to replicate the salt bridge formed between *Bs*GpsB$^{\text{Glu17}}$ and *Bs*PBP1$^{\text{Arg11}}$, and potentially introducing additional *Bs*DivIVA:*Bs*PBP1 contacts to strengthen the binding. This *Bs*DivIVA mutant had an almost GpsB-like affinity for *Bs*PBP1, being just ~2-fold weaker, with a measured Kd of 390 ± 40 µM in comparison to 150 ± 20 µM for *Bs*GpsB$_{1\text{-}68}$ *vs* *Bs*PBP1$_{1\text{-}32}$. The *Bs*DivIVA mutants that bound to *Bs*PBP1 with a sub mM Kd had a higher maximal binding to *Bs*PBP1 (maximum mP of ~200) compared to *Bs*GpsB (maximum mP of ~ 160). The higher polarisation value for the *Bs*DivIVA:*Bs*PBP1 interaction suggests there was less free fluorescent *Bs*PBP1$_{1\text{-}32}$ peptide in solution as an increase in polarisation was observed when the tumbling fluorescent peptide bound to the protein, slowing the tumbling and thus causing a polarised emission. An explanation for this observation could be the introduced mutations enabled two *Bs*PBP1 peptides to bind more easily to *Bs*DivIVA$_{1\text{-}62}$ than with WT *Bs*GpsB$_{1\text{-}68}$. If time had not been constrained, the stoichiometry of the interaction could have been examined by ITC.

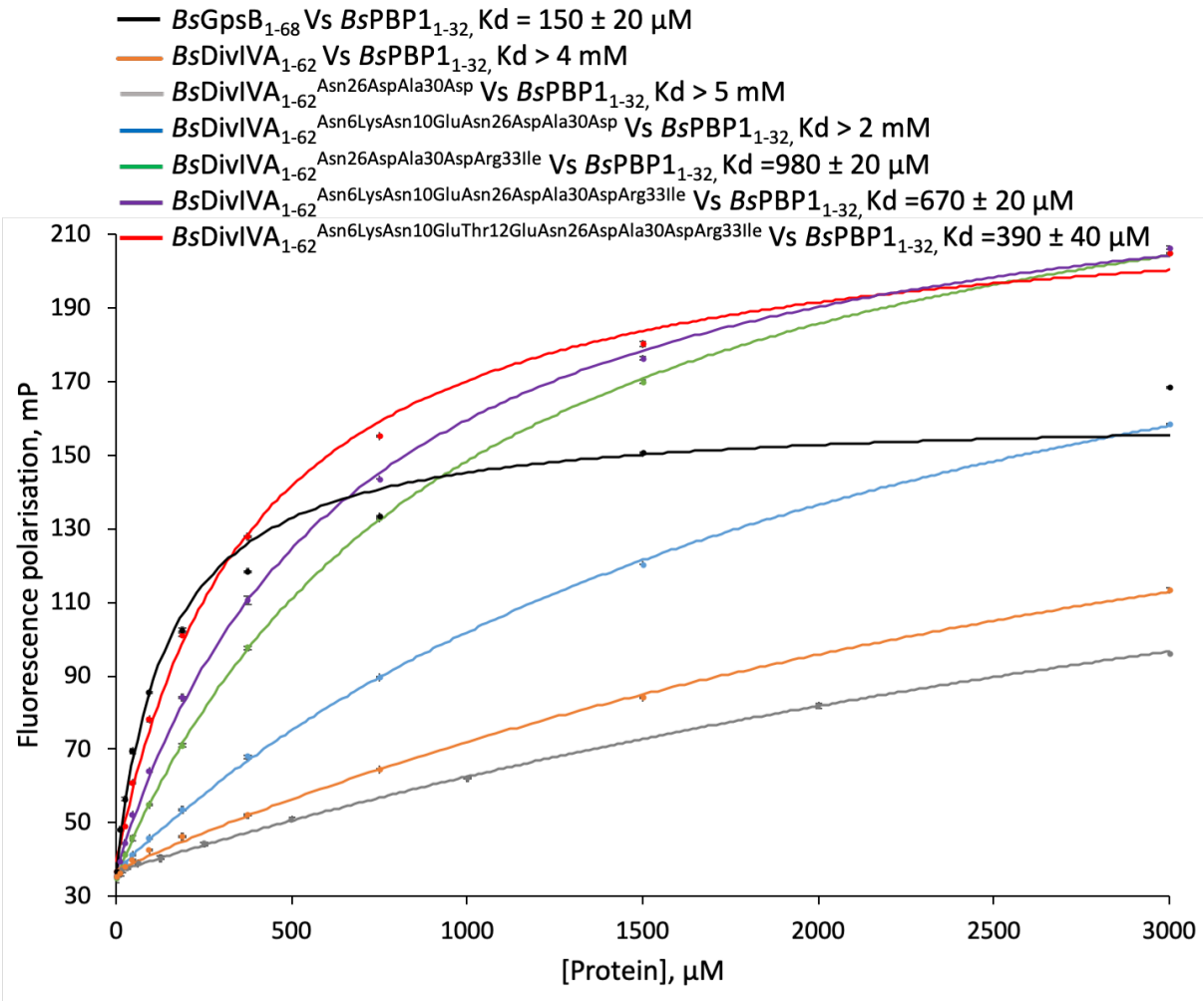

Figure 4.6: Interaction of a cytoplasmic domain peptide of *Bs*PBP1 with the N-terminal domain of *Bs*DivIVA mutants.
The interaction of fluorescein-labelled *Bs*PBP1$_{1-32}$ with wild-type *Bs*GpsB$_{1-68}$, *Bs*DivIVA$_{1-62}$ and engineered *Bs*DivIVA$_{1-62}$ variants, as monitored by fluorescence polarisation. Binding data and the fit of the data to a 1:1 binding model in Sigma plot for each of the data sets are plotted on the graph. The average of three technical replicates and the standard error for each data point is shown. The key shows which data set is represented by colouring and the respective Kd estimate that was determined in Sigma plot.

Since *Bs*DivIVA$_{1-62}$ could be mutated to bind to *Bs*PBP1$_{1-32}$ *in vitro*, the ability of a PBP-binding DivIVA mutant to supress a Δ*gpsB* phenotype was tested. The Halbedel group constructed *LmdivIVA* with Leu6Lys, Asn10Glu and Asn26Asp exchanges in an attempt to introduce *Lm*PBPA1 binding. It was concluded from complementation experiments that this was not sufficient to turn *divIVA* into *gpsB*. To test if different C-terminal domains of GpsB and DivIVA were the reason complementation was not seen, the C-terminal domains were exchanged to produce the N-terminal domain of *Lm*DivIVA encoded by the *LmdivIVA*^{Leu6LysAsn10GluAsn26Asp} triple mutant fused to the C-terminal domain of *gpsB.* Again, this did not achieve the desired

effect and as the genetics did not provide a clear-cut phenotype it was decided to call a halt to this avenue of research.

4.5 Secondary structure of *Bs*DivIVA mutants confirmed by Circular Dichroism.

Circular dichroism of the *Bs*DivIVA$_{1-62}$ mutants confirmed that the mutants were correctly folded and the CD spectra did not differ significantly compared to WT. (Figure 4.7 A). The secondary structure prediction of each of the mutants (Figure 4.7 B) revealed each variant was predominantly alpha-helical (42-53 %) which is consistent with the secondary structure observed in the *Bs*DivIVA$_{1-57}$ structure, which contains 69 % alpha-helical (residues 3-52) (Oliva et al., 2010). Therefore, there was negligible disruption to the secondary structure of *Bs*DivIVA when these mutations were introduced, just slight deviations in the overall structure, to open up the *Bs*PBP1 binding site and consistent with the design principles from the outset that sought to introduce new PBP1-binding functionality only.

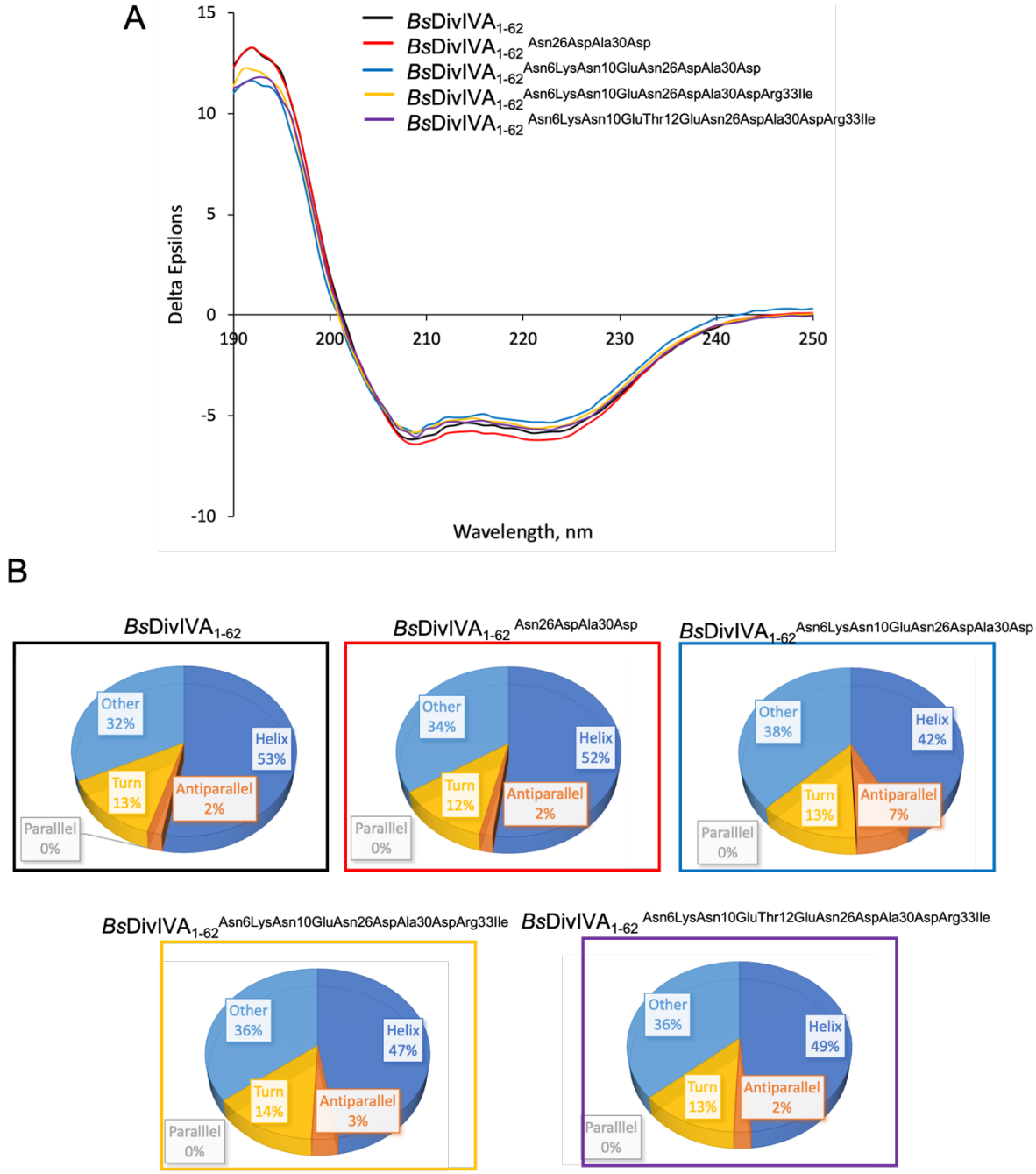

Figure 4.7: Secondary structure determination of wild type and mutants of N-*Bs*DivIVA.
A. Circular dichroism spectra of WT and engineered *Bs*DivIVA variants. These data were analysed using Bestsel (Micsonai et al., 2018) and CD spectra were converted from millidegrees to delta epsilon. Shown here is the experimental data and the key indicates which data set is represented on the graph. **B.** Secondary structure prediction of each of the *Bs*DivIVA mutants determined by BeStsel (Micsonai et al., 2018) from the CD spectra. The percentage of each element is displayed in a pie chart.

4.6 Summary

The aim of this chapter was to try and understand exactly what enables *Bs*GpsB to bind to PBPs and what the differences are that means *Bs*DivIVA is unable to so, despite the structures

sharing essential indistinguishable features. Close comparison of the structures of the N-terminal domains of *Bs*GpsB and *Bs*DivIVA showed there were subtle differences that may provide a rationale for the binding of the former only to *Bs*PBP1: *Bs*DivIVA is incapable of binding to *Bs*PBP1 because the *Bs*PBP1 binding site in *Bs*GpsB between helix 1 and 2 is blocked by a loop between the equivalent two helices in *Bs*DivIVA. This feature has been reversed by protein engineering by opening up the PBP-binding site in *Bs*DivIVA. The introduction of a lysine/glutamate pair at positions 6 and 10, together with the addition of a bulky isoleucine residue at position 33, glutamate at position 12 and the aspartate pair, essential for *Bs*PBP1-binding in *Bs*GpsB, the interaction of *Bs*DivIVA with *Bs*PBP1 approached levels close to that of the native *Bs*GpsB:*Bs*PBP1 interaction.

The question still remains, why is there such high structural homology between the N-terminal domains of DivIVA and GpsB? It is probable that GpsB arose from an initial gene duplication of *divIVA*, which is why they share a unique fold in their N-terminal domains. Their C-terminal domains have diverged quite significantly in structure and function, yet the N-terminal domains have not.

The C-terminal domain of DivIVA is considerably longer than the C-terminal domain of GpsB and while both are important in oligomerisation, the overall tertiary structure of the two proteins differ significantly. The *Bs*DivIVA C-terminal domain is a single helix that dimerises to form a parallel coiled coil dimer. Residues at the C-terminal ends of two dimers associate to form an elongated tetramer with N-terminal domain dimers at the respective ends (Oliva et al., 2010). The long C-terminal domain results in a distance between the N-terminal lipid binding domains which aids DivIVA in sensing membrane curvature with the C-terminal domain acting as a bridge from one part of the membrane to another (Halbedel & Lewis, 2019). The shorter *Bs*GpsB C-terminal domain forms a trimer of 3 parallel coiled coils that oligomerises into a hexamer (Rismondo et al., 2016). The overall tertiary structure of *Lm*GpsB, determined by SAXS, positions 3 N-terminal domain dimers as arms and two C-terminal trimers at the base of a tripod-like hexamer (Cleverley et al., 2016). This oligomerisation of GpsB increases its binding capacity to coordinate PBPs and potentially other proteins. The C-terminal domain of DivIVA has been shown to interact with a number of soluble proteins including the important sporulation protein RacA (Lenarcic et al., 2009; Schumacher et al., 2016) and chromosome segregation proteins ParA and ParB/Spo0J (Perry & Edwards, 2004; Donovan et al., 2012; Ginda et al., 2013). DivIVA seems to have varying functions and

interacting partners across Gram-positive bacteria (Halbedel & Lewis, 2019), which could explain why sequence conservation of the C-terminal domain is lacking. GpsB only seems to interact with membrane or membrane associated proteins through its N-terminal domain with the short C-terminal domain serving solely for oligomerisation.

ConSurf analysis (Landau et al., 2005) of the N-terminal domains of GpsB and DivIVA demonstrated a higher level of conservation at helix 1 and the adjacent region of helix 2, and the C-terminus of helix 2 was more variable (Figure 4.8). This suggested the conserved area is important for protein binding, although the conservation level in GpsB proteins is higher than in DivIVA. The essential PBP binding residues of *Bs*GpsB include Tyr25, Asp31, Asp35 and Ile38, and these are in areas of high conservation. By comparison, the equivalent residues in *Bs*DivIVA, Tyr20, Asn26, Ala30 and Arg33, are less well conserved and only Tyr20 maintains the same level of conservation, suggesting that DivIVA interactions with other proteins takes place at different sites. The loop region of *Bs*DivIVA including Asn10, that blocks the PBP binding site, is also well conserved in DivIVA proteins.

It has been shown by BACTH and co-immunoprecipitation that Wag31 (the DivIVA homologue in *M. tuberculosis*) interacted with the septum-specific peptidoglycan synthase PBP3 (FtsI) (Mukherjee et al., 2009; Plocinska et al., 2014). Under oxidative stress, Wag31 protected PBP3 from proteolysis (Mukherjee et al., 2009). PBP3 contains a cytoplasmic N-terminal domain located in close proximity to the cytoplasmic membrane (Lu et al., 2020) which would suggest the interaction takes place with the lipid binding N-terminal domain of Wag31. Wag31 contains a pair of aspartates at the same positions as the conserved aspartates in GpsB, essential for PBP binding. However, there is no lysine/arginine pair in helix one and the equivalent of *Bs*GpsB^{Ile38} is a glutamate, suggesting that Wag31 must interact with PBP3 via a different mechanism. DivIVA is required for the recruitment the division inhibitor MinCD to the cell poles, an interaction that is bridged by MinJ (Bramkamp et al., 2008). Domain swap experiments have located the MinJ binding site to the N-terminal domain of *Bs*DivIVA, however the molecular basis of this interaction is currently unknown (van Baarle et al., 2013).

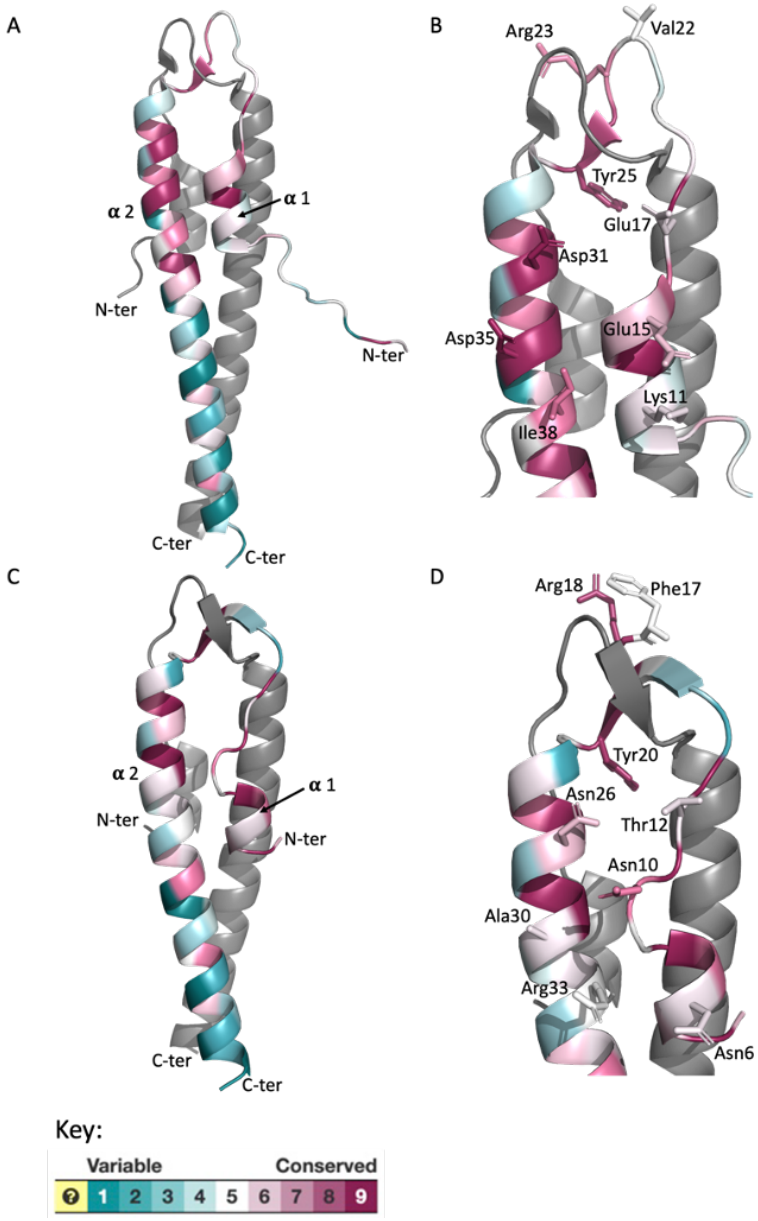

Figure 4.8: An estimation of the evolutionary conservation of the amino acids in the N-terminal regions of GpsB and DivIVA.
The structures of *Bs*GpsB$_{1-68}$ (PDB ID: 4UG3) and *Bs*DivIVA$_{1-57}$ (PDB ID: 2WUJ) were input to the ConSurf sever (Landau et al., 2005) which produced the resulting conservation models applied to chain A of each structure. The model of *Bs*GpsB$_{1-68}$ is shown in panels **A** and **B** and the model of *Bs*DivIVA$_{1-57}$ is shown in panels **C** and **D** in cartoon form. Panels **B** and **D** show a zoomed-in view of the PBP binding site with important binding residues labelled and shown as sticks. The conserved membrane association residues, Val22/Arg23 of *Bs*GpsB and Phe17/Arg18 of *Bs*DivIVA are also labelled and shown as sticks. The level of conservation is represented by colour which in indicated by the key.

An explanation for the homologous N-terminal structures could be that sufficient time has not elapsed since gene duplication for the structures to diverge but the sequences have, explaining why the N-terminal domains of GpsB and DivIVA have apparently different functions. The structural homology enables both DivIVA and GpsB to associate with the

membrane and act as scaffold proteins for different protein targets: DivIVA with proteins involved in various roles including division site selection (Kaval et al., 2014), sporulation (Lenarcic et al., 2009; Schumacher et al., 2016) and chromosome segregation (Perry & Edwards, 2006; Donovan et al., 2012; Ginda et al., 2013) and GpsB with peptidoglycan synthesis, cell elongation factors (Cleverley et al., 2019) and sporulation regulator SpoIIE (Muchová et al., 2020).

Chapter 5: Circumventing AMR: Targeting the Cell Division Regulator GpsB

5.1 Introduction

GpsB is a cell-cycle regulator that controls the switch between bacterial growth and division, and one of its key roles is to ensure the proper cellular localisation of the major peptidoglycan synthase in those bacteria that encode GpsB. GpsB in several Gram-positive bacteria interact with an array of binding partners, including major penicillin binding proteins, and mutations in GpsB in the interaction interface are lethal (Rismondo et al., 2016; Cleverley et al., 2016, 2019). The development of chemical probes that block these essential protein:protein interactions could help discriminate between essential and non-essential pairs of amino acids, that could be developed long-term into lead compounds for antibiotic drug discovery to address specifically infections caused by the Gram-positive pathogens streptococci, staphylococci and enterococci. Well-diffracting crystals of the N-terminal domain of GpsB from *Streptococcus pneumoniae* were already available that diffracted to a resolution of 1.9 Å (Section 3.5.1), as were well-characterised biochemical and genetic systems to investigate GpsB interactions in several bacteria (Cleverley et al., 2019). This chapter explores the X-ray crystallography-based fragment screening experiment of N-*Sp*GpsB, performed at the fragment screening XChem facility at Diamond Light Source.

5.2 Development of reproduceable crystals

In order to complete an XChem experiment the production of large, uniform and reproducible crystals needed to be established. The solvent channels in the original structure of *Sp*GpsB were inspected and it was determined that the binding site would be accessible for small ligands (Figure 5.1). The crystallisation condition was therefore developed from the already established conditions that *Sp*GpsB was crystallised in prior to XChem beamtime allocation (0.1 M Tris.HCl pH 8.5, 0.2 M $MgCl_2$, 20 % PEG 8000) (Section 3.5.1).

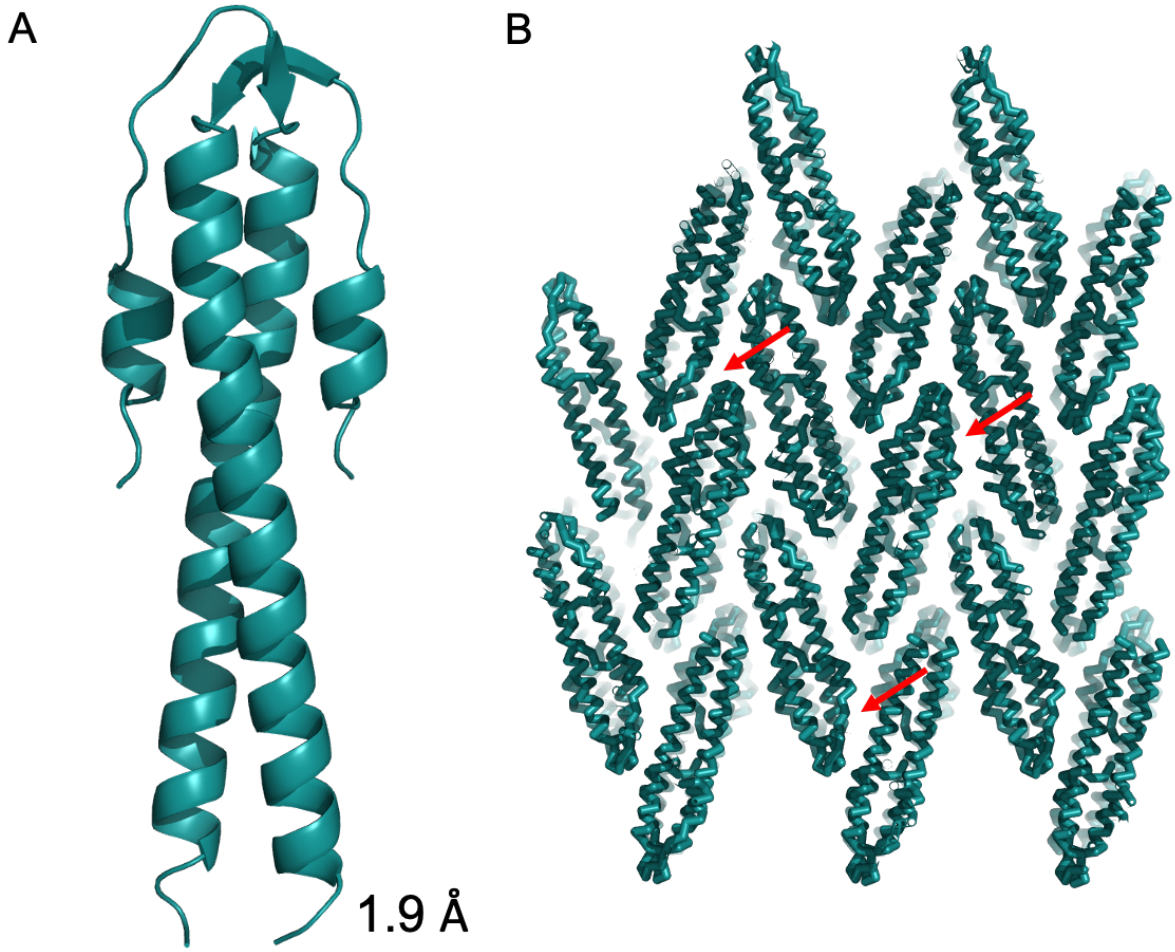

Figure 5.1: The arrangement of molecules in this *Sp*GpsB$_{4-63}$ structure makes it a suitable candidate for fragment soaking.
Panel **A** shows a single dimer of *Sp*GpsB$_{4-63}$ in cartoon and panel **B** is the arrangement of these dimers in the crystal. Solvent channels between each dimer at the target binding site are highlighted by red arrows.

Screening was carried out in MRC 2 well plates with 20 mg/mL of N-*Sp*GpsB (100 and 200 nL) and 0.1 M Tris pH 8.5, 0.2 M $MgCl_2$, with precipitant concentrations between 15-30 % PEG 8000 (100 nL). This method was not sufficient to obtain reproducible crystals and seeding was explored. Approximately 20 crystals no bigger than 200 µm in the largest dimension were crushed in a buffer of 50 uL of 0.1 M Tris.HCl pH 8.5, 0.2 M $MgCl_2$, 24 % PEG 8000 to create a microseed stock. Screening was carried out in SwissCi 3-drop plates with a Mosquito (TTP Lab Tec) pipetting workstation mixing 300 nL of N-*Sp*GpsB at 20 mg/mL, 100 nL of microseed stock and 200 nL of reservoir (0.1 M Tris pH 8.5, 0.2 M $MgCl_2$, 15-20% PEG 8000). Crystals from 16 % PEG 8000 diffracted to the highest resolution (1.6 Å) tested on an in-house Bruker gallium Metaljet. To obtain the adequate number of crystals required for an XChem experiment, approximately 600 crystals were produced under this condition (Figure 5.2).

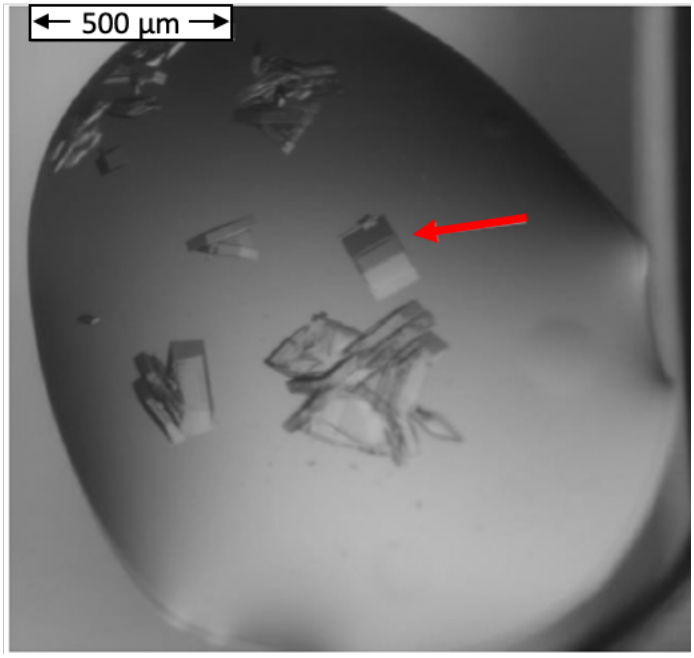

Figure 5.2: A crystal drop from the final seeding conditions of *Sp*GpsB$_{4-63}$.
The scale bar gives an indication of the size of the crystals in the drop and the red arrow points to a uniform crystal ~ 200 x 200 x 200 µm that was chosen for fragment soaking.

5.3 Experimental procedure at Diamond Light Source

Images of the crystal drops were recorded and TeXRank (Tsing Ng et al., 2014) was used to select the drops containing crystals to be soaked. The crystals were selected based on size and shape, and clusters or multiple crystals were automatically disregarded. 40 of these crystals were used for DMSO- and cryo-testing. It was determined from the diffraction patterns that the N-*Sp*GpsB crystals could withstand 20 % DMSO for up to 3 hours and that no additional cryoprotection was required. Each crystal was soaked with a fragment for 1 hour before harvesting began; in no instance did the soak time exceed 3 hours.

Subsequently, 547 crystals were soaked with fragments from the DSi-Poised Library (Enamine) using the XChem ECHO acoustic liquid handler (Labcyte). The final concentration of the fragment in each drop was 100 mM. The crystals in drops from a crystallisation plate containing 100-150 chosen drops was soaked for an hour and then the crystals were harvested manually with the aid of a Shifter (Oxford Lab Technologies) and cryo-cooled in liquid nitrogen directly into pucks. It took approximately 1-1.5 hours to harvest the crystals from a single tray. This same process was then repeated 4 times in order to sample a larger range of the chemical library. For each drop selected using TeXRank where harvesting was attempted, a note was made with regards to the condition of the drop. Examples of notes included, precipitation of

fragment, cracked crystal and dissolved crystal. It was then recorded if a crystal was successfully harvested from the given drop. In total, 540 crystals were harvested. Diffraction data were collected on the I04-1 beamline in automated, unattended mode using loop centring as the crystals were larger than the loops (> 200 µm). All crystals diffracted to between 1.2 and 1.8 Å.

5.4 Data processing and structure determination

A total of 536 useful diffraction datasets were collected and used for subsequent structural analysis. For the remaining 4 samples, data collection failed due to empty or broken loops. The data were processed using Diamond's automated processing pipeline (https://www.diamond.ac.uk/industry/Industry-News/Latest-News/Synchrotron-Industry-News---MXnews4/Auto-processing-Pipeline.html). The space group and unit cell parameters for each data set were unsurprisingly consistent with the structure of *Sp*GpsB$_{4\text{-}63}$ (Table 3.2). The data were then loaded onto XChemExplorer (XCE) (Krojer et al., 2017) which is a graphical workflow tool for large-scale protein-ligand structure determination. XCE automatically selected the best data for each dataset from the automated pipeline. Dimple (http://ccp4.github.io/dimple/), a programme used for batch molecular replacement, was used to solve the 536 datasets using the structure of *Sp*GpsB$_{4\text{-}63}$ as a reference 'ground-state' model.

5.5 Determining potential ligand binding sites by differential electron density

For each solved structure the ligand restraints corresponding to each fragment were generated using AceDRG (Long et al., 2017). A programme called PANDDA.analyse (Pan-dataset density analysis) (Pearce et al., 2017a) was used to find potential ligand binding sites. PANDDA.analyse compared all of the structures by aligning them to the *Sp*GpsB$_{4\text{-}63}$ reference structure and identified residual difference density that might correlate to the binding of a potential ligand. In total 122 datasets were identified by PANDDA.analyse as containing residual difference density.

5.6 Modelling small ligands into identified sites

PANDDA.inspect (Pearce et al., 2017b) was used to visually inspect the 122 datasets, make annotations and manually model the fragment within the coot interface. There were 77 datasets were a fragment was modelled satisfactorily (a 14 % 'hit' rate). For the remaining 45

datasets, the electron density identified by PANDDA.analyse was either not strong enough to confidently model the ligand or corresponded to unmodelled electron density at the N- or C-terminus of GpsB. An example of a modelled ligand and electron density that did not represent a ligand are shown in Figure 5.3. Conformations and rotamers of protein residues surrounding the fragment binding site that had changed due to binding were corrected during inspection. Water molecules surrounding the fragment binding site were also added at this stage. The resulting structures from PANDDA.inspect were not fully built, 'final' crystallographic models refined to convergence but bound-state models at the specific binding site. In total, there were 14 different 'hot-spots' in the crystal where ligands were bound (Figure 5.4). Of these 14, 10 sites were at or immediately adjacent to crystal packing interfaces, and are presumably of secondary importance to the goal of identifying functionally important binding sites. The remaining 4 'hot-spots' were either close to or at the target binding site, as defined as the interaction site for PBP peptides in GpsB, mutation of which is lethal (Cleverley et al., 2019).

The 77 datasets with bound ligands underwent a few rounds of refinement using REFMAC (Murshudov et al., 1997), including the addition of water molecules. 12 of these datasets contained a ligand that was identified as a binding site ligand. These structures were fully refined as they were the key focus of this experiment. The refinement statistics for the final 12 structures can be found in Table 5.1 and Table 5.2.

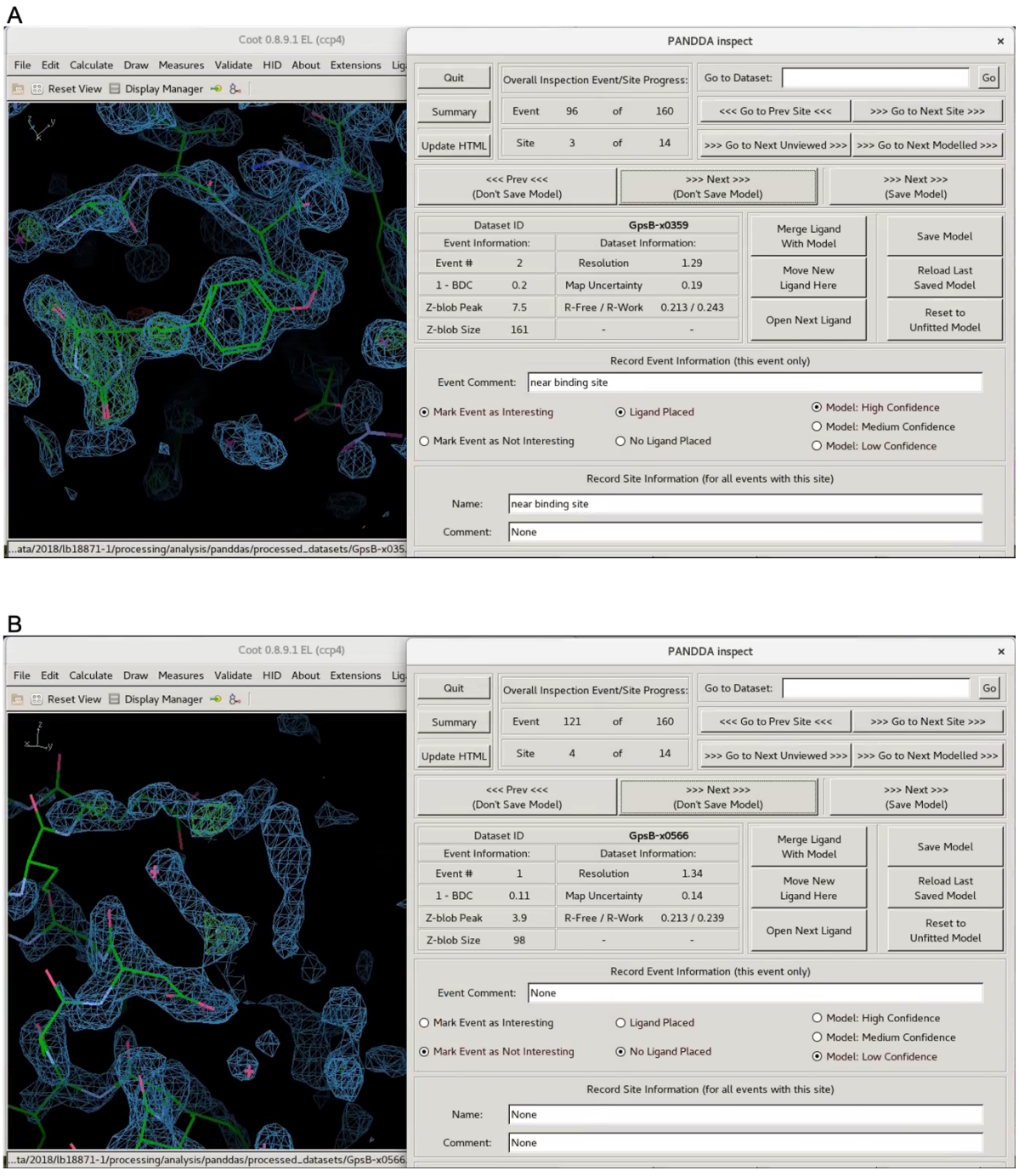

Figure 5.3: Screenshots from the PANDDA.inspect interface.
Panel **A** shows a dataset in which a fragment was modelled into the electron density identified by PANDDA.analyse. Panel **B** is an example of electron density identified that did not represent a bound ligand and the density could be representative of a PEG fragment.

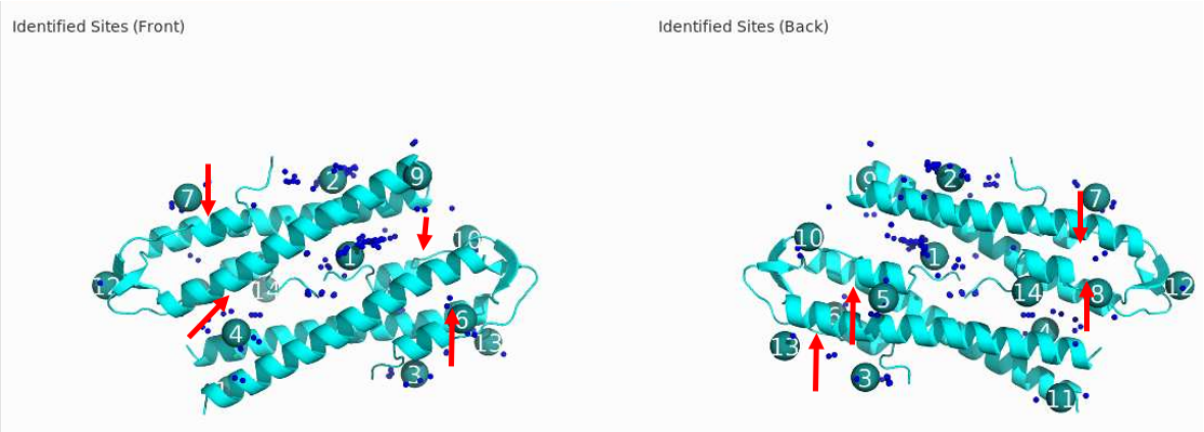

Figure 5.4: PANDDA.inspect summary.
Dark blue dots show the placement of a fragment on the *Sp*GpsB structure, which has 4 GpsB molecules (2 dimers) in the asymmetric unit. The numbers indicate a binding area identified by PANDDA.inspect. Sites 5, 6 and 8 were target binding sites. The red arrows point to the 4 PBP binding sites.

5.7 Target binding site ligands

The 12 binding site ligands were numbered 1-12 and details of each ligand can be found in Table 5.3. It is clear from the structures that these 12 ligands occupy a similar binding site in *Sp*GpsB to *Sp*PBP2a$_{27\text{-}40}$, between helix 1 and helix 2 of a GpsB monomer (Figure 5.5) with some ligands making contacts with symmetry-related molecules. The specific site in each structure where the ligand was built into the electron density is shown in Figure 5.6. The main grouping of 'hits' either bound directly or are in close proximity to residues in GpsB that are essential for viability *in vivo* and peptide-binding *in vitro*, including Tyr23, Val28, Asp29, Leu32 and Asp33 (Cleverley et al., 2019).

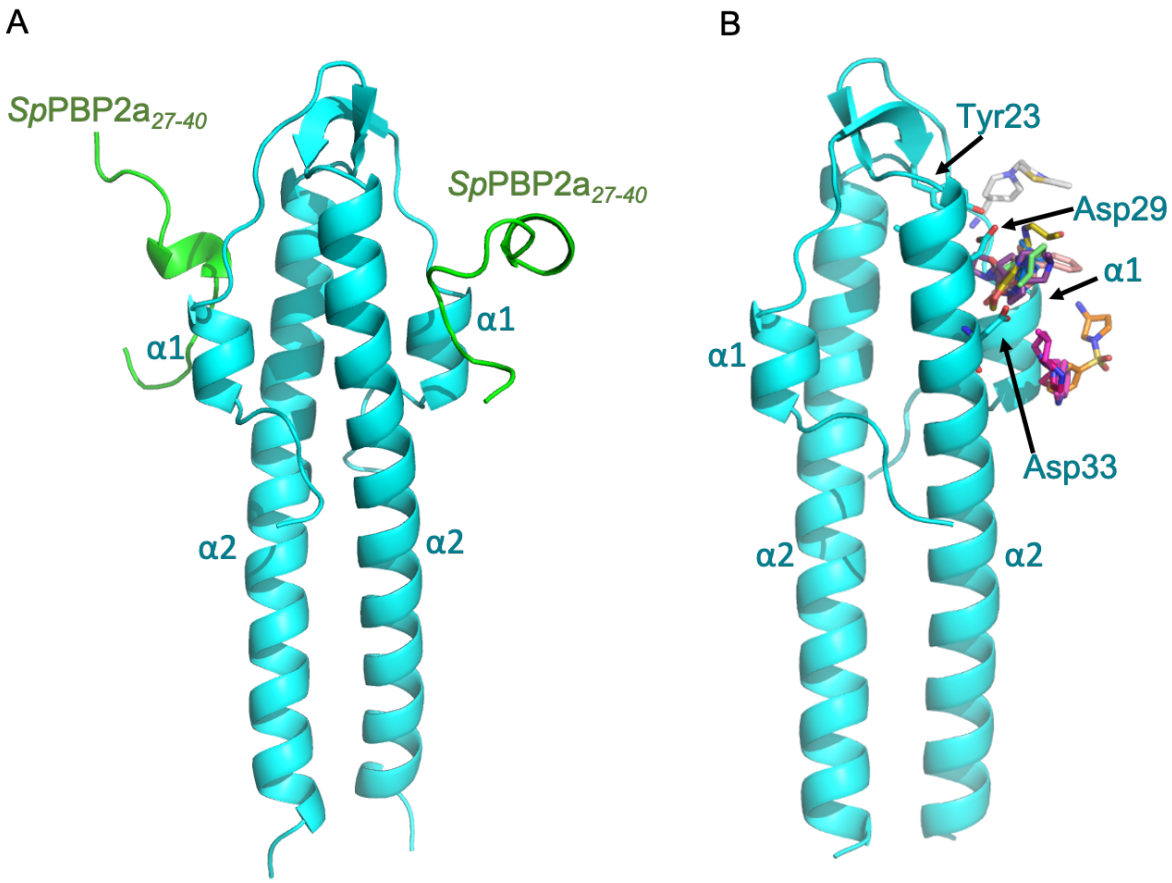

Figure 5.5: Ligands that occupy the PBP binding site of GpsB.
Panel **A** shows a cartoon of N-*Sp*GpsB bound to PBP2a. The GpsB dimer is coloured cyan and the PBP2a peptides are coloured green. Helix 1 (α1) and helix 2 (α2) of each GpsB dimer are labelled. Panel **B** shows the structure of N-*Sp*GpsB with the 12 ligands that bind in the PBP2a binding site, superimposed in one of the binding sites of the GpsB dimer. The 12 ligands are shown in stick form with a distinct colour. Three of the essential *Sp*GpsB residues required for PBP2a binding are shown in stick form and are labelled. Helix 1 (α1) and helix 2 (α2) of each GpsB dimer are labelled.

Analysis of the binding sites of ligands 1 and 6 indicated there were no hydrogen bonds between the ligand and the *Sp*GpsB monomer, but potential stacking interactions with Phe12 (Figure 5.7). Stacking with Phe12 was also seen with ligands 8, 9, 10 and 12 (Figure 5.8). Ligand 6 formed a hydrogen bond with the backbone carbonyl of Gln14 from a symmetry-related molecule and stacking with a symmetry related Phe12 was also observed. This might restrict the binding of this ligand to *Sp*GpsB in the crystal form and not in solution. Ligands 2 and 11 formed a salt bridge with their only nitrogen atom to Asp29 of *Sp*GpsB (Figure 5.7 and Figure 5.8). This interaction mimics the salt bridge that is formed between Arg31/33 of *Sp*PBP2a and Asp29 (Figure 3.17). The nitrogen atom of ligand 2 was also coordinated by a symmetry-related Glu40 (Figure 5.7). The second important *Sp*GpsB aspartic acid for PBP binding, Asp33, formed a hydrogen bond to a nitrogen atom in ligands 5 and 9 (Figure 5.7 and Figure 5.8). A

second nitrogen atom from ligand 9 formed a hydrogen bond with the carbonyl oxygen of Phe12 (Figure 5.8). Hydrogen bonding of the carbonyl oxygen of Phe12 was also seen with nitrogens of ligands 5, 7 and 10 (Figure 5.7 and Figure 5.8) and this same nitrogen atom in ligand 5 and 7 formed a hydrogen bond with the carbonyl oxygen of Gln14 (Figure 5.7 and Figure 5.8). Ligand 7 was also coordinated by hydrogen bonding from the backbone amide of Lys9 and side chain of Glu40 from a symmetry-related molecule. A salt bridge was important in the binding of ligand 8 between one of the two nitrogen atoms and Glu40 (Figure 5.8). In binding site 1 of both the *Sp*GpsB:*Sp*PBP2a and *Sp*GpsB:*Sp*PBP2x structures this same glutamate formed an interaction with *Sp*PPB2a^{Arg31} (Figure 3.17 B) and *Sp*PBP2x^{Arg22} (Figure 3.27 B). Ligand 8 also stacked with a symmetry-related Phe12. Ligands 3 and 12 involved a similar interaction between respective oxygen atoms and the side chain nitrogen of Lys9, and ligand 12 formed a sulphur H-bond with the backbone amide of Lys9 (Figure 5.7 and Figure 5.8). The binding of ligand 3 is strengthened via hydrogen bonding with carbonyl oxygens of Gln14 and Phe12 from a symmetry-related molecule (Figure 5.7). Ligand 4 bound in a slightly different site to the other 11 ligands on the other side of helix 1, where it formed a hydrogen bond with the carbonyl oxygen of Glu15 and a sulphur H-bond with the carbonyl oxygen of a symmetry-related Ala44 (Figure 5.7). This site is still in close proximity to the essential binding site residues Asp29 and Asp33. Glu15 was also involved in the binding of ligand 10, forming hydrogen bonds with a nitrogen atom (Figure 5.8). The importance of Glu15 in PBP binding was shown in the *Sp*GpsB:PBP2a structure where it formed a salt bridge with Arg36 in binding site 1 (Figure 3.17 B).

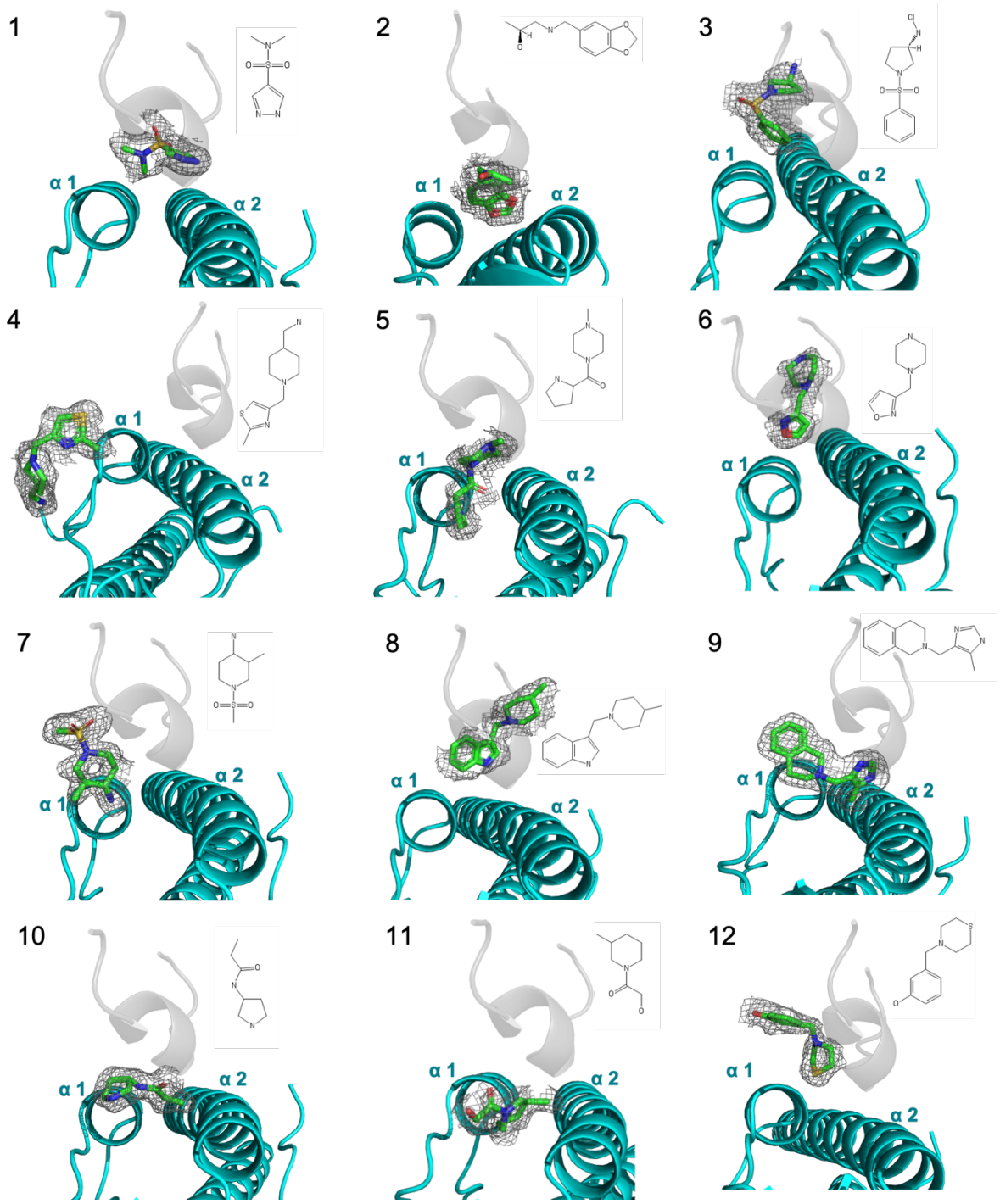

Figure 5.6: Structures of the 12 target binding site ligands bound to N-*Sp*GpsB.
Each numbered panel corresponds to a different ligand found in the first column of Table 5.3. N-*Sp*GpsB is shown as a cartoon and coloured cyan in each panel. Each ligand is shown in sticks with the carbon atoms coloured in green. The electron density of each ligand is shown by grey mesh. The map shown is the final Refmac-weighted $2mF_{obs}$-DF_{calc} map contoured at 0.16 electrons per Å3 with a carve of 1.6. In each panel chain A of GpsB in the *Sp*GpsB$_{4-63}$:*Sp*PBP2a$_{27-40}$ structure is superimposed onto the GpsB chain with a bound ligand and *Sp*PBP2a$_{27-40}$ shown as a cartoon at 70 % transparency and coloured grey. A sketch of each ligand is displayed to the right of each structure.

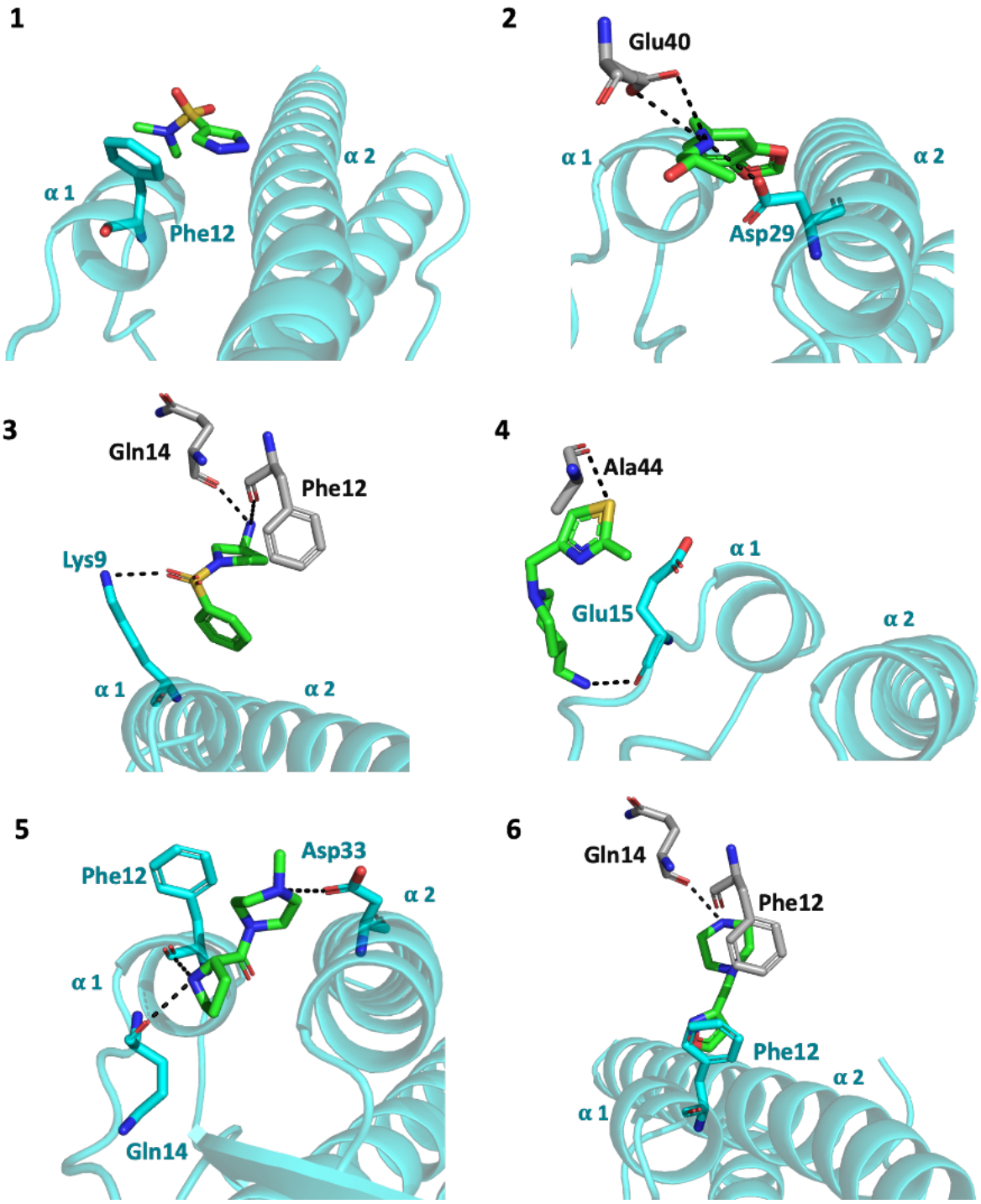

Figure 5.7: Binding site interactions of ligands 1-6 with N-*Sp*GpsB between helix one (α1) and helix two (α2) of a GpsB monomer.

Each numbered panel corresponds to a different ligand listed in the first column of Table 5.3. The two subunits of the N-terminal GpsB dimer are coloured cyan in cartoon form and each ligand is coloured green as sticks. Nitrogens are blue, oxygens are red and sulphurs are yellow. GpsB residues important in binding are shown as sticks and are labelled. Symmetry related residues involved in coordinating the ligand are shown as sticks and coloured grey. Salt bridges and hydrogen bonds are represented by dashed black lines.

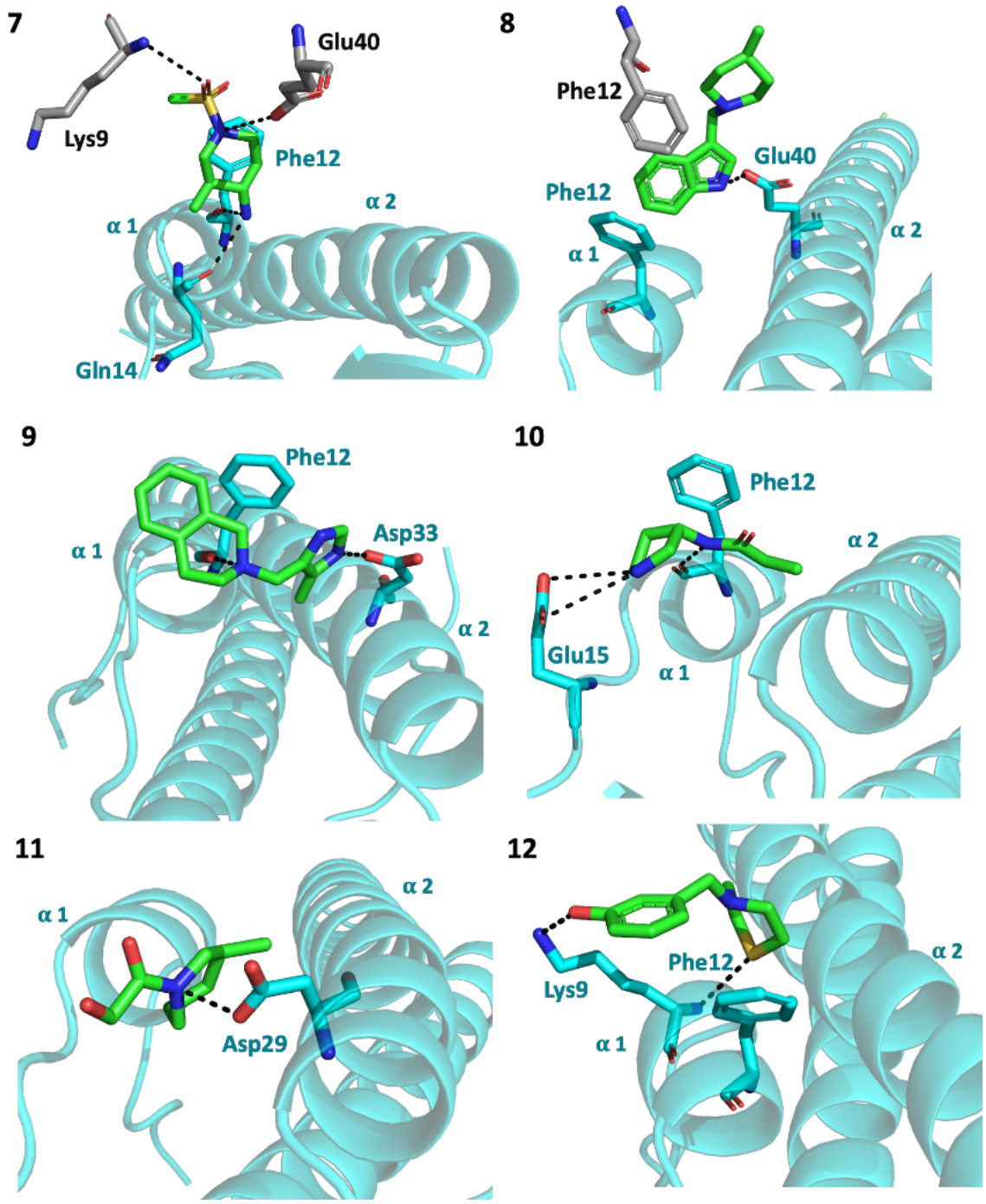

Figure 5.8: Binding site interactions of ligands 7-12 with N-*Sp*GpsB between helix one (α1) and helix two (α2) of a GpsB monomer.
Each numbered panel corresponds to a different ligand listed in the first column of Table 5.3. The two subunits of the N-terminal GpsB dimer are coloured cyan in cartoon form and each ligand is coloured green as sticks. Nitrogens are blue, oxygens are red and sulphurs are yellow. GpsB residues important in binding are shown as sticks and are labelled. Symmetry related residues involved in coordinating the ligand are shown as sticks and coloured grey. Salt bridges and hydrogen bonds are represented by dashed black lines.

5.8 The ability of small ligand hits to compete with *Sp*PBP2a binding to *Sp*GpsB

A competition assay was conducted to test if any of the 12 fragment hits were able to compete with *Sp*PBP2a for the *Sp*GpsB binding site. As the 12 fragments were dissolved in 100 % DMSO, the tolerance of the *Sp*PBP:*Sp*GpsB interaction was first tested in the presence of DMSO. The final concentration of DMSO in the crystal soaks was 20 % and the ability of TAMRA-labelled *Sp*PBP2a$_{23-45}$ to bind to *Sp*GpsB$_{1-63}$ monitored by fluorescence polarisation was not affected by DMSO up to 2% (Figure 5.9). The Kd of the interaction with no DMSO was 104 ± 19 µM and in the presence of 2% DMSO it was 93 ± 18 µM.

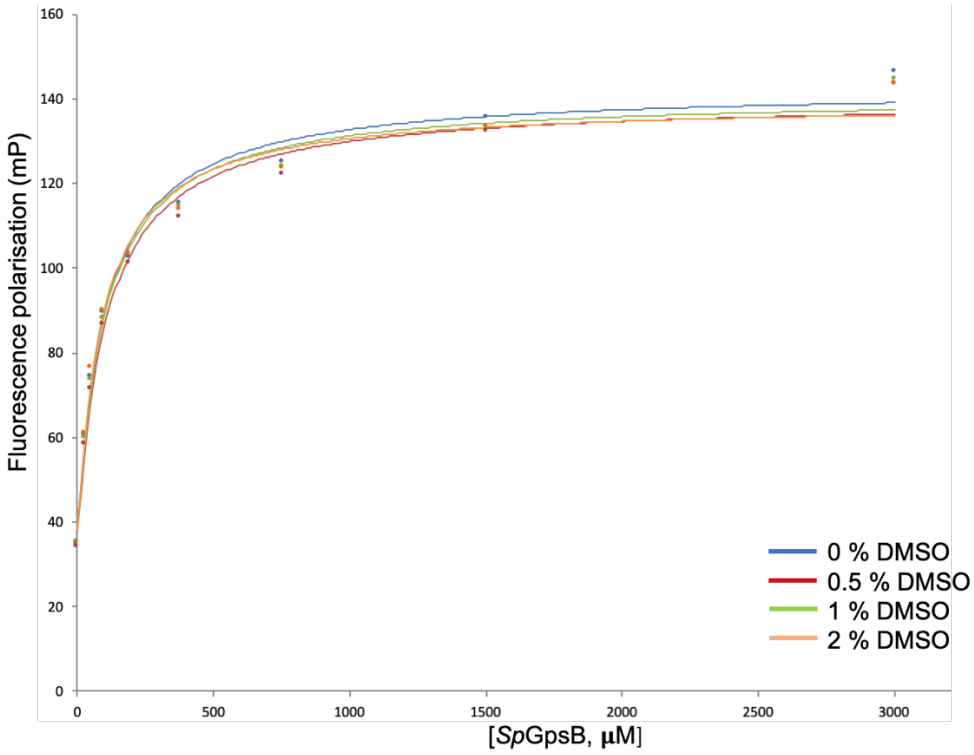

Figure 5.9: DMSO tolerance testing of the PBP:GpsB interaction.
The interaction of TAMRA-labelled *Sp*PBP2a$_{23-45}$ peptide with wild-type N-terminal domain of GpsB from *S. pneumoniae* (*Sp*GpsB$_{1-63}$) at varying DMSO concentrations. Binding data and the fit of the data produced in Sigma plot for each of the data sets are plotted on the graph. The key shows which data set is represented on the graph by colouring.

It was determined that 100 µM of *Sp*GpsB$_{1-63}$ would be used in the competition assay as it slightly higher than the Kd of the interaction measured by FP between *Sp*GpsB$_{1-63}$ and *Sp*PBP2a$_{23-45}$ (Kd of ~70 µM) and gave a constant and detectable FP value of ~90 mP with 40 nM of TAMRA-labelled *Sp*PBP2a$_{23-45}$. The concentrations of *Sp*GpsB$_{1-63}$ and TAMRA-labelled *Sp*PBP2a$_{23-45}$ remained consistent throughout the experiment and the concentration of each fragment was increased from 15.625 to 2000 µM. None of the 12 fragments were able to

displace TAMRA-*Sp*PBP2a$_{23-45}$ as the measured FP stayed at a constant level with increasing fragment concentration (Figure 5.10). If the fragment had been able to compete with TAMRA-*Sp*PBP2a$_{23-45}$ it would bind in place of the fluorescent peptide and the FP would decrease as the fragments were not fluorescently labelled. With 100 µM of *Sp*GpsB$_{1-63}$ and 40 nM of TAMRA-*Sp*PBP2a$_{23-45}$ in the displacement assay, the fragments were competing for 100 µM worth of sites meaning the bottom of the assay was 100 µM. It is therefore safe to conclude that the individual fragments did not bind to *Sp*GpsB$_{1-63}$ with an affinity higher than 100 µM, causing no displacement of TAMRA-*Sp*PBP2a$_{23-45}$. To test if TAMRA-*Sp*PBP2a$_{23-45}$ bound to *Sp*GpsB$_{1-63}$ could be displaced, a control reaction was carried out with un-labelled *Sp*PBP2a$_{27-40}$, again up to a 2 mM concentration. This showed that TAMRA-*Sp*PBP2a$_{23-45}$ was displaced by the un-labelled peptide as the FP value decreased from 89 to 44 mP (Figure 5.10).

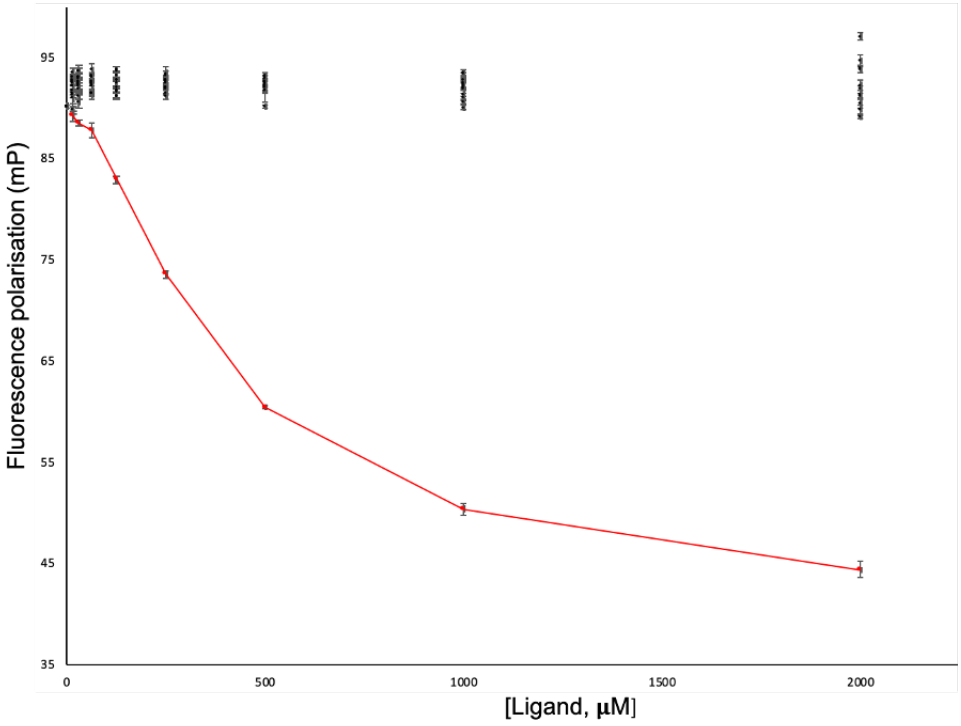

Figure 5.10: Competition assay monitored by fluorescence polarisation.
A constant concentration of *Sp*GpsB$_{1-63}$ (100 µM) and TAMRA-labelled *Sp*PBP2a$_{23-45}$ (40 nM) were used in each measurement with increasing concentrations of ligands/un-labelled *Sp*PBP2a$_{27-40}$ up to 2 mM. 3 measurements were taken at each data point and the average is plotted on the graph as well as the standard error. The fluorescence polarisation with up to 2 mM of any of the 12 ligands did not decrease (black symbols). Increasing the un-labelled *Sp*PBP2a$_{27-40}$ concentration up to 2 mM caused a decrease in FP (red curve).

5.9 Binding of ligands to N-terminal *Sp*GpsB by ITC

The ability of the ligand hits to bind to N-*Sp*GpsB without the presence of PBP2a was tested using ITC. Ligands 8 and 12 were not suitable for this experiment as they precipitated at a concentration of 20 mM. For the remaining 10 ligands, 20 aliquots of each ligand at 20 mM were injected into 30 µM *Sp*GpsB$_{1-63}$. It was not possible to detect an interaction with a Kd tighter than 5 mM and no sigmoidal binding curves were produced. To conclude, no detectable binding of the 10 ligands were observed by ITC.

5.10 Summary

This chapter explores the first X-ray crystallography-based fragment screening experiment applied to GpsB. It has been demonstrated that N-*Sp*GpsB crystals were a successful candidate for small fragment soaking, being able to withstand up to 20 % DMSO allowing the soaking at 100 mM of fragments, without crystals cracking or dissolving. In total 14 % of the crystals soaked lead to a dataset with a bound ligand and 2 % of those ligands were identified as *Sp*GpsB target binding site ligands. Analysis of the final 12 structures showed that the binding of 8 out of the 12 ligands involved the formation of van der Waals' interactions, hydrogen bonds or salt bridges of ligand nitrogen atoms with *Sp*GpsB residues (Phe12, Gln14, Glu15, Asp29, Asp33 and Glu40). The binding of *Sp*PBP2a and *Sp*PBP2x to *Sp*GpsB is heavily centred on the formation of hydrogen bonds and salt-bridges between these GpsB residues with arginine residues from the PBP cytoplasmic mini-domains and mutation of these residues abrogated peptide binding *in vitro* and produced *gpsB* null phenotypes *in vivo* (Cleverley et al., 2019).

None of the 12 binding site ligands identified by XChem bound to N-*Sp*GpsB with a high affinity, and they were unable to compete with *Sp*PBP2a for the binding site by biochemical interaction studies. The GpsB:PBP binding site is more of a binding surface than a binding cleft and the small fragments are only capable of making a few contacts to GpsB, inevitably giving them a low affinity. Half of the ligands made contacts with symmetry-related GpsB residues, providing more contacts for the ligand in the crystal to mimicking a binding cleft that is simply not present in solution.

Putting together the data from XChem and ITC interactions studies it seems that ligand 9 could be the best candidate for follow up experiments. Ligand 9 made multiple contacts to N-*Sp*GpsB

including the key Asp33 residue and ITC indicated weak binding in solution. This ligand could be used as a scaffold for the generation of a larger molecule capable of binding to *Sp*GpsB with a higher affinity. The ligand could benefit from more nitrogen residues capable of forming salt-bridges with conserved aspartate and glutamate residues and an overall increase in hydrogen bonding capacity. The production of a successful chemical probe that blocks the GpsB:PBP interaction in *S. pneumoniae*, where GpsB is essential (Rued et al., 2017), could provide the building block for development of a novel antibiotic or combination therapy required due to the ever-growing problem of antimicrobial resistance.

	1	2	3	4	5	6
Data Statistics						
Resolution (Å)	1.31	1.19	1.43	1.19	1.22	1.32
Beamline	I04-1	I04-1	I04-1	I04-1	I04-1	I04-1
Auto Processing	Xia2 3dii	Xia2 3dii	AutoPROC	AutoPROC	AutoPROC	AutoPROC
Wavelength (Å)	0.9159	0.9159	0.9159	0.9159	0.9159	0.9159
Resolution (Å)	37.76-1.31 (1.33-1.31)	59.20-1.19 (1.21-1.19)	58.24-1.43 (1.45-1.43)	59.13-1.19 (1.21-1.19)	37.65-1.22 (1.25-1.22)	40.48-1.32 (1.34-1.32)
Rpim	0.027 (0.749)	0.033 (0.715)	0.062 (1.147)	0.020 (1.168)	0.026 (0.311)	0.017 (0.547)
Space group	$P\,1\,2_1\,1$	$P\,1\,2_1\,1$	$P\,1\,2_1\,1$	$P\,1\,2_1\,1$	$P\,1\,2_1\,1$	$P\,1\,2_1\,1$
Unit-cell parameters						
a (Å)	39.36	39.33	39.92	39.44	39.26	39.30
b (Å)	55.52	55.54	56.38	55.67	55.53	55.59
c (Å)	61.50	61.61	60.35	61.60	61.71	61.57
α - β - γ (°)	90-106.38-90	90-106.07-90	90-105.20-90	90-106.26-90	90-106.57-90	90-106.41-90
No. of measured reflections	147199 (1729)	152870 (195)	128927 (4294)	155006 (228)	153206 (673)	148207 (1872)
No. of independent reflections	54945 (1480)	60877 (194)	46693 (2295)	61086 (224)	57127 (630)	56085 (1659)
Completeness (%)	89.9 (49.4)	75.2 (4.9)	97.0 (96.1)	75.2 (5.6)	76.3 (17.1)	92.9 (54.9)
Redundancy	2.7 (1.2)	2.5 (1.0)	2.8 (1.9)	2.5 (1)	2.7 (1.1)	2.6 (1.1)
CC1/2 (%)	99.7 (31.8)	99.6 (0.0)	99.4 (34.0)	99.9 (71.7)	99.8 (82.6)	99.9 (59.2)
<I>/<σ(I)>	12.9 (1.0)	12 (0.9)	8.7 (0.7)	17.1 (0.8)	13.5 (1.0)	16.7 (1.0)
Refinement Statistics						
R_{work}	0.199	0.198	0.231	0.193	0.190	0.192
R_{free}	0.226	0.221	0.268	0.217	0.211	0.217
No. of non-H atoms						
Protein	1954	1943	1984	1958	1949	1959
Ions	2	2		3	1	2
Ligands	23	27	19	31	40	24
Waters	304	307	275	322	303	316
R.m.s. deviation from ideal values						
Bond angle (°)	1.728	1.750	1.593	1.827	1.777	1.744
Bond length (Å)	0.0125	0.0132	0.0105	0.0150	0.0145	0.0127
Average B factor (Å²)						
Protein	21.64	18.85	19.56	18.02	18.58	20.9
Ions	26.8	23.27	/	26.24	31.21	27.66
Ligands	47.86	46.53	41.82	41.89	36.30	44.92
Waters	30.18	27.38	26.6	26.39	27.83	29.71

**Values in parenthesis are for the highest resolution shell*

Table 5.1: Data collection and refinement statistics for ligands 1-6

	7	8	9	10	11	12
Data Statistics						
Resolution (Å)	1.30	1.39	1.62	1.19	1.32	1.40
Beamline	I04-1	I04-1	I04-1	I04-1	I04-1	I04-1
Auto Processing	AutoPROC	AutoPROC	Xia2 3dii	AutoPROC	Xia2 3dii	AutoPROC
Wavelength (Å)	0.9159	0.9159	0.9159	0.9159	0.9159	0.9159
Resolution (Å)	40.59-1.30 (1.33-1.30)	40.38-1.39 (1.41-1.39)	58.99-1.62 (1.65-1.62)	40.586-1.19 (1.21-1.19)	40.53-1.32 (1.34-1.32)	40.65-1.40 (1.42-1.40)
Rpim	0.036 (0.520)	0.033 (0.723)	0.030 (0.598)	0.029 (0.370)	0.026 (0.359)	0.035 (0.952)
Space group	*P* 1 2_1 1	*P* 1 2_1 1	*P* 1 2_1 1	*P* 1 2_1 1	*P* 1 2_1 1	*P* 1 2_1 1
Unit-cell parameters						
a (Å)	39.35	39.28	39.38	39.33	39.38	39.39
b (Å)	55.85	55.34	55.69	55.81	55.68	56.99
c (Å)	61.59	61.46	61.39	61.57	61.58	61.53
α - β - γ (°)	90-106.39-90	90-106.12-90	90-106.07-90	90-106.19-90	90-106.30-90	90-106.11-90
No. of measured reflections	1540462 (1677)	139350 (3399)	103238 (4261)	154766 (231)	147046 (1914)	135268 (3615)
No. of independent reflections	56727 (1509)	47512 (1748)	32358 (1603)	54311 (187)	55199 (1512)	48897 (2091)
Completeness (%)	90.9 (49.1)	92.8 (64.4)	99.4 (99.01)	66.9 (4.6)	91.9 (50.87)	95.7 (83.1)
Redundancy	2.7 (1.1)	2.9 (1.9)	3.2 (2.7)	2.8 (1.2)	2.7 (1.3)	2.8 (1.7)
CC1/2 (%)	99.7 (40.4)	99.9 (37.2)	99.8 (59.8)	99.7 (78.5)	99.8 (76.9)	99.9 (32.6)
<I>/<σ(I)>	13.3 (1.5)	12.8 (0.7)	12.1 (1.2)	13.6 (0.8)	13.3 (1.1)	11.2 (0.5)
Refinement Statistics						
R_{work}	0.202	0.199	0.210	0.192	0.195	0.212
R_{free}	0.222	0.233	0.252	0.219	0.220	0.242
No. of non-H atoms						
Protein	1969	1969	1934	1959	1969	1944
Ions	2	2	2	1	2	2
Ligands	20	25	25	32	23	26
Waters	305	293	251	325	311	295
R.m.s. deviation from ideal values						
Bond angle (°)	1.777	1.620	1.541	1.740	1.744	1.588
Bond length (Å)	0.0133	0.0115	0.0097	0.0134	0.0128	0.0107
Average B factor (Å²)						
Protein	20.27	21.30	30.07	19.74	20.47	22.51
Ions	26.30	27.77	49.13	27.73	25.98	32.52
Ligands	37.63	49.85	40.98	37.16	37.05	49.57
Water	27.79	28.80	37.91	28.12	29.10	30.90

**Values in parenthesis are for the highest resolution shell*

Table 5.2: Data collection and refinement statistics for ligands 7-12

	Compound ID	Formula	MW	Smiles	Name
1	Z805551440	C5H9N3O2S	175.208	CN(C)S(=O)(=O)C=1C=NNC1	N,N-dimethyl-1H-pyrazole-4-sulfonamide
2	Z2856434941	C11H15NO3	209.241	C[C@H](O)CNCC=1C=CC=2OCOC2C1	(2S)-1-{[(2H-1,3-benzodioxol-5-yl)methyl]amino}propan-2-ol
3	Z2443429438	C10H15ClN2O2S	262.756	ClN[C@H]1CCN(C1)S(=O)(=O)C=2C=CC=CC2	(3S)-1-(benzenesulfonyl)pyrrolidin-3-amine hydrochloride
4	Z1259335913	C11H19N3S	225.353	CC1=NC(CN2CCC(CN)CC2)=CS1	1-{1-[(2-methyl-1,3-thiazol-4-yl)methyl]piperidin-4-yl}methanamine
5	Z241832786	C10H19N3O	197.277	CN1CCN(CC1)C(=O)C2CCCN2	1-methyl-4-(pyrrolidine-2-carbonyl)piperazine
6	Z1263714198	C8H13N3O	167.208	C(N1CCNCC1)C=2C=CON2	1-[(1,2-oxazol-3-yl)methyl]piperazine
7	Z1346370629	C7H16N2O2S	192.279	CC1CN(CCC1N)S(=O)(=O)C	1-methanesulfonyl-3-methylpiperidin-4-amine
8	Z2856434912	C15H20N2	228.332	CC1CCN(CC2=CNC=3C=CC=CC23)CC1	3-[(4-methylpiperidin-1-yl)methyl]-1H-indole
9	Z2856434879	C14H17N3	227.304	CC=1NC=NC1CN2CCC=3C=CC=CC3C2	2-[(5-methyl-1H-imidazol-4-yl)methyl]-1,2,3,4-tetrahydroisoquinoline
10	Z1650040241	C7H14N2O	142.198	CCC(=O)NC1CCNC1	N-(pyrrolidin-3-yl)propanamide
11	Z228585534	C8H15NO2	157.210	CC1CCCN(C1)C(=O)CO	2-hydroxy-1-(3-methylpiperidin-1-yl)ethan-1-one
12	Z2856434857	C8H15NO2	209.307	OC=1C=CC=C(CN2CCSCC2)C1	3-[(thiomorpholin-4-yl)methyl]phenol

Table 5.3: Binding site ligands

Chapter 6: How Does the Phosphoprotein ReoM Regulate Peptidoglycan Synthesis in *Listeria monocytogenes*?

6.1 Introduction

Transient protein phosphorylation is an important cellular process utilized by all living cells (Ardito et al., 2017). Bacteria use phosphoprotein signalling to respond efficiently to many external stimuli, such as being challenged with antibiotics (Bugrysheva et al., 2011). Gram-positive bacteria possess a conserved family of eukaryote-like serine/threonine protein kinases (eSTPKs) and partner phosphatases (eSTPs) that play a role in regulating many cellular processes, including virulence in *Staphylococcus aureus* (Zheng et al., 2018b).

One of the most well characterised eSTPKs is PrkC from *Bacillus subtilis,* which consists of an intracellular N-terminal kinase domain and an extracellular sensing region linked by a short transmembrane helix (Pompeo et al., 2018). The external regulatory region is comprised of three PASTA (**P**BP **a**nd **s**erine/**t**hreonine kinase **a**ssociated) domains that bind to peptidoglycans and compounds containing beta-lactams (Pompeo et al., 2015; Yeats et al., 2002). The principles of kinase autophosphorylation have been determined mostly in work in eukaryotes, and it has only recently been determined that this phenomenon also occurs in bacteria; the understanding of the activation mechanism in bacteria is, however, lacking (Manuse et al., 2015). In *S. aureus* the Kinase Domain (KD) of the eSTPK, Stk1, contains an activation loop that houses six phosphorylation sites to activate the kinase (Zheng et al., 2018b). Stk1 detects cell wall stress responses via its PASTA domains, which results in kinase cis-autophosphorylation on Thr172. Molecular modelling of Stk1 suggests that the autophosphorylation reconfigures the activation loop from a closed conformation to an open and active one, revealing the substrate binding site to allow trans-phosphorylation of a second kinase (Zheng et al., 2018b).

A number of eSTPK substrates are proteins involved in coordinating peptidoglycan synthesis within the division of Gram-positive bacteria (Manuse et al., 2015). Phospho-transfer profiling of the purified recombinant components has revealed that PknB, the eSTPK from *Mycobacterium tuberculosis*, phosphorylates the class A PBP PonA1 (Kieser et al., 2015) and GlmU (Parikh et al., 2009). GlmU is an important enzyme for the synthesis of UDP-Glc*N*Ac and upon phosphorylation its activity is reduced (Parikh et al., 2009). The IreK eSTPK in *Enterococcus faecalis* phosphorylates a substrate, IreB, which has been implicated as a negative regulator of cephalosporin resistance (Hall et al., 2013). The phosphorylation status of orthologous eSTPK enzymes is influenced by the presence of the cell division regulator,

GpsB, in at least *B. subtilis* and *Streptococcus pneumoniae* (Pompeo et al., 2015, 2018). As shown in Chapter 3 and previously, GpsB binds to and co-ordinates the activities of peptidoglycan synthases in *B. subtilis*, *L. monocytogenes* and *S. pneumoniae* (Cleverley et al., 2019). The Halbedel lab have identified numerous suppressor mutations in *L. monocytogenes* that restore the divisional phenotype observed with *gpsB* deletion. One of these mutations mapped to the ATPase subunit (*clpC*) of ClpCP, a heat stress protease that degrades MurA (Rismondo et al., 2017). MurA catalyses the first committed step of peptidoglycan synthesis via the transfer of enolpyruvyl from phosphoenolpyruvate to UDP-Glc*NA*c (Brown et al., 1995). Another *gpsB* suppressor mutation was mapped to the ribosomal binding site of the previously uncharacterised *lmo1503* gene, a homologue of *E. faecalis ireB* (Wamp et al., 2020).

This study will focus on the eSTPK/eSTP pair in *L. monocytogenes*, PrkA/PrpC and their relationship with a small phosphoprotein substrate, encoded by *lmo*1503, herein named ReoM. In this chapter, the phosphorylation profile of ReoM will be studied and the mechanism of activation of PrkA will be explored to identify the specific residues required for this activation. The crystal structure of full length ReoM is presented and a mechanism proposed to explain how protein:protein interactions of ReoM are affected by phosphorylation.

6.2 ReoM and PrkA form a complex

6.2.1 Native-PAGE analysis

The relationship between PrkA (encoded by *lmo1820*) and ReoM (*lmo1503*) was explored, initiated by the reported phosphorylation of the homologous IreB by IreK in *E. faecalis* (Hall et al., 2017). The kinase domain of PrkA (PrkA-KD) was first shown to interact with ReoM by native-PAGE gel electrophoresis. The isolated PrkA-KD and ReoM proteins each electrophoresed as a single species (lane 1 and lane 2, Figure 6.1). When ReoM was incubated with PrkA-KD, in the absence of ATP, a slower migrating species was observed and the individual band corresponding to PrkA-KD disappeared, indicating that the slower migrating species was a ReoM-PrkA-KD complex (lane 3 Figure 6.1). A faint band for ReoM remained, probably because the stoichiometry of the components applied to the gel did not quite match the biological stoichiometry.

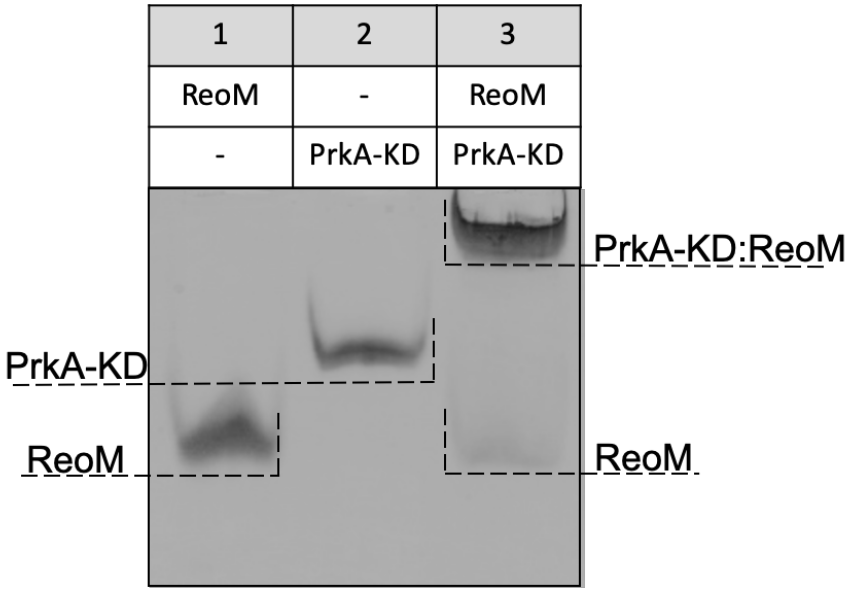

Figure 6.1: Native-PAGE analysis of the interaction between ReoM and PrkA-KD.
Components of each lane are annotated above the image and the position and identity of relevant bands are marked to the side.

Consequently, the stoichiometry of the ReoM:PrkA-KD complex was explored by incubating different ratios of the two proteins and running each of these on a native-PAGE gel (Figure 6.2). Ratios of 10:1, 5:1, 2:1 and 1:1 were chosen and the gel indicated that the ratio was close to 5:1 as there was excess ReoM in the 10:1 (Lane 3, Figure 6.2) and excess PrkA-KD in 1:1 and 2:1 (Lanes 4 and 5, Figure 6.2). The additional band beneath PrkA-KD in lanes 1, 4 and 5 (indicated by a red asterisk) was likely to be PrkA-KD with multiple phosphoryl groups as it ran further on the gel, possibly due to the presence of additional negative charge. A second band was also seen, just below the band of the PrkA-KD:ReoM complex in lanes 3 and 6 (indicated by a blue asterisk), which might represent a complex of ReoM with PrkA-KD carrying additional phosphoryl groups; the phosphorylation profile of PrkA-KD is explored in Section 6.6.4. These additional bands are not observed in Figure 6.1 and this could be explained by varying levels of PrkA-KD phosphorylation across different protein preparations of recombinantly expressed PrkA-KD. An alternative explanation for the presence of the additional bands is that the PrkA-KD run in Figure 6.2 was degrading, and the degradation product was still capable of binding to ReoM producing a faster migrating complex species.

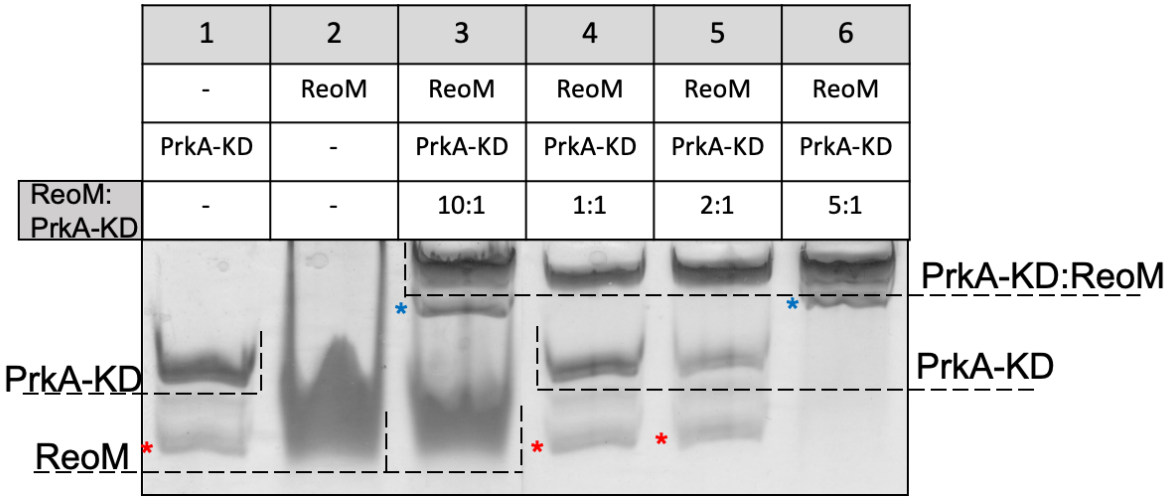

Figure 6.2: Native-PAGE analysis of ReoM:PrkA-KD stoichiometry.
Components of each lane are annotated above the image and the position and identity of relevant bands are marked to the side. The ratio of ReoM:PrkA-KD is shown in the bottom lane of the annotation. Additional bands are indicated by red and blue asterisks positioned on the left of the band, these bands are explained in the text.

6.2.2 Analytical size-exclusion chromatography

The formation of a ReoM:PrkA-KD complex was confirmed by size exclusion chromatography (Figure 6.3 A). Isolated ReoM and PrkA-KD eluted from an S200 increase column at 16 mL and 14 mL, respectively. The mixture of the two proteins with a 4-fold molar excess of ReoM (ratio determined from native-PAGE) eluted from the same column at 12 mL (Figure 6.3 B). SDS-PAGE analysis confirmed the presence of both ReoM and PrkA-KD under this peak (Fractions 17-19, Figure 6.3 C). The additional band observed in fractions 20-24 in Figure 6.3 C beneath the band for PrkA-KD was predicted to be a degradation product that is not observed when PrkA-KD is overloaded on the gel (last lane).

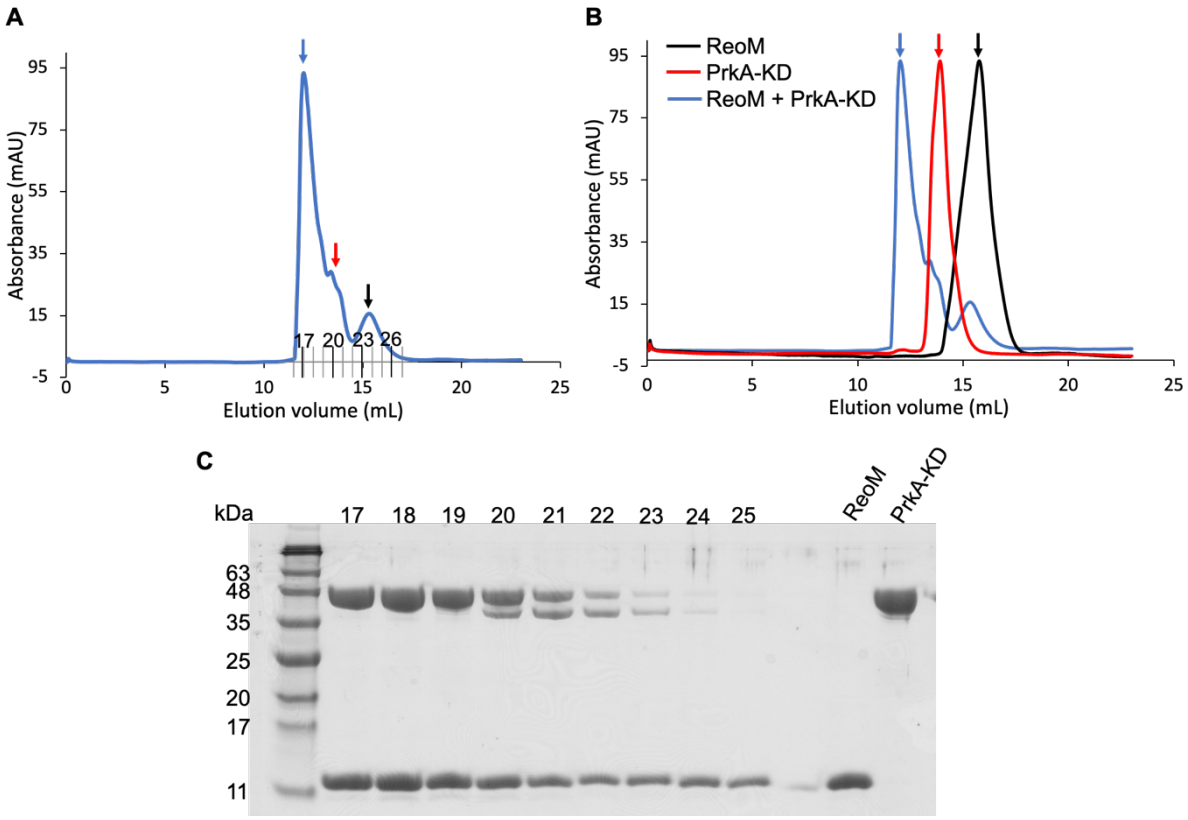

Figure 6.3: Analytical size-exclusion chromatography of ReoM and PrkA-KD.
Panel **A** is a chromatogram of an S200 10/300 GL column run of ReoM:PrkA-KD. The blue arrow indicates the elution volume of the complex, the red and black arrows show where uncomplexed PrkA-KD and ReoM elute, respectively. Fractions 17-25 were collected, and these fractions are labelled on the chromatogram. Panel **B** shows overlaid chromatograms of S200 10/300 GL column runs of ReoM, PrkA-KD and ReoM:PrkA-KD. The key indicates the colour coding for each run and the arrows above each peak indicate the elution volume. The ReoM and PrkA-KD runs have both been normalised to that of the complex. Panel **C** is an SDS-PAGE gel of the fractions collected from chromatogram shown in panel A and the number above each lane corresponds to the fraction collected. ReoM and PrkA-KD were loaded onto the final two lanes of the gel to aid identifying the proteins in each fraction. The additional band in fractions 20-24 is a predicted degradation product of PrkA-KD.

6.2.3 SEC-MALS

The oligomeric state of ReoM and PrkA-KD as well as the complex were determined using size-exclusion chromatography coupled to multi-angle light scattering (Figure 6.4). The experiments were performed and the data processed by Dr Owen Davies (Newcastle University). These data revealed ReoM had a predicted molecular mass of 25 kDa, which suggests the formation of a dimer in solution as a ReoM monomer has a mass of 10.6 kDa, a result that agrees with the oligomeric state of the homologue IreB (Hall et al., 2017). PrkA-KD had a molecular mass of 36 kDa, which is close to that expected of a monomer (37.4 kDa). The mass of the complex was determined as 82 kDa, which could account for 1:4 stoichiometry of

PrkA-KD:ReoM with 2 ReoM dimers (predicted mass 42.4 kDa) bound to a PrkA-KD monomer (37.4 kDa; total 79.8 kDa). This result also agrees with the predicted stoichiometry determined by native-PAGE analysis. The peak shapes are slightly asymmetrical, probably because the column used for the experiment had to be re-packed. The molecular masses, however, are reliable given their resemblance those predicted from sequences, the knowledge of the stoichiometry determined in an orthologous manner and that as BSA was run as a control and gave a mass of 67 kDa which is close to the known mass of 65 kDa.

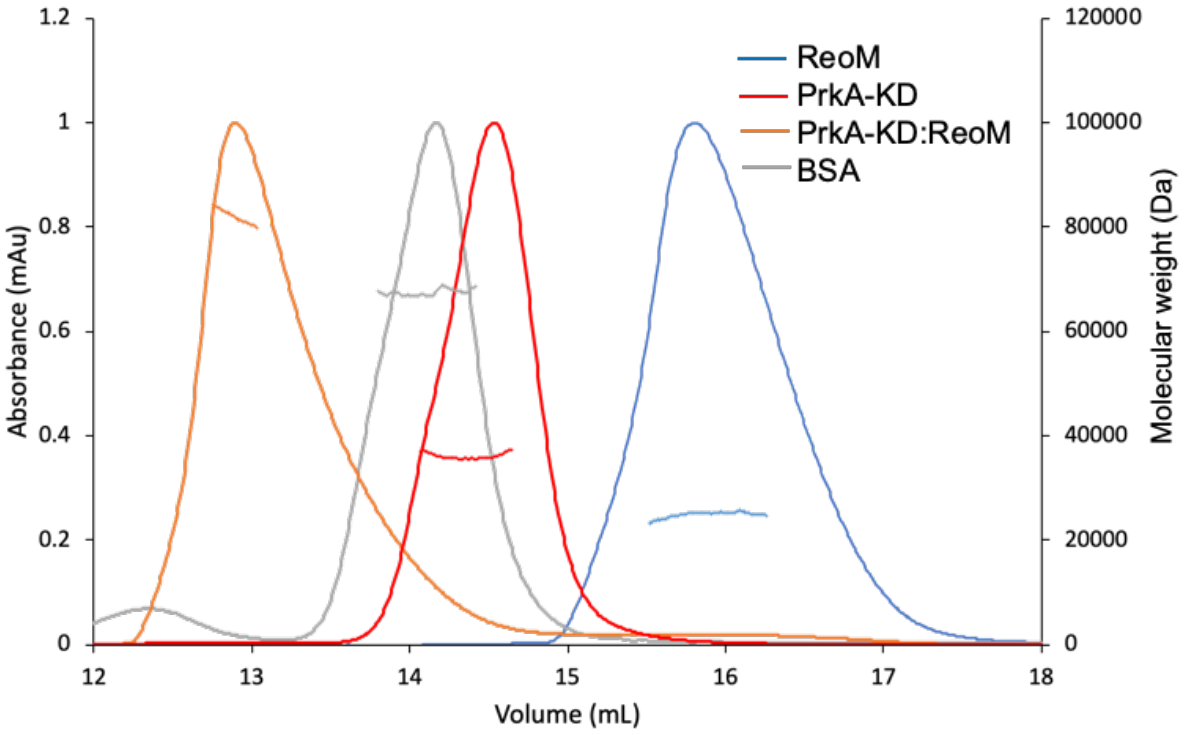

Figure 6.4: SEC-MALS analysis of ReoM, PrkA-KD and PrkA-KD:ReoM complex.
The chromatograms are relatively scaled and represent the analysis of each protein injected at 10 mg/mL, including BSA as a control. The deconvoluted molecular mass of the eluting species (coloured dots) are plotted on the right-hand axis and are coloured the same colour as the species from which they were determined. The average molecular weights determined were 25 kDa for ReoM (blue), 36 kDa for PrkA-KD (red), 82 kDa for the PrkA-KD:ReoM complex (orange) and 67kDa for BSA. The corresponding theoretical masses are 10.6 kDa (ReoM), 37.4 kDa (PrkA-KD) and 65 kDa (BSA), consistent with ReoM behaving as a dimer, PrkA-KD and BSA as monomers and the PrkA-KD:ReoM complex as a 1:2 trimer.

6.2.4 Analysis of ReoM and PrkA-KD binding by isothermal titration calorimetry

Isothermal titration calorimetry (ITC) was used to assess the binding of PrkA-KD to ReoM, which revealed a Kd of 187 ± 41.1 nM for the interaction (Figure 6.5). The binding enthalpy (ΔH) was favourable at -13.1 kcal mol^{-1}, which indicates the interaction is dominated by electrostatics. The entropic component (-TΔS) was unfavourable at 4.09 kcal mol^{-1}, also

consistent with the requirement of some conformational changes that had to take place, alongside the hydrogen bonding, for the interaction to occur. The N value determined was 0.256, which meant 4 molecules of ReoM bound to each PrkA-KD molecule, a result that agreed closely with the results from Native-PAGE and SEC-MALS. Buffer runs showed that ReoM and PrkA-KD produced negligible heat changes when injected into ITC buffer or when ITC buffer was injected into the cell containing either protein (Figure 6.5 B and C). This showed that the heat change for the interaction was not an artefact.

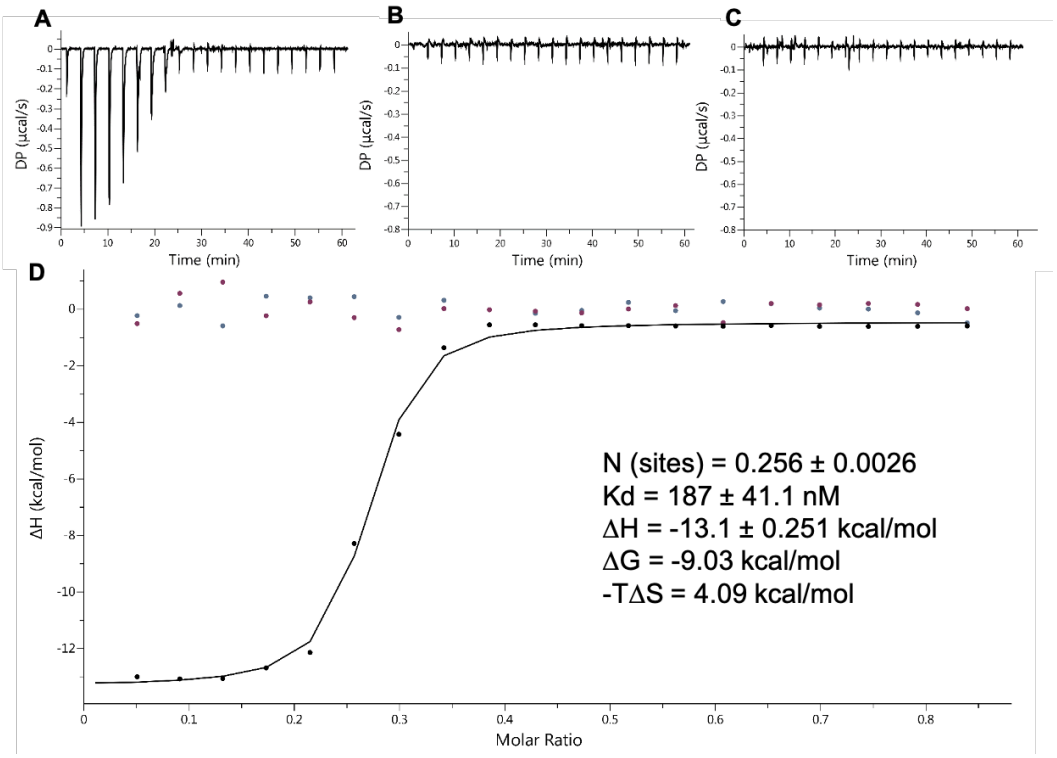

Figure 6.5: Interaction of ReoM and PrkA-KD analysed by ITC.
Panels **A** shows the ITC raw heat plot for 20 injections of PrkA-KD at 400 µM into 100 µM of ReoM in the cell. Panel **B** shows the ITC raw heats for 20 injections of PrkA-KD into buffer (10 mM HEPES pH 8, 100 mM NaCl) and panel **C** shows raw heats of 20 injections of buffer into ReoM. Panel **D** shows the integrated binding heats (black circles) fit to a single set of sites model (black line) to determine N, Kd, ΔH, ΔG and -TΔS. Integrated heats for the controls are also shown (B, blue; C, red).

A comparable Kd of 372 ± 137 nM was produced with ReoM in the syringe injected into the cell containing PrkA-KD (Figure 6.6), with a stoichiometry parameter N of 3.2, not inconsistent with that obtained in the reciprocal injection described above.

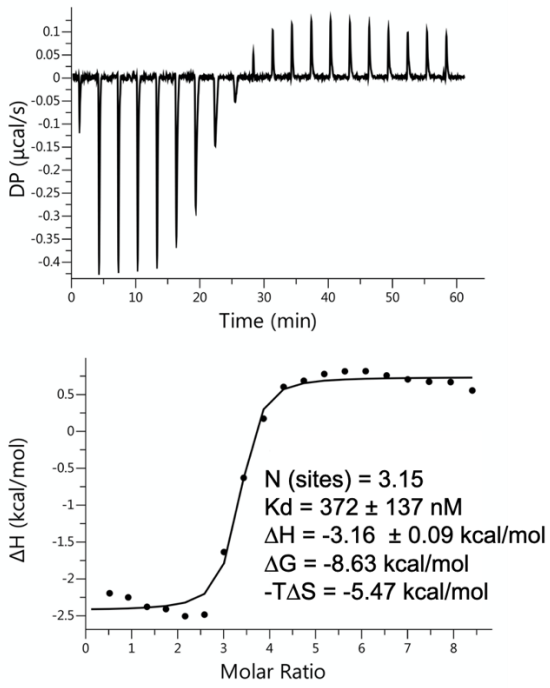

Figure 6.6: Interaction of ReoM and PrkA-KD analysed by ITC.
The top graph shows the ITC raw heat plot for 20 injections of ReoM at 1mM into 25 µM of PrkA-KD in the cell. Below are the integrated binding heats (black circles) fit to a single set of sites model (black line) to determine N, Kd, ΔH, ΔG and -TΔS.

6.3 Phosphorylation of ReoM by PrkA-KD

Some passages in this section have been quoted verbatim from Wamp *et al.* (2020) in which I am the second author. Any passages used are my own work.

6.3.1 Native-PAGE analysis of the phosphorylation of ReoM by PrkA-KD

Proteins with altered size, shape or charge can run differently on a native-PAGE gel therefore, phosphorylation of ReoM by PrkA-KD was first analysed by native-PAGE electrophoresis to see if the addition of a phosphoryl group caused the protein to run differently. When ReoM was incubated with PrkA-KD, Mg^{2+} (eSTPK enzymes are Mg^{2+} dependent (Pompeo et al., 2015)) and ATP, a band for free PrkA-KD was observed but there were no visible bands for ReoM and the ReoM:PrkA-KD complex. Instead a new species was present, migrating further in the gel than ReoM (lane 4, Figure 6.7), which is likely to be phosphorylated ReoM (P-ReoM). The additional negative charges on P-ReoM would cause the protein to visibly run further on the gel towards the cathode compared to ReoM. The absence of a ReoM:PrkA-KD complex with the addition of Mg and ATP suggested that the two proteins no longer associate after phosphorylation.

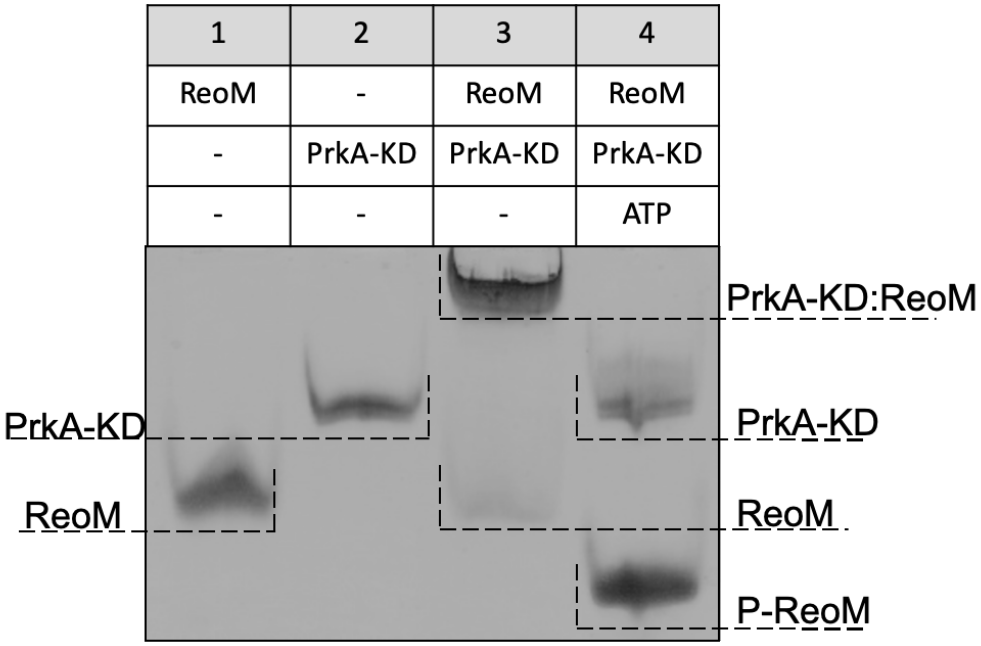

Figure 6.7: Native-PAGE analysis of the phosphorylation of ReoM by PrkA-KD.
Components of each lane are annotated above the image and the position and identity of relevant bands are marked to the side. P-ReoM is the phosphorylated form of ReoM.

6.3.2 Isolation of P-ReoM

The phosphorylation of ReoM was scaled up in order to isolate it from PrkA-KD and any unphosphorylated ReoM. P-ReoM was successfully purified by anion exchange (Figure 6.8 A) and confirmed by native-PAGE (Figure 6.8 B). Fraction 8 was chosen as P-ReoM for further analysis by LC-MS, ITC and native-PAGE.

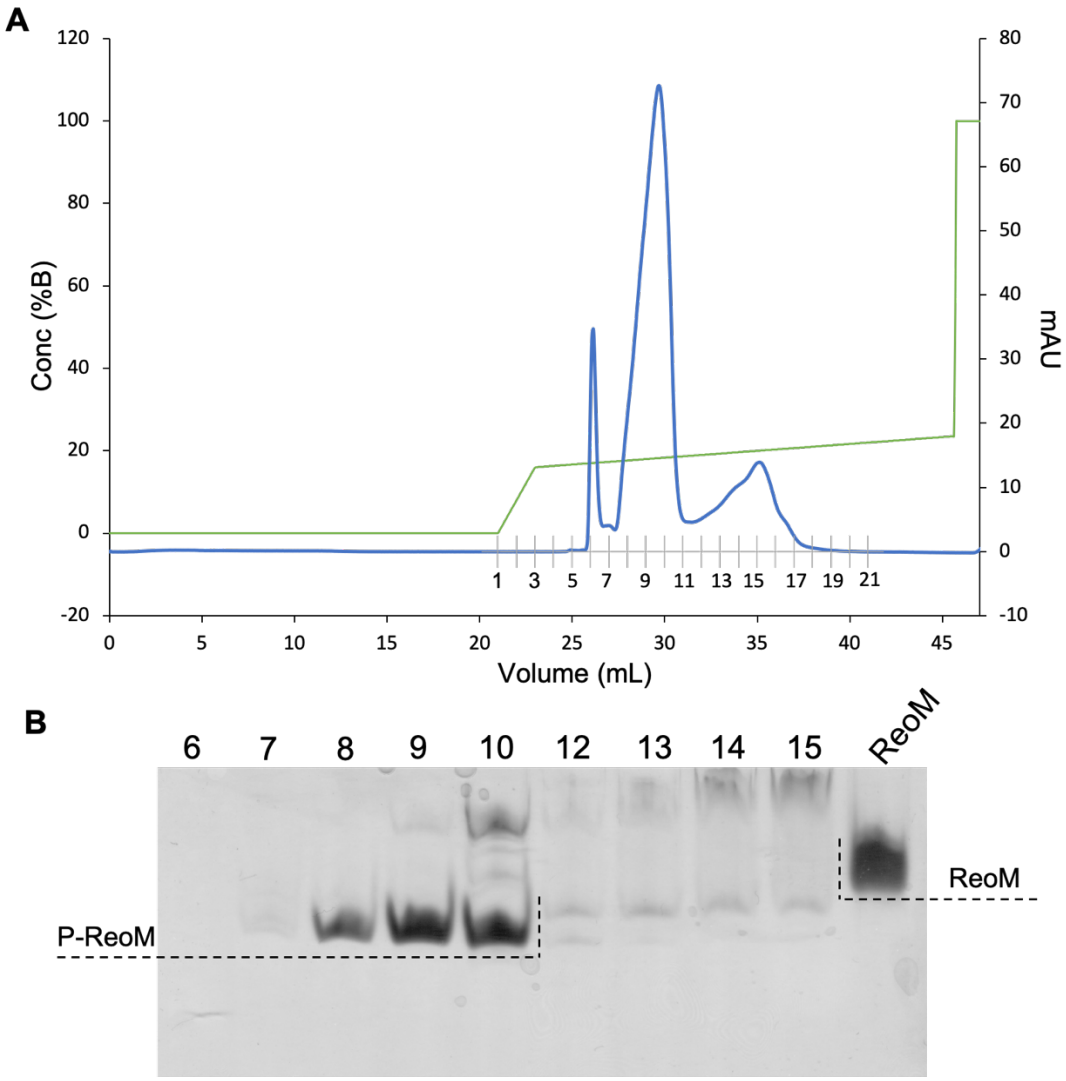

Figure 6.8: Purification of P-ReoM.
Panel **A** shows a MonoQ 5/50 GL chromatogram of a ReoM phosphorylation reaction. The blue trace is the measured mAU and the green trace is the concentration of NaCl (Conc % B). The fractions that were collected for analysis are labelled on the graph. Panel **B** shows a native-PAGE gel of the fractions collected in **A**. The corresponding fraction is labelled above each lane and the final lane contains ReoM as a control.

6.3.3 Mass spectrometry to identify the phosphorylated residue in ReoM

Liquid chromatography-mass spectrometry (LC-MS) analysis* of ReoM isolated from PrkA-KD after phosphorylation revealed the addition of 79.9 Da in comparison to the mass of unmodified ReoM (10671.5 Da), which corresponds to the formation of a singly-phosphorylated ReoM product of 10751.4 Da (Figure 6.9). MS/MS spectra obtained during peptide mass fingerprinting were also consistent with one phosphorylation event per protein chain; one ReoM peptide, spanning residues Asp5 to Lys22 with mass of 2151.89 Da, was increased by 79.96 Da after incubation with PrkA-KD and Mg/ATP. Analysis of the *y*- and *b*-

ions in the MS/MS fragmentation spectrum of this peptide was consistent only with Thr7 as the sole phosphosite in ReoM (Figure 6.10). This result is consistent with the observation from a phosphoproteomics study that identified Thr7 as a phosphorylation site in Lmo1503 (ReoM) (Misra et al., 2011). The importance of Thr7 in ReoM function is also highlighted by its high sequence conservation (96%) across all 2909 ReoM homologues present at NCBI.

*All Mass spectrometry experiments in this chapter were performed by Dr Claire Jennings, Newcastle University.

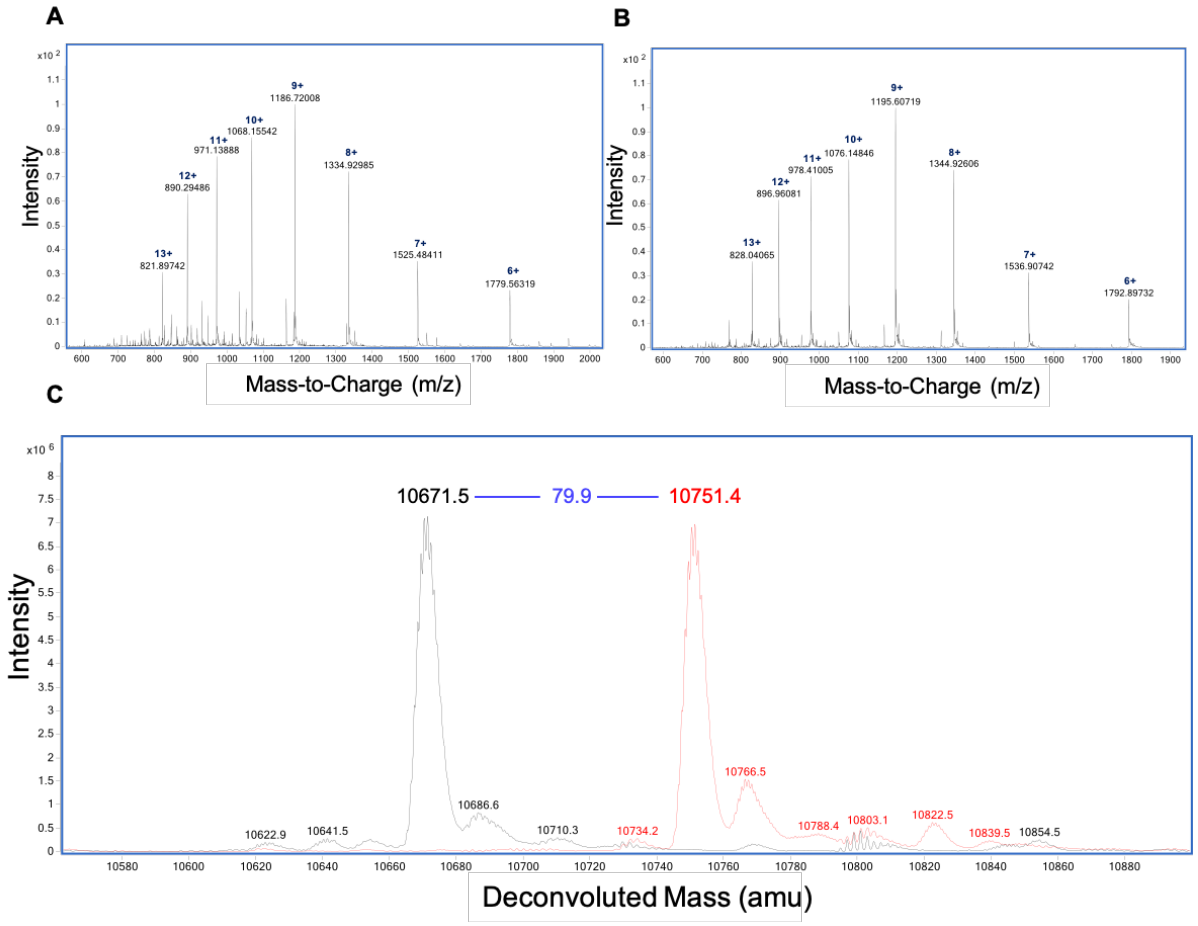

Figure 6.9: LC-MS analysis of ReoM and P-ReoM.
Panel **A** and **B** show the ESI-QTOF raw data for non-phosphorylated ReoM and mono-phosphorylated ReoM, respectively. Panel **C** is the deconvoluted mass spectrum for non-phosphorylated ReoM (black) overlaid over the equivalent spectrum for mono-phosphorylated ReoM, P-ReoM (red). The difference between the major peak of ReoM and P-ReoM is shown by blue labelling and is the equivalent of one phosphoryl group.

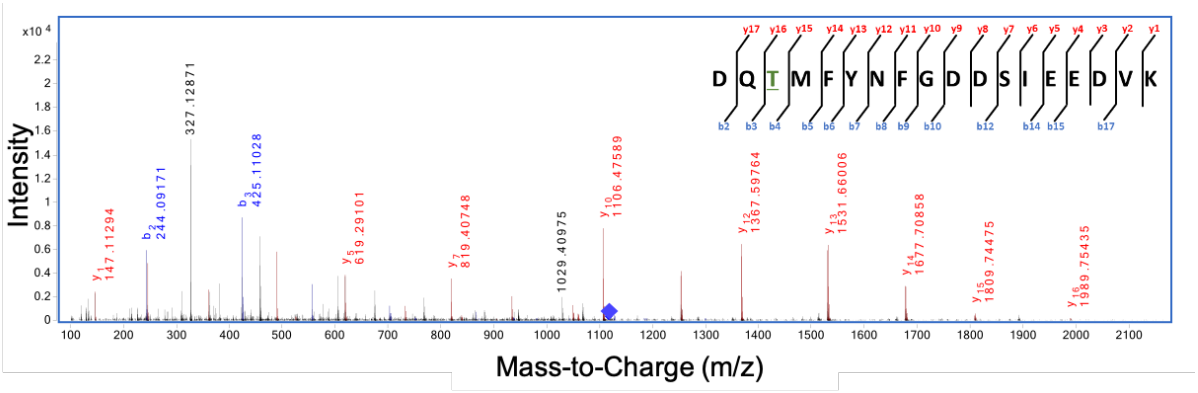

Figure 6.10: LC-MS/MS analysis of P-ReoM.
LC-MS/MS was used to perform peptide mapping analysis on P-ReoM, revealing Thr7 is the sole phosphosite. The MS/MS fragmentation spectra of the phosphorylated peptide encompassing Asp5-Lys22 is presented with *b*-ion fragmentation in blue and *y*-ion fragmentation shown in red, whilst the precursor ion (m/z 1116.86, z=2+) is represented by a blue diamond.

6.3.4 Analysis of the interaction between P-ReoM and PrkA-KD by isothermal titration calorimetry

The binding of P-ReoM to PrkA-KD was analysed by ITC to determine if there was a change in affinity after phosphorylation. No binding could be detected for the two proteins, which suggested that once ReoM is phosphorylated it can no longer bind to PrkA (Figure 6.11), consistent with the Native-PAGE analysis (Figure 6.7).

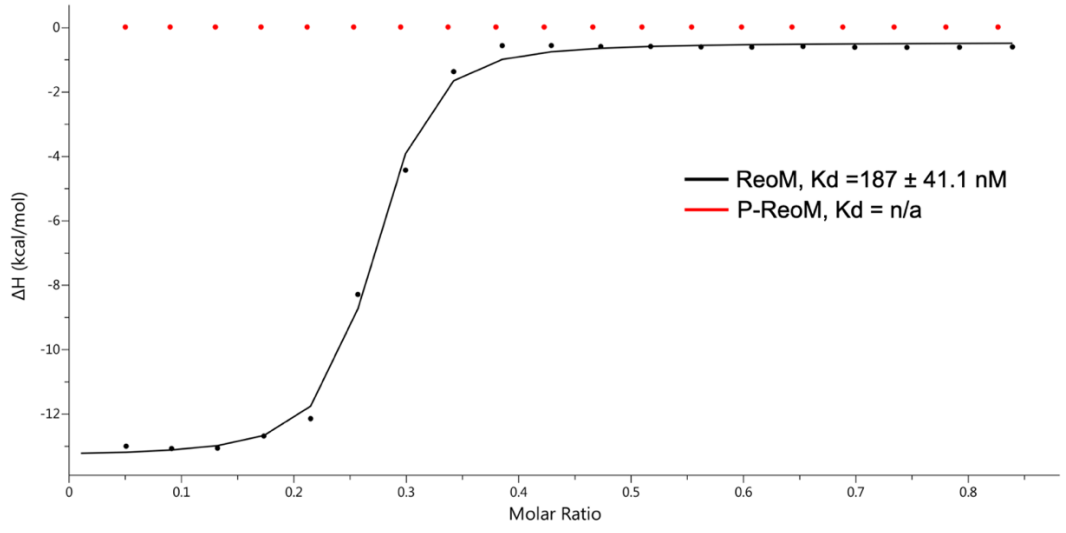

Figure 6.11: Interaction of ReoM and P-ReoM with PrkA-KD monitored by ITC.
Integrated ITC traces of ReoM and P-ReoM at 100 µM in the cell versus 400 µM of PrkA-KD in the syringe: the key indicates which variant is shown and their respective Kd.

6.3.5 Analytical size-exclusion chromatography and circular dichroism of ReoM and P-ReoM

Analysis of the oligomeric state of P-ReoM by size exclusion chromatography revealed that the protein behaved in solution the same as that of unphosphorylated ReoM; both variants eluted from the column at 14.6 mL (Figure 6.12) suggesting that the electrophoretic behaviour of P-ReoM on native-PAGE is not due to an altered oligomeric state. Circular dichroism of ReoM and P-ReoM also revealed that the two proteins had similar secondary structures and any structural changes due to phosphorylation did not grossly alter the structure, rather being limited to the movement of a loop or a flexible region (Figure 6.13).

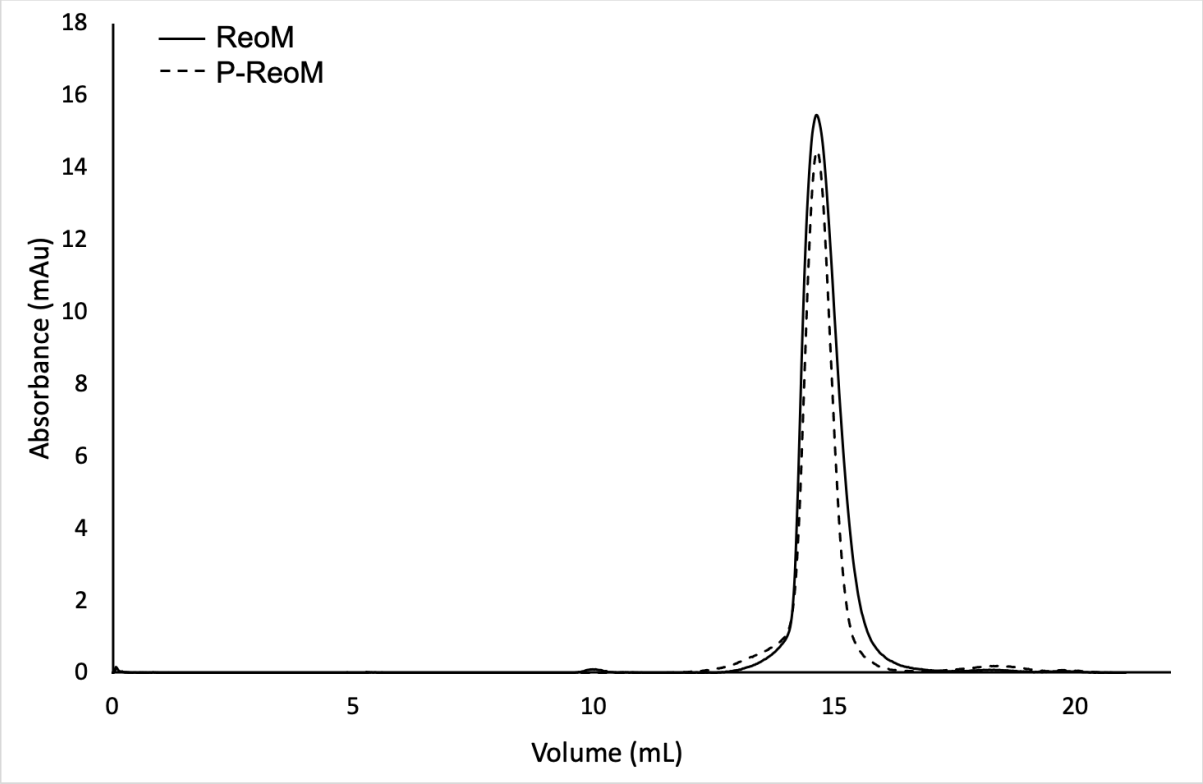

Figure 6.12: ReoM and P-ReoM have the same oligomeric state.
Size exclusion chromatography analysis of ReoM and P-ReoM showed that phosphorylation of ReoM did not alter its oligomeric state. Both ReoM (solid) and P-ReoM (dashed) had an elution volume at 14.6 mL. Details of the experimental procedure can be found in 2.2.8.

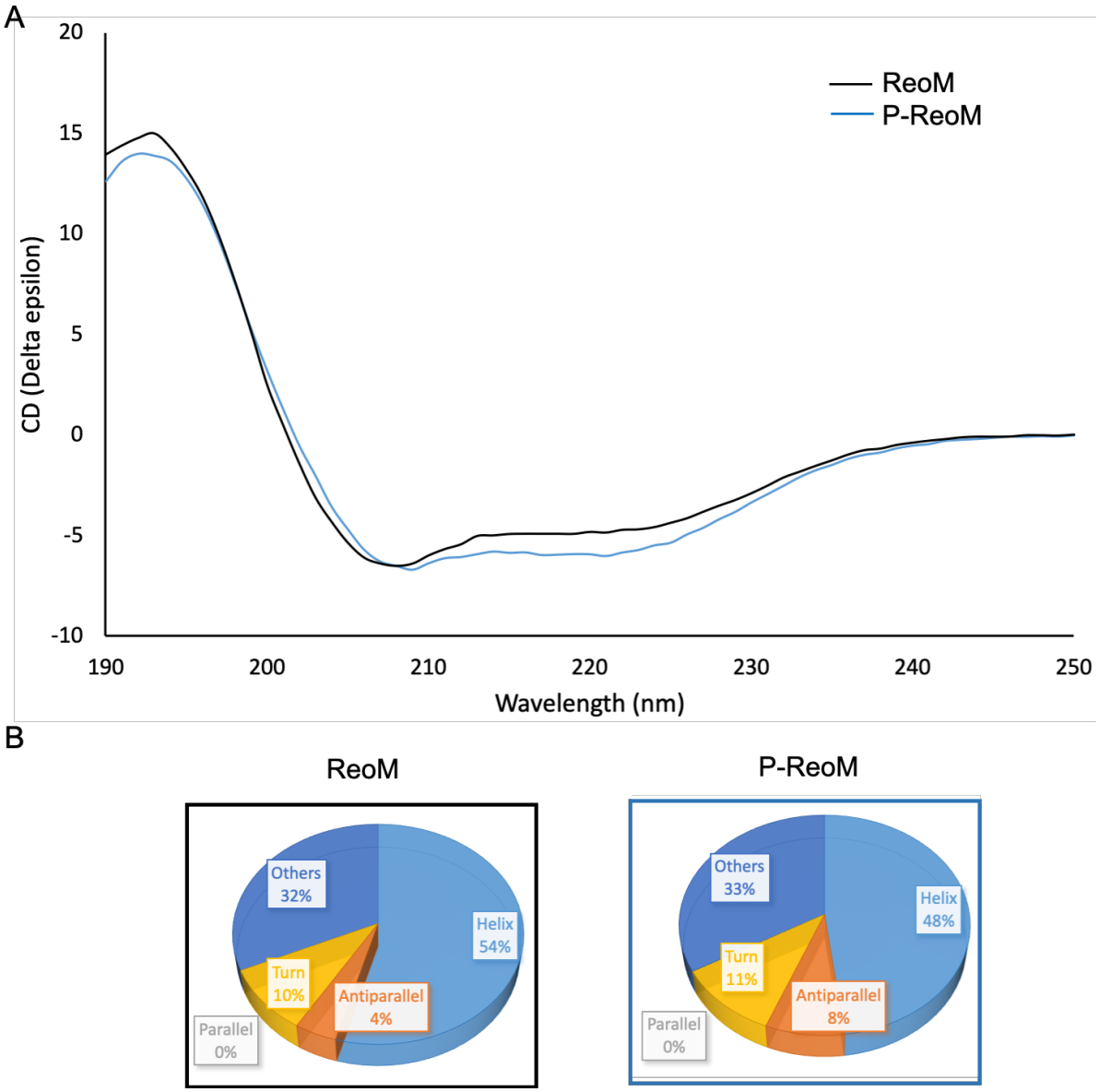

Figure 6.13: Secondary structure determination of ReoM and P-ReoM.
A. Circular dichroism spectra of ReoM and P-ReoM were analysed using BeStsel (Micsonai et al., 2018); CD spectra were converted from millidegrees to delta epsilon. Shown here is the experimental data and the key indicates which data set is represented. **B.** Secondary structure prediction of ReoM and P-ReoM determined by BeStsel (Micsonai et al., 2018) from the CD spectra. The percentage of each element is displayed in a pie chart. There is negligible structural change on phosphorylation of ReoM.

6.4 Crystallisation of ReoM

Some passages in this section have been quoted verbatim from Wamp *et al.* (2020) in which I am the second author. Any passages used are my own work.

6.4.1 Crystallisation trials

ReoM at a concentration of 23 mg/mL in a buffer of 10 mM Na-HEPES pH 8, 100 mM NaCl was subjected to crystallisation using a number of sparse matrix crystallisation screens. Crystals of ReoM grew in 3 different conditions from the JCSG+ crystallisation screen: A3 (0.2 M di-ammonium hydrogen citrate, 20 % PEG 3000), A6 (0.1 M phosphate/citrate pH 4.2, 0.2 M lithium sulfate, 20 % w/v PEG 1000) and C12 (10 % w/v PEG 1000/ 10 % w/v PEG 8000) (Figure 6.14). In each drop the crystals grew in clusters and were either rod shaped or cuboidal-like.

Crystallisation of P-ReoM and PrkA-KD:ReoM was attempted using a number of sparse matrix crystallisation screens but no crystals were obtained.

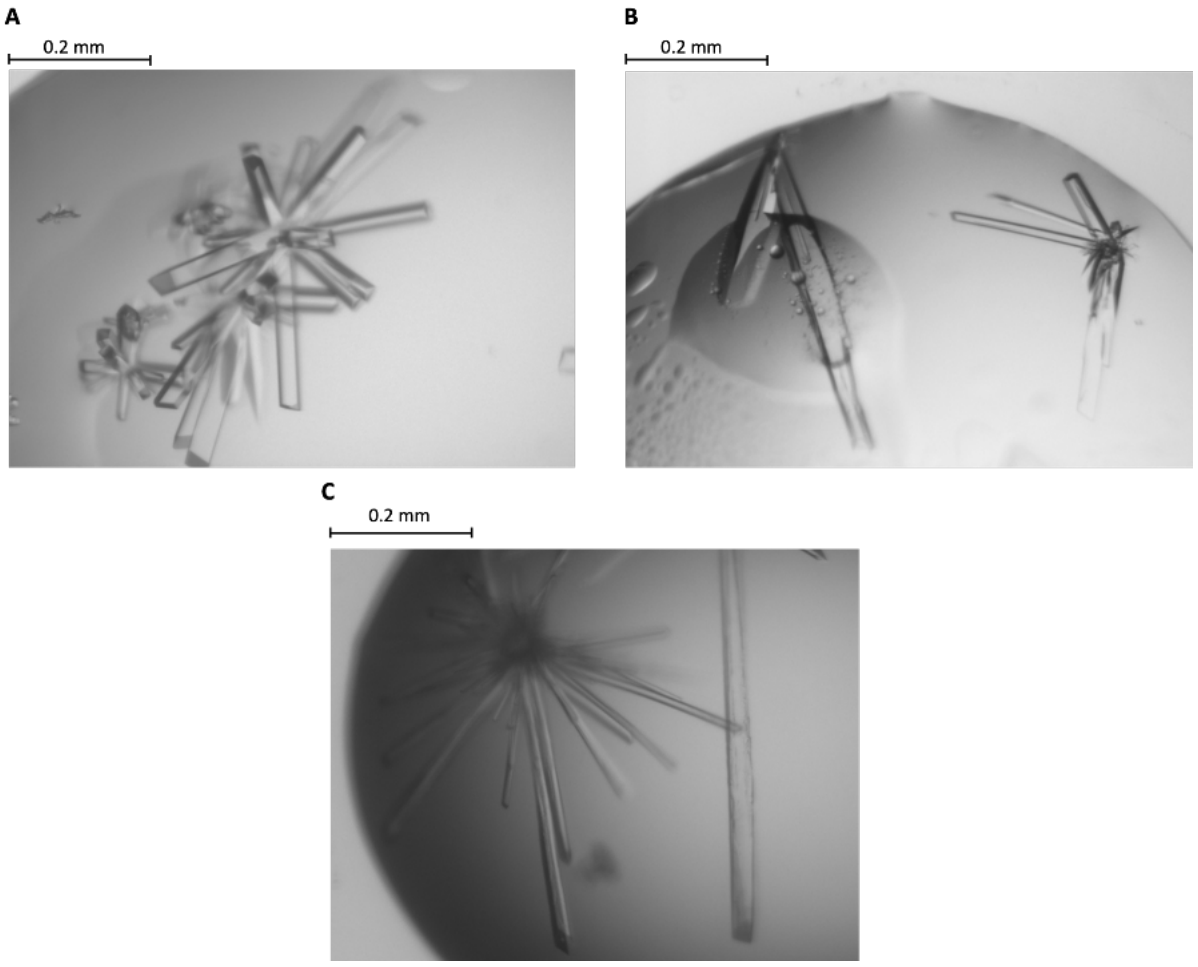

Figure 6.14: Crystals of ReoM.
Panel **A** is a drop from JCSG+ A6, panel **B** is a drop from JCSG+ A3 and panel **C** is a drop from JSCG+ C12 in which crystals grew with the addition of ReoM at 23 mg/mL. The scale bar above each image provide a visual indication of the size of each crystal.

6.4.2 Data processing, molecular replacement and model building

The diffraction data for a crystal harvested from JCSG+ A6 were collected at Diamond Light Source I03 beamline. Diffraction data were processed and the structure of ReoM was solved to 1.6 Å by molecular replacement using the NMR structure of IreB (PDB ID: 5US5) as described in 2.4.4. The resultant molecular model was refined to convergence and the data collection and refinement statistics for the final structure of ReoM can be found in Table 6.1.

6.4.3 Analysis of the ReoM structure

Perhaps unsurprisingly ReoM shares the same overall fold as IreB (Hall et al., 2017), each containing a compact 5-helical bundle (4 standard α-helices and one single-turned 3_{10}-helix between residues 52 and 54) with short loops between the secondary structure elements. Other than IreB (Hall et al., 2017), there are no structural homologues of ReoM with functional significance in the PDB (Figure 6.15).

No:	Chain	Z	rmsd	lali	nres	%id	PDB	Description
1:	5us5-A	11.0	1.9	73	89	64		MOLECULE: UPF0297 PROTEIN EF_1202;
2:	5us5-B	10.7	2.3	74	89	64		MOLECULE: UPF0297 PROTEIN EF_1202;
3:	6psv-L	5.1	4.0	79	474	8		MOLECULE: PROTEIN TRAR;
4:	6n58-L	4.8	3.8	79	547	8		MOLECULE: DNA-DIRECTED RNA POLYMERASE SUBUNIT ALPHA;
5:	4mey-F	4.8	4.0	79	464	8		MOLECULE: DNA-DIRECTED RNA POLYMERASE SUBUNIT ALPHA;
6:	6pst-L	4.7	4.1	80	558	9		MOLECULE: PROTEIN TRAR;
7:	5vt0-L	4.6	4.0	79	471	8		MOLECULE: DNA-DIRECTED RNA POLYMERASE SUBUNIT ALPHA;
8:	6psw-L	4.6	3.8	79	473	8		MOLECULE: DNA-DIRECTED RNA POLYMERASE SUBUNIT ALPHA;
9:	4wfg-B	4.5	4.8	76	255	5		MOLECULE: POTASSIUM CHANNEL SUBFAMILY K MEMBER 4;
10:	6ago-C	4.5	3.5	65	167	8		MOLECULE: HISTONE-LYSINE N-METHYLTRANSFERASE ASH1L;
11:	6ux7-A	4.5	4.3	64	304	8		MOLECULE: CALCIUM-GATED POTASSIUM CHANNEL MTHK;
12:	3ldc-A	4.5	4.3	64	82	8		MOLECULE: CALCIUM-GATED POTASSIUM CHANNEL MTHK;
13:	4qe7-A	4.5	4.1	62	81	8		MOLECULE: CALCIUM-GATED POTASSIUM CHANNEL MTHK;
14:	4llg-F	4.4	4.2	80	521	8		MOLECULE: DNA-DIRECTED RNA POLYMERASE SUBUNIT ALPHA;
15:	6u6e-D	4.4	4.9	70	304	10		MOLECULE: CALCIUM-GATED POTASSIUM CHANNEL MTHK;
16:	6ufe-A	4.4	4.4	65	90	6		MOLECULE: TRANSPORTER;
17:	2hoi-H	4.4	3.5	59	322	8		MOLECULE: LOXP DNA;
18:	6n61-F	4.4	3.7	78	395	6		MOLECULE: DNA-DIRECTED RNA POLYMERASE SUBUNIT ALPHA;
19:	3k06-A	4.4	4.4	65	90	6		MOLECULE: POTASSIUM CHANNEL PROTEIN NAK;
20:	4hz3-E	4.4	4.4	66	82	8		MOLECULE: CALCIUM-GATED POTASSIUM CHANNEL MTHK;

Figure 6.15: A DALI search (Holm, 2020) with ReoM.
The top 20 matches against the full PDB of ReoM. Matches are ordered based on Z-score and the top two matches shown in the red box are chain A and B of IreB (PDB ID: 5US5).

The helical bundles in both ReoM and IreB associate into homodimers with α-helices two and four from each protomer forming the majority of the homodimer interface, and these residues are highlighted in Figure 6.16 A. In agreement with the IreB structural analysis, 1200 $Å^2$ of surface area is buried in the ReoM dimer interface, representing 9% of the total solvent accessible surface area.

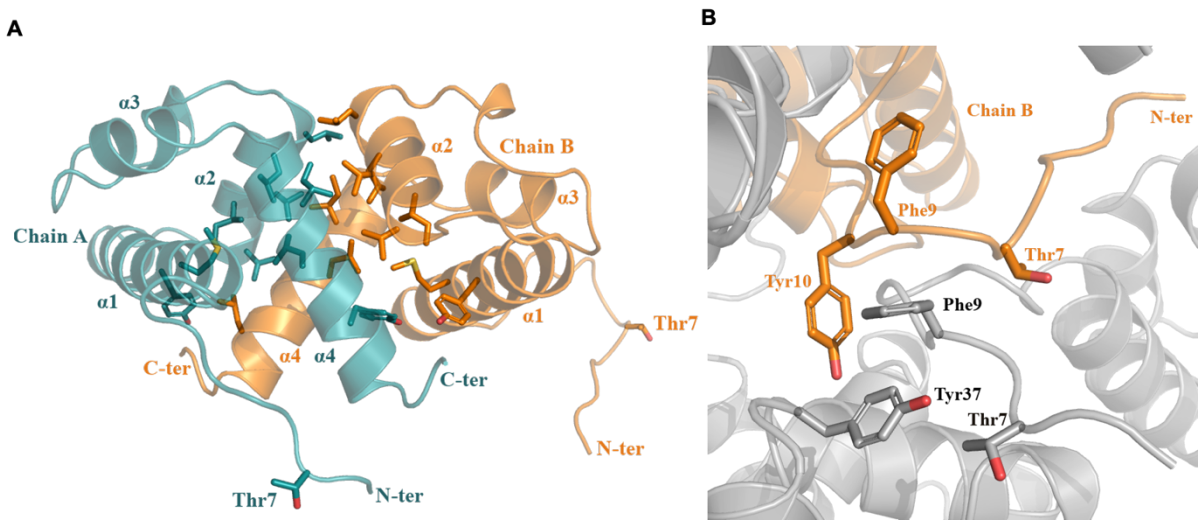

Figure 6.16: Crystal structure of ReoM.
Panel **A** is the structure of ReoM depicted as a cartoon with each protomer in the dimer coloured separately (cyan and orange). The secondary structure elements are numbered according to their position in the amino acid sequence. Thr7 and some of the key amino acids in the dimer interface and the hydrophobic core are drawn as stick figures. Panel **B** shows the stabilisation of the N-terminus in chain B. Chain B is coloured orange and symmetry related residues are in grey. The aromatic residues involved in a network of hydrophobic interactions are drawn in stick form as well as Thr7.

Other than the compact helical bundle of ReoM, there is a ~16 residue-long N-terminal tail, with B-factors 25% higher than the rest of the protein, prior to the start of α-helix 1 at residue Ile17. The equivalent N-terminal region is also disordered in the NMR structure of IreB (Hall et al., 2017). Despite the absence of secondary structure, the ReoM model covering this region could be built with confidence from Asp5 in chain A and Asp2 in chain B (Figure 6.17 A). The extended N-terminal regions are at least partially stabilised by crystal lattice interactions that, in chain B, include Phe9 and Tyr10 forming a network of hydrophobic interactions with other aromatic residues from symmetry equivalent molecules, including contributions from another copy of Phe9 and Tyr10 (Figure 6.16 B).

Consequently, it is possible to visualise Thr7, the target for phosphorylation by PrkA, in the flexible N-terminal region in both chains. The side chain of Thr7 in both chains makes no intramolecular interactions and is thus amenable to phosphorylation by PrkA. The presence of a sulphate ion (a component of the crystallisation reagent) adjacent to the sidechain of Thr7 could mimic what P-ReoM might look like (Figure 6.17). The sulphate ion is captured by a positively-charged micro-environment incorporating residues Lys35, Arg57, His58 and Arg62 from a symmetry-equivalent molecule (Figure 6.17 B).

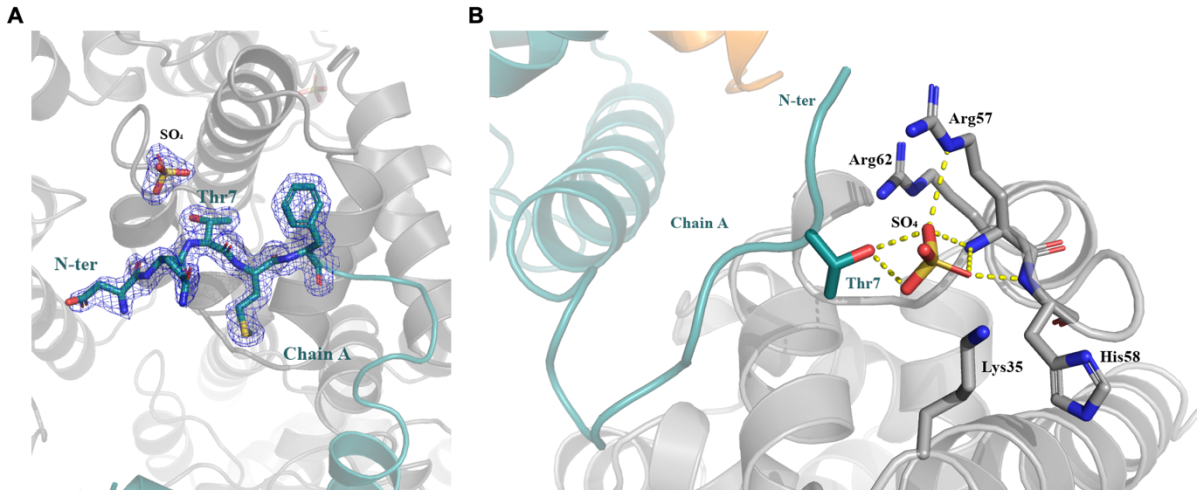

Figure 6.17: Microenvironment of the sulphate ion bound to Thr7.
Panel **A** shows the final $2F_{obs}$ -F_{calc} electron density map, contoured at a level of 0.42 electrons per $Å^3$, at the N-terminus of chain A (cyan) in the immediate vicinity of Thr7 and of a sulphate ion. Symmetry related residues are coloured grey. Panel **B** highlights the positively charged residues from a symmetry related molecule (drawn in stick form) that form hydrogen bonds (yellow dashed lines) with the sulphate.

6.5 Mutational analysis of ReoM

Some passages in this section have been quoted verbatim from Wamp *et al.* (2020) in which I am the second author. Any passages used are my own work.

6.5.1 Native-PAGE to analyse the behaviour of ReoM when threonine 7 is mutated

Since Thr7 had been identified as the phosphorylation site on ReoM, it was mutated to both an alanine and aspartic acid to explore the effect of ablating and mimicking phosphorylation, respectively. Both $ReoM^{Thr7Ala}$ and $ReoM^{Thr7Asp}$ appeared to interact with PrkA-KD, as a complex band was observed on native-PAGE when the mutants were mixed with the kinase (lanes 6 and 9, Figure 6.18). Unlike with wild-type ReoM (lane 3, Figure 6.18) this complex band remained after the addition of ATP with both mutants (lanes 7 and 10, Figure 6.18). As expected, this result indicates that a clear phosphorylation reaction did not occur, because after phosphorylation of wildtype ReoM it can no longer bind to PrkA-KD (Figure 6.11). In addition, only a slight shift was observed for $ReoM^{Thr7Ala}$, running further on the gel (lane 7, Figure 6.18) and no clear shift was seen with $ReoM^{Thr7Asp}$ (lane 10, Figure 6.18) after incubation with ATP, compared to wildtype ReoM (lane 3). The shift seen for $ReoM^{Thr7Ala}$ could point to a second, non-specific phosphorylation site. The band for $ReoM^{Thr7Asp}$ (lane 8, Figure 6.18) ran

further in the gel than ReoM (lane 1, Figure 6.18), as expected due to the additional aspartate residue (phosphomimetic) in place of a threonine residue.

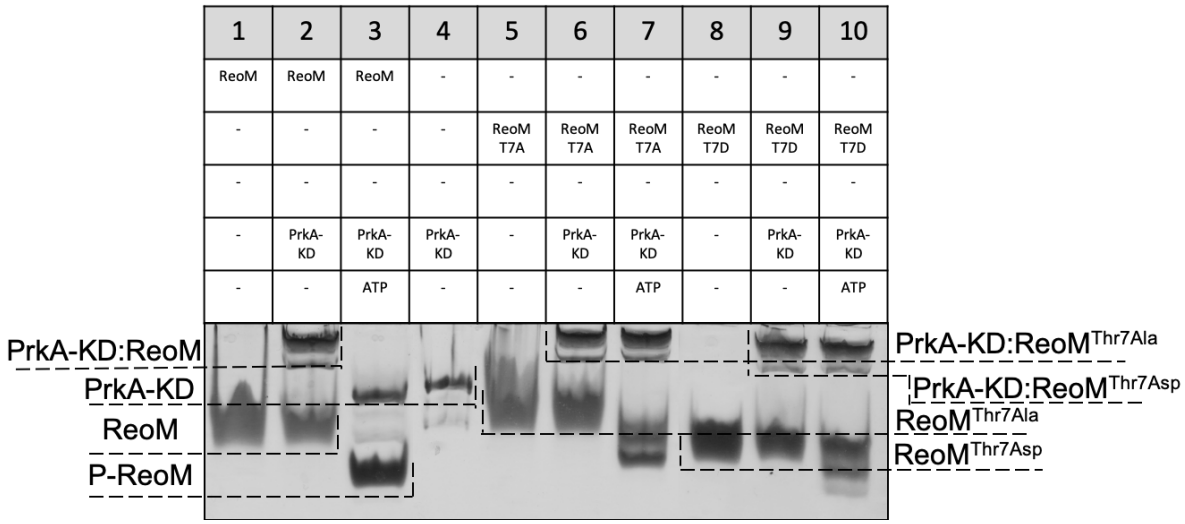

Figure 6.18: Native-PAGE of ReoM Thr7 mutation phosphorylation reactions.
Components of each lane are annotated above the image.

6.5.2 Analysis of the interaction between ReoM and ReoM variants with PrkA-KD using isothermal titration calorimetry

The strength of the interactions of Thr7 mutants with PrkA-KD was measured using ITC. ReoM^{Thr7Ala} had a Kd of 654 ± 127 nM for PrkA-KD, which was a 3-fold decrease in affinity compared to wild-type, whereas ReoM^{Thr7Asp} had a Kd of 855 ± 189 nM which was a 4-fold decrease in affinity compared to WT (Figure 6.19). The binding enthalpy in both cases was more favourable with values of -19.8 kcal mol^{-1} (Thr7Ala) and -14.1 kcal mol^{-1} (Thr7Asp), however the entropy factor was more unfavourable at 11.5 kcal mol^{-1} and 5.96 kcal mol^{-1}. An interaction could not be detected for P-ReoM with PrkA-KD, which is consistent with the results from native-PAGE with the complex band disappearing after phosphorylation. The slight reduction in affinity observed with ReoM^{Thr7Ala} could be explained by the loss of the hydroxyl group of Thr7 that weakly affected the interaction but not to a substantial degree. The retention of binding of PrkA-KD to ReoM^{Thr7Asp}, albeit with a 4-fold lower affinity than WT, indicates the mutation of threonine 7 to an aspartate is not an ideal phosphomimetic in this instance. Aspartate and glutamate residues are not complete chemical mimics of phosphothreonine and therefore phosphomimetic mutations do not work in every case (Dephoure et al., 2013). Aspartic and glutamic acid are smaller than phosphoserine/threonine and carry a net negative charge of -1 compared to -2 of the phospho-residue. Furthermore,

aspartic and glutamic acid have trigonal planar geometry which does not completely mimic the shape of a phosphoserine/threonine with tetrahedral geometry.

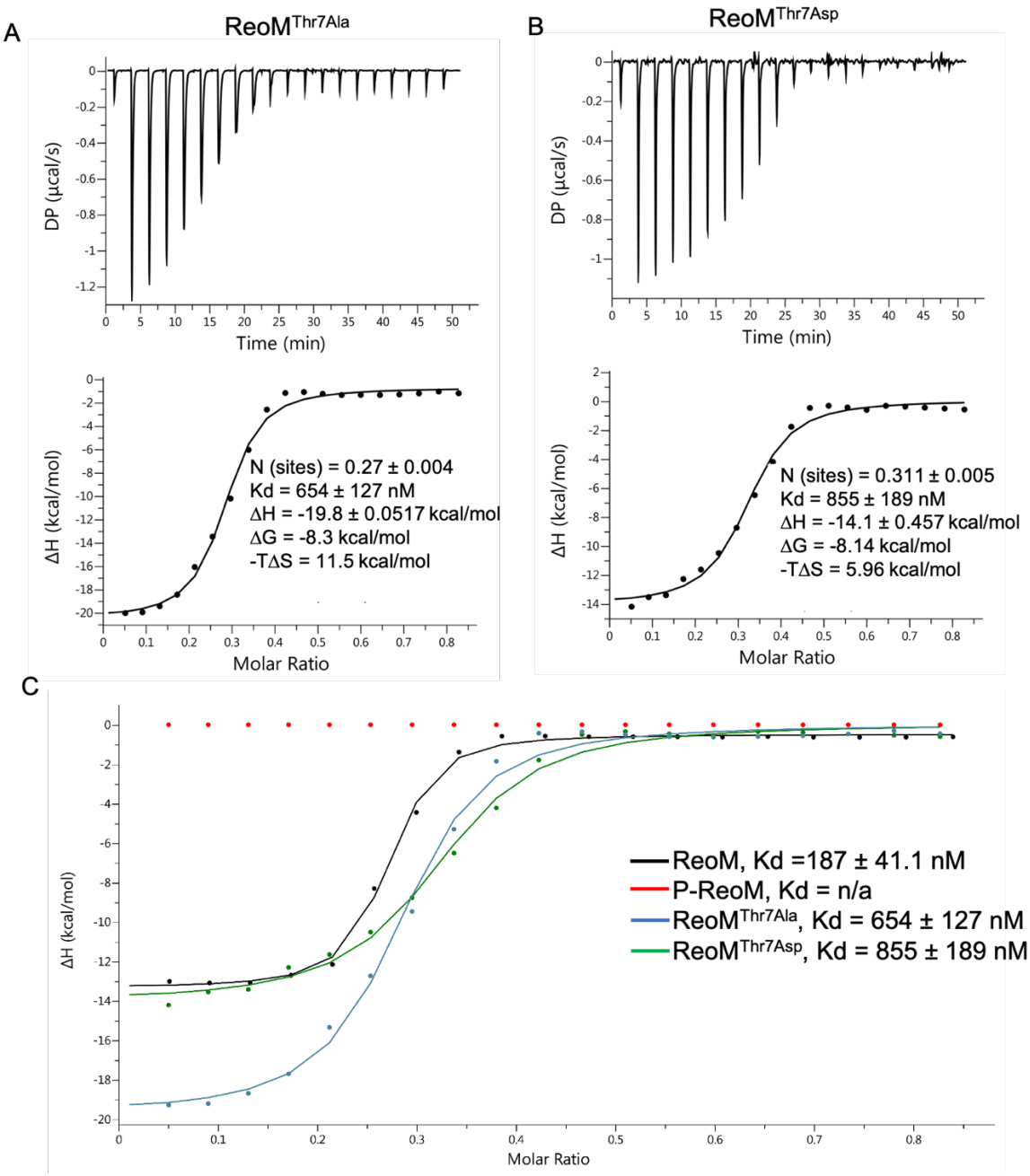

Figure 6.19: Interaction of ReoM and ReoM variants with PrkA-KD monitored by ITC.
ITC raw heat plots and integrated binding heats for 20 injections of PrkA-KD at 400 µM into 100 µM of ReoM^{Thr7Ala} (**A**) and ReoM^{Thr7Asp} (**B**) in the cell. Integrated binding heats were fit to a single set of sites model to determine N, Kd, ΔH, ΔG and -TΔS. **C.** Integrated ITC traces of ReoM variants at 100 µM in the cell versus 400 µM of PrkA-KD in the syringe. The key indicates which variant is shown and the respective Kd that was determined.

6.5.3 Mass spectrometry analysis of ReoM^{Thr7Ala}

The slight shift in ReoM^{Thr7Ala} on a native-PAGE gel after incubation with PrkA-KD prompted analysis of this mutant by intact LC-MS to see if there was a secondary phosphorylation site. Both ReoM^{Thr7Ala} and ReoM^{Thr7Ala} after incubation with ATP/Mg and PrkA-KD had an intact mass of 10641.9 (Figure 6.20). The predicted mass of ReoM^{Thr7Ala} by ProtParam (https://web.expasy.org/protparam/) was 10642.09 which meant neither variant of ReoM^{Thr7Ala} was phosphorylated and the shift observed on native-PAGE was not due to the addition of a phosphoryl group on a secondary ReoM site. The shift observed could be due to low level, non-specific phosphorylation that was not stable and/or did not accumulate sufficiently to be detected, even by modern MS methodologies.

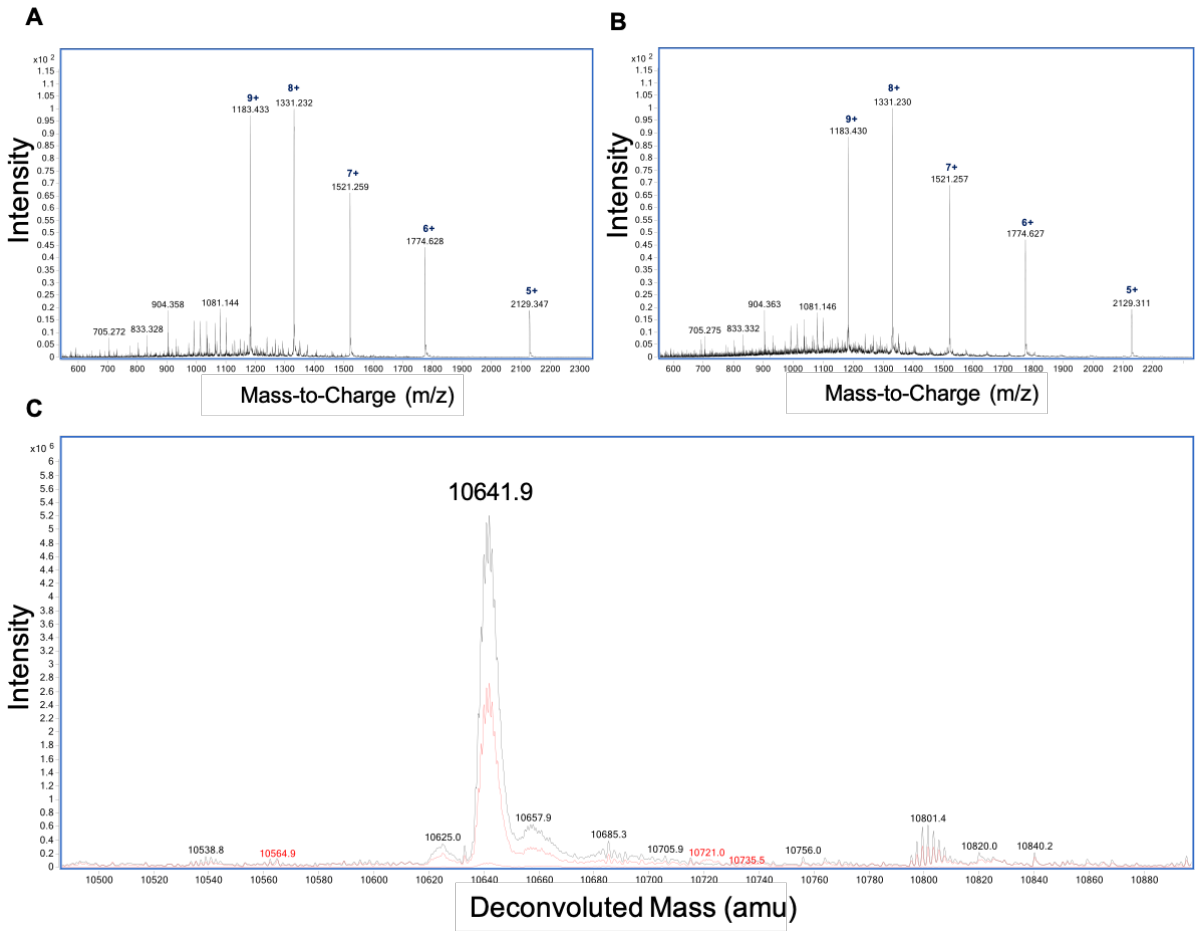

Figure 6.20: LC-MS analysis of intact ReoM^{Thr7Ala} mutant.
Panel **A** and **B** show the ESI-QTOF raw data for ReoM^{Thr7Ala} and ReoM^{Thr7Ala} following incubation with PrkA-KD. Panel **C** is the overlaid deconvoluted mass spectrum demonstrating lack of phosphorylation of ReoM^{Thr7Ala} in the absence (black) and presence of PrkA-KD (red).

6.6 Activation mechanism of PrkA

6.6.1 Identification of PrkA residues to be mutated

The activation mechanism of PrkA-KD was explored to determine if there was an equivalent residue to threonine 172 from *S. aureus* Stk1 that had to be phosphorylated in order for the kinase to become active (Zheng et al., 2018b). Appropriate alanine substitutions were made to 6 residues of PrkA-KD determined by the sequence alignment to be the equivalent of the activation loop residues in Stk1, as well as Ser169Ala as the equivalent residue in *S. aureus* Stk1 is histidine (Figure 6.21 A). The conservation of these activation loop residues in a range of Gram-positive bacteria is highlighted by the multiple sequence alignment in Figure 6.21 B.

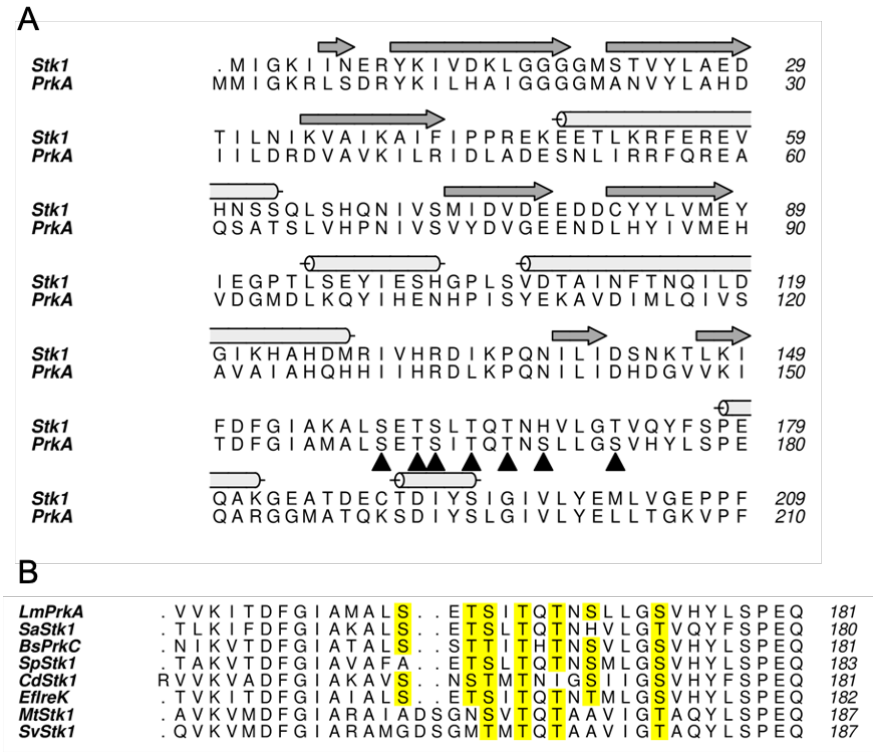

Figure 6.21: Sequence alignments of eSTPKs.
Panel **A** shows a sequence alignment of the kinase domains of Stk1 (*S. aureus*) and PrkA (*L. monocytogenes*). The secondary structure of Stk1 (PDB ID: 4EQM) is shown above the sequence. Residues selected for mutational analysis in PrkA are indicated by black triangles. Panel **B** shows a multiple sequence alignment of the activation loop region of eSTPKs from a range of Gram-positive bacteria. Serine and threonine residues are highlighted yellow to shown their conservation. Ser163 and Ser173 of *Lm*PrkA are conserved as either a Ser/Thr throughout the 8 species and Thr at the equivalent position of *Lm*PrkA^{Thr165} is highly conserved. Abbreviations: *Lm, Listeria monocytogenes; Sa, Staphylococcus aureus; Bs, Bacillus subtilis; Sp, Streptococcus pneumoniae; Cd, Clostridioides difficile; Ef, Enterococcus faecalis; Mt, Mycobacterium tuberculosis; Sv, Streptomyces venezuelae.*

6.6.2 Native-PAGE to assess the ability of PrkA-KD mutants to bind and phosphorylate ReoM

PrkA-KD mutants were analysed by native-PAGE to test their ability to both bind to and phosphorylate ReoM. Figure 6.22 shows the native gels of the phosphorylation reactions of ReoM with Serine 173, 169 and 167 mutants of PrkA-KD. As with wild-type PrkA-KD, PrkA-KD^{Ser173Ala} formed a complex with ReoM (PrkA-KD^{Ser173Ala} lane 2), but this complex appeared weaker with a less intense band than with the wild-type proteins, indicating that this mutant had a lower affinity for ReoM. There was also a much more prominent ReoM band in this lane compared to the wild-type reaction (PrkA-KD lane 2). This free ReoM supported the conclusion that PrkA-KD^{Ser173Ala} cannot bind to wild-type ReoM as strongly. With the addition of ATP/Mg to PrkA-KD^{Ser173Ala} and ReoM there was no visible shift in ReoM which suggested that this mutant kinase is unable to phosphorylate ReoM (PrkA-KD^{Ser173Ala} lane 3). PrkA-KD^{Ser173Asp} had a similar pattern to PrkA-KD^{Ser173Ala}, with even less evidence of a complex formation with ReoM and no evidence of phosphorylation (PrkA-KD^{Ser173Asp} lanes 2 and 3) suggesting strongly that mutating Ser173 to an aspartate could not mimic the phosphorylated residue. Both PrkA-KD^{Ser173Ala} and PrkA-KD^{Ser173Asp} ran higher on the gel than PrkA-KD, which could be explained by loss of negative charge because these mutants could not autophosphorylate. PrkA-KD^{Ser169Ala} and PrkA-KD^{Ser167Ala} had a similar pattern to wild-type PrkA-KD indicating that mutating either of these residues had no discernible impact on the ability of the kinase to autophosphorylate, bind ReoM, or act as a kinase.

The remaining activation loop residue mutants of PrkA-KD were analysed by native-PAGE and the results are shown in Figure 6.23. PrkA-KD^{Ser160Ala} ran as three distinct bands, which probably indicated the presence of multiple phosphorylation states (PrkA-KD^{Ser160Ala}, lane 1). Like wild-type PrkA-KD, this mutant was able to both bind to and to phosphorylate ReoM (PrkA-KD^{Ser160Ala}, lanes 2 and 3). PrkA-KD^{Thr162Ala} and PrkA-KD^{Ser163Ala} also behaved like wild-type but PrkA-KD^{Thr162Ala} appeared to have a single phosphorylation state (PrkA-KD^{Thr162Ala}, lane 1) whereas PrkA-KD^{Ser163Ala} had three (PrkA-KD^{Ser163Ala}, lane 1). PrkA-KD^{Thr165Ala} was the only other mutant to act differently as it demonstrated no ability to phosphorylate ReoM (PrkA-KD^{Thr165Ala}, lane 3), although it could bind to it.

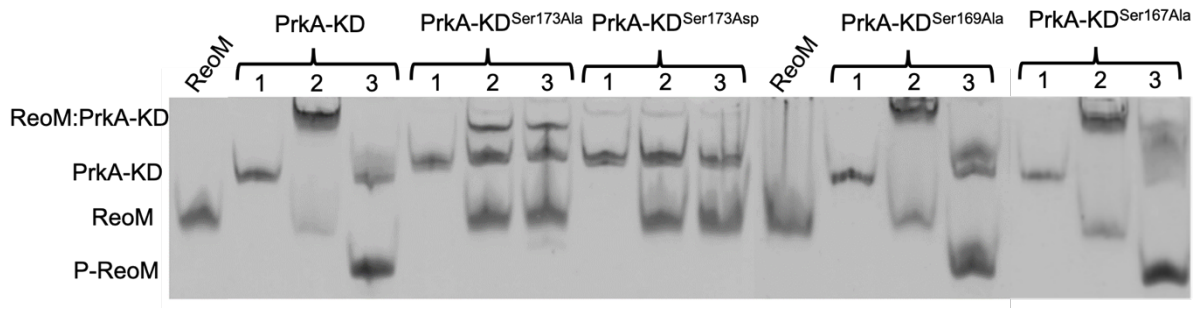

Figure 6.22: A native gel comparing the phosphorylation activity of wild-type PrkA-KD with mutants.
For each PrkA-KD variant lane 1 was the kinase on its own, lane 2 was the kinase plus ReoM and lane 3 was the kinase plus ReoM, ATP and $MgCl_2$.

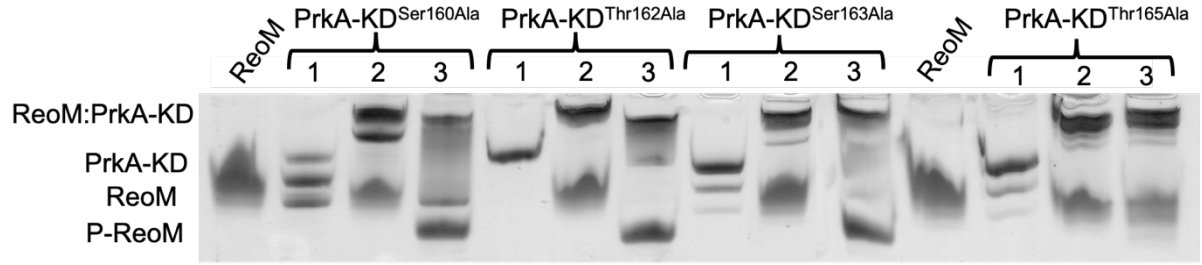

Figure 6.23: A native gel comparing the activity of wild-type PrkA-KD with mutants.
For each PrkA-KD variant lane 1 was the kinase on its own, lane 2 was the kinase plus ReoM and lane 3 was the kinase plus ReoM, ATP and $MgCl_2$.

Finally, Gly18 of PrkA is a part of a conserved glycine rich loop in the kinase domain that is thought to be important in binding ATP during phosphorylation (Rakette et al., 2012). During genetic constructions designed to delete *prkA* and *prpC* from the chromosome, the Halbedel lab made the observation that the only Δ*prpC* clone they could isolate contained a suppressor mutation in *prkA*, which removed the Gly18 codon of *prkA*. The effect of removing this glycine residue on the activity of PrkA-KD was therefore tested *in vitro*. Native-PAGE analysis showed that removing this glycine residue did not impact the ability of the kinase to both bind to and to phosphorylate ReoM (Figure 6.24), and therefore, the presence of three other glycine residues in close spatial and sequential proximity is likely to impart the necessary flexibility on the local structure of the ATP-wrapping loop to maintain wildtype-like levels of kinase function.

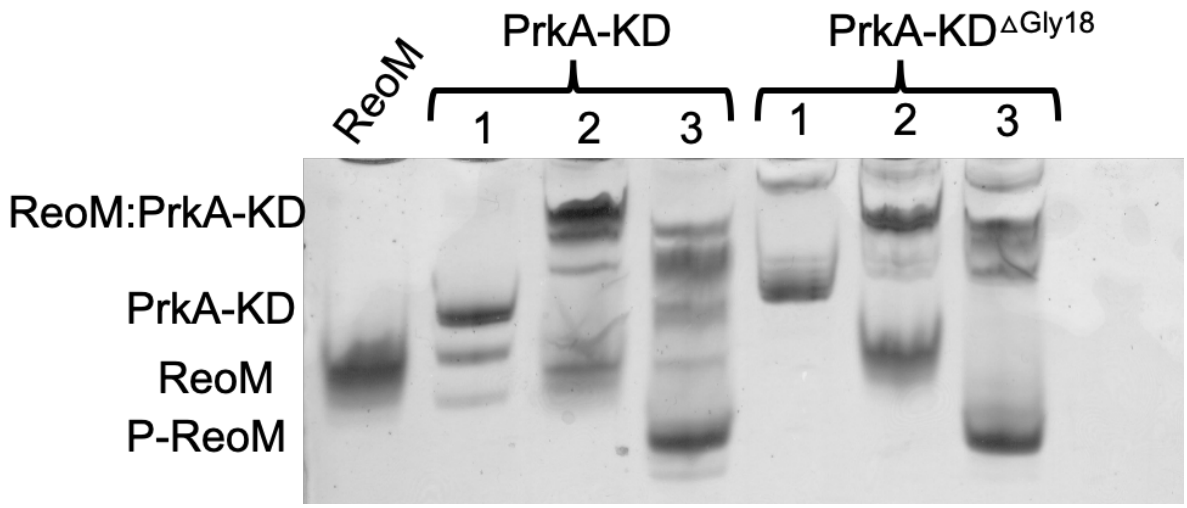

Figure 6.24: A native gel comparing the activity of wild-type PrkA-KD with Gly18 deletion mutant.
For each PrkA-KD variant lane 1 was the kinase on its own, lane 2 was the kinase plus ReoM and lane 3 was the kinase plus ReoM, ATP and $MgCl_2$.

6.6.3 Analysis of the interaction between PrkA-KD mutants and ReoM by isothermal titration calorimetry

ITC was used to assess the binding of all PrkA-KD variants to ReoM (Figure 6.25 and Figure 6.26). Mutating Ser173 had the most visible hinderance on binding to and phosphorylating ReoM, as observed by native-PAGE. When the interaction of PrkA-KD^{Ser173Ala} with ReoM was probed with the same conditions used for WT, there was no observable binding (Figure 6.25 B). The same result was observed for PrkA-KD^{Ser173Asp} (Figure 6.25 C). The concentration of ReoM in the cell was reduced to 25 µM and the concentration of PrkA-KD^{Ser173Ala} increased to 650 µM in effort to detect lower affinity binding. A Kd of 2.2 ± 0.3 µM was observed, 10-fold lower affinity than WT but the heat change was so low that it cannot be considered a reliable result (Figure 6.27). The binding enthalpy also was more unfavourable than wild-type, with a value of -3.4 kcal/mol whereas the entropy factor was lower at -4.2 kcal/mol and together these values suggest that in this interaction there are fewer conformational changes and the interaction is based more on hydrophobic interactions than with the wild-type.

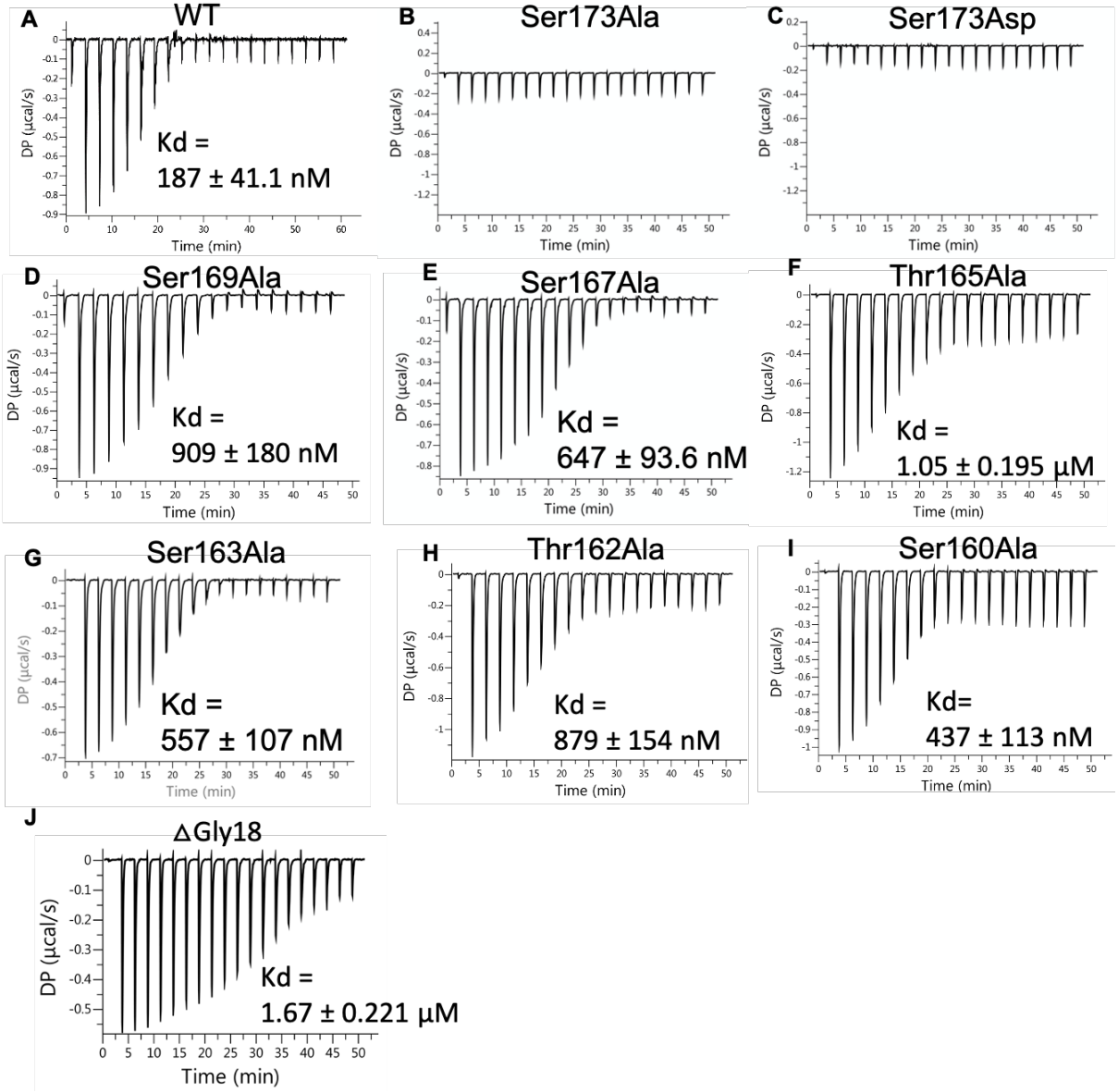

Figure 6.25: Interaction of PrkA-KD WT and mutants to ReoM analysed by ITC.
The ITC raw heats for 20 injections of PrkA-KD at 400 µM into 100 µM ReoM in the cell. **A**= WT, PrkA-KD, **B**= PrkA-KD^{Ser173Ala}, **C**= PrkA-KD^{Ser173Asp}, **D**= PrkA-KD^{Ser169Ala}, **E**= PrkA-KD^{Ser167Ala}, **F**= PrkA-KD^{Thr165Ala}, **G**= PrkA-KD^{Ser163Ala}, **H**= PrkA-KD^{Thr162Ala}, **I**= PrkA-KD^{Ser160Ala} and **J**= PrkA-KD$^{\triangle Gly18}$. The Kd determined for each of the variants is shown.

The rest of the activation loop Ser/Thr mutants were subjected to ITC runs under the same conditions as WT PrkA-KD (Figure 6.25 and Figure 6.26). A summary of the binding affinities and thermodynamic parameters determined can be found in Table 6.2. Each of the mutants had a reduction in affinity for ReoM compared to wild-type PrkA-KD, between 2- and 5-fold in all cases. The phosphorylated residues in the activation loop could be important in binding kinase substrates, such as ReoM, by participating in electrostatic interactions with the partner protein. Inhibiting the phosphorylation of these individual PrkA-KD residues could reduce the hydrogen bonding capacity of PrkA-KD for ReoM, thus reducing the affinity. Apart from PrkA-

KD$^{Ser173Ala/Asp}$, the only other mutant unable to phosphorylate ReoM (determined by native-PAGE) was PrkA-KD^{Thr165Ala}, and this had the second lowest affinity of the activation loop residue mutants for ReoM. A reduction of affinity of over 5-fold was observed compared to wild-type (Figure 6.25 F), suggesting that Thr165 may have a more specific role in the phosphorylation of substrates. This is supported by the observation from native-PAGE that PrkA-KD^{Thr165Ala} is unable to phosphorylate ReoM and this residue is highly conserved in the multiple sequence alignment generated in Figure 6.21 B.

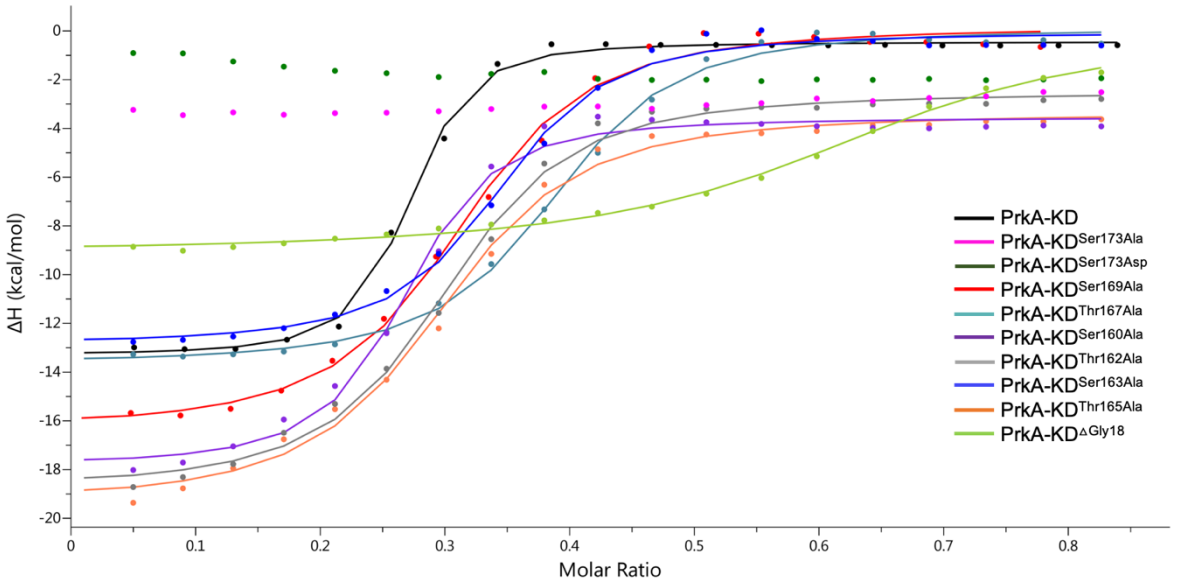

Figure 6.26: Affinity of PrkA-KD WT and mutants binding to ReoM determined by ITC.
The integrated heats of binding of PrkA-KD WT and mutants vs ReoM overlaid. Where binding was observed the data were fit to a single set of sites binding model (solid line) to determine binding parameters that can be found in Table 6.2.

PrkA-KD$^{\Delta Gly18}$ had the most impact on the affinity of the kinase for ReoM, other than mutating Ser173. A Kd of 1.7 ± 0.2 µM was measured which is an 8-fold decease in affinity compared to wild-type (Figure 6.25 J). The binding enthalpy was more unfavourable than wild-type with a value of -8.9 ± 0.3 kcal/mol and the entropy factor was more favourable at 1.2 kcal/mol. This could suggest that not as many conformational changes were involved in this interaction and it was perhaps more dependent on hydrogen bonding.

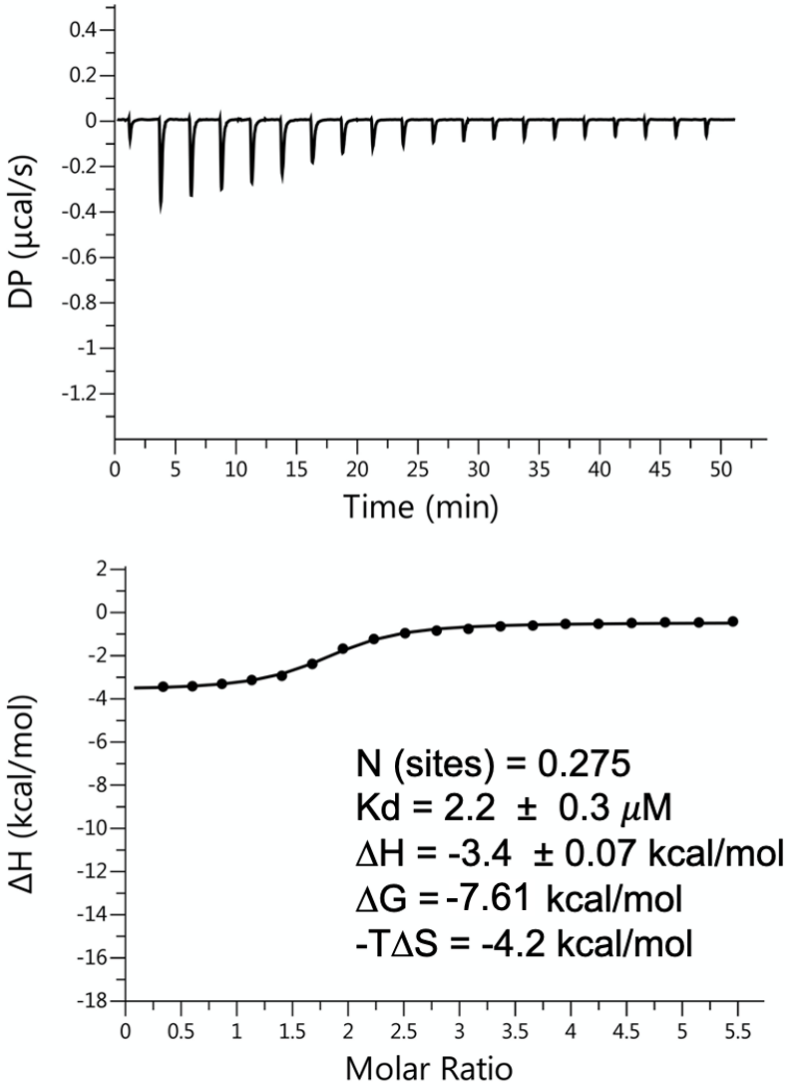

Figure 6.27: Interaction of PrkA-KD^{Ser173Ala} with ReoM analysed by ITC.
ITC raw heat plots and integrated binding heats for 20 injections of PrkA-KD^{Ser173Ala} at 650µM into 25 µM ReoM in the cell. Integrated binding heats (black dots) were fit to a single set of sites model (black line) to determine N, Kd, ΔH, ΔG and -TΔS.

All of the PrkA-KD mutants were analysed by circular dichroism. The data confirmed all mutants were correctly folded and had a comparable CD spectrum to wild-type that is consistent with a mixed α/β fold of structure expected of eSTPKs (Zheng et al., 2018b) (Figure 6.28). As the overall secondary structure of the mutants was globally the same, it could be said that difference in binding to and phosphorylating ReoM was not due to the incorrect folding of the mutant and more likely it was more subtle structural changes behind the differences in affinity.

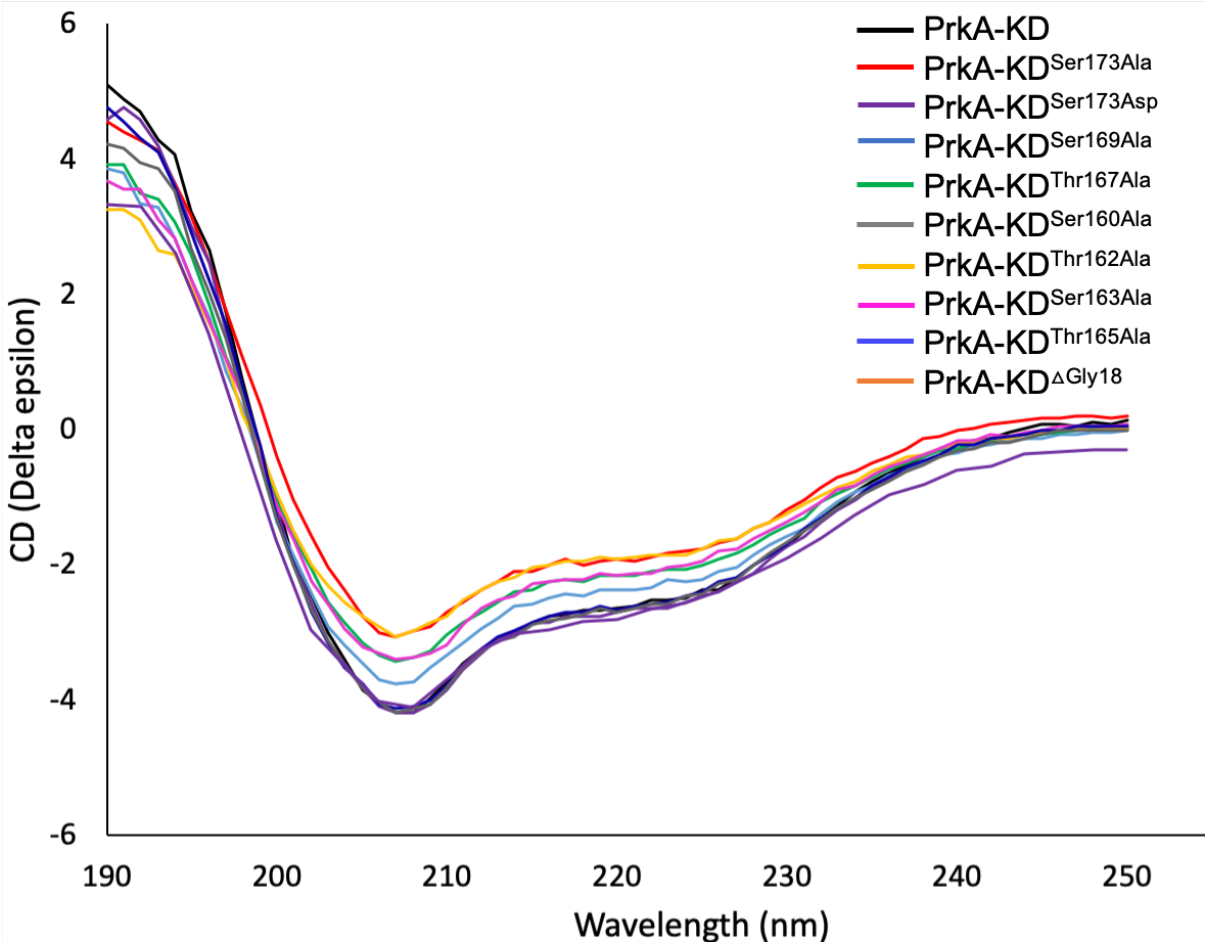

Figure 6.28: Circular Dichroism spectra of PrkA-KD WT and mutants.
Circular dichroism spectra of PrkA-KD variants were analysed using BeStsel (Micsonai et al., 2018); CD spectra were converted from millidegrees to delta epsilon. Shown here is the experimental data and the key indicates which data set is represented. Single mutations did not have a significant impact on the structure of PrkA-KD; all PrkA-KD mutants had a comparable CD spectrum to wild-type which is also consistent with the expected mixed α/β fold structure of eSTPks (Zheng et al., 2018b).

6.6.4 Mass spectrometry to assess the phosphorylation state of PrkA-KD mutants

The impact of the mutations on the ability of PrkA-KD to autophosphorylate was explored by LC-MS. Intact LC-MS was performed to analyse how the mutation impacted the number of species present. Wild-type PrkA-KD spectra showed 5 major peaks (Figure 6.29) with each peak separated by 79-81 amu, typical of a phosphorylation profile as a phosphoryl group has a molecular mass of 80 Da. The 5 peaks corresponded to the expected mass of PrkA-KD (37414.91 Da) plus 4-8 phosphoryl groups. There was no observable peak for unphosphorylated PrkA-KD. The multiple phosphorylation states of PrkA-KD gives an explanation as to why multiple bands were observed by native-PAGE, the two main bands corresponding to the two major peaks of PrkA-KD species with 5 and 6 phosphoryls.

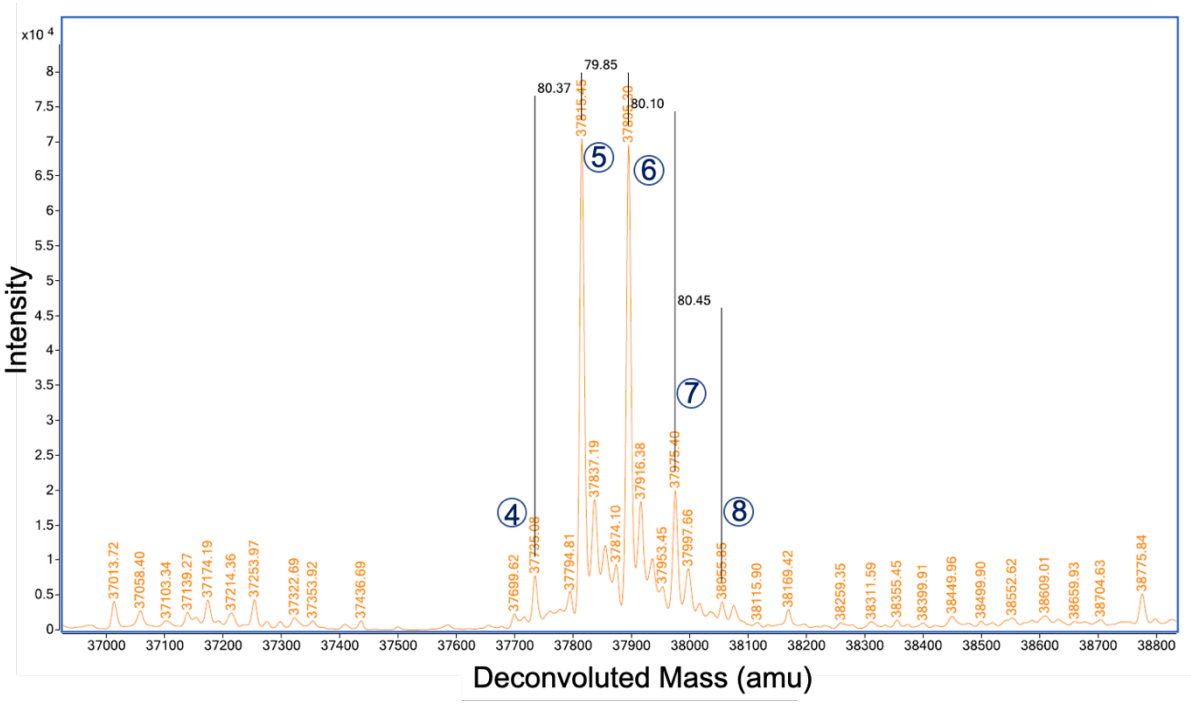

Figure 6.29: LC-MS analysis of WT PrkA-KD.
The peaks have amu values labelled and each peak in the central zone of the spectrum has an encircled number representing the number of phosphoryl groups for that species.

PrkA-KD^{Ser173Ala} showed four major peaks, again representative of a phosphorylation profile (Figure 6.30). The smallest major peak on the spectrum represented PrkA-KD^{Ser173Ala} without any phosphoryl groups with a molecular mass of 37399.9 Da. The largest major peak has a molecular mass of 37639.6 Da, an increase of 239.7 Da consistent with a phosphorylation profile of 0-3 phosphoryls. Abolishing phosphorylation of Ser173 severely hindered the ability of PrkA to autophosphorylate and the phosphorylation profile observed for PrkA-KD^{Ser173Ala} could in fact lie outside of the activation loop. PrkA-KD^{Ser169Ala} had six major peaks, each again separated by 79-80 amu, with a phosphorylation profile almost identical to wild-type (Figure 6.31). This demonstrates unequivocally that Ser173 and not Ser169 is important for the autophosphorylation of PrkA.

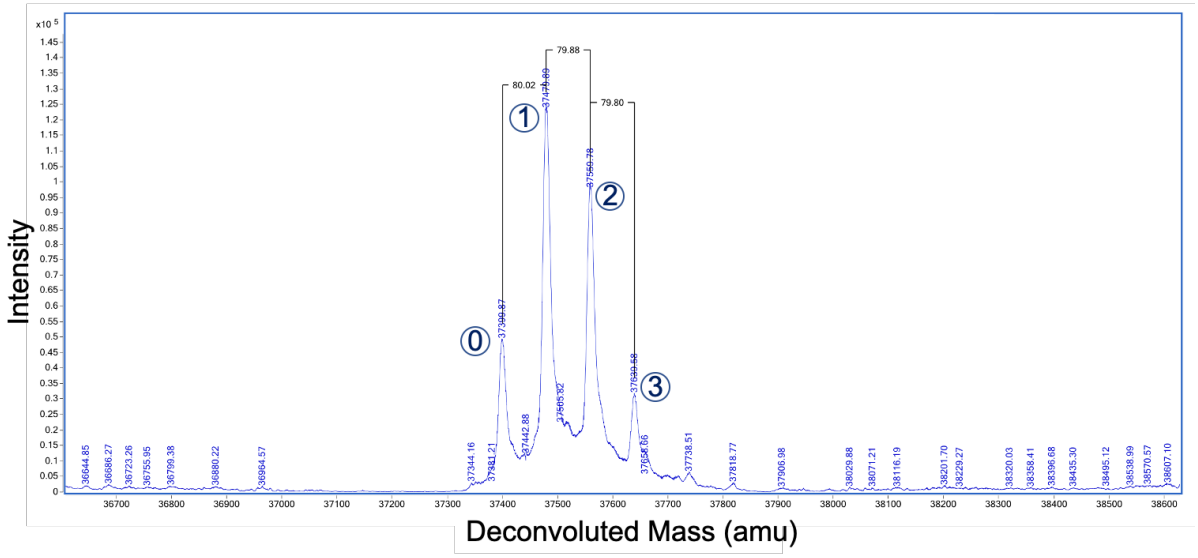

Figure 6.30: LC-MS analysis of PrkA-KD^{Ser173Ala}.
The peaks have amu values labelled and each peak in the central zone of the spectrum has an encircled number representing the number of phosphoryl groups for that species.

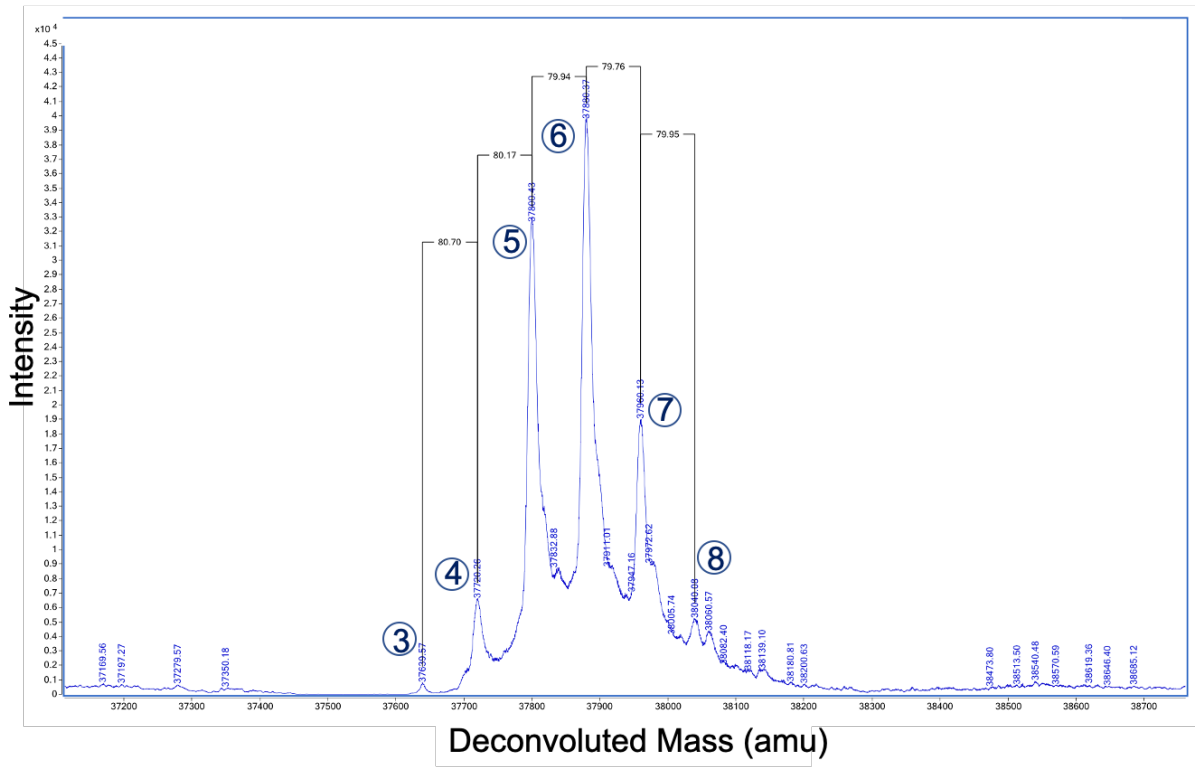

Figure 6.31: LC-MS analysis of PrkA-KD^{Ser169Ala}.
The peaks have amu values labelled and each peak in the central zone of the spectrum has an encircled number representing the number of phosphoryl groups for that species.

Finally, lambda phosphatase treated PrkA-KD displayed one peak at 37416.1 Da, which indicates completely unphosphorylated protein, supporting the conclusion that the multiple peaks observed are indeed different phosphorylation states (Figure 6.32).

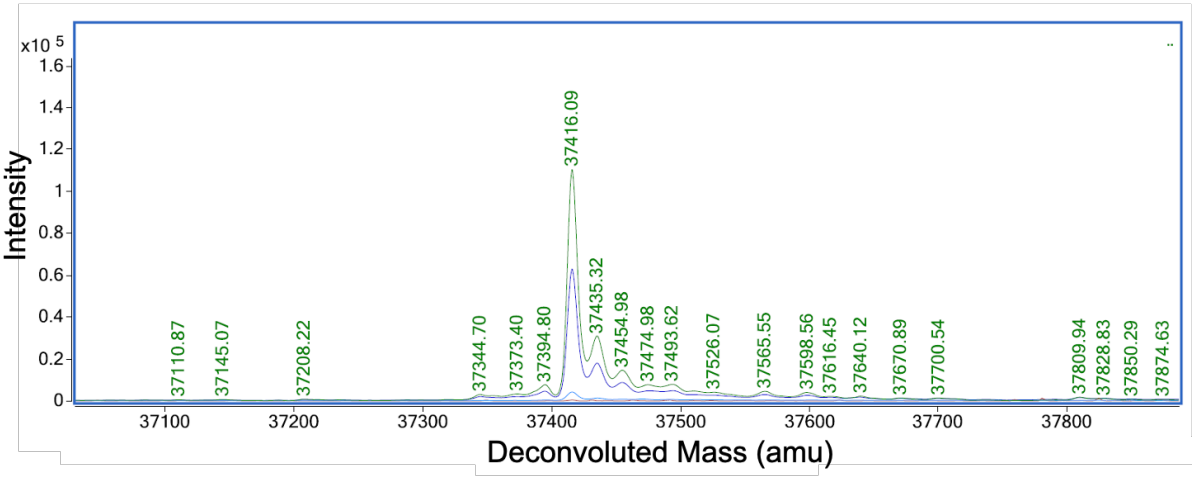

Figure 6.32: LC-MS analysis of PrkA-KD treated with lamda phosphatase.
The peaks have amu values labelled and the single large peak in the middle represents PrkA-KD without any phosphoryl groups attached.

6.7 PrpC dephosphorylates both P-ReoM and PrkA-KD

Some passages in this section have been quoted verbatim from Wamp *et al.* (2020) in which I am the second author. Any passages used are my own work.

6.7.1 Native-PAGE analysis of the dephosphorylation reactions of PrkA-KD and P-ReoM by PrpC

The ability of PrpC, the partner phosphatase to PrkA in *L. monocytogenes,* to interact with and remove phosphoryl groups from PrkA-KD and P-ReoM was also tested *in vitro*. PrkA and purified P-ReoM were each incubated with PrpC in the absence and presence of $MnCl_2$, since divalent cations are essential co-factors for the PPM phosphatase family to which PrpC belongs (Kennelly, 2001), and the products were analysed by native-PAGE. Unlike with ReoM and PrkA-KD, no stable protein:protein complexes were formed either in the presence or absence of endogenous $MnCl_2$ (Figure 6.33). The incubation of P-ReoM with PrpC and manganese resulted in the almost complete disappearance of the band corresponding to P-ReoM (lane 6, Figure 6.33) in comparison to the same reaction conducted without the addition of $MnCl_2$ (lane 5, Figure 6.33). The new band, corresponding to ReoM alone in lane 6, is masked by that for PrpC which migrates similarly to ReoM (lanes 1 and 4, Figure 6.33) under these electrophoresis conditions. When incubated with PrpC in the presence of manganese ions, the band for PrkA-KD electrophoresed more slowly than for PrkA-KD in isolation (lanes 3 and 8, Figure 6.33), indicating that PrkA-KD had been dephosphorylated by PrpC and confirming biochemically that phosphorylated PrkA is a substrate for PrpC.

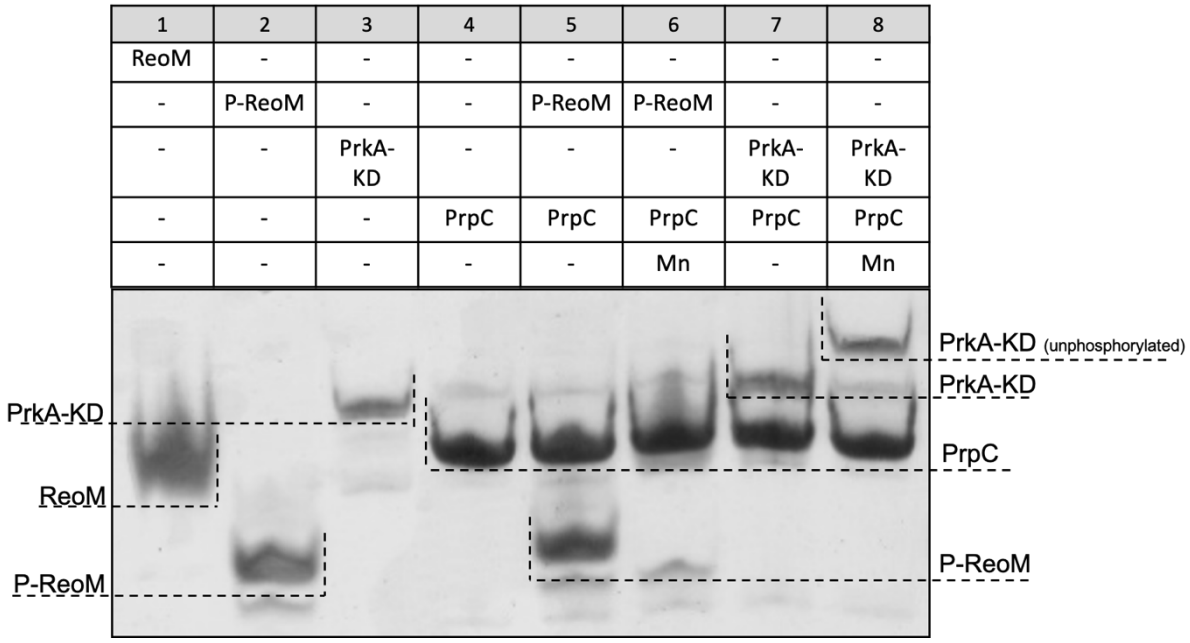

Figure 6.33: Native-PAGE analysis of PrkA-KD and P-ReoM dephosphorylation by PrpC. Components of each lane are annotated above the image and the position and identity of relevant bands are marked to the side.

6.7.2 Isolation of dephosphorylated PrkA-KD

To determine the phosphorylation state and activity of PrkA-KD after the incubation with PrpC, it was isolated from the mixture by immobilised metal affinity chromatography. PrpC was purposely left with the His_6-tag on after purification so that after the incubation with PrkA-KD and $MnCl_2$ the two proteins could be separated by passing the mix over an Ni-NTA column. As PrkA-KD did not have a His_6-tag it was collected in the flow through and PrpC bound to the column and was eluted with imidazole. Figure 6.34 is a native-PAGE gel with the results of the purification of dephosphorylated PrkA-KD and its activity. Lane 3 shows the dephosphorylation reaction and lane 4 shows the flow through (FT) from the Ni-NTA column. The band for PrkA-KD has shifted upwards indicating the loss of negative charge by the removal of phosphoryl groups. Lane 5 is the elution of PrpC, which runs the same as before the reaction. Lanes 6 and 7 show that dephosphorylated PrkA-KD is no longer able to bind to and phosphorylate ReoM under the reaction conditions used. There is no complex band for the incubation of dephosphorylated PrkA-KD (FT) with ReoM in Lane 6 and the band for ReoM in lane 7 does not run as P-ReoM does in lane 8. PrpC is therefore capable of completely inactivating PrkA-KD making it unable to bind to and phosphorylate its substrate ReoM.

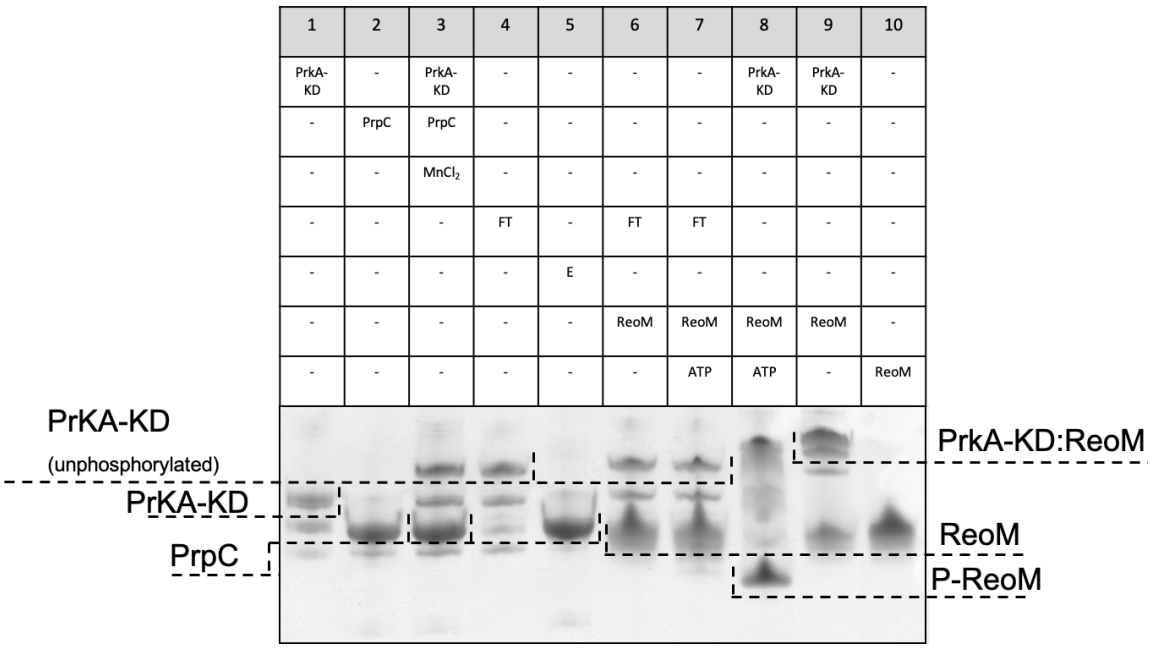

Figure 6.34: Native-PAGE analysis of PrkA-KD activity.
Components of each lane are annotated above the image and the position and identity of relevant bands are marked to the side. PrkA-KD was incubated with His_6-PrpC and $MnCl_2$ and passed over a Ni-NTA column. FT is the flow through from the Ni-NTA column and E is the elution from the column with 250 mM imidazole.

6.7.3 Mass spectrometry of P-ReoM and PrkA-KD after incubation with PrpC

The presence of unphosphorylated ReoM and the absence of P-ReoM after incubation with PrpC was confirmed by LC-MS (Figure 6.35). There was a single peak at 10670.53 Da which is only a single Dalton different from the estimated unphosphorylated mass of 10671.5 Da. LC-MS analysis of PrkA-KD that had been incubated with PrpC/$MnCl_2$ yielded a single major species of 37,413.2 Da, consistent with the predicted mass of the expressed recombinant construct, and the absence of a peak corresponding to phosphorylated PrkA-KD, P-PrkA-KD (Figure 6.36). PrkA-KD is therefore capable of autophosphorylation when recombinantly expressed, a phenomenon that has been observed previously with the related eSTPKs, *B. subtilis* PrkC and *E. faecalis* IreK (Madec et al., 2003; Kristich et al., 2011). Autophosphorylation of PrkC and IreK is important for kinase activity which has been demonstrated through the phosphorylation of an exogenous substrate, MBP (myelin basic protein), a routinely used substrate of eSTPKs (Madec et al., 2003; Kristich et al., 2011). PrkC activity is important for biofilm formation and sporulation (Madec et al., 2002) and IreK along with its partner phosphatase IreP act in a signal transduction event to regulate the adaption *E. faecalis* to cephalosporin-induced stress (Kristich et al., 2011).

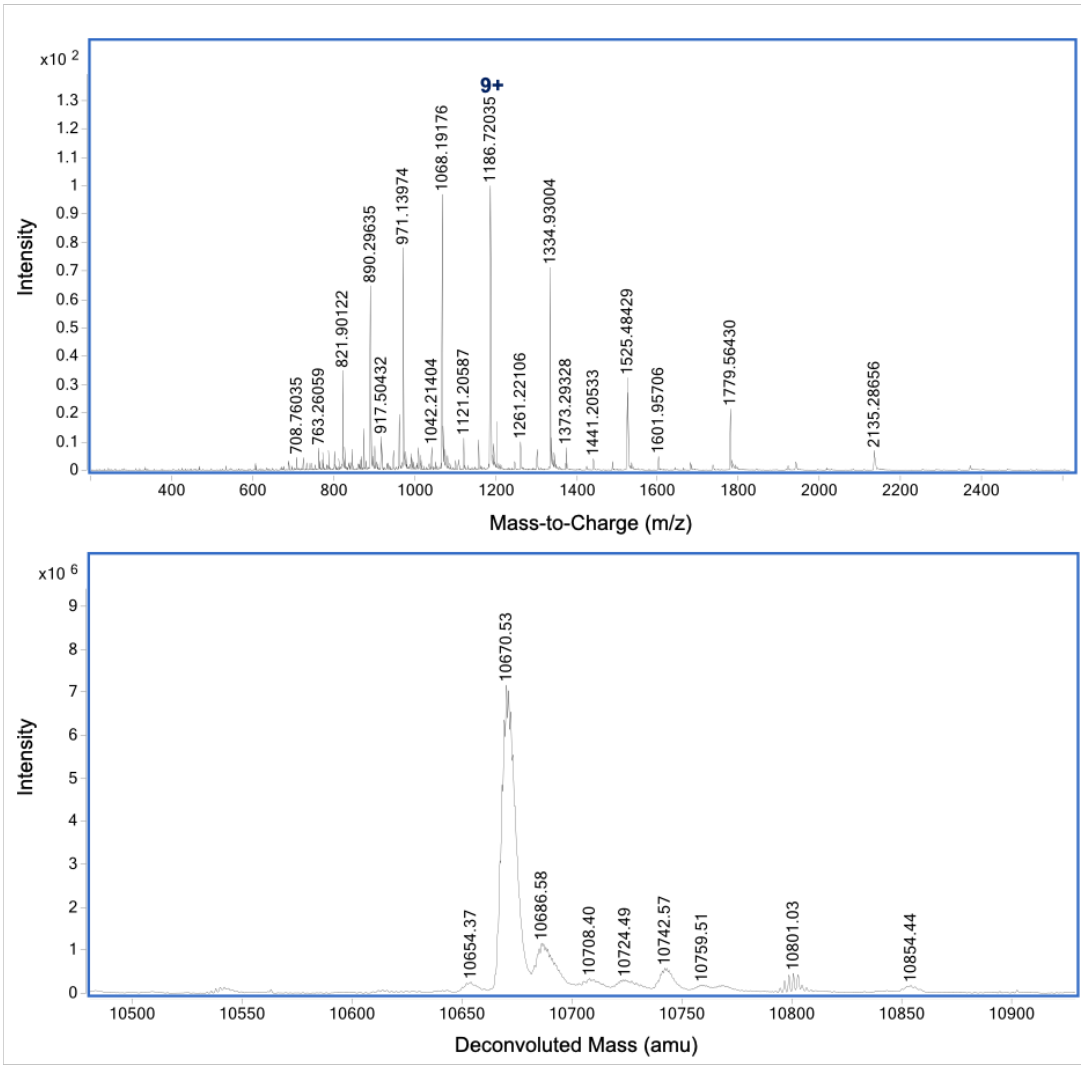

Figure 6.35: LC-MS analysis of ReoM after incubation with PrpC.
Panel **A** is the ESI-QTOF raw data and **B** is the deconvoluted mass spectrum demonstrating the presence of non-phosphorylated ReoM.

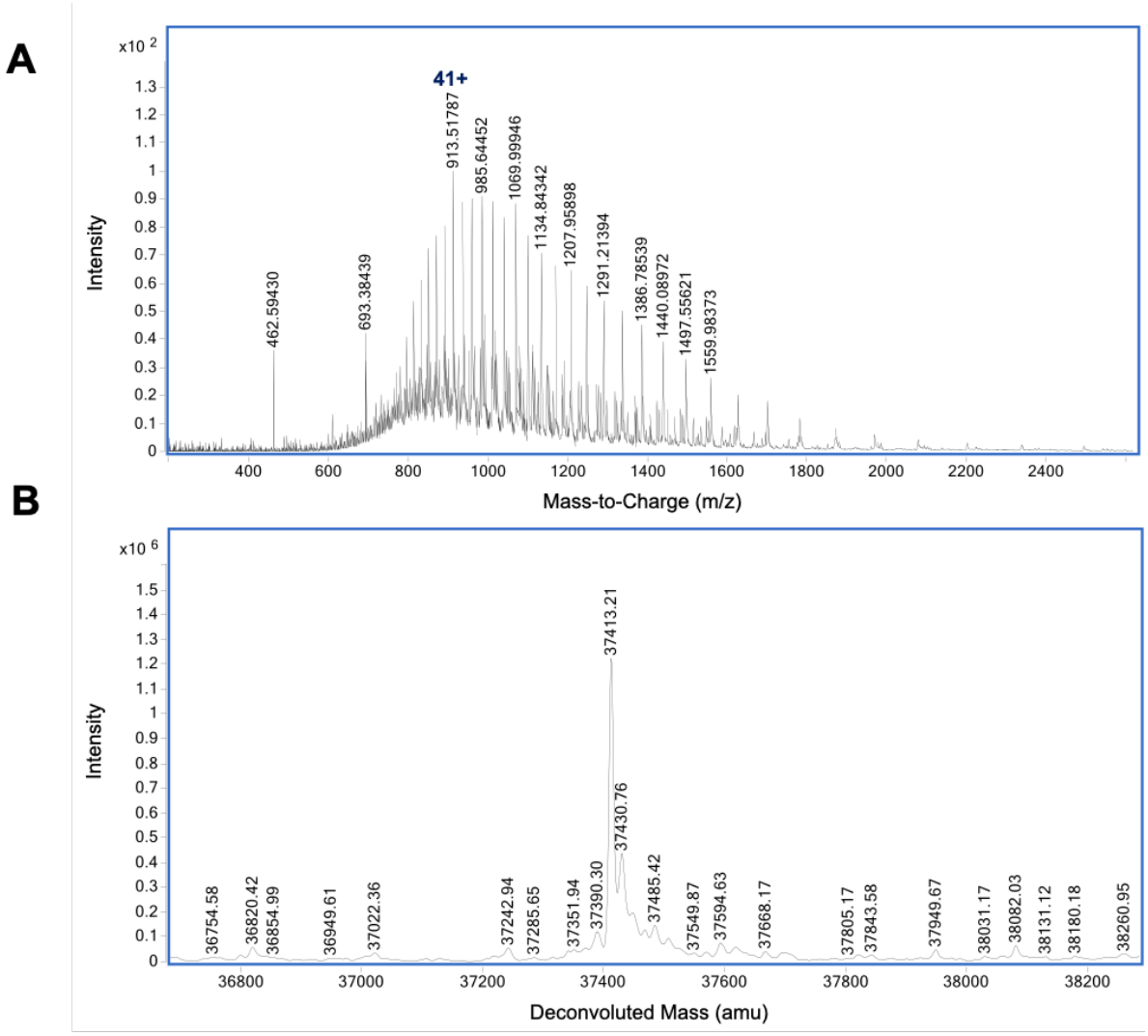

Figure 6.36: LC-MS analysis of PrkA-KD after incubation with PrpC.
Panel **A** is the ESI-QTOF raw data and **B** is the deconvoluted mass spectrum demonstrating the presence of non-phosphorylated PrkA-KD.

6.8 Small angle X-ray scattering of ReoM, PrkA-KD and PrkA-KD:ReoM complex

SAXS data of ReoM, PrkA-KD and the PrkA-KD complex were collected and processed by Dr Owen Davies (Newcastle University). The SAXS molecular masses were estimated at 28 kDa for ReoM, 38 kDa for PrkA-KD and 77 kDa for the complex, in agreement with those determined by SEC-MALS (25 kDa, 36 kDa and 82 kDa). Dummy atom models (DAM) were generated with DAMMIF and the crystal structure of a ReoM dimer and a Phyre2 model (Kelley et al., 2015) of PrkA-KD were manually docked into the mesh of the DAM models. The average chi-squared values for the agreement of the SAXS data to the rapid *ab initio* bead models were 1.28 (ReoM), 1.34 (PrkA-KD) and 1.22 (PrkA-KD:ReoM). The DAM models of ReoM and PrkA-KD were globular with apparent flexible tails (Figure 6.37). The explanation for this with regards to ReoM is likely the presence of the ~16 residue N-terminal flexible tail observed in

the crystal structure but the elongated region of the PrkA-KD DAM model was unexpected from the structures of the isolated proteins/homologs. The structures of 2 ReoM dimers and one PrkA-KD monomer were manually modelled into the DAM model of the PrkA-KD:ReoM complex based on the stoichiometry determined from ITC, native-PAGE and SEC-MALS. The site/sites at which PrkA-KD interacts with ReoM are unknown but one theory could be that the flexible N-terminal regions of two separate ReoM dimers bind near the activation loop of PrkA-KD.

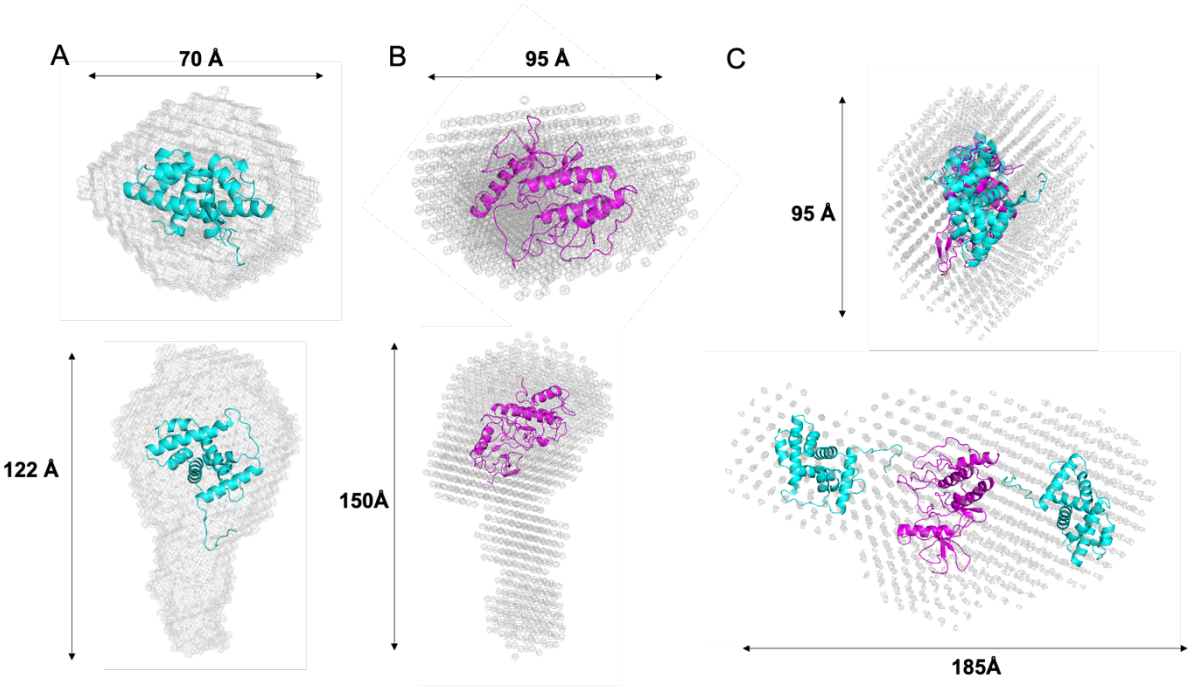

Figure 6.37: SAXS analysis of ReoM, PrkA-KD and PrkA-KD:ReoM.
SAXS-derived *ab-initio* dummy atom models (DAM) of ReoM (A), PrkA (B) and PrkA-KD:ReoM (C) calculated with DAMMIF from small-angle X-ray scattering profiles. The DAM models are shown in mesh and a top and side profile is displayed. The cartoon structure of ReoM (cyan) and Phyre2 model of PrkA-KD (magenta) (Kelley et al., 2015) have been manually docked into the mesh.

6.9 The importance of ReoM *in vivo*

This study was a collaboration with the Halbedel lab who performed a number of *in vivo* experiments alongside the *in vitro* work presented here. Described below are a number of key experiments reported in Wamp *et al.* (2020).

The sole deletion of *reoM* did not cause a growth or divisional defect in *L. monocytogenes*, the cells grew at a comparable rate to wild-type and observation by scanning electron microscopy revealed the cells had a normal rod-shape. Δ*reoM* did however, affect the stability of MurA

and the deletion caused an accumulation of MurA by at least 8-fold compared to WT. The role of MurA is to transfer an enoylpyruvate moiety to UDP-Glc*N*Ac in the first committed step of peptidoglycan synthesis (Brown et al., 1995). It had been shown previously that MurA accumulated in a Δ*clpC* mutant strain, a heat stress protease responsible for the degradation of MurA (Rismondo et al., 2017). The MurA levels were the same in a double Δ*reoM* Δ*clpC* mutant compared to a single Δ*reoM* mutant demonstrating that ReoM exerts its effect on MurA levels in a ClpC dependent manner. The degradation of MurA was analysed over time in cells with blocked protein synthesis induced by the treatment with chloramphenicol. No MurA degradation was observed in mutants lacking *reoM* or *clpC*, compared to wild-type, showing that the two proteins are just as important for MurA degradation. The MurA accumulation caused by a *reoM* deletion stimulated peptidoglycan biosynthesis as there were thicker PG layers at the cell poles of Δ*reoM* and cells had an increased resistance to ceftriaxone (a cephalosporin antibiotic).

The importance of the phosphorylation of Thr7 on ReoM was explored using a Thr7Ala mutant. In a Δ*reoM* mutant, cells did not grow with *reoM Thr7Ala* under an IPTG inducible promoter, in the presence of IPTG and only a small amount of wild-type MurA levels could be detected in cells expressing *reoM Thr7Ala.* ReoM^{Thr7Ala} was completely incapable of being phosphorylated by PrkA-KD *in vitro* (Section 6.5.3), although the two proteins were still capable of interacting with a nanomolar affinity (Section 6.5.2). Together, this showed that the phosphorylation of ReoM is essential for the viability of *L. monocytogenes.* The inducible *reoM Thr7Ala* did grow, even with IPTG, when *clpC* was deleted suggesting that the phosphorylation of ReoM inhibits the ClpCP dependent degradation of MurA. There was an accumulation of MurA levels in a *prpC* depletion strain and no MurA could be detected in cells depleted of *prkA*, which supports the conclusion that phosphorylated ReoM caused an accumulation of MurA.

6.10 Summary

This chapter explored the relationship between the protein kinase/phosphatase pair PrkA/PrpC and a small phosphoprotein named ReoM (Regulator of MurA degradation) in *L. monocytogenes* in the context of cell signalling and the link to peptidoglycan synthesis. eSTPKs are important for the regulation of many cellular processes in Gram-positive bacteria (Madec et al., 2002) and the respective kinase from *L. monocytogenes*, PrkA*,* is essential (Wamp et al.,

2020). ReoM has been identified as a substrate of PrkA-KD, the two proteins bound with nanomolar affinity and did not associate after phosphorylation of the former by the latter. The results from ITC, Native-PAGE and SEC-MALS were consistent with a 1:4 binding ratio of PrkA-KD:ReoM, however, the exact binding sites for ReoM on PrkA-KD are yet to be identified. ReoM is phosphorylated by PrkA-KD on a single site at Thr7 that is present in a flexible N-terminal region. The phosphorylation of Thr7 is essential for the viability of *L. monocytogenes* and this phosphorylation inhibits the ClpCP dependent degradation of MurA (Wamp et al., 2020).

It was shown by mass spectrometry that PrkA-KD has multiple phosphorylation sites and by native-PAGE that the phosphorylation of Ser173 is essential for the activity of the kinase. When Ser173 was mutated, PrkA-KD was rendered inactive and it could not bind with optimal affinity to ReoM and was unable to phosphorylate it. The requirement of an activating Ser/Thr residue for kinase activity has also been identified in eSTPKs from range of Gram-positive species (Shakir et al., 2010; Ravala et al., 2015; Zheng et al., 2018b). The kinase activation model proposed by Zheng *et al*., as applied to PrkA, would suggest that PrkA-KD is in an inactive conformation when Ser173 is not phosphorylated, and the activation loop mimics a substrate thus preventing binding of either PrkA molecules or ReoM. The binding of ATP and *cis* autophosphorylation of Ser173 induces a conformational change in PrkA and the activation loop moves out of the substrate binding site into an active conformation (Figure 6.38). An activated kinase molecule can then interact with another and *trans* autophosphorylation of the other activation loop Ser/Thr residues can occur (Zheng et al., 2018b).

The phosphorylation of PrkA-KD and ReoM can be reversed by the partner phosphatase PrpC. After an incubation with PrpC to remove phosphoryl groups, PrkA-KD was unable to bind to and phosphorylate ReoM and this inability to function as a kinase is supported by mutational analysis that PrkA-KD needs to be phosphorylated to be active.

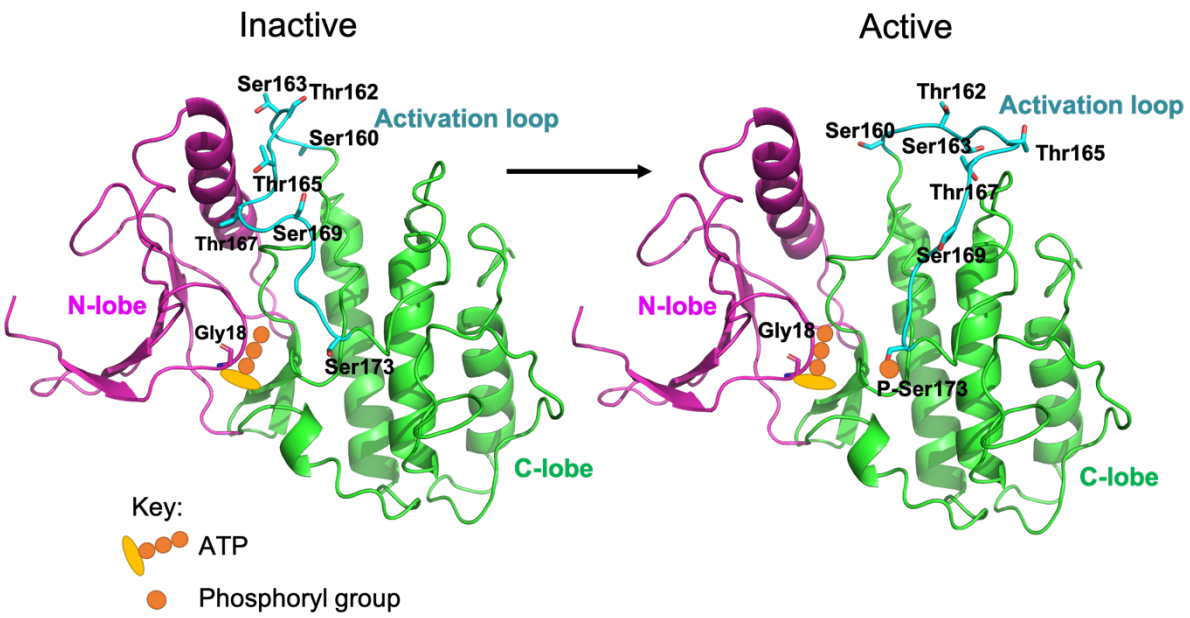

Figure 6.38: Model of PrkA-KD activation.
A prediction of the kinase domain structure of PrkA generated in Phyre2 (Kelley et al., 2015) modelled into an inactive and active conformation. The Phyre2 model was highly based on the structure of PknB from *S. aureus* (PDBID: 4EQM). The structure is represented in cartoon form with the N-lobe coloured magenta, C-lobe is green and the activation loop is cyan. Ser/Thr residues in the activation loop are shown in stick form and are labelled. The binding of ATP to the ATP binding loop (Gly18, shown in stick form) induces *cis* phosphorylation of Ser173 and a conformational change of the activation loop occurs.

The structure of ReoM was used to propose a model of the conformational changes that might take place upon phosphorylation of Thr7. After phosphorylation a substantial movement of Thr7 is proposed such that it then interacts with a positively-charged surface on helix 3, which comprises 4 arginine residues at positions 57, 62, 66 and 70. These residues are highly conserved amongst all 2909 ReoM homologues in the NCBI sequence database at 57 %, 99 %, 76 % and 98 % conserved, respectively. This approaching the level of conservation observed for the phosphorylation site (96 %). In order to assess the likely relevance of this model, the wild-type *reoM* allele was replaced by alanine substitutions at each of these positions and the viability of each corresponding *L. monocytogenes* strain assessed. Mutant strains harbouring ReoM substitutions Arg66Ala or Arg70Ala grew as wild-type and there was no discernible gross phenotypic change (Wamp et al., 2020). By contrast, *L. monocytogenes* strains carrying ReoM Arg57Ala and Arg62Ala mutations were unviable, a lethality reminiscent of the expression of ReoM Thr7Ala (Wamp et al., 2020). Thus, Arg57 and Arg62 are certainly important for ReoM structure/function; the possibility of their mutation Ala causing substantial disruption of the tertiary structure of ReoM is unlikely since they are both surface-

exposed and make little intramolecular interactions. Therefore, the impact on viability is more likely to stem from an impact on ReoM function, perhaps because the co-ordination of P-Thr7 is lost, and therefore the conformation and the position of the flexible N-terminal region is disrupted (Figure 6.39). Confirmation of the molecular consequences of ReoM phosphorylation, however, remains to be determined.

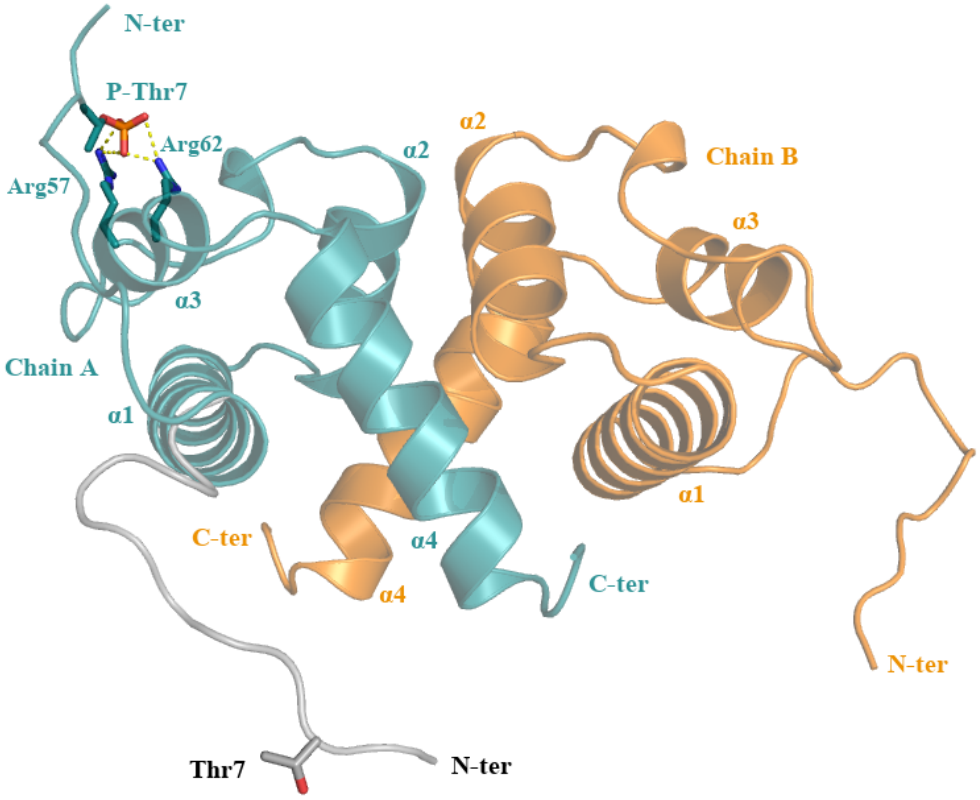

Figure 6.39: A model of the predicted conformational change induced by the phosphorylation of ReoM.
The grey cartoon represents the original positioning of the N-terminus of chain A in the crystal structure of ReoM. The N-terminus of chain A coloured in cyan represents where it could be positioned after a conformational change following phosphorylation of Thr7. The yellow dashed lines show the potential hydrogen bonds formed between P-Thr7 and Arg57/Arg62.

In addition to ReoM, a second novel factor named ReoY, has been identified for the ClpCP-dependent degradation of MurA (Wamp et al., 2020). Like *reoM*, *reoY* had no divisional defects when singly deleted and an accumulation of MurA was observed in a Δ*reoY* mutant (Wamp et al., 2020). It has also been shown previously that the deletion of *murZ* contributed to the accumulation of MurA (Rismondo et al., 2017). The separate deletions of *clpC*, *reoY* and *murZ* overcame the lethality of the inducible *reoM Thr7Ala* mutant which suggested that ClpCP, ReoY and MurZ all act down stream of ReoM (Wamp et al., 2020). BACTH experiments showed that ReoM interacted with MurA, and ReoY interacted with ClpC, ClpP and ReoM, which

implies ReoM and ReoY are the connecting factors between MurA and ClpCP (Wamp et al., 2020). Together these results have led to the suggestion that ReoM plays a key role in the phosphorylation signalling mechanism linking cell wall integrity sensing, by the PASTA domains of PrkA, to the control of peptidoglycan synthesis by MurA and this model is summarised in Figure 6.40.

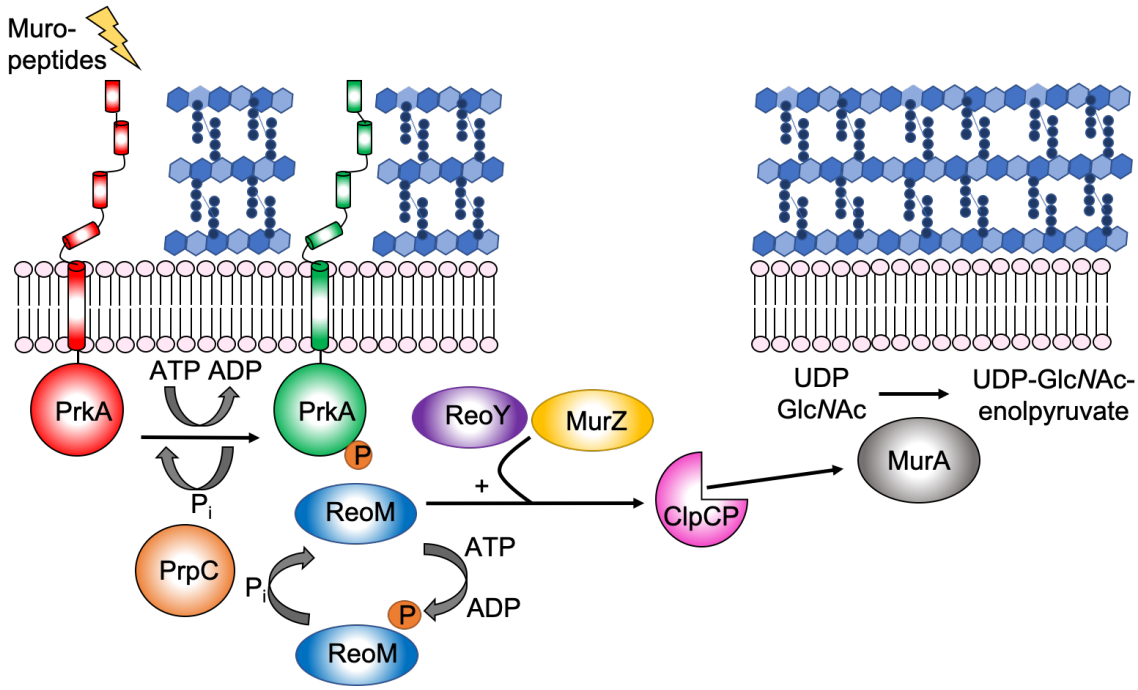

Figure 6.40: A model illustrating the role of ReoM as a substrate of PrkA and a regulator of ClpCP.
The diagram shows how PrkA is activated by autophosphorylation after detecting an external muropeptide signal via its PASTA domains (inactive PrkA in red and activated PrkA in green). Active PrkA then phosphorylates ReoM. The phosphorylation of ReoM and PrkA is reversed by PrpC. Unphosphorylated ReoM along with ReoY and MurZ activate MurA degradation by ClpCP. MurA catalyses the first step of peptidoglycan synthesis. The phosphorylation of ReoM by PrkA prevents the ClpCP-dependent degradation of MurA so that MurA can accumulate and peptidoglycan synthesis can happen.

Data Statistics*		Refinement Statistics*	
Beamline	Diamond I03	**R_{work}**	0.153
Date	20/05/18	**R_{free}**	0.214
Wavelength (Å)	0.976	**No. of non-H atoms**	
Resolution (Å)	74.45-1.60 (1.63-1.60)	**Protein**	1399
		Ligand/Ion	20
Space group	P 2_1 2_1 2_1	**Water**	94
Unit-cell parameters		**R.m.s. deviation from ideal values**	
a (Å)	38.79		
b (Å)	58.62		
c (Å)	74.45	**Bond angle (°)**	1.79
α - β - γ (°)	90-90-90	**Bond length (Å)**	0.015
Rpim	0.064 (0.533)		
Solvent content (%)	38	**Average B factor (Å²)**	
No. of measured reflections	111229 (5581)	**Protein**	26.4
		Ligand/Ion	50.5
		Water	37.7
No. of independent reflections	23059 (1129)		
Completeness (%)	99.8 (99.8)		
Redundancy	4.8 (4.9)		
CC1/2 (%)	98.6 (62.0)		
<I>/<σ(I)>	8.2 (2.2)		

**Values in parenthesis are for the highest resolution shell*

Table 6.1: Data statistics and refinement details of the ReoM structure

Mutant	Kd	N	ΔH	ΔG	-TΔS
WT	187 ± 41.0 nM	0.26 ± 0.003	-13.1 ± 0.251	-9.03	4.09
Ser173Ala	2.2 ± 0.3 µM	0.28 ± 0.004	-3.4 ± 0.01	-7.61	-4.2
Ser173Asp	/				
Ser169Ala	909 ± 180 nM	0.30 ± 0.005	-16.6 ± 0.50	-8.11	8.46
Thr167Ala	647 ± 94.0 nM	0.37 ± 0.004	-13.8 ± 0.27	-8.31	5.48
Thr165Ala	1.05 ± 0.20 µM	0.29 ± 0.005	-16.1 ± 0.48	-8.02	8.03
Ser163Ala	557 ± 110 nM	0.33 ± 0.004	-12.7 ± 0.31	-8.39	4.29
Thr162Ala	879 ± 150 nM	0.29 ± 0.004	-16.3 ± 0.43	-8.12	8.2
Ser160Ala	437 ± 110 nM	0.25 ± 0.004	-14.3 ± 0.41	-8.49	5.83
△Gly18	1.67 ± 0.220 µM	0.62 ± 0.01	-8.91 ± 0.38	- 7.75	1.16

Table 6.2: A summary of the binding affinities and thermodynamic parameters determined for the interaction of PrkA-KD mutants with ReoM, analysed by ITC.

Results are from the injection of 400 µM PrkA-KD into 100 µM ReoM except for Ser173Ala (highlighted blue) which was from 650 µM PrkA-KD into 25 µM ReoM.

Chapter 7: Discussion and Future Work

7.1 Overview

Bacterial cell division is a complex process that requires the coordination of DNA replication, chromosome segregation, membrane fission and cell wall remodelling. Protein interactions, signalling mechanisms and the formation of protein complexes involved in these cellular processes ensure their tight regulation. The molecular, genetic, biochemical and biophysical characterisation of proteins involved in bacterial cell division will help understand this fundamental biological process and aid in the design of novel antibiotics required due to the increasing and wide-spread resistance to existing drugs. In this thesis, the functions of two important proteins in the division of Gram-positive bacteria, GpsB and ReoM, were explored. A summary of the key findings from this thesis and how these results have aided in the characterisation of Gram-positive cell division are discussed below.

7.2 Extension of the GpsB interactome

In Chapter 3, the specific molecular interactions were identified between the N-terminal domain of GpsB and the cytoplasmic mini-domains of PBPs from two human pathogens *L. monocytogenes* and *S. pneumoniae,* to add to the known information of the interaction between GpsB and PBP1 in the Gram-positive division model organism, *B. subtilis.* Prior to this study, the N-terminal domain of GpsB had been shown by BACTH to interact with the major bi-functional class A PBP from *L. monocytogenes* (*Lm*PBPA1), and it was implicated that GpsB acted as a negative regulator of this peptidoglycan synthase (Rismondo et al., 2016). In *S. pneumoniae,* GpsB and the class A PBP, PBP2a were pulled down by co-IP (Rued et al., 2017), however, no previous interaction had been determined between GpsB and the class B PBP, PBP2x and this work represents the first demonstration of a specific interaction between these proteins.

The crystal structures of GpsB in complex with the cytoplasmic mini-domains of *Lm*PBPA1, *Sp*PBP2a and *Sp*PBP2x, along with the previously solved *Bs*GpsB$_{5\text{-}64}$:*Bs*PBP1$_{1\text{-}17}$ structure, revealed the positively charged PBPs bound to a negatively charged groove between helix 1 and helix 2 of a GpsB monomer (Figure 7.1). A conserved feature of the GpsB:PBP interaction was discovered in the form of a single arginine that poked into the negatively charged groove of GpsB and was in the same orientation in each species, forming a similar set of interactions. This central arginine was required to be in an alpha helical conformation or in a beta-turn, which demonstrated that the binding of PBP peptides to GpsB is favoured by secondary

structural elements. The binding of *Bs*PBP1$_{1-17}$ and *Sp*PBP2a$_{27-40}$ involved a second arginine residue Arg11 and Arg36, respectively, that made important contacts to GpsB. No such feature was seen in the structures of *Bs*GpsB$_{5-64}^{Lys32Glu}$:*Lm*PBPA1$_{1-15}$ and *Sp*GpsB$_{4-63}$:*Sp*PBP2x$_{13-28}$. FP analysis suggested that Arg12 of *Lm*PBPA1 could fulfil the role of the second arginine residue, but this could not be confirmed by structural information due to the lack of ordered peptide in the crystal structure. FP studies suggested that the interaction between *Sp*GpsB and *Sp*PBP2x was more transient than the interactions with the class A PBPs, which may explain why the binding of this PBP is centred only on a single arginine residue. Two modes of binding were observed with *Sp*PBP2a, either Arg31 or Arg33 could act as the central arginine residue and when one form of binding was inhibited, either by crystal contacts or by mutation, the peptide could compensate by binding in the other form.

The importance of the identified PBP binding residues in GpsB were supported by a number of *in vivo* experiments. For instance, growth defects in *L. monocytogenes* and a lethal phenotype in *S. pneumoniae* were observed with mutations in the conserved GpsB aspartic acid pair and tyrosine residue required for PBP binding (Tyr27/Asp33/Asp37 in *L. monocytogenes* and Tyr23/Asp29/Asp33 in *S. pneumoniae*) (Cleverley et al., 2019). These phenotypes were similar to *gpsB* deletions, showing that these residues are essential for one of the main biological functions of GpsB (Rismondo et al., 2016; Rued et al., 2017). It was further shown in *L. monocytogenes* that the N-terminal domain of GpsB is required for the binding of both PBPA1 and MreC but that slightly different surfaces/residues are involved (Cleverley et al., 2019). The depletion of *gpsB* in *S. pneumoniae* and a *gpsB* deletion in *L. monocytogenes* led to a more severe phenotype than the mutation of the cytoplasmic mini-domain of *Sppbp2a* or deletion of *LmpbpA1*, suggesting that the co-ordination of PBPs is not the sole function of GpsB and there are other GpsB-dependent interactions that cause the more severe phenotype.

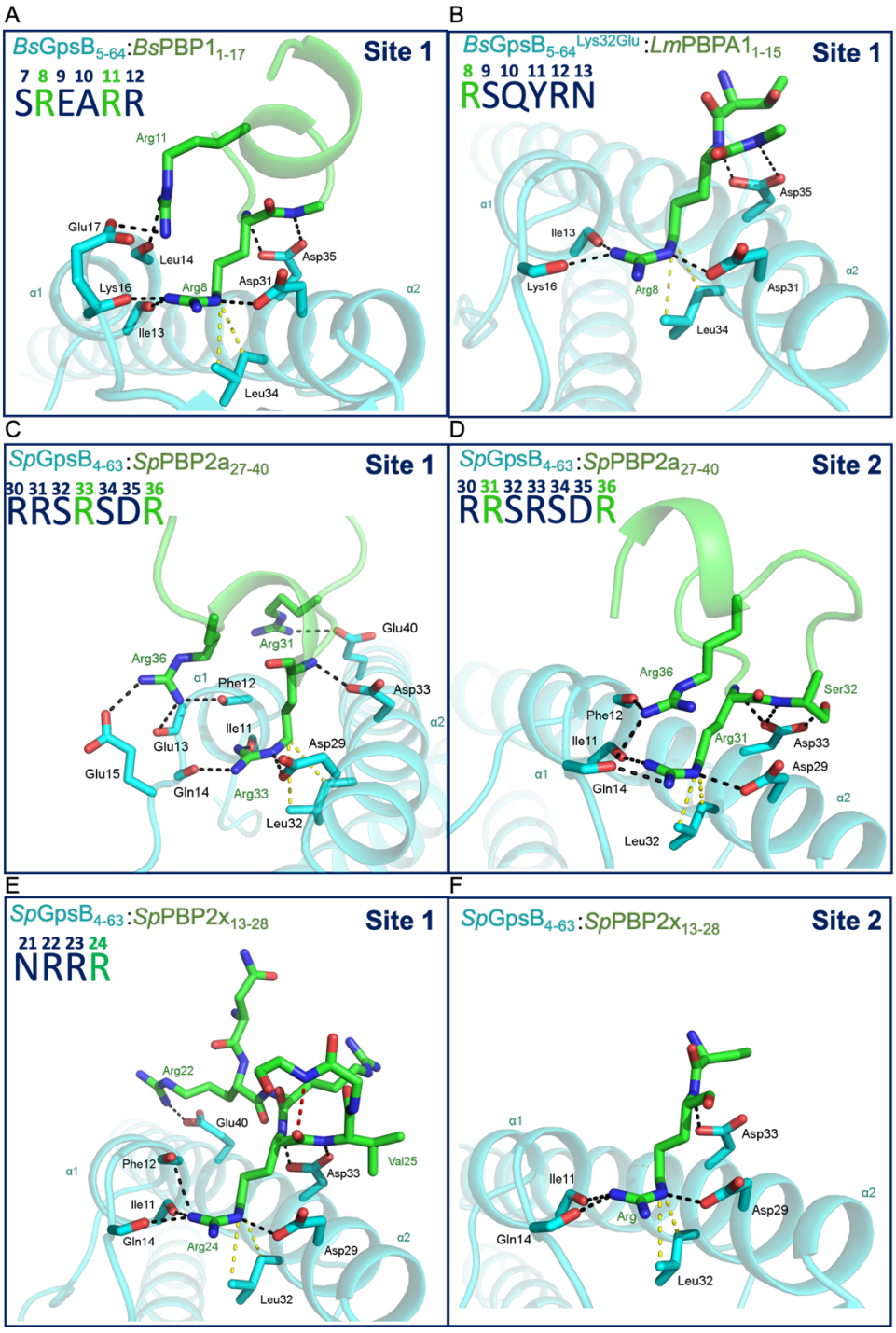

Figure 7.1: Comparison of the binding sites of all solved GpsB:PBP complexes.
Panel **A** shows the binding site of *Bs*GpsB$_{5-64}$:*Bs*PBP1$_{1-17}$, Panel **B** shows the binding site of *Bs*GpsB$^{Lys32Glu}_{5-64}$:*Lm*PBPA1$_{1-15}$, Panels **C** and **D** are binding site 1 and 2 of *Sp*GpsB$_{4-63}$:*Sp*PBP2a$_{27-40}$, respectively and Panels **E** and **F** are binding site 1 and 2 of *Sp*GpsB$_{4-63}$:*Sp*PBP2x$_{13-28}$, respectively. Residues important in binding are shown as sticks coloured by atom. Salt bridges and hydrogen bonds are represented by dashed black lines, van der Waals' interactions by dashed yellow lines and intra-molecular interactions by a dashed red line. In each panel apart from Panel **F** (were the identity of the arginine could not be determined), a section of the binding sequence from the respective PBP is shown with the main coordinated arginine or arginine pairs coloured green.

Since a number of GpsB interacting partners with various division functions have been identified across Gram-positive bacteria, it is not surprising that the phenotype of a *gpsB* mutant is not solely caused by the loss of a single PBP binding partner. Current knowledge of the GpsB interactome shows conserved interactions across a range of Gram-positive bacteria with peptidoglycan synthases (Claessen et al., 2008; Rismondo et al., 2016; Cleverley et al., 2016; Rued et al., 2017; Cleverley et al., 2019), the elongation factor MreC (Claessen et al., 2008; Rued et al., 2017; Cleverley et al., 2019) and the FtsZ regulator EzrA (Claessen et al., 2008; Steele et al., 2011; Fleurie et al., 2014a; Pompeo et al., 2015; Rued et al., 2017). An interaction between GpsB and the late division proteins DivIB and DivIC as well as the FtsZ tethering protein SepF have been identified in *L. monocytogenes* (Cleverley et al., 2019) but not *B. subtilis* (Claessen et al., 2008) and *S. aureus* is the only species were a direct interaction between FtsZ and GpsB has been shown thus far (Eswara et al., 2018). The hexameric structure of GpsB enables the binding of multiple interacting partners, whether that be clustering multiple PBP molecules to a specific area for peptidoglycan synthesis or the bringing together of different divisome components. GpsB has been shown to coordinate peptidoglycan synthesis during elongation, vegetative division and asymmetric division during sporulation, at least in *B. subtilis* (Claessen et al., 2008; Cleverley et al., 2019; Muchová et al., 2020). *L. monocytogenes* does not sporulate and GpsB is conserved in spherical bacteria that do not elongate, although they do need to remodel the peripheral cell wall during division (Rued et al., 2017). All told, these observations suggest that GpsB has varying functions across Gram-positive bacteria.

The conserved PBP1 motif in *Bacillaceae* (S/T/N)RxxR(R/K) has been used to identify the novel *Bs*GpsB binding partners *Bs*YrrS and *Bs*YpbE that are predicted to be peptidoglycan remodelling proteins and an interaction network with the additional proteins *Bs*YrrR, *Bs*RodZ and *Bs*PBP1 has been proposed (Cleverley et al., 2019). *Bs*YrrS is in a bicistronic operon with *Bs*YrrR (Wei et al., 2004) and the latter gene encodes PBP4b, a class B PBP the expression of which is regulated by sporulation sigma factors E (Wei et al., 2004) and F (Steil et al., 2005), which further supports a role for GpsB in sporulation. An extension of this approach could be used to identify the novel GpsB interacting proteins in *Streptococcaceae*, however, this may prove challenging: the RSxxxR motif identified in most streptococci class A PBPs is present in *Sp*PBP2a with the first arginine of the motif corresponding to Arg31. Multiple binding modes were observed for *Sp*PBP2a, binding with the exact contacts to GpsB varying between arginine

residues. Multiple binding modes, the requirement of local sequence structure as well as the requirement of the motif to be close to the membrane are some reasons why sequence-based searches alone are not sufficient to complete the GpsB interaction network.

Future work on this area of research should involve characterising the GpsB interactome across various Gram-positive species, through different stages of the cell-cycle and during the stress response to different factors such as temperature or being challenged with antibiotics, where GpsB has an important function in *L. monocytogenes* (Rismondo et al., 2016). Solving the structures of GpsB in complex with other binding partners will identify the exact binding surfaces and show the molecular basis of the interactions. The structures of multi-protein complexes will provide information on how they assemble and what proteins are able to bind to GpsB simultaneously, and these molecular studies need to be complemented with functional assays so that the effect of GpsB interaction on the new proteins can be quantified. Identifying new PBP interacting partners would also extend the current knowledge of the GpsB:PBP interactome and it would be invaluable in determining if any other PBPs are capable of binding in multiple binding modes like *Sp*PBP2a. To investigate the conserved and apparent species-specific roles of GpsB across Gram-positive bacteria, complementation experiments could be performed. Δ*gpsB* mutants in different species could be complemented with various *gpsB* homologues and the impact on localisation, co-localisation and interacting partners tested.

7.3 Functional divergence between GpsB and DivIVA

GpsB and DivIVA have slightly different roles in overlapping areas in cell division of Gram-positive bacteria. In Chapter 4, the importance of the high structural homology between the N-terminal domains of *Bs*GpsB and *Bs*DivIVA with relation to protein function was analysed. The N-terminal domains of *Bs*GpsB and *Bs*DivIVA were closely compared and specific features were identified to suggest why *Bs*GpsB can bind to *Bs*PBP1 but *Bs*DivIVA cannot. *Bs*DivIVA is incapable of binding to *Bs*PBP1 because the *Bs*PBP1 binding site in *Bs*GpsB between helix 1 and 2 is blocked by a loop between the equivalent two helices in *Bs*DivIVA. *Bs*PBP1 binding capability was successfully introduced into *Bs*DivIVA by protein engineering in the form of 6-residue mutant (*Bs*DivIVA$_{1\text{-}62}^{\text{Asn6LysAsn10GluThr12GluAsn26AspAla30AspArg33Ile}}$) that incorporated conserved PBP binding residues of GpsB and opened up the blocked binding site in *Bs*DivIVA.

Conservation analysis of the N-terminal domains of GpsB and DivIVA revealed a higher level of conservation in GpsB than DivIVA at the identified PBP binding surface. In both proteins, the level of conservation at helix 1 and the adjacent region of helix 2 was higher than at the C-terminus suggesting that this is the region in both proteins that makes contacts with interacting partners. Different residues at slightly different positions with varying conservation levels might suggest why GpsB and DivIVA do not have the same N-terminal interacting partners.

It is likely that GpsB arose from an initial gene duplication of *divIVA* and since this duplication sufficient time has elapsed for the sequences to diverge but not the gross structures of the N-terminal domains. The shared unique N-terminal fold positions a conserved hydrophobic-arginine pair important for lipid binding (Halbedel & Lewis, 2019), demonstrating an important requirement for the structure in both proteins. The divergence in sequence might suggest why the N-terminal domains of each protein have apparent different functions, for example, GpsB for binding and coordinating PBPs (Cleverley et al., 2019) and DivIVA for the recruitment of the division inhibitor MinCD to the cell poles via MinJ (Bramkamp et al., 2008; van Baarle et al., 2013). The C-terminal domains of GpsB and DivIVA appear to have diverged significantly in both sequence and structure, thus providing the main differences between the overall functions of GpsB and DivIVA. The small C-terminal domain of GpsB appears to only be important for oligomerisation (Rismondo et al., 2016), whereas the longer C-terminal domain of DivIVA is important for oligomerisation (Oliva et al., 2010), protein binding (Perry & Edwards, 2006; Donovan et al., 2012; Ginda et al., 2013; Lenarcic et al., 2009; Schumacher et al., 2016) and for acting as a bridge from one N-terminal dimer to another to enable DivIVA to sense membrane curvature (Halbedel & Lewis, 2019).

A recent study demonstrated a relationship between GpsB and the essential sporulation protein SpoIIE in the early stages of sporulation in *B. subtilis*, confirmed by a direct interaction between GpsB and SpoIIE by BACTH and pull-down assays (Muchová et al., 2020). It had previously been shown that DivIVA and SpoIIE co-immunoprecipitated and that DivIVA localised and anchored SpoIIE to the cell poles during sporulation (Bradshaw & Losick, 2015). Since SpoIIE is a membrane protein with a cytosolic region and both GpsB and DivIVA interact with it, it could be suggested that this interaction mediated their N-terminal domains, serving a specific purpose for the maintained structural homology. This theory could be tested by

BACTH with specific domains of GpsB/DivIVA and SpoIIE, mutational analysis with *in vitro* interaction studies and by solving the co-crystal structures.

7.4 The regulation of peptidoglycan synthesis in *L. monocytogenes* by the phosphoprotein ReoM

In Chapter 6, the relationship between the essential *L. monocytogenes* protein kinase PrkA and its partner phosphatase PrpC with the small phosphoprotein ReoM was explored. The Halbedel lab provided a link between ReoM and the regulation of peptidoglycan synthesis through the control of MurA levels. ReoM was identified as a substrate of the PrkA/PrpC pair and was found to be solely phosphorylated on Thr7 in its flexible N-terminus. ReoM interacted with the kinase domain of PrkA (PrkA-KD) with a nanomolar Kd and a 1:4 binding ratio of PrkA-KD to ReoM was determined by various techniques. *In vitro* phosphorylation and dephosphorylation of ReoM was determined by PrkA-KD and PrpC, respectively, and upon phosphorylation, ReoM no longer interacted with PrkA-KD.

The role of MurA in the cell-cycle is to transfer an enoylpyruvate moiety to UDP-Glc*N*Ac in the first committed step of peptidoglycan synthesis (Brown et al., 1995). MurA levels accumulated in a *reoM* mutant and it was shown that this accumulation was dependent on ClpCP (Wamp et al., 2020), a heat stress protease responsible for the degradation of MurA (Rismondo et al., 2017). The phosphorylation of ReoM on Thr7 was shown to be essential for *L. monocytogenes*. With a *reoM*^{Thr7Ala} mutant, phosphorylation by PrkA was abolished meaning ClpCP inactivation by P-ReoM was abrogated, thus causing increased degradation of MurA to a level were the cells were no longer viable (Wamp et al., 2020).

PrKA-KD was required to be autophosphorylated to be active and capable of phosphorylating ReoM. Autophosphorylation appears to be a characteristic trait of eSTPKs as it is also important for the kinase activity of *Bs*PrkC, *Ef*IreK and *Sa*Stk1 (Madec et al., 2003; Kristich et al., 2011; Zheng et al., 2018b). The requirement of an activating Ser/Thr residue for autophosphorylation and kinase activity has been identified in eSTPKs from range of Gram-positive species (Shakir et al., 2010; Ravala et al., 2015; Zheng et al., 2018b). Ser173 was identified as the activating residue required for the autophosphorylation of the activation loop of PrkA-KD, the single mutation reduced the phosphorylation profile from 4-8 phosphoryls for wild-type to 0-3 for the PrkA-KD^{Ser173Ala} mutant. The inability to autophosphorylate due to the PrkA-KD^{Ser173Ala} mutation, or by complete removal of the phosphoryl groups by PrpC, not only

rendered the PrkA-KD inactive but also reduced its binding affinity for ReoM and consequently was no longer capable of phosphorylating ReoM.

The crystal structure of ReoM was solved, revealing a 5-helical bundle that associated into a homodimer, consistent with the structure of its homologue IreB (Hall et al., 2017). A model was proposed for the conformational change that may occur upon phosphorylation of Thr7 in the flexible N-terminal tail. After phosphorylation, the P-Thr7 residue moves to interact with surface-exposed Arg57 and Arg62 in helix 3. This model was supported by the high conservation of Arg57 and Arg62 and *in vivo* mutational analysis showed they were critical for the function of ReoM (Wamp et al., 2020). The conformational change could impact the ability of ReoM to interact with its binding partners, which might explain why ReoM no longer interacts with PrkA after phosphorylation.

Two other proteins that were found to affect the ClpCP-dependent degradation of MurA were ReoY and MurZ (Rismondo et al., 2017; Wamp et al., 2020). The separate deletions of *clpC*, *reoY* and *murZ* overcame the lethality of the inducible *reoM*^{Thr7Ala} mutant, which suggested that ClpCP, ReoY and MurZ all act down stream of ReoM (Wamp et al., 2020). ReoM homologues are present across *Firmicutes*, whereas ReoY homologues are restricted to bacilli. YrzL and YpiB are the *B. subtilis* homologues of ReoM and ReoY, respectively. MurAA levels in *B. subtilis* increased by at least 12-fold in Δ*yrzL*, Δ*ypiB* and Δ*clpC* strains, demonstrating that the functions of these proteins are conserved (Wamp et al., 2020). Taking together all of the results from *in vitro* and *in vivo* experiments, a novel cell division phosphorylation signalling mechanism was identified with ReoM playing an important role. Along with ReoY, MurZ and ClpCP, ReoM is the link between cell wall integrity sensing by the PASTA domains of PrkA and the control of peptidoglycan synthesis by MurA (Figure 6.40).

There are areas for improvement and future work in various aspects of this chapter. MS/MS spectra and peptide analysis of PrkA-KD would confirm the exact activation loop residues that are phosphorylated in the active kinase. Peptide analysis of PrkA-KD^{Ser173Ala} in comparison to wild-type would be useful for identifying phosphorylation sites outside of the activation loop and the functional relevance of these sites could be tested. The importance of PrkA Thr165 requires more exploration as it was the only activation loop Ser/Thr residue, other than Ser173, that was required to be phosphorylated for the activity of the kinase. A phosphorylation profile of PrkA-KD^{Thr165Ala} would show if this mutant had an impact on

autophosphorylation resulting in an inactive kinase, or whether phosphorylation of this residue is specifically required for substrate phosphorylation. Solving the crystal structure of PrkA-KD would provide more information for the function of Thr165 and other activation loop residues as their relative position to other functional components of the kinase would be determined. The multiple bands of PrkA-KD on native-PAGE should have been excised and examined by MS to determine if they were a degradation product or multiple phosphorylation states.

The PrkA:ReoM complex requires more analysis to understand how this complex assembles. Ideally a co-crystal structure would be solved to provide the specific molecular basis of the interaction, however, this is easier said than done and there were multiple failed attempts to obtain this structure. Better quality SAXS data and more extensive analysis using multiphase *ab initio* modelling and modelling of complexes by multidomain proteins would provide more reliable information on the assembly of the PrkA:ReoM complex. The first 16 amino acids of ReoM that make up the flexible N-terminus could be deleted and the ability of this variant to bind to PrkA tested *in vitro*, to determine if it is solely this region that binds to PrkA or if there are other residues of ReoM involved. The ability of PrkA homologues to bind to and phosphorylate ReoM, and PrkA to phosphorylate ReoM homologues could be explored to gain further knowledge of the conserved features required for this mechanism.

The molecular consequences of the phosphorylation of ReoM are yet to be determined and solving the structure of P-ReoM would ultimately shed light on the proposed conformational change theory. The effect of ReoM phosphorylation and how exactly ReoM controls the activity of ClpCP at the molecular level is an important question still to be addressed.

Finally, the phosphorylation levels of ReoM could be measured *in vivo* at different stages of the cell-cycle and in response to various external stimuli using P-Thr antibodies. This could indicate at which stages of the cell-cycle ReoM is phosphorylated and inhibiting the degradation of MurA by ClpCP. It could also confirm if the phosphorylation of ReoM by PrkA changes in response to peptidoglycan fragments. It has been proposed in *B. subtilis* that PrkC is only activated by peptidoglycan fragments during the stationary phase and otherwise PrkC dispersed around the cell (Pompeo et al., 2018). Phosphorylation of ReoM by PrkA in response to muropeptides could restart peptidoglycan synthesis at this stage of the cell-cycle. Pompeo *et al*. also proposed that GpsB activates PrkC during cell division in the exponential phase of

growth. The impact of GpsB on the phosphorylation and activity of both PrkA and ReoM is an area for future work to test if this mechanism is maintained across species or if it is specific for *B. subtilis* and what reasons there might be for this.

7.5 New potential antibiotic targets

The importance of GpsB, PrkA and ReoM in the division of Gram-positive bacteria, specifically in the synthesis of peptidoglycan, has been demonstrated in this thesis, adding to the overall picture of cell division. GpsB is essential in *S. pneumoniae* (Rued et al., 2017), conditionally essential in *L. monocytogenes* (Rismondo et al., 2016) and PrkA and P-ReoM are required for the viability of *L. monocytogenes* (Wamp et al., 2020). *L. monocytogenes* infections can lead to human listeriosis which is coupled to a high mortality rate of 25-30 % (Lomonaco et al., 2015) and *S. pneumoniae* diseases range from mild respiratory tract infections to pneumococcal pneumonia and meningitis (Henriques-Normark & Tuomanen, 2013). Listeriosis is particularly dangerous for pregnant women and can result in miscarriages and neonatal deaths (Segado-Arenas et al., 2018), whereas small children and the elderly are at highest risk with *S. pneumoniae* infections (Henriques-Normark & Tuomanen, 2013). The only feasible treatment for *Listeria* infections are antibiotics, predominantly a combination therapy of aminoglycosides and penicillins (Luque-Sastre et al., 2018) and for decades penicillin was the standard treatment for pneumococcal infections (Henriques-Normark & Tuomanen, 2013). Like many forms of bacteria, *Listeria* and *pneumococci* are rapidly acquiring resistance to antimicrobial compounds (Henriques-Normark & Tuomanen, 2013; Luque-Sastre et al., 2018). Since there is an absence of GpsB and ReoM homologues in humans, they offer the potential to be targets for novel antibiotics to treat infections caused by Gram-positive bacteria.

In Chapter 5, an X-ray crystallography-based fragment screening experiment with the N-terminal domain of *Sp*GpsB was performed to identify small ligands that could be used as a scaffold to generate a chemical probe to block the GpsB:PBP interaction. Two of the ligands (3 and 9) bound with millimolar affinity to GpsB and ligand 9 was identified as the best scaffold candidate for the generation of a larger molecule capable of binding to *Sp*GpsB with a higher affinity. Building the GpsB interactome and identifying the molecular basis of the interactions could lead to the discovery of new antibiotic targets. N-terminal GpsB ligands identified by XChem that bind in novel GpsB interaction sites could be used as starter molecules for the

production of chemical probes. The development of probes that block essential bacterial division processes is only a small stepping-stone in the production of a novel antibiotics that are so desperately required due to the growing resistance of bacteria to existing antimicrobials.

References

Absalon, C., Obuchowski, M., Madec, E., Delattre, D., Holland, I.B. & Séror, S.J. (2009) CpgA, EF-Tu and the stressosome protein YezB are substrates of the Ser/Thr kinase/phosphatase couple, PrkC/PrpC, in *Bacillus subtilis*. *Microbiology*. 155 (3), 932–943.

Afonine, P. V., Mustyakimov, M., Grosse-Kunstleve, R.W., Moriarty, N.W., Langan, P. & Adams, P.D. (2010) Joint X-ray and neutron refinement with phenix.refine. *Acta Crystallographica Section D Biological Crystallography*. 66 (11), 1153–1163.

Angeles, D.M., Macia-Valero, A., Bohorquez, L.C. & Scheffers, D.-J. (2019) The PASTA domains of *Bacillus subtilis* PBP2B stabilize the interaction of PBP2B with DivIB. *bioRxiv*. 1 (18), 527–530.

Ardito, F., Giuliani, M., Perrone, D., Troiano, G. & Muzio, L. Lo (2017) The crucial role of protein phosphorylation in cell signalingand its use as targeted therapy (Review). *International Journal of Molecular Medicine*. 40 (2), 271–280.

van Baarle, S., Celik, I.N., Kaval, K.G., Bramkamp, M., Hamoen, L.W. & Halbedel, S. (2013) Protein-protein interaction domains of *Bacillus subtilis* DivIVA. *Journal of Bacteriology*. 195 (5), 1012–1021.

Bakshi, S., Siryaporn, A., Goulian, M. & Weisshaar, J.C. (2012) Superresolution imaging of ribosomes and RNA polymerase in live *Escherichia coli* cells. *Molecular Microbiology*. 85 (1), 21–38.

Barák, I. & Muchová, K. (2018) The positioning of the asymmetric septum during sporulation in *Bacillus subtilis* Eric Cascales (ed.). *PLoS ONE*. 13 (8), e0201979.

Barák, I. & Youngman, P. (1996) SpoIIE mutants of *Bacillus subtilis* comprise two distinct phenotypic classes consistent with a dual functional role for the SpoIIE protein. *Journal of bacteriology*. 178 (16), 4984–4989.

Battye, T.G.G., Kontogiannis, L., Johnson, O., Powell, H.R. & Leslie, A.G.W. (2011) iMOSFLM : a new graphical interface for diffraction-image processing with MOSFLM. *Acta Crystallographica Section D Biological Crystallography*. 67 (4), 271–281.

Begg, K.J. & Donachie, W.D. (1998) Division planes alternate in spherical cells of *Escherichia coli*. *Journal of Bacteriology*. 180 (9), 2564–2567.

Beilsten-Edmands, J., Winter, G., Gildea, R., Parkhurst, J., Waterman, D. & Evans, G. (2020) Scaling diffraction data in the DIALS software package: algorithms and new approaches for multi-crystal scaling. *Acta Crystallographica Section D Structural Biology*. 76 (4), 385–399.

Berg, K.H., Straume, D. & Håvarstein, L.S. (2014) The function of the transmembrane and cytoplasmic domains of pneumococcal penicillin-binding proteins 2x and 2b extends beyond that of simple anchoring devices. *Microbiology*. 160 (8), 1585–1598.

Bisson-Filho, A.W., Hsu, Y.-P., Squyres, G.R., Kuru, E., Wu, F., Jukes, C., Sun, Y., Dekker, C., Holden, S., VanNieuwenhze, M.S., Brun, Y. V. & Garner, E.C. (2017) Treadmilling by FtsZ filaments drives peptidoglycan synthesis and bacterial cell division. *Science*. 355 (6326), 739–743.

den Blaauwen, T., Hamoen, L.W. & Levin, P.A. (2017) The divisome at 25: the road ahead. *Current Opinion in*

Microbiology. 3685–94.

Boersma, M.J., Kuru, E., Rittichier, J.T., VanNieuwenhze, M.S., Brun, Y. V. & Winkler, M.E. (2015) Minimal Peptidoglycan (PG) Turnover in Wild-Type and PG Hydrolase and Cell Division Mutants of *Streptococcus pneumoniae* D39 Growing Planktonically and in Host-Relevant Biofilms P. de Boer (ed.). *Journal of Bacteriology*. 197 (21), 3472–3485.

Boes, A., Olatunji, S., Breukink, E. & Terrak, M. (2019) Regulation of the peptidoglycan polymerase activity of PBP1b by antagonist actions of the core divisome proteins FtsBLQ and FtsN. *mBio*. 10 (1), 1–16.

Bottomley, A.L., Kabli, A.F., Hurd, A.F., Turner, R.D., Garcia-Lara, J. & Foster, S.J. (2014) *Staphylococcus aureus* DivIB is a peptidoglycan-binding protein that is required for a morphological checkpoint in cell division. *Molecular Microbiology*. 94 (5), 1041–1064.

Bottomley, A.L., Liew, A.T.F., Kusuma, K.D., Peterson, E., Seidel, L., Foster, S.J. & Harry, E.J. (2017) Coordination of Chromosome Segregation and Cell Division in *Staphylococcus aureus*. *Frontiers in Microbiology*. 8 (AUG), 1–13.

Bradshaw, N. & Losick, R. (2015) Asymmetric division triggers cell-specific gene expression through coupled capture and stabilization of a phosphatase. *eLife*. 4 (OCTOBER2015), 1–18.

Bramkamp, M., Emmins, R., Weston, L., Donovan, C., Daniel, R.A. & Errington, J. (2008) A novel component of the division-site selection system of *Bacillus subtilis* and a new mode of action for the division inhibitor MinCD. *Molecular Microbiology*. 70 (6), 1556–1569.

Brown, E.D., Vivas, E.I., Walsh, C.T. & Kolter, R. (1995) MurA (MurZ), the enzyme that catalyzes the first committed step in peptidoglycan biosynthesis, is essential in *Escherichia coli*. *Journal of Bacteriology*. 177 (14), 4194–4197.

Buddelmeijer, N. & Beckwith, J. (2004) A complex of the *Escherichia coli* cell division proteins FtsL, FtsB and FtsQ forms independently of its localization to the septal region. *Molecular Microbiology*. 52 (5), 1315–1327.

Bugrysheva, J., Froehlich, B.J., Freiberg, J.A. & Scott, J.R. (2011) Serine/threonine protein kinase Stk is required for virulence, stress response, and penicillin tolerance in *Streptococcus pyogenes*. *Infection and Immunity*. 79 (10), 4201–4209.

Bukau, B. & Horwich, A.L. (1998) The Hsp70 and Hsp60 Chaperone Machines. *Cell*. 92 (3), 351–366.

Chen, V.B., Arendall, W.B., Headd, J.J., Keedy, D.A., Immormino, R.M., Kapral, G.J., Murray, L.W., Richardson, J.S. & Richardson, D.C. (2010) MolProbity : all-atom structure validation for macromolecular crystallography. *Acta Crystallographica Section D Biological Crystallography*. 66 (1), 12–21.

Cho, H., Wivagg, C.N., Kapoor, M., Barry, Z., Rohs, P.D.A., Suh, H., Marto, J.A., Garner, E.C. & Bernhardt, T.G. (2016) Bacterial cell wall biogenesis is mediated by SEDS and PBP polymerase families functioning semi-autonomously. *Nature Microbiology*. 1 (10), 16172.

Cladière, L., Hamze, K., Madec, E., Levdikov, V.M., Wilkinson, A.J., Holland, I.B. & Séror, S.J. (2006) The GTPase, CpgA(YloQ), a putative translation factor, is implicated in morphogenesis in *Bacillus subtilis*. *Molecular*

Genetics and Genomics. 275 (4), 409–420.

Claessen, D., Emmins, R., Hamoen, L.W., Daniel, R.A., Errington, J. & Edwards, D.H. (2008) Control of the cell elongation–division cycle by shuttling of PBP1 protein in *Bacillus subtilis*. *Molecular Microbiology*. 68 (4), 1029–1046.

Cleverley, R. & Lewis, R. (2015) EzrA: a spectrin-like scaffold in the bacterial cell division machinery. *Microbial Cell*. 2 (2), 59–61.

Cleverley, R.M., Barrett, J.R., Baslé, A., Bui, N.K., Hewitt, L., Solovyova, A., Xu, Z.-Q., Daniel, R.A., Dixon, N.E., Harry, E.J., Oakley, A.J., Vollmer, W. & Lewis, R.J. (2014) Structure and function of a spectrin-like regulator of bacterial cytokinesis. *Nature Communications*. 5 (1), 5421.

Cleverley, R.M., Rismondo, J., Lockhart-Cairns, M.P., Van Bentum, P.T., Egan, A.J.F., Vollmer, W., Halbedel, S., Baldock, C., Breukink, E. & Lewis, R.J. (2016) Subunit Arrangement in GpsB, a Regulator of Cell Wall Biosynthesis. *Microbial Drug Resistance*. 22 (6), 446–460.

Cleverley, R.M., Rutter, Z.J., Rismondo, J., Corona, F., Tsui, H.-C.T., Alatawi, F.A., Daniel, R.A., Halbedel, S., Massidda, O., Winkler, M.E. & Lewis, R.J. (2019) The cell cycle regulator GpsB functions as cytosolic adaptor for multiple cell wall enzymes. *Nature Communications*. 10 (1), 261.

Contreras-Martel, C., Job, V., Di Guilmi, A.M., Vernet, T., Dideberg, O. & Dessen, A. (2006) Crystal structure of penicillin-binding protein 1a (PBP1a) reveals a mutational hotspot implicated in β-lactam resistance in *Streptococcus pneumoniae*. *Journal of Molecular Biology*. 355 (4), 684–696.

Contreras-Martel, C., Martins, A., Ecobichon, C., Trindade, D.M., Matteï, P.J., Hicham, S., Hardouin, P., Ghachi, M. El, Boneca, I.G. & Dessen, A. (2017) Molecular architecture of the PBP2-MreC core bacterial cell wall synthesis complex. *Nature Communications*. 8 (1), 1–10.

Cowan, S.W., Schirmer, T., Rummel, G., Steiert, M., Ghosh, R., Pauptit, R.A., Jansonius, J.N. & Rosenbusch, J.P. (1992) Crystal structures explain functional properties of two *E. coli* porins. *Nature*. 358 (6389), 727–733.

Cowtan, K. (2012) Completion of autobuilt protein models using a database of protein fragments. *Acta Crystallographica Section D Biological Crystallography*. 68 (4), 328–335.

Cox, S., Radzio-Andzelm, E. & Taylor, S.S. (1994) Domain movements in protein kinases. *Current Opinion in Structural Biology*. 4 (6), 893–901.

Dephoure, N., Gould, K.L., Gygi, S.P. & Kellogg, D.R. (2013) Mapping and analysis of phosphorylation sites: A quick guide for cell biologists. *Molecular Biology of the Cell*. 24 (5), 535–542.

Diederichs, K., McSweeney, S. & Ravelli, R.B.G. (2003) Zero-dose extrapolation as part of macromolecular synchrotron data reduction. *Acta Crystallographica Section D Biological Crystallography*. 59 (5), 903–909.

Dion, M.F., Kapoor, M., Sun, Y., Wilson, S., Ryan, J., Vigouroux, A., van Teeffelen, S., Oldenbourg, R. & Garner, E.C. (2019) *Bacillus subtilis* cell diameter is determined by the opposing actions of two distinct cell wall synthetic systems. *Nature Microbiology*. 4 (8), 1294–1305.

Divakaruni, A. V., Loo, R.R.O., Xie, Y., Loo, J.A. & Gober, J.W. (2005) The cell-shape protein MreC interacts with

extracytoplasmic proteins including cell wall assembly complexes in *Caulobacter crescentus*. *Proceedings of the National Academy of Sciences of the United States of America*. 102 (51), 18602–18607.

Doig, A.J. & Baldwin, R.L. (1995) N- and C-capping preferences for all 20 amino acids in α-helical peptides. *Protein Science*. 4 (7), 1325–1336.

Dominguez-Escobar, J., Chastanet, A., Crevenna, A.H., Fromion, V., Wedlich-Soldner, R. & Carballido-Lopez, R. (2011) Processive Movement of MreB-Associated Cell Wall Biosynthetic Complexes in Bacteria. *Science*. 333 (6039), 225–228.

Donovan, C., Sieger, B., Krämer, R. & Bramkamp, M. (2012) A synthetic *Escherichia coli* system identifies a conserved origin tethering factor in Actinobacteria. *Molecular Microbiology*. 84 (1), 105–116.

Dramsi, S., Magnet, S., Davison, S. & Arthur, M. (2008) Covalent attachment of proteins to peptidoglycan. *FEMS Microbiology Reviews*. 32 (2), 307–320.

Drozdetskiy, A., Cole, C., Procter, J. & Barton, G.J. (2015) JPred4: A protein secondary structure prediction server. *Nucleic Acids Research*. 43 (W1), W389–W394.

Duguid, J.P. (1946) The sensitivity of bacteria to the action of penicillin. *Edinburgh medical journal*. 53 (8), 401–412.

Durán, R., Villarino, A., Bellinzoni, M., Wehenkel, A., Fernandez, P., Boitel, B., Cole, S.T., Alzari, P.M. & Cerveñansky, C. (2005) Conserved autophosphorylation pattern in activation loops and juxtamembrane regions of *Mycobacterium tuberculosis* Ser/Thr protein kinases. *Biochemical and Biophysical Research Communications*. 333 (3), 858–867.

Edwards, D.H. & Errington, J. (1997) The *Bacillus subtilis* DivIVA protein targets to the division septum and controls the site specificity of cell division. *Molecular Microbiology*. 24 (5), 905–915.

Egan, A.J.F., Biboy, J., van't Veer, I., Breukink, E. & Vollmer, W. (2015) Activities and regulation of peptidoglycan synthases. *Philosophical Transactions of the Royal Society B: Biological Sciences*. 370 (1679), 20150031.

Egan, A.J.F., Cleverley, R.M., Peters, K., Lewis, R.J. & Vollmer, W. (2017) Regulation of bacterial cell wall growth. *The FEBS Journal*. 284 (6), 851–867.

Egan, A.J.F. & Vollmer, W. (2013) The physiology of bacterial cell division. *Annals of the New York Academy of Sciences*. 1277 (1), 8–28.

Emami, K., Guyet, A., Kawai, Y., Devi, J., Wu, L.J., Allenby, N., Daniel, R.A. & Errington, J. (2017) RodA as the missing glycosyltransferase in *Bacillus subtilis* and antibiotic discovery for the peptidoglycan polymerase pathway. *Nature Microbiology*. 2 (3), 16253.

Emsley, P., Lohkamp, B., Scott, W.G. & Cowtan, K. (2010) Features and development of Coot. *Acta Crystallographica Section D: Biological Crystallography*. 66 (4), 486–501.

Van Den Ent, F., Leaver, M., Bendezu, F., Errington, J., De Boer, P. & Löwe, J. (2006) Dimeric structure of the cell shape protein MreC and its functional implications. *Molecular Microbiology*. 62 (6), 1631–1642.

Eswara, P.J., Brzozowski, R.S., Viola, M.G., Graham, G., Spanoudis, C., Trebino, C., Jha, J., Aubee, J.I., Thompson,

K.M., Camberg, J.L. & Ramamurthi, K.S. (2018) An essential *Staphylococcus aureus* cell division protein directly regulates FtsZ dynamics. *eLife*. 71–24.

Evans, P.R. & Murshudov, G.N. (2013) How good are my data and what is the resolution? *Acta Crystallographica Section D Biological Crystallography*. 69 (7), 1204–1214.

Fadda, D., Santona, A., D'Ulisse, V., Ghelardini, P., Ennas, M.G., Whalen, M.B. & Massidda, O. (2007) *Streptococcus pneumoniae* DivIVA: Localization and Interactions in a MinCD-Free Context. *Journal of Bacteriology*. 189 (4), 1288–1298.

Feucht, A., Magnin, T., Yudkin, M.D. & Errington, J. (1996) Bifunctional protein required for asymmetric cell division and cell-specific transcription in *Bacillus subtilis*. *Genes and Development*. 10 (7), 794–803.

Figge, R.M., Divakaruni, A. V. & Gober, J.W. (2004) MreB, the cell shape-determining bacterial actin homologue, co-ordinates cell wall morphogenesis in *Caulobacter crescentus*. *Molecular Microbiology*. 51 (5), 1321–1332.

Fleurie, A., Cluzel, C., Guiral, S., Freton, C., Galisson, F., Zanella-Cleon, I., di Guilmi, A.M. & Grangeasse, C. (2012) Mutational dissection of the S/T-kinase StkP reveals crucial roles in cell division of *Streptococcus pneumoniae*. *Molecular Microbiology*. 83 (4), 746–758.

Fleurie, A., Lesterlin, C., Manuse, S., Zhao, C., Cluzel, C., Lavergne, J.-P., Franz-Wachtel, M., Macek, B., Combet, C., Kuru, E., VanNieuwenhze, M.S., Brun, Y. V., Sherratt, D. & Grangeasse, C. (2014b) MapZ marks the division sites and positions FtsZ rings in *Streptococcus pneumoniae*. *Nature*. 516 (7530), 259–262.

Fleurie, A., Manuse, S., Zhao, C., Campo, N., Cluzel, C., Lavergne, J.-P., Freton, C., Combet, C., Guiral, S., Soufi, B., Macek, B., Kuru, E., VanNieuwenhze, M.S., Brun, Y. V., Di Guilmi, A.-M., Claverys, J.-P., Galinier, A. & Grangeasse, C. (2014a) Interplay of the serine/threonine-kinase StkP and the paralogs DivIVA and GpsB in pneumococcal cell elongation and division. Patrick H. Viollier (ed.). *PLoS genetics*. 10 (4), e1004275.

Foulquier, E., Pompeo, F., Freton, C., Cordier, B., Grangeasse, C. & Galinier, A. (2014) PrkC-mediated phosphorylation of overexpressed YvcK protein regulates PBP1 protein localization in *Bacillus subtilis mreB* mutant cells. *Journal of Biological Chemistry*. 289 (34), 23662–23669.

Fraipont, C., Sapunaric, F., Auger, G., Devreese, B., Lioux, T., Blanot, D., Mengin-Lecreulx, D., Herdewijn, P., Van Beeumen, J., Frère, J.M. & Nguyen-Distèche, M. (2006) Glycosyl transferase activity of the *Escherichia coli* penicillin-binding protein 1b: Specificity profile for the substrate. *Biochemistry*. 45 (12), 4007–4013.

Gamba, P., Veening, J.-W., Saunders, N.J., Hamoen, L.W. & Daniel, R.A. (2009) Two-Step Assembly Dynamics of the *Bacillus subtilis* Divisome. *Journal of Bacteriology*. 191 (13), 4186–4194.

Garner, E.C., Bernard, R., Wang, W., Zhuang, X., Rudner, D.Z. & Mitchison, T. (2011) Coupled, Circumferential Motions of the Cell Wall Synthesis Machinery and MreB Filaments in *B. subtilis*. *Science*. 333 (6039), 222–225.

Ginda, K., Bezulska, M., Ziólkiewicz, M., Dziadek, J., Zakrzewska-Czerwińska, J. & Jakimowicz, D. (2013) ParA of Mycobacterium smegmatis co-ordinates chromosome segregation with the cell cycle and interacts with the polar growth determinant DivIVA. *Molecular Microbiology*. 87 (5), 998–1012.

Glauert, A.M. & Thornley, M.J. (1969) The Topography of the Bacterial Cell Wall. *Annual Review of Microbiology*. 23 (1), 159–198.

Goehring, N.W., Gonzalez, M.D. & Beckwith, J. (2006) Premature targeting of cell division proteins to midcell reveals hierarchies of protein interactions involved in divisome assembly. *Molecular Microbiology*. 61 (1), 33–45.

Goffin, C. & Ghuysen, J.-M. (1998) Multimodular Penicillin-Binding Proteins: An Enigmatic Family of Orthologs and Paralogs. *Microbiology and Molecular Biology Reviews*. 62 (4), 1079–1093.

Gonzalez, M.D., Akbay, E.A., Boyd, D. & Beckwith, J. (2010) Multiple interaction domains in FtsL, a protein component of the widely conserved bacterial FtsLBQ cell division complex. *Journal of Bacteriology*. 192 (11), 2757–2768.

Gordon, E., Mouz, N., Duée, E. & Dideberg, O. (2000) The crystal structure of the penicillin-binding protein 2x from *Streptococcus pneumoniae* and its acyl-enzyme form: Implication in drug resistance. *Journal of Molecular Biology*. 299 (2), 477–485.

Görke, B., Foulquier, E. & Galinier, A. (2005) YvcK of *Bacillus subtilis* is required for a normal cell shape and for growth on Krebs cycle intermediates and substrates of the pentose phosphate pathway. *Microbiology*. 151 (11), 3777–3791.

Gruszczyński, P., Obuchowski, M. & Kaźmierkiewicz, R. (2010) Phosphorylation and ATP-binding induced conformational changes in the PrkC, Ser/Thr kinase from *B. subtilis*. *Journal of Computer-Aided Molecular Design*. 24 (9), 733–747.

Halbedel, S. & Lewis, R.J. (2019) Structural basis for interaction of DivIVA/GpsB proteins with their ligands. *Molecular Microbiology*. 111 (6), 1404–1415.

Hall, C.L., Lytle, B.L., Jensen, D., Hoff, J.S., Peterson, F.C., Volkman, B.F. & Kristich, C.J. (2017) Structure and Dimerization of IreB, a Negative Regulator of Cephalosporin Resistance in *Enterococcus faecalis*. *Journal of Molecular Biology*. 429 (15), 2324–2336.

Hall, C.L., Tschannen, M., Worthey, E.A. & Kristich, C.J. (2013) IreB, a Ser/Thr kinase substrate, influences antimicrobial resistance in *Enterococcus faecalis*. *Antimicrobial Agents and Chemotherapy*. 57 (12), 6179–6186.

Hammond, L.R., White, M.L. & Eswara, P.J. (2019) ¡vIVA la DivIVA! William Margolin (ed.). *Journal of bacteriology*. 201 (21), 1–14.

Hamoen, L.W., Meile, J.C., De Jong, W., Noirot, P. & Errington, J. (2006) SepF, a novel FtsZ-interacting protein required for a late step in cell division. *Molecular Microbiology*. 59 (3), 989–999.

Hendrickx, A.P.A., Budzik, J.M., Oh, S.Y. & Schneewind, O. (2011) Architects at the bacterial surface-sortases and the assembly of pili with isopeptide bonds. *Nature Reviews Microbiology*. 9 (3), 166–176.

Henriques-Normark, B. & Tuomanen, E.I. (2013) The Pneumococcus: Epidemiology, Microbiology, and Pathogenesis. *Cold Spring Harbor Perspectives in Medicine*. 3 (7), a010215–a010215.

Henriques, A.O., Glaser, P., Piggot, P.J. & Moran, C.P. (1998) Control of cell shape and elongation by the *rodA* gene in *Bacillus subtilis*. *Molecular Microbiology*. 28 (2), 235–247.

Holm, L. (2020) DALI and the persistence of protein shape. *Protein Science*. 29 (1), 128–140.

Huse, M. & Kuriyan, J. (2002) The conformational plasticity of protein kinases. *Cell*. 109 (3), 275–282.

Hussain, S., Wivagg, C.N., Szwedziak, P., Wong, F., Schaefer, K., Izoré, T., Renner, L.D., Holmes, M.J., Sun, Y., Bisson-Filho, A.W., Walker, S., Amir, A., Löwe, J. & Garner, E.C. (2018) MreB filaments align along greatest principal membrane curvature to orient cell wall synthesis. *eLife*. 71–45.

Iqbalsyah, T.M. (2004) Effect of the N3 residue on the stability of the -helix. *Protein Science*. 13 (1), 32–39.

Ishino, F., Mitsui, K., Tamaki, S. & Matsuhashi, M. (1980) Dual enzyme activities of cell wall peptidoglycan synthesis, peptidoglycan transglycosylase and penicillin-sensitive transpeptidase, in purified preparations of Escherichia coli penicillin-binding protein 1A. *Biochemical and Biophysical Research Communications*. 97 (1), 287–293.

Jones, L.J.F., Carballido-López, R. & Errington, J. (2001) Control of cell shape in bacteria: Helical, actin-like filaments in *Bacillus subtilis*. *Cell*. 104 (6), 913–922.

Kabsch, W. (2010) XDS. *Acta Crystallographica Section D Biological Crystallography*. 66 (2), 125–132.

Kahne, D., Leimkuhler, C., Lu, W. & Walsh, C. (2005) Glycopeptide and lipoglycopeptide antibiotics. *Chemical Reviews*. 105 (2), 425–448.

Kang, C.M., Abbott, D.W., Sang, T.P., Dascher, C.C., Cantley, L.C. & Husson, R.N. (2005) The *Mycobacterium tuberculosis* serine/threonine kinases PknA and PknB: Substrate identification and regulation of cell shape. *Genes and Development*. 19 (14), 1692–1704.

Kaval, K.G., Rismondo, J. & Halbedel, S. (2014) A function of DivIVA in *Listeria monocytogenes* division site selection. *Molecular Microbiology*. 94 (3), 637–654.

Kelley, L.A., Mezulis, S., Yates, C.M., Wass, M.N. & Sternberg, M.J.E. (2015) The Phyre2 web portal for protein modeling, prediction and analysis. *Nature Protocols*. 10 (6), 845–858.

Kennelly, P.J. (2001) Protein phosphatases - A phylogenetic perspective. *Chemical Reviews*. 101 (8), 2291–2312.

Kieser, K.J., Boutte, C.C., Kester, J.C., Baer, C.E., Barczak, A.K., Meniche, X., Chao, M.C., Rego, E.H., Sassetti, C.M., Fortune, S.M. & Rubin, E.J. (2015) Phosphorylation of the Peptidoglycan Synthase PonA1 Governs the Rate of Polar Elongation in Mycobacteria. *PLoS Pathogens*. 11 (6), 1–28.

Kohanski, M.A., Dwyer, D.J. & Collins, J.J. (2010) How antibiotics kill bacteria: From targets to networks. *Nature Reviews Microbiology*. 8 (6), 423–435.

Kristich, C.J., Little, J.L., Hall, C.L. & Hoff, J.S. (2011) Reciprocal regulation of cephalosporin resistance in *Enterococcus faecalis*. *mBio*. 2 (6), 1–9.

Krojer, T., Talon, R., Pearce, N., Collins, P., Douangamath, A., Brandao-Neto, J., Dias, A., Marsden, B. & von Delft, F. (2017) The XChemExplorer graphical workflow tool for routine or large-scale protein–ligand structure

determination. *Acta Crystallographica Section D Structural Biology*. 73 (3), 267–278.

Kruse, T., Bork-Jensen, J. & Gerdes, K. (2005) The morphogenetic MreBCD proteins of *Escherichia coli* form an essential membrane-bound complex. *Molecular Microbiology*. 55 (1), 78–89.

Kuk, A.C.Y., Hao, A., Guan, Z. & Lee, S.-Y. (2019) Visualizing conformation transitions of the Lipid II flippase MurJ. *Nature Communications*. 10 (1), 1736.

Kuk, A.C.Y., Mashalidis, E.H. & Lee, S. (2017) Crystal structure of the MOP flippase MurJ in an inward-facing conformation. *Nature Structural & Molecular Biology*. 24 (2), 171–176.

Kuru, E., Hughes, H.V., Brown, P.J., Hall, E., Tekkam, S., Cava, F., De Pedro, M.A., Brun, Y. V. & Vannieuwenhze, M.S. (2012) In situ probing of newly synthesized peptidoglycan in live bacteria with fluorescent D-amino acids. *Angewandte Chemie - International Edition*. 51 (50), 12519–12523.

Land, A.D., Luo, Q. & Levin, P.A. (2014) Functional domain analysis of the cell division inhibitor EzrA. *PLoS ONE*. 9 (7), 1–14.

Land, A.D., Tsui, H.-C.T., Kocaoglu, O., Vella, S.A., Shaw, S.L., Keen, S.K., Sham, L.-T., Carlson, E.E. & Winkler, M.E. (2013) Requirement of essential Pbp2x and GpsB for septal ring closure in *Streptococcus pneumoniae* D39. *Molecular Microbiology*. 90 (5), 939–955.

Landau, M., Mayrose, I., Rosenberg, Y., Glaser, F., Martz, E., Pupko, T. & Ben-Tal, N. (2005) ConSurf 2005: the projection of evolutionary conservation scores of residues on protein structures. *Nucleic Acids Research*. 33 (Web Server), W299–W302.

Lau, I.F., Filipe, S.R., Søballe, B., Økstad, O.A., Barre, F.X. & Sherratt, D.J. (2003) Spatial and temporal organization of replicating *Escherichia coli* chromosomes. *Molecular Microbiology*. 49 (3), 731–743.

Leaver, M. & Errington, J. (2005) Roles for MreC and MreD proteins in helical growth of the cylindrical cell wall in *Bacillus subtilis*. *Molecular Microbiology*. 57 (5), 1196–1209.

Lee, J.C. & Stewart, G.C. (2003) Essential nature of the *mreC* determinant of *Bacillus subtilis*. *Journal of Bacteriology*. 185 (15), 4490–4498.

Lenarcic, R., Halbedel, S., Visser, L., Shaw, M., Wu, L.J., Errington, J., Marenduzzo, D. & Hamoen, L.W. (2009) Localisation of DivIVA by targeting to negatively curved membranes. *The EMBO Journal*. 28 (15), 2272–2282.

Levin, P.A., Kurtser, I.G. & Grossman, A.D. (1999) Identification and characterization of a negative regulator of FtsZ ring formation in *Bacillus subtilis*. *Proceedings of the National Academy of Sciences of the United States of America*. 96 (17), 9642–9647.

Liu, Y. & Breukink, E. (2016) The Membrane Steps of Bacterial Cell Wall Synthesis as Antibiotic Targets. *Antibiotics*. 5 (3), 28.

Lomonaco, S., Nucera, D. & Filipello, V. (2015) The evolution and epidemiology of *Listeria monocytogenes* in Europe and the United States. *Infection, Genetics and Evolution*. 35172–183.

Long, F., Nicholls, R.A., Emsley, P., Gražulis, S., Merkys, A., Vaitkus, A. & Murshudov, G.N. (2017) AceDRG: A

stereochemical description generator for ligands. *Acta Crystallographica Section D: Structural Biology*. 73 (2), 112–122.

Loose, M. & Mitchison, T.J. (2014) The bacterial cell division proteins FtsA and FtsZ self-organize into dynamic cytoskeletal patterns. *Nature Cell Biology*. 16 (1), 38–46.

Lovering, A.L., De Castro, L.H., Lim, D. & Strynadka, N.C.J. (2007) Structural insight into the transglycosylation step of bacterial cell-wall biosynthesis. *Science*. 315 (5817), 1402–1405.

Lovering, A.L., Safadi, S.S. & Strynadka, N.C.J. (2012) Structural Perspective of Peptidoglycan Biosynthesis and Assembly. *Annual Review of Biochemistry*. 81 (1), 451–478.

Lovering, A.L. & Strynadka, N.C.J. (2007) High-resolution Structure of the Major Periplasmic Domain from the Cell Shape-determining Filament MreC. *Journal of Molecular Biology*. 372 (4), 1034–1044.

Lu, Z., Wang, H., Zhang, A., Liu, X., Zhou, W., Yang, C., Guddat, L., Yang, H., Schofield, C.J. & Rao, Z. (2020) Structures of *Mycobacterium tuberculosis* Penicillin-Binding Protein 3 in Complex with Five β-Lactam Antibiotics Reveal Mechanism of Inactivation. *Molecular pharmacology*. 97 (4), 287–294.

Lupoli, T.J., Tsukamoto, H., Doud, E.H., Wang, T.S.A., Walker, S. & Kahne, D. (2011) Transpeptidase-mediated incorporation of d-amino acids into bacterial peptidoglycan. *Journal of the American Chemical Society*. 133 (28), 10748–10751.

Luque-Sastre, L., Arroyo, C., Fox, E.M., McMahon, B.J., Bai, L., Li, F. & Fanning, S. (2018) 'Antimicrobial Resistance in *Listeria* Species', in *Antimicrobial Resistance in Bacteria from Livestock and Companion Animals*. [Online]. American Society of Microbiology. pp. 237–259.

Lutkenhaus, J. & Addinall, S.. (1997) Bacterial cell division and the septal ring. *Biochemistry*. 66 (3), 92–116.

Macheboeuf, P., Contreras-Martel, C., Job, V., Dideberg, O. & Dessen, A. (2006) Penicillin binding proteins: Key players in bacterial cell cycle and drug resistance processes. *FEMS Microbiology Reviews*. 30 (5), 673–691.

Macheboeuf, P., Di Guilmi, A.M., Job, V., Vernet, T., Dideberg, O. & Dessen, A. (2005) Active site restructuring regulates ligand recognition in class A penicillin-binding proteins. *Proceedings of the National Academy of Sciences of the United States of America*. 102 (3), 577–582.

Madec, E., Laszkiewicz, A., Iwanicki, A., Obuchowski, M. & Séror, S. (2002) Characterization of a membrane-linked Ser/Thr protein kinase in *Bacillus subtilis*, implicated in developmental processes. *Molecular Microbiology*. 46 (2), 571–586.

Madec, E., Stensballe, A., Kjellström, S., Cladière, L., Obuchowski, M., Jensen, O.N. & Séror, S.J. (2003) Mass spectrometry and site-directed mutagenesis identify several autophosphorylated residues required for the activity of PrkC, a Ser/Thr kinase from *Bacillus subtilis*. *Journal of Molecular Biology*. 330 (3), 459–472.

Maestro, B., Novaková, L., Hesek, D., Lee, M., Leyva, E., Mobashery, S., Sanz, J.M. & Branny, P. (2011) Recognition of peptidoglycan and β-lactam antibiotics by the extracellular domain of the Ser/Thr protein kinase StkP from *Streptococcus pneumoniae*. *FEBS Letters*. 585 (2), 357–363.

Manuse, S., Fleurie, A., Zucchini, L., Lesterlin, C. & Grangeasse, C. (2015) Role of eukaryotic-like serine/threonine

kinases in bacterial cell division and morphogenesis. *FEMS Microbiology Reviews*. 40 (1), 41–56.

Marrec-Fairley, M., Piette, A., Gallet, X., Brasseur, R., Hara, H., Fraipont, C., Ghuysen, J.M. & Nguyen-Distèche, M. (2000) Differential functionalities of amphiphilic peptide segments of the cell-septation penicillin-binding protein 3 of *Escherichia coli*. *Molecular Microbiology*. 37 (5), 1019–1031.

Marston, A.L., Thomaides, H.B., Edwards, D.H., Sharpe, M.E. & Errington, J. (1998) Polar localization of the MinD protein of *Bacillus subtilis* and its role in selection of the mid-cell division site. *Genes & Development*. 12 (21), 3419–3430.

Massidda, O., Anderluzzi, D., Friedli, L. & Feger, G. (1998) Unconventional organization of the division and cell wall gene cluster of *Streptococcus pneumoniae*. *Microbiology*. 144 (11), 3069–3078.

McCoy, A.J., Grosse-Kunstleve, R.W., Adams, P.D., Winn, M.D., Storoni, L.C. & Read, R.J. (2007) Phaser crystallographic software. *Journal of Applied Crystallography*. 40 (4), 658–674.

Meberg, B.M., Sailer, F.C., Nelson, D.E. & Young, K.D. (2001) Reconstruction of *Escherichia coli mrcA* (PBP 1a) mutants lacking multiple combinations of penicillin binding proteins. *Journal of Bacteriology*. 183 (20), 6148–6149.

Medina, E. & Pieper, D.H. (2016) 'Tackling Threats and Future Problems of Multidrug-Resistant Bacteria', in *How to Overcome the Antibiotic Crisis Facts, Challenges, Technologies and Future Perspectives*. [Online]. pp. 3–33.

Meeske, A.J., Riley, E.P., Robins, W.P., Uehara, T., Mekalanos, J.J., Kahne, D., Walker, S., Kruse, A.C., Bernhardt, T.G. & Rudner, D.Z. (2016) SEDS proteins are a widespread family of bacterial cell wall polymerases. *Nature*. 537 (7622), 634–638.

Micsonai, A., Wien, F., Bulyáki, É., Kun, J., Moussong, É., Lee, Y.H., Goto, Y., Réfrégiers, M. & Kardos, J. (2018) BeStSel: A web server for accurate protein secondary structure prediction and fold recognition from the circular dichroism spectra. *Nucleic Acids Research*. 46 (W1), W315–W322.

Mir, M., Asong, J., Li, X., Cardot, J., Boons, G.-J. & Husson, R.N. (2011) The Extracytoplasmic Domain of the *Mycobacterium tuberculosis* Ser/Thr Kinase PknB Binds Specific Muropeptides and Is Required for PknB Localization William R. Bishai (ed.). *PLoS Pathogens*. 7 (7), e1002182.

Misra, S.K., Milohanic, E., Aké, F., Mijakovic, I., Deutscher, J., Monnet, V. & Henry, C. (2011) Analysis of the serine/threonine/tyrosine phosphoproteome of the pathogenic bacterium *Listeria monocytogenes* reveals phosphorylated proteins related to virulence. *Proteomics*. 11 (21), 4155–4165.

Mohammadi, T., Van Dam, V., Sijbrandi, R., Vernet, T., Zapun, A., Bouhss, A., Diepeveen-De Bruin, M., Nguyen-Distéche, M., De Kruijff, B. & Breukink, E. (2011) Identification of FtsW as a transporter of lipid-linked cell wall precursors across the membrane. *EMBO Journal*. 30 (8), 1425–1432.

Muchová, K., Chromiková, Z. & Barák, I. (2020) Linking the peptidoglycan synthesis protein complex with asymmetric cell division during *Bacillus subtilis* sporulation. *International Journal of Molecular Sciences*. 21 (12), 1–13.

Muchová, K., Kutejová, E., Scott, D.J., Brannigan, J.A., Lewis, R.J., Wilkinson, A.J. & Barák, I. (2002) Oligomerization of the *Bacillus subtilis* division protein DivIVA. *Microbiology*. 148 (3), 807–813.

Mukherjee, P., Sureka, K., Datta, P., Hossain, T., Barik, S., Das, K.P., Kundu, M. & Basu, J. (2009) Novel role of Wag31 in protection of mycobacteria under oxidative stress. *Molecular Microbiology*. 73 (1), 103–119.

Murray, H. (2016) Connecting chromosome replication with cell growth in bacteria. *Current Opinion in Microbiology*. 3413–17.

Murshudov, G.N., Vagin, A.A. & Dodson, E.J. (1997) Refinement of macromolecular structures by the maximum-likelihood method. *Acta Crystallographica Section D: Biological Crystallography*. 53 (3), 240–255.

Nakagawà, J., Tamaki, S. & Matsuhashi, M. (1979) Purified Penicillin Binding Proteins 1Bs from *Escherichia coli* Membrane Showing Activities of Both Peptidoglycan Polymerase and Peptidoglycan Crosslinking Enzyme. *Agricultural and Biological Chemistry*. 43 (6), 1379–1380.

Neuhaus, F.C. & Baddiley, J. (2003) A Continuum of Anionic Charge: Structures and Functions of D-Alanyl-Teichoic Acids in Gram-Positive Bacteria. *Microbiology and Molecular Biology Reviews*. 67 (4), 686–723.

Nováková, L., Bezoušková, S., Pompach, P., Špidlová, P., Sasková, L., Weiser, J. & Branny, P. (2010) Identification of multiple substrates of the StkP Ser/Thr protein kinase in *Streptococcus pneumoniae*. *Journal of Bacteriology*. 192 (14), 3629–3638.

Oliva, M.A., Halbedel, S., Freund, S.M., Dutow, P., Leonard, T.A., Veprintsev, D.B., Hamoen, L.W. & Löwe, J. (2010) Features critical for membrane binding revealed by DivIVA crystal structure. *The EMBO Journal*. 29 (12), 1988–2001.

Pace, C.N. & Scholtz, J.M. (1998) A helix propensity scale based on experimental studies of peptides and proteins. *Biophysical journal*. 75 (1), 422–427.

Page, R., Grzechnik, S.K., Canaves, J.M., Spraggon, G., Kreusch, A., Kuhn, P., Stevens, R.C. & Lesley, S.A. (2003) Shotgun crystallization strategy for structural genomics: an optimized two-tiered crystallization screen against the *Thermotoga maritima* proteome. *Acta Crystallographica Section D Biological Crystallography*. 59 (6), 1028–1037.

Paracuellos, P., Ballandras, A., Robert, X., Kahn, R., Hervé, M., Mengin-Lecreulx, D., Cozzone, A.J., Duclos, B. & Gouet, P. (2010) The Extended Conformation of the 2.9-Å Crystal Structure of the Three-PASTA Domain of a Ser/Thr Kinase from the Human Pathogen *Staphylococcus aureus*. *Journal of Molecular Biology*. 404 (5), 847–858.

Parikh, A., Verma, S.K., Khan, S., Prakash, B. & Nandicoori, V.K. (2009) PknB-Mediated Phosphorylation of a Novel Substrate, N-Acetylglucosamine-1-Phosphate Uridyltransferase, Modulates Its Acetyltransferase Activity. *Journal of Molecular Biology*. 386 (2), 451–464.

Pazos, M., Peters, K., Casanova, M., Palacios, P., VanNieuwenhze, M., Breukink, E., Vicente, M. & Vollmer, W. (2018) Z-ring membrane anchors associate with cell wall synthases to initiate bacterial cell division. *Nature Communications*. 9 (5090), .

Pearce, N.M., Krojer, T., Bradley, A.R., Collins, P., Nowak, R.P., Talon, R., Marsden, B.D., Kelm, S., Shi, J., Deane, C.M. & von Delft, F. (2017a) A multi-crystal method for extracting obscured crystallographic states from conventionally uninterpretable electron density. *Nature Communications*. 8 (1), 15123.

Pearce, N.M., Krojer, T. & von Delft, F. (2017b) Proper modelling of ligand binding requires an ensemble of bound and unbound states. *Acta Crystallographica Section D Structural Biology*. 73 (3), 256–266.

Perlstein, D.L., Wang, T.S.A., Doud, E.H., Kahne, D. & Walker, S. (2010) The role of the substrate lipid in processive glycan polymerization by the peptidoglycan glycosyltransferases. *Journal of the American Chemical Society*. 132 (1), 48–49.

Perry, S.E. & Edwards, D.H. (2004) Identification of a polar targeting determinant for *Bacillus subtilis* DivIVA. *Molecular Microbiology*. 54 (5), 1237–1249.

Perry, S.E. & Edwards, D.H. (2006) The *Bacillus subtilis* DivIVA Protein Has a Sporulation-Specific Proximity to Spo0J. *Journal of Bacteriology*. 188 (16), 6039–6043.

Pinho, M.G. & Errington, J. (2004) A *divIVA* null mutant of *Staphylococcus aureu*s undergoes normal cell division. *FEMS Microbiology Letters*. 240 (2), 145–149.

Plocinska, R., Martinez, L., Gorla, P., Pandeeti, E., Sarva, K., Blaszczyk, E., Dziadek, J., Madiraju, M. V. & Rajagopalan, M. (2014) *Mycobacterium tuberculosis* MtrB sensor kinase interactions with FtsI and Wag31 proteins reveal a role for MtrB distinct from that regulating MtrA activities. *Journal of Bacteriology*. 196 (23), 4120–4129.

Pompeo, F., Byrne, D., Mengin-Lecreulx, D. & Galinier, A. (2018) Dual regulation of activity and intracellular localization of the PASTA kinase PrkC during *Bacillus subtilis* growth. *Scientific Reports*. 8 (1), 1660.

Pompeo, F., Foulquier, E., Serrano, B., Grangeasse, C. & Galinier, A. (2015) Phosphorylation of the cell division protein GpsB regulates PrkC kinase activity through a negative feedback loop in *Bacillus subtilis*. *Molecular Microbiology*. 97 (1), 139–150.

Pompeo, F., Freton, C., Wicker-Planquart, C., Grangeasse, C., Jault, J.M. & Galinier, A. (2012) Phosphorylation of CpgA protein enhances both its GTPase activity and its affinity for ribosome and is crucial for *Bacillus subtilis* growth and morphology. *Journal of Biological Chemistry*. 287 (25), 20830–20838.

Rakette, S., Donat, S., Ohlsen, K. & Stehle, T. (2012) Structural Analysis of *Staphylococcus aureus* Serine/Threonine Kinase PknB Inari Kursula (ed.). *PLoS ONE*. 7 (6), e39136.

Ravala, S.K., Singh, S., Yadav, G.S., Kumar, S., Karthikeyan, S. & Chakraborti, P.K. (2015) Evidence that phosphorylation of threonine in the GT motif triggers activation of PknA, a eukaryotic-type serine/threonine kinase from *Mycobacterium tuberculosis*. *FEBS Journal*. 282 (8), 1419–1431.

Rismondo, J., Bender, J.K. & Halbedel, S. (2017) Suppressor Mutations Linking gpsB with the First Committed Step of Peptidoglycan Biosynthesis in *Listeria monocytogenes*. *Journal of Bacteriology*. 199 (1), e00393-16.

Rismondo, J., Cleverley, R.M., Lane, H. V., Großhennig, S., Steglich, A., Möller, L., Mannala, G.K., Hain, T., Lewis, R.J. & Halbedel, S. (2016) Structure of the bacterial cell division determinant GpsB and its interaction with

penicillin-binding proteins. *Molecular Microbiology*. 99 (5), 978–998.

Robson, S.A. & King, G.F. (2006) Domain architecture and structure of the bacterial cell division protein DivIB. *Proceedings of the National Academy of Sciences of the United States of America*. 103 (17), 6700–6705.

Rohs, P.D.A., Buss, J., Sim, S.I., Squyres, G.R., Srisuknimit, V., Smith, M., Cho, H., Sjodt, M., Kruse, A.C., Garner, E.C., Walker, S., Kahne, D.E. & Bernhardt, T.G. (2018) A central role for PBP2 in the activation of peptidoglycan polymerization by the bacterial cell elongation machinery. *PLoS Genetics*. 14 (10), 1–25.

Rubin, G.M., Yandell, M.D., Wortman, J.R., Gabor Miklos, G.L., Nelson, C.R., Hariharan, I.K., Fortini, M.E., Li, P.W., Apweiler, R., Fleischmann, W., Cherry, J.M., Henikoff, S., Skupski, M.P., Misra, S., Ashburner, M., Birney, E., Boguski, M.S., Brody, T., Brokstein, P., et al. (2000) Comparative genomics of the eukaryotes. *Science*. 287 (5461), 2204–2215.

Rued, B.E., Zheng, J.J., Mura, A., Tsui, H.C.T., Boersma, M.J., Mazny, J.L., Corona, F., Perez, A.J., Fadda, D., Doubravová, L., Buriánková, K., Branny, P., Massidda, O. & Winkler, M.E. (2017) Suppression and synthetic-lethal genetic relationships of Δ*gpsB* mutations indicate that GpsB mediates protein phosphorylation and penicillin-binding protein interactions in *Streptococcus pneumoniae* D39. *Molecular Microbiology*. 103 (6), 931–957.

Ruggiero, A., Squeglia, F., Marasco, D., Marchetti, R., Molinaro, A. & Berisio, R. (2011) X-ray structural studies of the entire extracellular region of the serine/threonine kinase PrkC from *Staphylococcus aureus*. *Biochemical Journal*. 435 (1), 33–41.

Ruiz, N. (2008) Bioinformatics identification of MurJ (MviN) as the peptidoglycan lipid II flippase in *Escherichia coli*. *Proceedings of the National Academy of Sciences of the United States of America*. 105 (40), 15553–15557.

Sankaran, K. & Wu, H.C. (1994) Lipid modification of bacterial prolipoprotein. Transfer of diacylglyceryl moiety from phosphatidylglycerol. *Journal of Biological Chemistry*. 269 (31), 19701–19706.

Sauvage, E., Kerff, F., Terrak, M., Ayala, J.A. & Charlier, P. (2008) The penicillin-binding proteins: Structure and role in peptidoglycan biosynthesis. *FEMS Microbiology Reviews*. 32 (2), 234–258.

Scheffers, D.J. & Tol, M.B. (2015) LipidII: Just Another Brick in the Wall? *PLoS Pathogens*. 11 (12), 1–12.

Schneider, T. & Sahl, H.-G. (2010) An oldie but a goodie – cell wall biosynthesis as antibiotic target pathway. *International Journal of Medical Microbiology*. 300 (2–3), 161–169.

Schumacher, M.A., Lee, J. & Zeng, W. (2016) Molecular insights into DNA binding and anchoring by the *Bacillus subtilis* sporulation kinetochore-like RacA protein. *Nucleic Acids Research*. 44 (11), 5438–5449.

Segado-Arenas, A., Atienza-Cuevas, L., Broullon-Molanes, J.R., Rodriguez-Gonzalez, M. & Lubian-Lopez, S.P. (2018) Late stillbirth due to listeriosis. *Autopsy and Case Reports*. 8 (4), e2018051.

Shah, I.M., Laaberki, M.-H., Popham, D.L. & Dworkin, J. (2008) A Eukaryotic-like Ser/Thr Kinase Signals Bacteria to Exit Dormancy in Response to Peptidoglycan Fragments. *Cell*. 135 (3), 486–496.

Shakir, S.M., Bryant, K.M., Larabee, J.L., Hamm, E.E., Lovchik, J., Lyons, C.R. & Ballard, J.D. (2010) Regulatory

interactions of a virulence-associated serine/threonine phosphatase-kinase pair in *Bacillus anthracis*. *Journal of Bacteriology*. 192 (2), 400–409.

Sham, L.-T., Butler, E.K., Lebar, M.D., Kahne, D., Bernhardt, T.G. & Ruiz, N. (2014) MurJ is the flippase of lipid-linked precursors for peptidoglycan biogenesis. *Science*. 345 (6193), 220–222.

Sieger, B., Schubert, K., Donovan, C. & Bramkamp, M. (2013) The lipid II flippase RodA determines morphology and growth in *Corynebacterium glutamicum*. *Molecular Microbiology*. 90 (5), 966–982.

Silhavy, T.J., Kahne, D. & Walker, S. (2010) The Bacterial Cell Envelope. *Cold Spring Harbor Perspectives in Biology*. 2 (5), a000414–a000414.

Söderström, B. & Daley, D.O. (2017) The bacterial divisome: more than a ring? *Current Genetics*. 63 (2), 161–164.

Squeglia, F., Marchetti, R., Ruggiero, A., Lanzetta, R., Marasco, D., Dworkin, J., Petoukhov, M., Molinaro, A., Berisio, R. & Silipo, A. (2011) Chemical basis of peptidoglycan discrimination by PrkC, a key kinase involved in bacterial resuscitation from dormancy. *Journal of the American Chemical Society*. 133 (51), 20676–20679.

Steele, V.R., Bottomley, A.L., Garcia-Lara, J., Kasturiarachchi, J. & Foster, S.J. (2011) Multiple essential roles for EzrA in cell division of S*taphylococcus aureus*. *Molecular Microbiology*. 80 (2), 542–555.

Steil, L., Serrano, M., Henriques, A.O. & Völker, U. (2005) Genome-wide analysis of temporally regulated and compartment-specific gene expression in sporulating cells of *Bacillus subtilis*. *Microbiology*. 151 (2), 399–420.

Straume, D., Stamsås, G.A., Berg, K.H., Salehian, Z. & Håvarstein, L.S. (2017) Identification of pneumococcal proteins that are functionally linked to penicillin-binding protein 2b (PBP2b). *Molecular Microbiology*. 103 (1), 99–116.

Taguchi, A., Welsh, M.A., Marmont, L.S., Lee, W., Sjodt, M., Kruse, A.C., Kahne, D., Bernhardt, T.G. & Walker, S. (2019) FtsW is a peptidoglycan polymerase that is functional only in complex with its cognate penicillin-binding protein. *Nature Microbiology*. 4 (4), 587–594.

Tavares, J.R., de Souza, R.F., Meira, G.L.S. & Gueiros-Filho, F.J. (2008) Cytological Characterization of YpsB, a Novel Component of the *Bacillus subtilis* Divisome. *Journal of Bacteriology*. 190 (21), 7096–7107.

Taylor, S.S., Radzio-Andzelm, E. & Hunter, T. (1995) How do protein kinases discriminate between serine/threonine and tyrosine? Structural insights from the insulin receptor protein-tyrosine kinase. *The FASEB Journal*. 9 (13), 1255–1266.

Tipper, D.J. & Strominger, J.L. (1965) Mechanism of action of penicillins: a proposal based on their structural similarity to acyl-D-alanyl-D-alanine. *Proceedings of the National Academy of Sciences*. 54 (4), 1133–1141.

Tomasz, A. (1979) The Mechanism of the Irreversible Antimicrobial Effects of Penicillins: How the Beta-Lactam Antibiotics Kill and Lyse Bacteria. *Annual Review of Microbiology*. 33 (1), 113–137.

Tsing Ng, J., Dekker, C., Kroemer, M., Osborne, M. & von Delft, F. (2014) Using textons to rank crystallization droplets by the likely presence of crystals. *Acta Crystallographica Section D Biological Crystallography*. 70

(10), 2702–2718.

Tsirigos, K.D., Peters, C., Shu, N., Käll, L. & Elofsson, A. (2015) The TOPCONS web server for consensus prediction of membrane protein topology and signal peptides. *Nucleic Acids Research*. 43 (W1), W401–W407.

Turner, R.D., Vollmer, W. & Foster, S.J. (2014) Different walls for rods and balls: The diversity of peptidoglycan. *Molecular Microbiology*. 91 (5), 862–874.

Typas, A., Banzhaf, M., Gross, C.A. & Vollmer, W. (2012) From the regulation of peptidoglycan synthesis to bacterial growth and morphology. *Nature Reviews Microbiology*. 10 (2), 123–136.

Vollmer, W., Blanot, D. & De Pedro, M.A. (2008) Peptidoglycan structure and architecture. *FEMS Microbiology Reviews*. 32 (2), 149–167.

Wamp, S., Rutter, Z.J., Rismondo, J., Jennings, C.E., Möller, L., Lewis, R.J. & Halbedel, S. (2020) PrkA controls peptidoglycan biosynthesis through the essential phosphorylation of ReoM. *eLife*. 9 (e56048), 1–75.

Wang, J.D. & Levin, P.A. (2009) Metabolism, cell growth and the bacterial cell cycle. *Nature Reviews Microbiology*. 7 (11), 822–827.

Wang, W. & Malcolm, B.A. (1999) Two-Stage PCR Protocol Allowing Introduction of Multiple Mutations, Deletions and Insertions Using QuikChange TM Site-Directed Mutagenesis. *BioTechniques*. 26 (4), 680–682.

Waxman, D.J., Yocum, R.R. & Strominger, J.L. (1980) Penicillins and cephalosporins are active site-directed acylating agents: evidence in support of the substrate analogue hypothesis. *Philosophical transactions of the Royal Society of London. Series B, Biological sciences*. 289 (1036), 257–271.

Wei, Y., McPherson, D.C. & Popham, D.L. (2004) A Mother Cell-Specific Class B Penicillin-Binding Protein, PBP4b, in *Bacillus subtilis*. *Journal of Bacteriology*. 186 (1), 258–261.

White, C.L., Kitich, A. & Gober, J.W. (2010) Positioning cell wall synthetic complexes by the bacterial morphogenetic proteins MreB and MreD. *Molecular Microbiology*. 76 (3), 616–633.

Willis, L. & Huang, K.C. (2017) Sizing up the bacterial cell cycle. *Nature Reviews Microbiology*. 15 (10), 606–620.

Wise, E.M. & Park, J.T. (1965) Penicillin: its basic site of action as an inhibitor of a peptide cross-linking reaction in cell wall mucopeptide synthesis. *Proceedings of the National Academy of Sciences of the United States of America*. 54 (1), 75–81.

Wright, G.D. (2005) Bacterial resistance to antibiotics: Enzymatic degradation and modification. *Advanced Drug Delivery Reviews*. 57 (10), 1451–1470.

Yeats, C., Finn, R.D. & Bateman, A. (2002) The PASTA domain: A β-lactam-binding domain. *Trends in Biochemical Sciences*. 27 (9), 438–440.

Young, K.D. (2006) The Selective Value of Bacterial Shape. *Microbiology and Molecular Biology Reviews*. 70 (3), 660–703.

Zhao, H., Patel, V., Helmann, J.D. & Dörr, T. (2017) Don’t let sleeping dogmas lie: new views of peptidoglycan synthesis and its regulation. *Molecular Microbiology*. 106 (6), 847–860.

Zheng, S., Sham, L.T., Rubino, F.A., Brock, K.P., Robins, W.P., Mekalanos, J.J., Marks, D.S., Bernhardt, T.G. & Kruse, A.C. (2018a) Structure and mutagenic analysis of the lipid II flippase MurJ from *Escherichia coli*. *Proceedings of the National Academy of Sciences of the United States of America*. 115 (26), 6709–6714.

Zheng, W., Cai, X., Li, S. & Li, Z. (2018b) Autophosphorylation Mechanism of the Ser/Thr Kinase Stk1 From *Staphylococcus aureus*. *Frontiers in Microbiology*. 9 (758), 1–10.

Zucchini, L., Mercy, C., Garcia, P.S., Cluzel, C., Gueguen-Chaignon, V., Galisson, F., Freton, C., Guiral, S., Brochier-Armanet, C., Gouet, P. & Grangeasse, C. (2018) PASTA repeats of the protein kinase StkP interconnect cell constriction and separation of *Streptococcus pneumoniae*. *Nature Microbiology*. 3 (2), 197–209.

Appendix A: Plasmid Maps

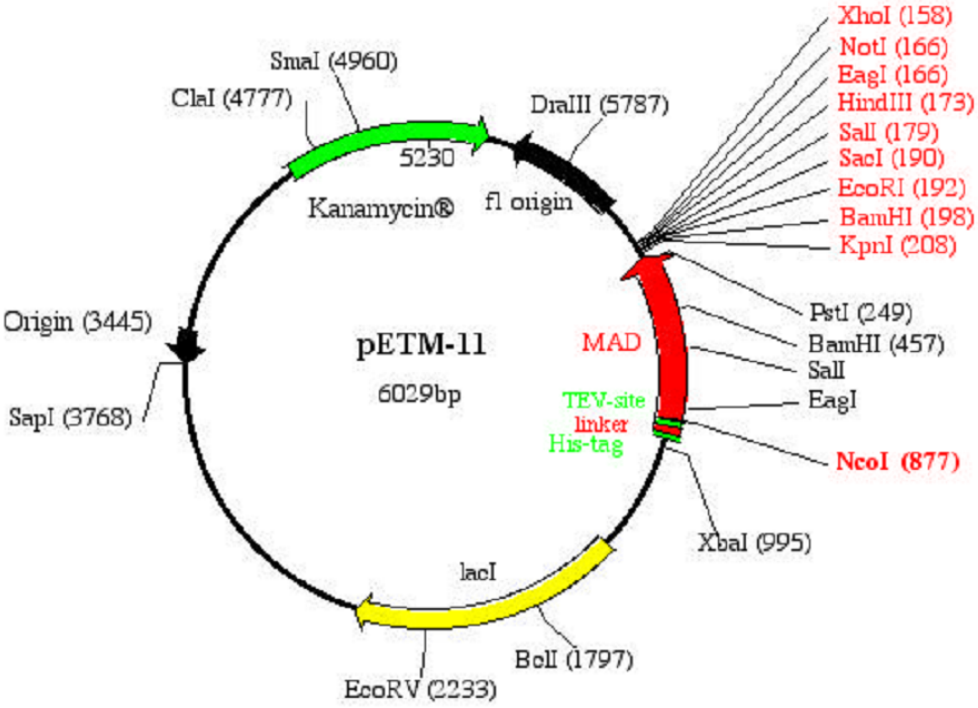

Figure Apx A.1: Plasmid map of pETM-11, image taken from SubtiWiki http://subtiwiki.uni-goettingen.de/wiki/index.php/PETM-11

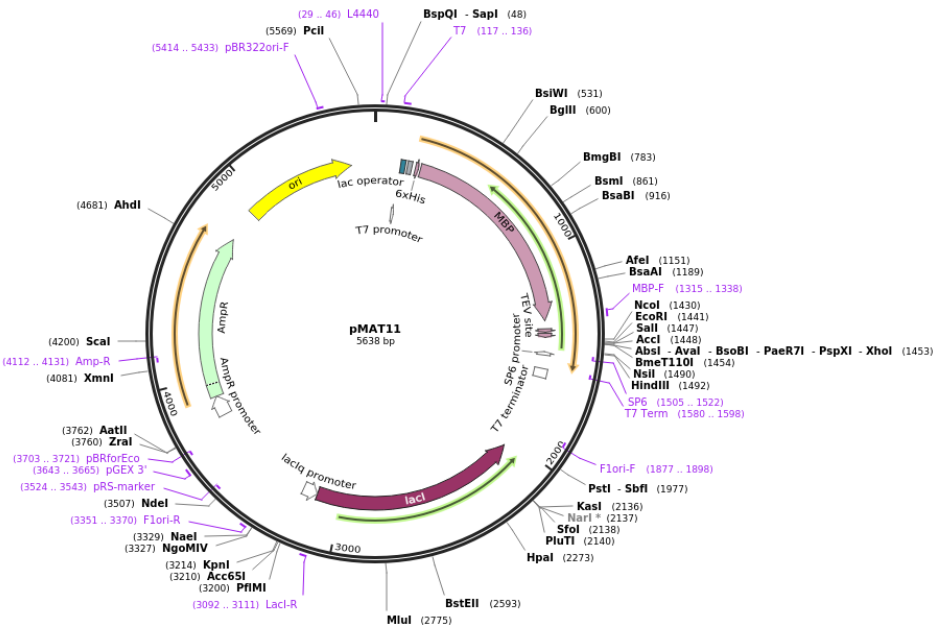

Figure Apx A.2: Plasmid map of pMAT11, image taken from addgene website https://www.addgene.org/112592/

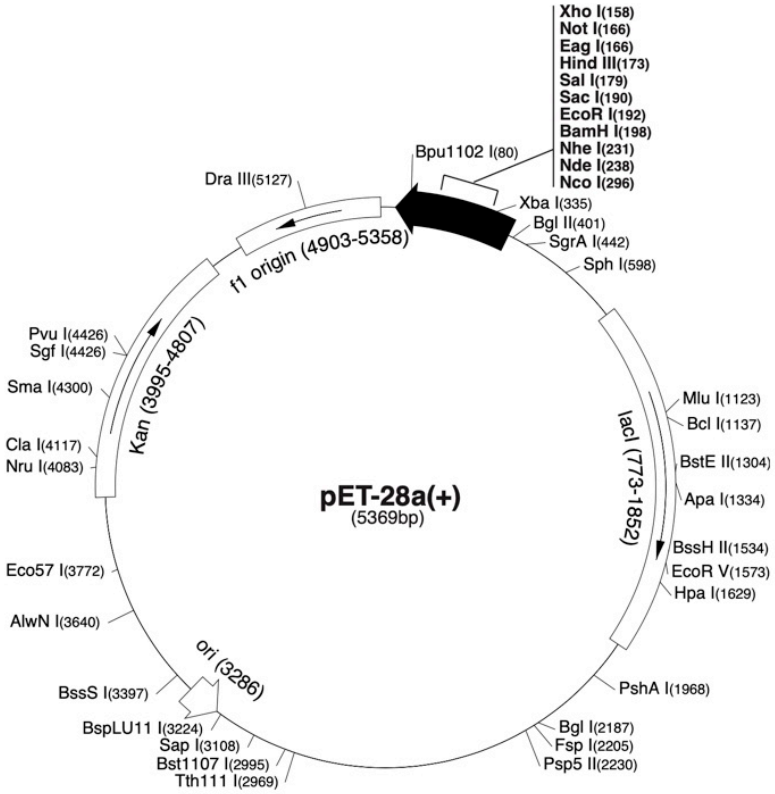

Figure Apx A.3: Plasmid map of pET-28a, image taken from Merck Millipore website https://www.merckmillipore.com/GB/en/product/pET-28a+-DNA-Novagen,EMD_BIO-69864#anchor_VMAP

Appendix B: Primers Used in This Study

Primer	Sequence 5' to 3'	Mutation introduced
*Bs*DivIVA$_{1-62}$		
N26DA30DF	GATATGATGAAGATGAAGTAGATGAATTCCTAGACCAAGTCAGAAAAGATTACG	Mutate Asn26 and Ala30 to Asp in *Bs*DivIVA$_{1-62}$
N26DA30DR	CGTAATCTTTTCTGACTTGGTCTAGGAATTCATCTACTTCATCTTCATCATATC	Mutate Asn26 and Ala30 to Asp in *Bs*DivIVA$_{1-62}$
N6KN10EF	CCATATGCCATTAACGCCAAAAGATATTCACGAAAAGACGTTTACAAAAAGTTTTCGC	Mutate Asn6 to Lys and Asn10 to Glu in *Bs*DivIVA$_{1-62}^{N26DA30D}$
N6KN10ER	GCGAAAACTTTTTGTAAACGTCTTTTCGTGAATATCTTTTGGCGTTAATGGCATATGG	Mutate Asn6 to Lys and Asn10 to Glu in *Bs*DivIVA$_{1-62}^{N26DA30D}$
R33IF	GTAGATGAATTCCTAGACCAAGTCATAAAAGATTACGAAATTGTTCTCCG	Mutate Arg33 to Ile in *Bs*DivIVA$_{1-62}^{N26DA30D}$
R33IR	CGGAGAACAATTTCGTAATCTTTTATGACTTGGTCTAGGAATTCATCTAC	Mutate Arg33 to Ile in *Bs*DivIVA$_{1-62}^{N26DA30D}$
T12EF	CGCCAAAAGATATTCACGAAAAGGAGTTTACAAAAAGTTTTCGCGG	Mutate Thr12 to Glu to in *Bs*DivIVA$_{1-62}^{N6KN10EN26DA30DR33I}$
T12ER	CCGCGAAAACTTTTTGTAAACTCCTTTTCGTGAATATCTTTTGGCG	Mutate Thr12 to Glu to in *Bs*DivIVA$_{1-62}^{N6KN10EN26DA30DR33I}$
*Bs*GpsB$_{1-68}$		
K32EF	GAGGCTACAAGCAAGAAGACGTTGACGAATTTTTAGATATGATTATTAAGG	Mutate Lys32 to Glu in *Bs*GpsB$_{1-68}$
K32ER	CCTTAATAATCATATCTAAAAATTCGTCAACGTCTTCTTGCTTGTAGCCTC	Mutate Lys32 to Glu in *Bs*GpsB$_{1-68}$
D35AF	GAAGACGTTGACAAATTTTTAGCTATGATTATTAAGGATTATGAAACCTTCCATC	Mutate Asp35 to Ala in *Bs*GpsB$_{1-68}$
D35AR	GATGGAAGGTTTCATAATCCTTAATAATCATAGCTAAAAATTTGTCAACGTCTTC	Mutate Asp35 to Ala in *Bs*GpsB$_{1-68}$
*Lm*PBPA1		
S19CK21STOPF	CAGTATCGCAATAAACAAAGTGGTGGTTGTAAATAGAAATCCCAAAAACGAGG	Mutate Ser19 to Cys and Lys21 to a stop codon in *Lm*PBPA1
S19CK21STOPR	CCTCGTTTTTGGGATTTCTATTTACAACCACCACTTTGTTTATTGCGATACTG	Mutate Ser19 to Cys and Lys21 to a stop codon in *Lm*PBPA1
R8AF	GGCAGATAAACCGCAGACAGCATCTCAGTATCGCAATAAACAAAG	Mutate Arg8 to Ala in *Lm*PBPA1$_{1-20}$
R8AR	CTTTGTTTATTGCGATACTGAGATGCTGTCTGCGGTTTATCTGCC	Mutate Arg8 to Ala in *Lm*PBPA1$_{1-20}$
Q10PF	GATAAACCGCAGACAAGATCTCCGTATCGCAATAAACAAAGTGG	Mutate Gln10 to Pro in *Lm*PBPA1$_{1-20}$
Q10PR	CCACTTTGTTTATTGCGATACGGAGATCTTGTCTGCGGTTTATC	Mutate Gln10 to Pro in *Lm*PBPA1$_{1-20}$
R12AF	GATAAACCGCAGACAAGATCTCAGTATGCCAATAAACAAAGTGGTGGTTG	Mutate Arg12 to Ala in *Lm*PBPA1$_{1-20}$
R12AR	CAACCACCACTTTGTTTATTGGCATACTGAGATCTTGTCTGCGGTTTATC	Mutate Arg12 to Ala in *Lm*PBPA1$_{1-20}$
S16RF	CTCAGTATCGCAATAAACAACGTGGTGGTTGTAAATAGAAATCCC	Mutate Ser16 to Arg in *Lm*PBPA1$_{1-20}^{R8A}$
S16RR	GGGATTTCTATTTACAACCACCACGTTGTTTATTGCGATACTGAG	Mutate Ser16 to Arg in *Lm*PBPA1$_{1-20}^{R8A}$
Y11AF	GGCAGATAAACCGCAGACAAGATCTCAGGCTCGCAATAAACAAAGTGGTGGTTG	Mutate Tyr11 to Ala in *Lm*PBPA1$_{1-20}$
Y11AR	CAACCACCACTTTGTTTATTGCGAGCCTGAGATCTTGTCTGCGGTTTATCTGCC	Mutate Tyr11 to Ala in *Lm*PBPA1$_{1-20}$
*Sp*PBP2a		
G43CR46STOPF	GTGATCGAAAAAAATTAGCCCAAGTATGTCCGATTTGAAAATTCTGGCGTCGTTATC	Mutate Gly43 to Cys and Arg46 to Stop codon in *Sp*PBP2a
G43CR46STOPR	GATAACGACGCCAGAATTTTCAAATCGGACATACTTTGGGCTAATTTTTTTCGATCAC	Mutate Gly43 to Cys and Arg46 to Stop codon in *Sp*PBP2a
R30AF	GACTCTGATTCTACTATCTTAGCTCGCTCTCGTAGTGATCGAAAAAAATTAGCCC	Mutate Arg30 to Ala in *Sp*PBP2a$_{23-45}$
R30AR	GGGCTAATTTTTTTCGATCACTACGAGAGCGAGCTAAGATAGTAGAATCAGAGTC	Mutate Arg30 to Ala in *Sp*PBP2a$_{23-45}$
D35PF	CTATCTTACGTCGCTCTCGTAGTCCTCGAAAAAAATTAGCCCAAGTATGTCC	Mutate Asp35 to Pro in *Sp*PBP2a$_{23-45}$
D35PR	GGACATACTTGGGCTAATTTTTTTCGAGGACTACGAGAGCGACGTAAGATAG	Mutate Asp35 to Pro in *Sp*PBP2a$_{23-45}$
R33AF	GACTCTGATTCTACTATCTTACGTCGCTCTGCTAGTGATCGAAAAAAATTAGCCC	Mutate Arg33 to Ala in *Sp*PBP2a$_{23-45}$
R33AR	GGGCTAATTTTTTTCGATCACTAGCAGAGCGACGTAAGATAGTAGAATCAGAGTC	Mutate Arg33 to Ala in *Sp*PBP2a$_{23-45}$

S32AF	GACTCTGATTCTACTATCTTACGTCGCGCTCGTAG TGATCGAAAAAAATTAGCCC	Mutate Ser32 Ala in *Sp*PBP2a$_{23-45}$
S32AR	GGGCTAATTTTTTTCGATCACTACGAGCGCGACGT AAGATAGTAGAATCAGAGTC	Mutate Ser32 to Ala in *Sp*PBP2a$_{23-45}$
R30KF	GGACTCTGATTCTACTATCTTAAAGCGCTCTCGTA GTGATCGAAAAAAATTAG	Mutate Arg30 to Lys in *Sp*PBP2a$_{23-45}$
R30KR	CTAATTTTTTTCGATCACTACGAGAGCGCTTTAAG ATAGTAGAATCAGAGTCC	Mutate Arg30 to Lys in *Sp*PBP2a$_{23-45}$
R31KF	CAGGGTTCCATGGACTCTGATTCTACTATCTTACG TAAATCTCGTAGTGATCG	Mutate Arg31 to Lys in *Sp*PBP2a$_{23-45}$
R31KR	CGATCACTACGAGATTTACGTAAGATAGTAGAAT CAGAGTCCATGGAACCCTG	Mutate Arg31 to Lys in *Sp*PBP2a$_{23-45}$
R33KF	CTCTGATTCTACTATCTTACGTCGCTCTAAAAGTG ATCGAAAAAAATTAGCCCAAG	Mutate Arg33 to Lys in *Sp*PBP2a$_{23-45}$
R33KR	CTTGGGCTAATTTTTTTCGATCACTTTTAGAGCGA CGTAAGATAGTAGAATCAGAG	Mutate Arg33 to Lys in *Sp*PBP2a$_{23-45}$
R31KR33KF	CAGGGTTCCATGGACTCTGATTCTACTATCTTACG TAAATCTAAAAGTGATCG	Mutate Arg31 to Lys and Arg33 to Lys in *Sp*PBP2a$_{23-45}$
R31KR33KR	CGATCACTTTTAGATTTACGTAAGATAGTAGAATC AGAGTCCATGGAACCCTG	Mutate Arg31 to Lys and Arg33 to Lys in *Sp*PBP2a$_{23-45}$
R36AF	CTTACGTCGCTCTCGTAGTGATGCAAAAAAATTAG CCCAAGTATG	Mutate Arg36 to Ala in *Sp*PBP2a$_{23-45}$
R36AR	CATACTTGGGCTAATTTTTTTGCATCACTACGAGA GCGACGTAAG	Mutate Arg36 to Ala in *Sp*PBP2a$_{23-45}$
I28AL29AF	GTTCCATGGACTCTGATTCTACTGCCGCACGTCGC TCTCGTAGTGATCG	Mutate Ile28 to Ala and Leu 29 to Ala in *Sp*PBP2a$_{23-45}$
I28AL29AR	CGATCACTACGAGAGCGACGTGCGGCAGTAGAA TCAGAGTCCATGGAAC	Mutate Ile28 to Ala and Leu29 to Ala in *Sp*PBP2a$_{23-45}$
*Sp*PBP2x		
CysSerSTOPF	GAAAACAGACGCAGAGTTGGAAAAAGTCTGTGTT CATAATCTGTCTTTGTTTTTGCC	Mutate Ser30 to Cys, Leu31 to Ser and Leu32 to Stop codon in *Sp*PBP2x
CysSerSTOPR	GGCAAAAACAAAGACAGATTATGAACACAGACTT TTTCCAACTCTGCGTCTGTTTTC	Mutate Ser30 to Cys, Leu31 to Ser and Leu32 to Stop codon in *Sp*PBP2x
N21AF	GGAAATCGCCGGCTGAAGCCAGACGCAGAGTTG GAAAAAGTC	Mutate Asn21 to Ala in *Sp*BPB2x$_{12-31}$
N21AR	GACTTTTTCCAACTCTGCGTCTGGCTTCAGCCGGC GATTTCC	Mutate Asn21 to Ala in *Sp*BPB2x$_{12-31}$
R24KF	GGCTGAAAACAGACGCAAAGTTGGAAAAAGTCT GTGTTC	Mutate Arg24 to Lys in *Sp*BPB2x$_{12-31}^{N21A}$
R24KR	GAACACAGACTTTTTCCAACTTTGCGTCTGTTTTCA GCC	Mutate Arg24 to Lys in *Sp*BPB2x$_{12-31}^{N21A}$
R22KF	GGAAATCGCCGGCTGAAAACAAACGCAGAGTTG GAAAAAGTC	Mutate Arg22 to Lys in *Sp*BPB2x$_{12-31}^{N21A}$
R22KR	GACTTTTTCCAACTCTGCGTTTGTTTTCAGCCGGC GATTTCC	Mutate Arg22 to Lys in *Sp*BPB2x$_{12-31}^{N21A}$
*Sp*GpsB		
SPGPSBDELF	CCA CTA CTG AGA ATC TTT ATT TTC AGG GCG CCA TTA TTT TTT CAG CG	Deletion of residues 1-3 in *Sp*GpsB$_{1-63}$
SPGPSBDELR	CGC TGA AAA AAT AAT GGC GCC CTG AAA ATA AAG ATT CTC AGT AGT GG	Deletion of residues 1-3 in *Sp*GpsB$_{1-63}$
D33AF	GTAGAAGTTGACGAGTTTTTAGCCGATGTCATCA AGGACTATG	Mutate Asp33 to Ala in *Sp*GpsB$_{4-63}$
D33AR	CATAGTCCTTGATGACATCGGCTAAAAACTCGTCA ACTTCTAC	Mutate Asp33 to Ala in *Sp*GpsB$_{4-63}$
*Lm*ReoM		
T7AF	GCCATGGATTCAAAAGATCAAGCAATGTTTTACA ACTTCGGCGATGATTC	Mutate Thr7 to Ala in *Lm*ReoM
T7AR	GAATCATCGCCGAAGTTGTAAAACATTGCTTGATC TTTTGAATCCATGGC	Mutate Thr7 to Ala in *Lm*ReoM
T7DF	GGGCGCCATGGATTCAAAAGATCAAGACATGTTT TACAACTTCGGCGATGATTC	Mutate Thr7 to Asp in *Lm*ReoM
T7DR	GAATCATCGCCGAAGTTGTAAAACATGTCTTGATC TTTTGAATCCATGGCGCCC	Mutate Thr7 to Asp in *Lm*ReoM
*Lm*PrkA		
S169AF	CATCTATTACACAAACGAATGCTTTACTAGGTTCG GTGCATTAC	Mutate Ser169 to Ala in *Lm*PrkA-KD
S169AR	GTAATGCACCGAACCTAGTAAAGCATTCGTTTGT GTAATAGATG	Mutate Ser169 to Ala in *Lm*PrkA-KD
S160AF	GATTTTGGTATTGCAATGGCACTTGCAGAAACATC TATTACACAAAC	Mutate Ser160 to Ala in *Lm*PrkA-KD

S160AR	GTTTGTGTAATAGATGTTTCTGCAAGTGCCATTGCAATACCAAAATC	Mutate Ser160 to Ala in *Lm*PrkA-KD
S163AF	GCAATGGCACTTTCAGAAACAGCTATTACACAAACGAATTCTTTAC	Mutate Ser163 to Ala in *Lm*PrkA-KD
S163AR	GTAAAGAATTCGTTTGTGTAATAGCTGTTTCTGAAAGTGCCATTGC	Mutate Ser163 to Ala in *Lm*PrkA-KD
S169DF	CATCTATTACACAAACGAATGATTTACTAGGTTCGGTGCATTACTTATCCCC	Mutate Ser169 to Asp in *Lm*PrkA-KD
S169DR	GGGGATAAGTAATGCACCGAACCTAGTAAATCATTCGTTTGTGTAATAGATG	Mutate Ser169 to Asp in *Lm*PrkA-KD
S173AF	CAAACGAATTCTTTACTAGGTGCGGTGCATTACTTATCCCCAG	Mutate Ser173 to Ala in *Lm*PrkA-KD
S173AR	CTGGGGATAAGTAATGCACCGCACCTAGTAAAGAATTCGTTTG	Mutate Ser173 to Ala in *Lm*PrkA-KD
S173DF	CACAAACGAATTCTTTACTAGGTGATGTGCATTACTTATCCCCAGAACAAGC	Mutate Ser173 to Asp in *Lm*PrkA-KD
S173DR	GCTTGTTCTGGGGATAAGTAATGCACATCACCTAGTAAAGAATTCGTTTGTG	Mutate Ser173 to Asp in *Lm*PrkA-KD
T162AF	GCAATGGCACTTTCAGAAGCATCTATTACACAAACGAATTCTTTAC	Mutate Thr162 to Ala in *Lm*PrkA-KD
T162AR	GTAAAGAATTCGTTTGTGTAATAGATGCTTCTGAAAGTGCCATTGC	Mutate Thr162 to Ala in *Lm*PrkA-KD
T165AF	GGCACTTTCAGAAACATCTATTGCACAAACGAATTCTTTACTAGG	Mutate Thr165 to Ala in *Lm*PrkA-KD
T165AR	CCTAGTAAAGAATTCGTTTGTGCAATAGATGTTTCTGAAAGTGCC	Mutate Thr165 to Ala in *Lm*PrkA-KD
T167AF	GAAACATCTATTACACAAGCGAATTCTTTACTAGGTTCGGTG	Mutate Thr167 to Ala in *Lm*PrkA-KD
T167AR	CACCGAACCTAGTAAAGAATTCGCTTGTGTAATAGATGTTTC	Mutate Thr167 to Ala in *Lm*PrkA-KD
G18DELF	CAATAGGCGGCGGAATGGCCAATGTG	Deletion of Gly18 in *Lm*PrkA-KD
G18DELR	CACATTGGCCATTCCGCCGCCTATTG	Deletion of Gly18 in *Lm*PrkA-KD

Table Apx B.1: Mutagenic primers used in this study

Primer	Sequence 5' to 3'	Cloning
SPGPSBF	GCTATACCATGGCAAGTATTATTTTTTCAGCG	Cloning *Sp*GpsB residues 1-64 into pETM11 at *Nco*I and *Xho*I sites
SPGPSBR	CGATATCTCGAGTAACTACTTAAAAATCTGAGTTATC	Cloning *Sp*GpsB residues 1-64 into pETM11 at *Nco*I and *Xho*I sites
REOMF	GCTATACCATGGATTCAAAAGATCAAACAATGTTTTACAAC	Cloning ReoM (*lmo*1503) into pETM11 at *Nco*I and *Xho*I sites
REOMR	CGATATCTCGAGTCATTTCTCACCAATTTCGTTATTTTTCAG	Cloning ReoM (*lmo*1503) into pETM11 at *Nco*I and *Xho*I sites
PRKAF	GCTATACCATGGCAATGATGATTGGTAAGCGATTAAGCG	Cloning PrkA-KD (*lmo*1820) into pETM11 at *Nco*I and *Xho*I sites
PRKAR	CGATATCTCGAGTCATTTTTTCTTTTTCTTATCTTTTTTCTCCTCAGG	Cloning PrkA-KD (*lmo*1820) into pETM11 at *Nco*I and *Xho*I sites
PRKPF	GCTATACCATGGCAATGCATGCAGAATTTAGAACAGATAGAG	Cloning PrkP (*lmo*1821) into pETM11 at *Nco*I and *Xho*I sites
PRKPR	CGATATCTCGAGTCATGAAGCATCCCTCCCTTTC	Cloning PrkP (*lmo*1821) into pETM11 at *Nco*I and *Xho*I sites
PBPA1F	GATTTTCCATGGCAGATAAACCGCAGACAAG	Cloning *Lm*PBPA1 into pMAT11 between *Nco*I and *Xho*I sites
PBPA1R	GTAGACCCTCGAGAACGTTTTACTTGGGTTGCATAGTTATAAC	Cloning *Lm*PBPA1 into pMAT11 between *Nco*I and *Xho*I sites
PBP2AF	GCTGCGACTCTGGCAGGGATGCTCGAGGGGCCGG	Cloning *Sp*PBP2a into pMAT11 between *Nco*I and *Xho*I sites
PBP2AR	CCGGCCCCTCGAGCATCCCTGCCAGAGTCGCAGC	Cloning *Sp*PBP2a into pMAT11 between *Nco*I and *Xho*I sites
PBP2XF	GACTTTTTCTCGAGGTTTTGCACACTCAAGTAACG	Cloning *Sp*PBP2x into pMAT11 between *Nco*I and *Xho*I sites
PBP2XR	CAAAACCTCGAGAAAAAGTCATCATTCTGCC	Cloning *Sp*PBP2x into pMAT11 between *Nco*I and *Xho*I sites

Table Apx B.2: Primers for the construction of plasmids expressing recombinant proteins

Papers Arising from This Study

Cleverley, R.M., Rutter, Z.J., Rismondo, J., Corona, F., Tsui, H.-C.T., Alatawi, F.A., Daniel, R.A., Halbedel, S., Massidda, O., Winkler, M.E. & Lewis, R.J. (2019) The cell cycle regulator GpsB functions as cytosolic adaptor for multiple cell wall enzymes. Nature Communications. 10 (1), 261

Wamp, S., Rutter, Z.J., Rismondo, J., Jennings, C.E., Möller, L., Lewis, R.J. & Halbedel, S. (2020) PrkA controls peptidoglycan biosynthesis through the essential phosphorylation of ReoM. eLife. 9 (e56048), 1–75